Technische Universität München
Fakultät für Physik

Max-Planck-Institut für Physik
(Werner-Heisenberg-Institut)

CLAWS - a novel time resolved study of backgrounds during the first commissioning phase of SuperKEKB

Dissertation by

Miroslav Alois Aaron Maria Gabriel

München, November 2019

TECHNISCHE UNIVERSITÄT MÜNCHEN
Fakultät für Physik

Max-Planck-Institut für Physik
(Werner-Heisenberg-Institut)

CLAWS - a novel time resolved study of backgrounds during the first commissioning phase of SuperKEKB

Miroslav Alois Aaron Maria Gabriel

Vollständiger Abdruck der von der Fakultät für Physik der Technischen Universität München zur Erlangung des akademischen Grades eines

Doktors der Naturwissenschaften (Dr. rer. nat.)

genehmigten Dissertation.

Vorsitzende:

Prof. Dr. Nora Brambilla

Prüfer der Dissertation:

1. Hon.-Prof. Dr. Allen C. Caldwell
2. Prof. Dr. Stephan Paul

Die Dissertation wurde am 13.09.2019 bei der Technischen Universität München eingereicht und durch die Fakultät für Physik am 30.10.2019 angenommen.

Abstract

The asymmetric e^+e^- collider SuperKEKB is a second generation flavor factory designed to achieve an unprecedented luminosity of $8 \cdot 10^{35}\,\mathrm{cm}^{-2}\mathrm{s}^{-1}$, a factor 40 higher than its record-breaking predecessor KEKB. This ambitious design luminosity is expected to cause challenging levels of beam backgrounds for various subsystems of the corresponding Belle II experiment, in particular for its pixel vertex detector. Understanding and mitigating these beam backgrounds early on is critical for the successful operation of SuperKEKB and Belle II. In particular, backgrounds related to continuous top-up injections of new particles can not be simulated with sufficient accuracy and have to be determined by direct measurements. Phase 1 of the commissioning of SuperKEKB in 2016 focused on the basic operation of the accelerator and thus the detector and the final focusing systems were not installed and no collisions took place. A suite of dedicated beam background detectors collectively known as BEAST II used this collision-free environment to study beam-induced backgrounds. One of these detectors is the CLAWS experiment.

This thesis describes the sensor technology and the overall setup of CLAWS and presents the measurements of beam-induced backgrounds it performed. The detector system consists of eight plastic scintillator tiles with directly coupled SiPMs read out continuously over up to several milliseconds. The sub-nanosecond time resolution and single particle energy resolution of the sensors allow bunch-by-bunch measurements, enable CLAWS to perform a novel time resolved analysis of beam backgrounds and make it uniquely suited for the study of injection backgrounds. We present measurements of various aspects of regular and injection backgrounds which include particle composition of regular backgrounds, time structure and decay behavior of injection backgrounds, hit energy spectra and overall background rates. These measurements show that in both rings the majority of the injection backgrounds are typically observed withing the first 500 µs after the injection. Another major finding is that the time structure of injection backgrounds is determined by different timing patterns connected to properties of the accelerator, such as betatron and synchrotron oscillations. We directly determine the frequencies of these patterns from detector data, mostly with sub-nanosecond precision. In addition, beam-gas and Touschek backgrounds are measured in a dedicated background study and are compared to simulations. We find a clear excess in data over simulation which ranges from a factor three up to two orders of magnitude. The studies presented in this thesis make several noteworthy contributions to advancing the understanding of beam-induced backgrounds and injection mechanisms in high luminosity flavor factories. The described sensor technology and analysis methodology also serve as the basis for upgraded versions of the CLAWS detector system which will monitor beam backgrounds during Phase 2 and full physics operation of SuperKEKB.

Contents

Chapter 1

Introduction

Particle accelerators play a key role in advancing our understanding of the basic constituents of matter and their interactions. At the heart of our current understanding is the Standard Model (SM) of particle physics which is a remarkable achievement of modern physics.

However, while it is extremely successful in describing subatomic processes at energy scales up to $\mathcal{O}(1\text{ TeV})$ the SM fails to explain many significant observations. Several measurements, which are dating back as far as the 1930s, implicate the existence of *dark matter* and *dark energy* but the SM does not provide suitable explanations for them [1]. Despite the fact that its prediction was a great accomplishment of the SM, the true nature of the Higgs boson is another topic of major interest. It is still unclear whether the boson found at the LHC [2, 3] is the only such particle or if it is part of a broader Higgs sector together with other Higgs-like particles, as for example suggested by supersymmetry. Up to now, it is also unknown how to incorporate the masses of the neutrinos [4, 5] or if the neutrinos themselves are in fact their own antiparticles (*Majorana particles*). And it is unclear if the three fundamental interactions of the SM, the electromagnetic, the weak and the strong interaction, can be unified into a single force and if gravity can also be described by a field theory.

Several of the most significant open issues are connected to the flavor sector of the SM. We have strong evidence that there are exactly three generations of fermions, and yet the SM does not provide a reason for such an arrangement or the related hierarchy of the fermion masses. It also can not explain why the Cabibbo-Kobayashi-Maskawa (CKM) matrix, describing the mixing of quarks, is almost diagonal while the Pontecorvo-Maki-Nakagawa-Sakata (PMNS) matrix, describing the mixing of leptons, is comparatively uniform. Central to flavor physics is the study of the violation of the charge-parity (CP)

symmetry. This CP violation is a necessary requirement for the evolution of a matter dominated universe as we observe it. To date, CP violation has been observed in the quark sector, where it was first discovered in the Kaon system [6], and CP conservation has been excluded in the neutrino sector with a confidence level of 90% [7, 8]. In the quark sector, it was widely studied by precision measurements of the decays of a large amount of B-meson pairs in the so-called B or flavor factories LCHb [9], BaBar [10] and, most importantly, Belle [11]. The observed violation, however, is many orders of magnitude too small to explain the matter-antimatter asymmetry in the universe. It can therefore be assumed that there are additional yet undiscovered sources of CP asymmetry which require new mechanisms.

Taken together, theses open questions suggest that the SM is only an effective theory for the description of the known elementary particles and their interactions and can not serve as the final theory of particle physics. Instead, there is a variety of New Physics (NP) scenarios which propose a large number of new particles and processes in order to answer the open questions and to extend the SM beyond its shortcomings.

These open questions are studied widely in high energy physics by extensively searching for NP phenomena. This search is carried out via two complementary approaches. At the energy frontier, the ATLAS [12] and CMS [13] experiments at the LHC [14] are seeking to discover new particles which are directly produced in proton-proton collisions with center-of-mass energies of up to 14 TeV. At the intensity frontier, on the other hand, signatures of new particles or processes can be observed by probing the predictions of the SM for discrepancies in precision measurements and by looking for rare reactions which are naturally suppressed in the SM. These searches are being pursued by the LHCb, Belle and BaBar experiments, as well as the next generation of flavor factories.

The SuperKEKB accelerator [15] and the corresponding Belle II experiment [16] are such a next generation flavor factory with the main aim of probing the flavor sector with highest precision. They are direct upgrades of their predecessors KEKB and Belle located in Tsukuba, Japan and are operated by the Japanese High Energy Research Organization (KEK). SuperKEKB is an asymmetric energy electron-positron collider designed for different center-of-mass energies which correspond to the Υ resonances $(1S)$ through $(6S)$. The majority of the run time, however, will be spent to operate the machine at an energy which corresponds to the mass of the $\Upsilon(4S)$ of 10.58 GeV, where it is possible to produce a large number of B-meson pairs without additional particles. The energy asymmetry of the 7 GeV electrons in the high energy ring (HER) and the 4 GeV positrons in the low energy ring (LER) boosts the center-of-mass system relative to the laboratory system, which enables measurements of time-dependent CP violation.

Compared to KEKB, SuperKEKB has a 40 times higher design luminosity of an unprecedented $8 \cdot 10^{35}\,\mathrm{cm}^{-2}\mathrm{s}^{-1}$.

With the new flavor factory, the focus will shift from simply confirming the theory of the SM, as done at Belle, to specifically searching for deviations from its predictions which could hint at NP phenomena. Central to the majority of these measurements is the particle identification and the track reconstruction performed by the newly equipped inner detector systems and, in particular, its pixel vertex detector (PXD). It is intended that Belle II will accumulate $50\,\mathrm{ab}^{-1}$ over a time of 5 years.

The ambitious design luminosity is expected to cause challenging levels of beam-induced backgrounds for the Belle II experiment. Current simulations for the full design luminosity predict that the lifetimes and the performance of various subsystems of Belle II are significantly impacted by the different types of backgrounds. It is of the utmost importance to confirm and review the significance and the accuracy of these predictions by experimental results. Of particular interest are backgrounds related to the continuous top-up injection of new particles, or *injection backgrounds*, since they can not be simulated with sufficient precision and have to be determined by direct measurement.

In order to prime SuperKEKB and Belle II for physics operation and full luminosities, an extensive commissioning campaign is performed. This campaign is divided into three phases. The work presented in this thesis is based on measurements performed during the runtime of the first commissioning phase, or Phase 1, in 2016. Phase 1 focused on the basic operation of SuperKEKB and thus the final focusing system and the Belle II detector have not yet been installed at the IP and no intended collisions took place. Focused beams and collisions are always accompanied by luminosity dependent backgrounds which make up a significant part of the overall backgrounds. Measurements performed during Phase 1, by contrast, represent the unique opportunity to independently study single beam and injection backgrounds in a collision-free environment. For this purpose, we installed a set of dedicated beam background detectors at the IP to which we collectively refer to as BEAST II. The main objectives of the BEAST II experiment are the following: verifying that radiation levels are safe for the installation of Belle II, validating beam background simulations and providing real time feedback to the operators of the accelerator on how machine parameters influence background levels at the IP.

One of the subsystems of BEAST II is the CLAWS detector system. On February 10th and 26th 2016, CLAWS observed the very first beam bunches which were successfully circulated in the LER and the HER of SuperKEKB, respectively [17]. Its name originates from the employed sensor technology and is an acronym for s**C**intillating **L**ight **A**nd **W**aveform **S**ensors. This thesis presents the detectors and the overall installation of

CLAWS, discusses how the recorded data is processed, and, most importantly, describes the measurements it performed during Phase 1. The detector system consists of several plastic scintillators with directly coupled silicon photomultipliers (SiPM) read out by electronics and a custom DAQ which are capable of continuously recording data over periods up to several milliseconds. The detectors are primarily sensitive to charged particles, but in principle also show responses to high-energy photons and to MeV neutrons. The goal of the CLAWS experiment is a novel time resolved analysis of backgrounds during the first commissioning phase. A time resolved analysis here implies three things: the achieved time and energy resolutions are sufficient to resolve energy deposits of single particles which allows us to infer the type of background particles and the responsible background process. Second, the achieved time resolution is well below the expected maximum rate of signals given by the bunch spacing and, thus, we are able to map energy deposits to single bunches. And third, the length of the measurement covers several milliseconds which is sufficient to study the time evolution of backgrounds over hundreds of revolutions in the rings. The last two capabilities are imperative for the investigation of backgrounds connected to continuous top-up injections. Such injection backgrounds require an interruption of data taking in several subsystems of Belle II, in particular in the PXD, and, thus, substantially reduce the data taking efficiency. Due to their significant impact on the physics program, injection backgrounds represent the primary concern of CLAWS. The presented findings provide an important opportunity to advance the understanding of backgrounds and injection mechanisms in high luminosity flavor factories.

Including this introductory chapter, this thesis is subdivided into eleven chapters. Chapter 2 begins by laying out the theoretical motivation for the research performed by SuperKEKB and Belle II. Subsequently, the Chapters 3 and 4 give a brief overview of the SuperKEKB accelerator, the Belle II detector and the BEAST II experiment, including a description of the different sources of beam backgrounds. In Chapter 5, we present the experimental setup of CLAWS by describing its sensors, readout hardware and data acquisition (DAQ) software. Chapter 6 describes the data processing, which is the basis for the analyses performed in the following chapters.

Having introduced the setup and the underlying procedures, we turn to the discussion of the findings from the CLAWS experiment. In Chapter 7, we present a comprehensive time resolved analysis of beam backgrounds which focuses especially on backgrounds caused by continuous top-up injections. We also describe a number of different timing patterns encountered in the data and motivate how they are dictated by the betatron and synchrotron oscillations performed by the beam particles while propagating along the beam lines. Building on this, Chapter 8 presents a novel analysis of these timing patterns. As part of BEAST II, CLAWS also participated in a comprehensive program of non-injection background studies. In Chapter 9, we present results of one of these studies based solely on CLAWS data. This study demonstrates a combined measurement of beam-gas and Touschek backgrounds and a method for disentangling both types of backgrounds in experimental data. Chapter 10 summarizes the key findings of CLAWS, briefly discusses their implications for the Belle II experiment and and concludes by giving an outlook for Phases 2 and 3 of the commissioning campaign, as well as the further operation of SuperKEKB and Belle II.

Chapter 2

Theoretical concepts and physics at Belle II

In this chapter, we provide a brief overview of the theory of flavor physics and motivate the research that will be performed by SuperKEKB and Belle II. We focus here on the underlying concepts and their phenomenological aspects rather than discussing calculations in too much detail. For more elaborate reviews on the theory of flavor physics see [18–21]; a comprehensive overview of the intended physics program of Belle II is given in [22, 23].

We begin by briefly introducing the theoretical concepts relevant to flavor physics in Section 2.1. Since measurements of Belle II are largely based on various decays of B-mesons, these concepts are then extended to the B system in Section 2.2. Finally, we provide a brief overview of the physics prospects of Belle II in Section 2.3.

2.1 Flavor physics and CP violation in a nutshell

The field of *flavor physics* is concerned with transitions between different kinds (flavors) of fermions. Within the SM, weak interactions involving $\mathrm{W}^{\pm}$ bosons are the only processes which are capable of such changes of the flavor. These weak interactions are also the only operation (in the SM) which can give rise to differences in the decay patterns of matter and antimatter ("CP violation") required to explain the observation of a matter dominated universe. Flavor physics is thus closely related to the study of CP violation and holds the key to several of the most important issues of present particle physics.

The following section introduces the basic concepts of flavor physics and CP violation. It begins by establishing the terms C, P and T symmetries in Section 2.1.1. This is followed by a description of the weak interactions of quarks and the mechanism of the CKM matrix in Sections 2.1.2 and 2.1.3, respectively. Finally, in Sections 2.1.4 and 2.1.5 these concepts are consolidated by applying them to the neutral kaon system and introducing the *unitarity triangles*.

2.1.1 C, P and T symmetry

Symmetries play a fundamental role in our current description of particle physics. According to Noether's theorem [24], every symmetry of the Lagrangian can be directly associated with a conservation law what is widely exploited to simplify calculations and offers great insights into the underlying laws. An invariance under translations in space, for example, implies the conservation of the total momentum of a system. Most interestingly, the discrete C, P and T symmetries and, in particular, the violation of the same are closely related to the field of flavor physics. In the following, we formally define these symmetries and briefly introduce the concept of violation of the CP symmetry.

- **P symmetry** A *parity conjugation* represents a spatial inversion through the origin of the coordinate system which is equivalent to a mirror reflection and a subsequent rotation by 180°. In that way, the coordinates, x, the momentum, p, and the angular momentum, l, translate as follows:

  $$\begin{aligned}\hat{P}\left|x\right\rangle &= \left|-x\right\rangle ,\\ \hat{P}\left|p\right\rangle &= \left|-p\right\rangle ,\\ \hat{P}\left|l\right\rangle &= \left|l\right\rangle .\end{aligned}$$

  In quantum mechanics, a parity transformation is performed by the parity operator, $\hat{P}$. The outcome of the application of $\hat{P}$ is defined as the P *parity* and corresponds to an observable property of a quantum-mechanical system. In that way, $\hat{P}$ either yields an eigenvalue of $+1$, what is referred to as *positive parity*, or -1 what indicates *negative parity*. An interaction is symmetric with respect to parity conjugations when the P parity is conserved.
  An intrinsic parity can be assigned to all fundamental particles. By definition, spin-half particles possess positive parity, whereas their antiparticles and the vector bosons mediating the electromagnetic, weak and strong forces all carry negative parity. The parity of multiparticle states is determined by the product of all intrinsic parities multiplied by a factor of $(-1)^L$, where L is the angular momentum of the combined system.

Furthermore, also physical quantities can be classified based on their behavior under parity conjugations. Scalar and axial vector quantities,[1] as for example the mass or the angular momentum of a particle, are invariant. Pseudoscalar and vector quantities like the helicity or the momentum, on the other hand, do change their sign under parity transformations.

- ***C* symmetry** A *charge conjugation* transforms a particle, q, into its corresponding antiparticle, $\overline{q}$, and vice versa:

  $$\hat{C}\left|q\right\rangle = \left|\overline{q}\right\rangle ,$$

  where $\hat{C}$ is the charge conjugation operator. In that way, $\hat{C}$ inverts the signs of all quantum charges like electric charge and of all flavor charges such as strangeness, but it does not affect the momentum, the angular momentum or the spin.
  Eigenstates of $\hat{C}$ possess a dedicated quantum number which is referred to as *C parity*. Note that only neutral systems such as the photon or particle-antiparticle bound states constitute eigenstates of $\hat{C}$. An interaction is invariant under a charge conjugation, also referred to as symmetric with respect to the C symmetry, if the C parity is conserved. In other words, the interaction of the charge conjugated system must occur with the same rate and kinematics as for the original system.

- ***T* symmetry** Similar to a charge or a parity conjugation, a *time reversal* is a symmetry operation which reverses the direction of motion (i.e. the momentum) and the angular momentum of a particle but does not affect its position or charge:

  $$\begin{aligned}\hat{T}\left|p\right\rangle &= \left|-p\right\rangle ,\\ \hat{T}\left|l\right\rangle &= \left|-l\right\rangle ,\\ \hat{T}\left|x\right\rangle &= \left|x\right\rangle ,\\ \hat{T}\left|q\right\rangle &= \left|q\right\rangle .\end{aligned}$$

  In other words, T symmetry implies that for a given interaction with certain initial and final states the time reversed version of this interaction will return from the predefined final state to the exact same initial state.
  On a macroscopic scale, T symmetry is clearly not conserved as exemplified by the second law of thermodynamics. On a microscopic scale, on the other hand, T symmetry is generally conserved in interactions.

---

[1] Axial vector quantities are generated by the cross product of two vector quantities.

The C parity as well as the P parity are conserved in electromagnetic and strong interactions. The vector minus axial-vector ("$V - A$") chiral structure of the charged-current, however, implies that parity is maximally violated in weak interactions. The maximal violation of C symmetry is evident in the case of a charge conjugation of left-handed fermions into left-handed antifermions, which generally do not participate in weak interactions. In the same way, P symmetry is violated since a parity conjugation generates left-handed antineutrinos by reversing the momentum of the particles but leaving their spins unaffected, which are not observable in nature.[2]

A successive application of a charge and a parity conjugation, on the other hand, transforms left-handed fermions into right-handed antifermions leading again to valid physical states. Weak interactions therefore seem to be invariant with respect to such a combined CP symmetry what is referred to as *CP conservation*. Furthermore, the *CPT theorem* [26] states that all local Lorentz-invariant Quantum Field Theories have to be invariant under combined C, P and T transformations. In other words, a conservation of Lorentz invariance necessarily requires a conservation of CPT which is believed to be an exact symmetry of the universe. Note that a conservation of CP symmetry thus also implies a conservation of T symmetry and vice versa.

As pointed out earlier however, there is a major problem with the conservation of CP symmetry: the development of a matter dominated universe as we observe it necessarily requires CP violation [27]. And in fact, slight violations of the CP symmetry can be observed in weak interactions in the quark sector and are very actively searched for in the lepton sector. The CP violation in the quark sector is further discussed in the following sections.

2.1.2 The weak interaction of quarks

Having introduced the concept of P, C, T and CP symmetries, we now move on to describing weak processes involving quarks. We also demonstrate how these interactions can violate the CP symmetry by discussing the mixing of neutral mesons.

An important example for a weak charged current interaction in which the flavor of a participating quark is changed is the β-decay of neutrons, as illustrated in Figure 2.1 (*left*). First, one of the down quarks of the neutron is converted to an up quark (which has a slightly different mass and a charge of $\frac{2}{3}$ instead of $-\frac{1}{3}$ of the elementary charge) by the emission of an intermediate W boson. Subsequently, the W decays into an e^- and a corresponding $\overline{\nu}_\mathrm{e}$. The probability for such a decay to occur is proportional to the

---

[2] P parity violation was confirmed in β-decays of polarized nuclei by Wu et al. in 1957 [25].

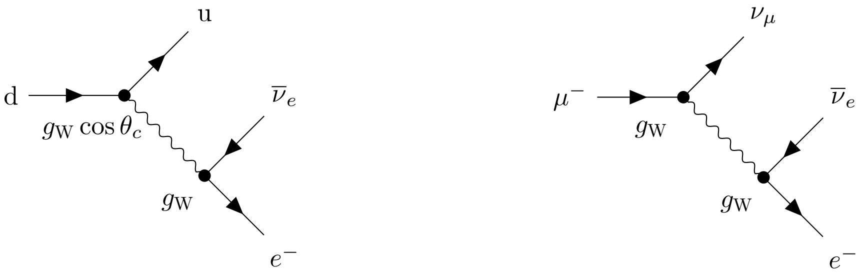

Figure 2.1: Lowest-order Feynman diagrams for the underlying process in the β-decay of a neutron (*left*) and the μ^--decay (*right*).

matrix element squared, $|M|^2$. The matrix element itself is proportional to the coupling strength at the ud quark vertex, as well as to the coupling strength at the $\overline{\nu}_e e^-$ lepton vertex. The strength of the weak interactions between the W and the fermions at one of the vertices is determined by the weak coupling constant, g_W. For an universal coupling strength, the couplings at the vertices of an equivalent muon decay should be identical, as illustrated in Figure 2.1 (*right*). Most interestingly however, it was found that the coupling at the ud vertex of the β-decay is about 5% smaller than at the corresponding $\mu^-\overline{\nu}_\mu$ vertex, suggesting a non-uniformity of the weak interaction. Similar observations were also made for certain hadronic decay modes such as the strongly suppressed decay rate in $K^- \to \mu^-\overline{\nu}_\mu$.

Cabibbo was the first who argued that a universal coupling strength can still be maintained if the weak eigenstates of the quarks are not identical to their mass eigenstates [28]. Extended by a fourth quark (charm),[3] the Cabibbo mechanism states that the weak eigenstates, indicated by d′ and s′, are connected to the mass eigenstates, d and s, by a unitary 2 × 2 matrix:

$$\begin{pmatrix} \mathrm{d}' \\ \mathrm{s}' \end{pmatrix} = \begin{pmatrix} \cos\,\theta_c & \sin\,\theta_c \\ -\sin\,\theta_c & \cos\,\theta_c \end{pmatrix} \begin{pmatrix} \mathrm{d} \\ \mathrm{s} \end{pmatrix},$$

where θ_c is referred to as the Cabibbo angle. That means in interactions involving charged currents, the mass eigenstate $|\mathrm{u}\rangle$ is not interacting with the mass eigenstate $|\mathrm{d}\rangle$ but with the linear combination $|\mathrm{d}'\rangle = \cos\theta_C\,|\mathrm{d}\rangle + \sin\theta_C\,|\mathrm{s}\rangle$. Note that it is purely conventional if the ds pair or the uc pair or both are rotated, only the relative angle counts.

In that way, the coupling strength at the ud vertex in the β-decay is modified by $g_W \cos\theta_c$.

---

[3] In 1974, Glashow, Illiopoulus and Maiani extended the Cabibbo mechanism by predicting the charm quark in order to explain the lower than anticipated branching ratio of the neutral kaon decay $K_L \to \mu^+\mu^-$ [29].

After accounting for phase space, the Cabibbo hypothesis with an angle of $\theta_c \approx 13°$ accurately describes the rates observed in β-decays and similar processes. Furthermore, it restores the universality of the weak interaction.

2.1.3 The CKM matrix

To be able to incorporate *CP* violation in the SM, the mixing matrix needs to contain an irreducible complex phase which is unequal to zero. Since the only parameter of the 2×2 matrix is a real angle, the concept of the Cabibbo mechanism was extended to include a third generation of quarks (t and b). Their weak interactions are then described by the unitary Cabibbo-Kobayashi-Mask (CKM) matrix, V_{CKM}, which, as before, relates the weak eigenstates, d′, s′ and b′, to their mass eigenstates, d, s and b:

$$\begin{pmatrix} \mathrm{d}' \\ \mathrm{s}' \\ \mathrm{b}' \end{pmatrix} = \begin{pmatrix} V_{\text{ud}} & V_{\text{us}} & V_{\text{ub}} \\ V_{\text{cd}} & V_{\text{cs}} & V_{\text{cb}} \\ V_{\text{td}} & V_{\text{ts}} & V_{\text{tb}} \end{pmatrix} \begin{pmatrix} \mathrm{d} \\ \mathrm{s} \\ \mathrm{b} \end{pmatrix} .$$

The coupling strength at the vertex for a transition from a quark of type i to a quark of type j is given by the respective matrix element, V_{ij}. That means the $\cos\theta_C$ term encountered earlier simply corresponds to V_{ud}. The probability for such a transition is then proportional to $|V_{ij}|^2$. For *CPT* symmetry to be conserved, the CKM matrix necessarily needs be unitary and hence the matrix elements are correlated.

Generally, the CKM matrix can be described by four independent parameters: three real rotational angles and a complex phase. While there are different ways of defining the matrix, a rather common representation is given by

$$\begin{pmatrix} V_{\text{ud}} & V_{\text{us}} & V_{\text{ub}} \\ V_{\text{cd}} & V_{\text{cs}} & V_{\text{cb}} \\ V_{\text{td}} & V_{\text{ts}} & V_{\text{tb}} \end{pmatrix} = \begin{pmatrix} 1 & 0 & 0 \\ 0 & c_{23} & s_{23} \\ 0 & -s_{23} & c_{23} \end{pmatrix} \times \begin{pmatrix} c_{13} & 0 & s_{13}e^{-i\delta} \\ 0 & 1 & 0 \\ -s_{13}e^{i\delta} & 0 & c_{13} \end{pmatrix} \times \begin{pmatrix} c_{12} & s_{12} & 0 \\ -s_{12} & c_{12} & 0 \\ 0 & 0 & 1 \end{pmatrix} ,$$

where $s_{ij} = \sin\theta_{ij}$ and $c_{ij} = \cos\theta_{ij}$; θ_{12}, θ_{13} and θ_{23} are the three angles; and δ represents the complex phase. Note that the angle θ_{12} corresponds to the Cabibbo angle, θ_c, discussed for the case of two quark families and is the largest of the mixing angles. In order for *CP* violation to occur in the quark sector, the parameter δ then needs to be unequal to zero.

It can be beneficial to express the elements of the matrix in terms of an expansion in the comparably small but real parameter $\lambda = \sin\theta_{12} \approx 0.22$. In addition, three other real parameters, A, ρ and η, are defined such that

$$A\lambda^2 = \sin\theta_{23} \quad \text{and} \quad A\lambda^3(\rho - i\eta) = \sin\theta_{13}e^{-i\delta}.$$

Up to $\mathcal{O}(\lambda^4)$, the CKM matrix can then be written as

$$V_{CKM} = \begin{pmatrix} 1-\lambda^2/2 & \lambda & A\lambda^3(\rho - i\eta) \\ -\lambda & 1-\lambda^2/2 & A\lambda^2 \\ A\lambda^3(1-\rho-i\eta) & -A\lambda^2 & 1 \end{pmatrix} + \mathcal{O}(\lambda^4). \tag{2.1}$$

This widely used representation is referred to as the Wolfenstein parameterization [30]. It has the advantage that all the complex components of the CKM matrix are located entirely in the entries V_{ub} and V_{td} and that the parameter η is responsible for the complex phase.[4]

Each of the nine individual elements in the CKM matrix is connected to a different transition between quarks which allows to measure them separately. The magnitudes of the elements can hence be obtained in experimental measurements of decay rates and branching ratios of various transitions. As shown earlier, $|V_{\text{ud}}|$ can be determined from superallowed nuclear β-decays. The values of $|V_{\text{us}}|$ and $|V_{\text{cs}}|$ are obtained from processes such as $\mathrm{K}^0 \to \pi^- e^+ \nu_e$ and $D_s^+ \to \mu^+\nu_\mu$, whereas $|V_{\text{cd}}|$ can be studied in deep inelastic neutrino-nucleon scattering. The elements $|V_{\text{ub}}|$, $|V_{\text{cb}}|$, $|V_{\text{td}}|$ and $|V_{\text{ts}}|$ can be most precisely determined at so called *flavor factories* such as SuperKEKB and Belle II where they are studied in decays of large amounts of B-mesons (see Sections 2.2 and 2.3). However, the approach of measuring decay rates and branching fractions fails to provide any information about the complex phase. For this purpose, it is necessary to find processes which are sensitive to the amplitude of the respective elements such as certain measurements in the neutral kaon and B-meson systems.

2.1.4 CP violation in the kaon system

The neutral kaon system allows us to examine the weak interactions of quarks introduced in the previous sections with respect to *CP* violation. The $\mathrm{K}^0(\mathrm{d\bar{s}})$ and its antiparticle $\overline{\mathrm{K}}^0(\mathrm{\bar{d}s})$ are the lightest mesons containing strange quarks and can hence only decay via (flavor changing) weak interactions. The $\mathrm{K}^0(\mathrm{d\bar{s}})$ and the $\overline{\mathrm{K}}^0(\mathrm{\bar{d}s})$ represent eigenstates of the strong interaction and are also referred to as the *flavor states.* They have a definite quark content and are convenient to understand the production and decay of

---

[4] Note that this neglects terms of $\mathcal{O}(\lambda^5)$ included in V_{cd} and V_{ts}.

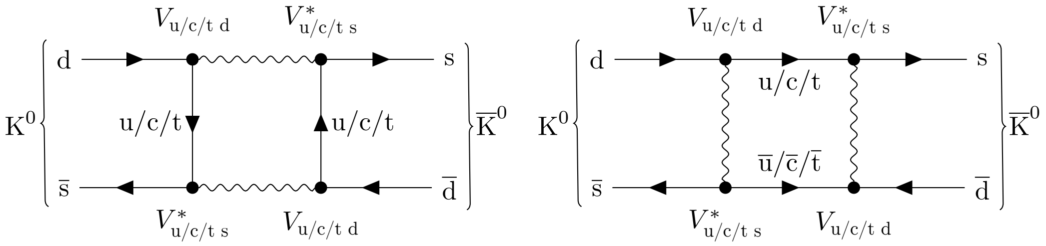

Figure 2.2: Leading-order Feynman diagrams or box diagrams for $\mathrm{K}^0 \leftrightarrow \overline{\mathrm{K}}^0$ mixing.

these mesons.

Most interestingly, both neutral kaons can decay into the same final states, namely two pion states ($|\pi^0\pi^0\rangle$ and $|\pi^+\pi^-\rangle$) or three pion states ($|\pi^0\pi^0\pi^0\rangle$ and $|\pi^+\pi^-\pi^0\rangle$). In the quark picture, it can be seen that the identical final states effectively lead to a coherent mixing between the two particles, as illustrated in Figure 2.2. The probability for such a $\mathrm{K}^0 \leftrightarrow \overline{\mathrm{K}}^0$ transition is determined by the products of the respective CKM matrix elements and the weak coupling strength at the four vertices. Measurements of such processes therefore offer an effective way of probing elements of the CKM matrix.

The oscillation process implies that while they are created separately the kaons propagate as linear combinations of K^0 and $\overline{\mathrm{K}}^0$. These linear combinations are referred to as the "short lived" K_S and the "long lived" K_L and represent real physical states which are mass eigenstates. As will be described in Section 2.2.2 for the case of neutral B-mesons, the mass eigenstates K_S and K_L both have different real masses, m_S and m_L, and different decay rates, Γ_S and Γ_L.

As far as the decay products of the kaons are concerned, the two pion final states are *CP* eigenstates with an eigenvalue of +1, whereas the three pion final states are *CP* eigenstates with −1. Assuming *CP* is conserved in weak interactions, the kaon states before the decay are also required to a have a well defined *CP* parity. It is possible to construct the *CP* eigenstates of the kaons, K_1 and K_2, by superposition of the flavor states:

$$|\mathrm{K}_1\rangle = \frac{1}{\sqrt{2}}\big(\,|\mathrm{K}^0\rangle - \overline{\mathrm{K}}^0\big) \qquad \text{with} \qquad \hat{C}\hat{P}\,|\mathrm{K}_1\rangle = +1\cdot|\mathrm{K}_1\rangle\,,$$
$$|\mathrm{K}_2\rangle = \frac{1}{\sqrt{2}}\big(\,|\mathrm{K}^0\rangle + \overline{\mathrm{K}}^0\big) \qquad \text{with} \qquad \hat{C}\hat{P}\,|\mathrm{K}_2\rangle = -1\cdot|\mathrm{K}_2\rangle\,.$$

In that way, $|\mathrm{K}_1\rangle$ describes the state decaying into two pions and $|\mathrm{K}_2\rangle$ is associated with a three pion decay. If *CP* would be a fully conserved symmetry the physical states should be identically with the *CP* eigenstates:

$$|\mathrm{K}_S\rangle = |\mathrm{K}_1\rangle \qquad \text{and} \qquad |\mathrm{K}_L\rangle = |\mathrm{K}_2\rangle\,.$$

The rest mass of three pions is almost the same as the mass of a kaon itself what leads to a smaller phase space and a notable suppression of such a decay. As a consequence, the lifetime of the $|\mathrm{K}_L\rangle$ ($\approx 5 \times 10^{-8}$ s) is three orders of magnitude larger than the lifetime of the $|\mathrm{K}_S\rangle$ ($\approx 9 \times 10^{-11}$ s), further explaining the nomenclature. That means, after a certain amount of time the K_S component of a mixed kaon beam will have fully decayed away and it should only be possible to observe three pion final states.

In 1964 Christenson, Cronin, Fitch and Turlay [6], however, found that with a small probability the long lived $|\mathrm{K}_L\rangle$ can also decay into two pions. This finding was unexpected and suggested that *CP* symmetry is to a certain extent violated in weak interactions. It further implied that the mass eigenstates are slightly different from the *CP* eigenstates what can be expressed by

$$\begin{aligned}
|\mathrm{K}_S^0\rangle &= \frac{1}{\sqrt{1+|\epsilon|^2}}\big(\,|\mathrm{K}_1^0\rangle + \epsilon\,|\mathrm{K}_2^0\rangle\big),\\
|\mathrm{K}_L^0\rangle &= \frac{1}{\sqrt{1+|\epsilon|^2}}\big(\epsilon\,|\mathrm{K}_1^0\rangle + |\mathrm{K}_2^0\rangle\big),
\end{aligned}$$

where ϵ is a small (and complex) mixing parameter which is responsible for admixtures of the opposing *CP* eigenstate. This measurement provided the first experimental evidence for the violation of *CP* symmetry.

The case of *CP* violation in the mixing of neutral mesons is also referred to as *indirect* CP violation; this and other types of *CP* violation are further discussed based on measurements in the neutral B-meson system in Section 2.2.5.

2.1.5 The unitarity triangle

An important implication of the unitarity requirement of the CKM matrix ($V_{\mathrm{CKM}}V_{\mathrm{CKM}}^{\dagger} = I$) is that measurements of the individual elements can be used to over-constrain the matrix in order to find deviations from SM predictions. For this purpose, the products of rows and columns are used to establish separate *unitarity relations* of specific elements of the matrix. For the case of transitions to b quarks the respective relation is given by

$$V_{\mathrm{ub}}V_{\mathrm{ub}}^{*} + V_{\mathrm{cb}}V_{\mathrm{cb}}^{*} + V_{\mathrm{tb}}V_{\mathrm{tb}}^{*} = 0,$$

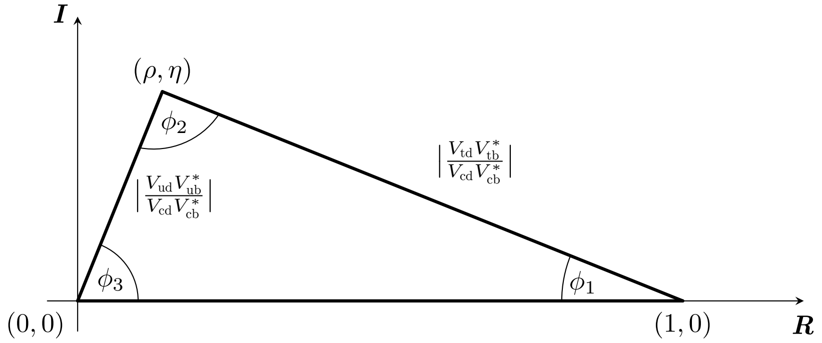

Figure 2.3: Unitarity triangle for the unitarity relation $V_{\mathrm{ub}}V_{\mathrm{ub}}^* + V_{\mathrm{cb}}V_{\mathrm{cb}}^* + V_{\mathrm{tb}}V_{\mathrm{tb}}^* = 0$ of the CKM matrix, shown in the ρ-η plane.

where all three terms are of $\mathcal{O}(A\lambda^3)$. Since the matrix elements represent complex values, this relation can further be expressed as a triangle in the complex plane as illustrated in Figure 2.3. It is convention to normalize the sides of the triangle by $V_{\mathrm{cd}}V_{\mathrm{cd}}^*$ such that the corners are located at the coordinates $(0, 0)$, $(1, 0)$ and (ρ, η). The normalized triangle is fully defined by any two of the parameters (length of the remaining two sides or the three angles). The sides of the triangle only close if the CKM matrix is indeed unitary and a measurement of *CP* violation is equivalent to determining any one of the angles. Different measurements of the parameters can, therefore, be used to over-constrain the triangle and test the CKM theory. Other unitarity relations lead to similar triangles which are commonly referred to as unitarity triangles.

As shown in Figure 2.4, current measurements of various parameters suggest that the unitarity triangle is indeed closed and consistent with predictions of the SM, and that *CP* violation is caused by a single complex phase. Observing deviations from these predictions is a major area of interest within the field of flavor physics and would immediately hint at NP.

2.2 B-meson physics

While the previous section introduced the underlying concepts, we now apply them to the B-meson system. The study of different decay channels of charged and neutral B-mesons represents the major part of the physics program of Belle II. Examining the branching ratios of these decays can be used to determine the sides of the unitarity triangle, whereas measurements of *CP* violation yield the angles of the triangle.

We begin by discussing the production of charged and neutral B-mesons in Section 2.2.1.

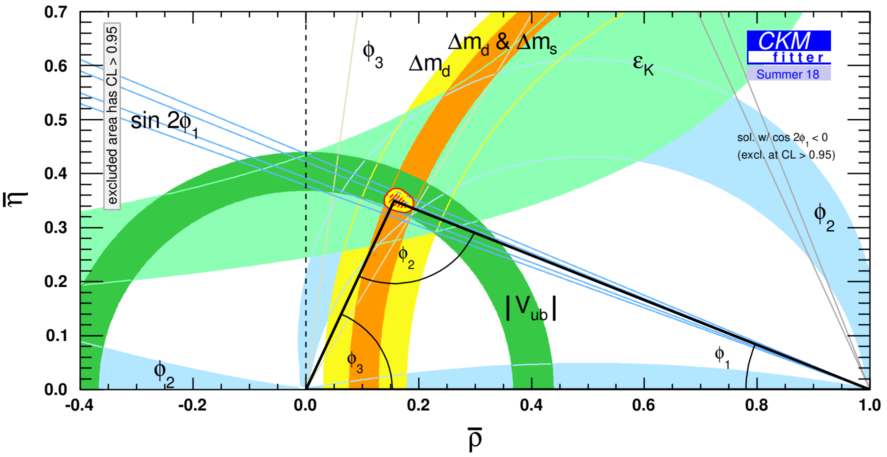

Figure 2.4: Constraints on the unitarity triangle taking measurements up to summer 2018 into account. Figure taken from [31].

This is followed by the phenomenological description of the mixing of neutral B-mesons in Section 2.2.2 and their time-dependent oscillations in Section 2.2.3. In Section 2.2.4, we then discuss tangible measurements of the $|V_{\mathrm{td}}|$ and $|V_{\mathrm{ts}}|$ elements of the CKM matrix and their corresponding oscillations frequencies, Δm_d and Δm_s. Finally, Section 2.2.5 describes the phenomenology of *CP* violation in the B-meson system and an exemplary measurement of the unitarity angle $\sin(2\phi_1)$.

2.2.1 Production of neutral and charged B-mesons

As mentioned earlier, SuperKEKB will mainly operate at a center-of-mass energy of 10.58 GeV which corresponds to the mass of the $\Upsilon(4S)$ resonance. Generally, the various Υ resonances are meson bound states of a b quark and its antiparticle $(\mathrm{b}\bar{\mathrm{b}})$. A key role among these resonances is assumed by the $\Upsilon(4S)$ since it is the first excited state with a sufficiently large mass to decay into a pair of B-mesons. The production and subsequent decay of such an $\Upsilon(4S)$ is illustrated in Figure 2.5. Its dominant decay channels are $\Upsilon(4S) \rightarrow \mathrm{B}^0(\bar{\mathrm{b}}\mathrm{d})\overline{\mathrm{B}}^0(\mathrm{b}\bar{\mathrm{d}})$ and $\Upsilon(4S) \rightarrow \mathrm{B}^+(\bar{\mathrm{b}}\mathrm{u})\mathrm{B}^-(\mathrm{b}\bar{\mathrm{u}})$ with branching fractions of 48.6% and 51.4%, respectively [32]. Because the mass of the resonance is only slightly larger than the combined mass of the decay products, the charged and neutral B-meson pairs are essentially created at rest in the center-of-mass system of the $\Upsilon(4S)$. This further implies that the relatively short lived B-mesons ($\tau = 1.519 \times 10^{-12}$ s) have low velocities and propagate only a short distance before decay. Important for their further evolution

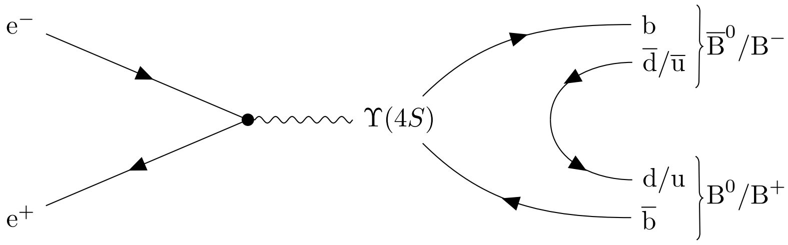

Figure 2.5: Leading-order Feynman diagram for the production of $\Upsilon(4S)$ resonances in e^+e^- collisions and the subsequent decays into quantum correlated pairs of neutral B-mesons; there are analogous diagrams for decays into charged B-mesons.

is the fact that they are produced in quantum correlated $J^{PC} = 1^{--}$ states.
At SuperKEKB, the positron beam energies are smaller than the electron energies so that the center-of-mass system is effectively boosted with respect to the laboratory system. The mean distance between the decay vertices of the neutral B-mesons is therefore amplified what allows the high-precision PXD to reconstruct the vertices separately.
The charged and neutral B-mesons either decay fully hadronic to lighter mesons or semi-leptonic to pairs of leptons and lighter mesons. They are important probes for the study of QCD and *CP* violation phenomena and have various rare decays which are sensitive to NP. The approach of producing large amounts of B-mesons in e^+e^--collisions at center-of-mass energies close to Υ resonances has already been pursued by the first generation of B factories, the predecessors KEKB and the PEP2 collider at SLAC.

2.2.2 Mixing of neutral B-mesons

Using diagrams analogous to the one for kaons shown in Figure 2.2 and described in Section 2.1.4, oscillations of neutral mesons can also be observed in other systems, as for example in the B system The neutral B-mesons are created in the flavor eigenstates B^0 and $\overline{\mathrm{B}}^0$ and decay as physical mass or *CP* eigenstates. They propagate through space as mass eigenstates with well defined lifetimes, which are different from their flavor eigenstates. In the following, we present the quantum mechanical treatment used to describe the oscillations of the neutral B-mesons.
In general, an arbitrary linear combination of the B^0 and $\overline{\mathrm{B}}^0$ flavor eigenstates,

$$a\,|\mathrm{B}^0\rangle + b\,|\overline{\mathrm{B}}^0\rangle\,,$$

evolves according to the time-dependent Schrödinger equation:

$$i\frac{\partial}{\partial t}\begin{pmatrix} a \\ b \end{pmatrix} = (\boldsymbol{M} - \frac{i}{2}\boldsymbol{\Gamma})\begin{pmatrix} a \\ b \end{pmatrix}, \tag{2.2}$$

with the (non-Hermitian) effective Hamiltonian, $\boldsymbol{H} = (\boldsymbol{M} - \frac{i}{2}\boldsymbol{\Gamma})$, and the (Hermitian) 2×2 matrices, $\boldsymbol{M}$ and $\boldsymbol{\Gamma}$.[5] The diagonal elements of $\boldsymbol{M}$ and $\boldsymbol{\Gamma}$ are real quantities which represent the masses and the lifetimes of the initial flavor eigenstates. Their off-diagonal elements, on the other hand, are related to the mixing process and can generally be complex. The conservation of CPT symmetry dictates that the B^0 and $\overline{\mathrm{B}}^0$ have identical masses and lifetimes and, therefore, $M = M_{11} = M_{22}$ and $\Gamma = \Gamma_{11} = \Gamma_{22}$. Without the mixing process, all off-diagonal elements of these matrices would be zero and Equation 2.2 would decouple into two separate equations independently describing the time evolution of the flavor states. As a consequence of them being non-zero, however, the B^0 and $\overline{\mathrm{B}}^0$ are not eigenstates of the effective Hamiltonian.

Instead, it can be shown that the eigenstates describing the time-evolution of the combined B-meson system are given by

$$\begin{aligned} |\mathrm{B}_L\rangle &= p\,|\mathrm{B}^0\rangle + q\,|\overline{\mathrm{B}}^0\rangle\,, \\ |\mathrm{B}_H\rangle &= p\,|\mathrm{B}^0\rangle - q\,|\overline{\mathrm{B}}^0\rangle\,, \end{aligned} \tag{2.3}$$

where the indexes reflect the fact that the eigenstates are divided into a lighter (L) and a slightly heavier state (H). The coefficients p and q are complex numbers with the normalization $|p|^2 + |q|^2 = 1$, for which the ratio is given by

$$\frac{q}{p} = -\sqrt{\frac{M_{12}^* - \frac{i}{2}\Gamma_{12}^*}{M_{12} - \frac{i}{2}\Gamma_{12}}}. \tag{2.4}$$

If $|\frac{q}{p}| \neq 1$, then the mass eigenstates do not correspond to the CP eigenstates which means that CP is not conserved in the time-evolution of the system. This ratio has important implications for the violation of CP symmetry which is further discussed in Section 2.2.5.

---

[5] As a result of the non-Hermiticity of the Hamiltonian, the probability in the B^0 and $\overline{\mathrm{B}}^0$ subspace is not conserved what is reflected by the decays of the mesons.

The eigenvalues corresponding to the lighter and heavier states are given by

$$\omega_L = m_L - \frac{i}{2}\Gamma_L = M - \frac{i}{2}\Gamma + \frac{p}{q}(M_{12} - \frac{i}{2}\Gamma_{12}),$$
$$\omega_H = m_H - \frac{i}{2}\Gamma_H = M - \frac{i}{2}\Gamma - \frac{p}{q}(M_{12} - \frac{i}{2}\Gamma_{12}),$$

where the masses, $m_{L,H}$, and decay widths, $\Gamma_{L,H}$, are generally expressed by the observables

$$M = \frac{1}{2}(m_L + m_H), \qquad \Delta m_d = m_H - m_L,$$
$$\Gamma = \frac{1}{2}(\Gamma_L + \Gamma_H), \qquad \Delta\Gamma = \Gamma_H - \Gamma_L.$$

By convention, the solutions are labeled in such a way that Δm_d is positive; $\Delta\Gamma$ can in principle be negative or positive.

Since the neutral B-mesons are relatively massive, the B^0 and $\overline{\mathrm{B}}^0$ have a large number of possible decay channels available of which only few are accessible by both mesons. The interference between the decay modes is hence small and can be neglected:

$$\Gamma_{12} = \Gamma_{12}^* \approx 0 \quad \rightarrow \quad \frac{q}{p} \approx \frac{M_{12}^*}{|M_{12}|} \quad \text{and} \quad |\frac{q}{p}| \approx 1.$$

This also implies that the B_L and B_H have approximately the same lifetime: $\Gamma \approx \Gamma_L \approx \Gamma_H$ and $\Delta\Gamma = 0$. In the B system, only box diagrams including top quarks contribute significantly to the mixing of the mesons and hence it can be shown that the difference in mass between the two states is given by

$$\Delta m_d \simeq 2|M_{12}| \propto |(V_{\mathrm{td}}V_{\mathrm{tb}}^*)^2|. \tag{2.5}$$

Considering that $V_{\mathrm{tb}} \approx 1$, a measurement of Δm_d then corresponds to determining the CKM element $|V_{\mathrm{td}}|$. We will see later that it is possible to obtain Δm_d by constructing dedicated CP asymmetries from the decays of the B^0 and $\overline{\mathrm{B}}^0$.

Having determined the eigenstates of the effective Hamiltonian for $t = 0$, their time evolution is then simply given by

$$|\mathrm{B}_{L,H}(t)\rangle = e^{-i\omega_{L,H}t}\,|\mathrm{B}_{L,H}\rangle\,. \tag{2.6}$$

2.2.3 Neutral B-meson oscillations

We use the time-evolution of the mass eigenstates obtained in the previous section to determine the time-evolution of mesons that at time $t = 0$ have been produced as pure B^0 or $\overline{\mathrm{B}}^0$ states. Reversing Equation 2.3 allows to express the flavor states as a linear combination of B_L and B_H, such as in

$$|\mathrm{B}^0\rangle = \frac{1}{\sqrt{2}}(|\mathrm{B}_L\rangle + |\mathrm{B}_H\rangle).$$

The time dependent representations of the pure flavor states can then be obtained by inserting Equation 2.6 and are given by

$$\begin{aligned} |\mathrm{B}^0(t)\rangle &= g_+(t)\,|\mathrm{B}^0\rangle + \frac{q}{p}g_-(t)\,|\overline{\mathrm{B}}^0\rangle\,, \\ |\overline{\mathrm{B}}^0(t)\rangle &= \frac{p}{q}g_-(t)\,|\mathrm{B}^0\rangle + g_+(t)\,|\overline{\mathrm{B}}^0\rangle\,, \end{aligned} \tag{2.7}$$

where the time dependence is encoded in the factors

$$\begin{aligned} g_+(t) &= e^{-iMt}e^{-\Gamma t/2}\cos{(\Delta m_d t/2)}, \\ g_-(t) &= e^{-iMt}e^{-\Gamma t/2}i\sin{(\Delta m_d t/2)}. \end{aligned}$$

These states describe how a B-meson created in a pure flavor eigenstate oscillates while propagating with a frequency which is determined by the mass difference of the mass eigenstates, Δm_d. If $|\frac{q}{p}| \neq 1$, then the probability for a B^0 to oscillate into a $\overline{\mathrm{B}}^0$ is not equivalent to the charge conjugated process. These equations therefore further emphasize that CP symmetry is not conserved in such a case.

Subsequently, we derive the time-dependent decay rates to an actual observable final state, f, which is an CP eigenstate and is accessible from both the B^0 and $\overline{\mathrm{B}}^0$. For this purpose, we define the two transition amplitudes from the flavor states to the final state:

$$A_f = \langle f|\,\boldsymbol{H}\,|\mathrm{B}^0\rangle \quad \text{and} \quad \overline{A}_f = \langle f|\,\boldsymbol{H}\,|\overline{\mathrm{B}^0}\rangle\,, \tag{2.8}$$

where $\boldsymbol{H}$ is the weak interaction Hamiltonian causing the decay. The decay from the flavor state B^0 to f can then take place directly, $\mathrm{B}^0 \to f$, or after mixing, $\mathrm{B}^0 \to \overline{B}^0 \to f$. The time-dependent decay rate, $\Gamma_{\mathrm{B}^0\to f}(t)$, consists of contributions from both A_f and

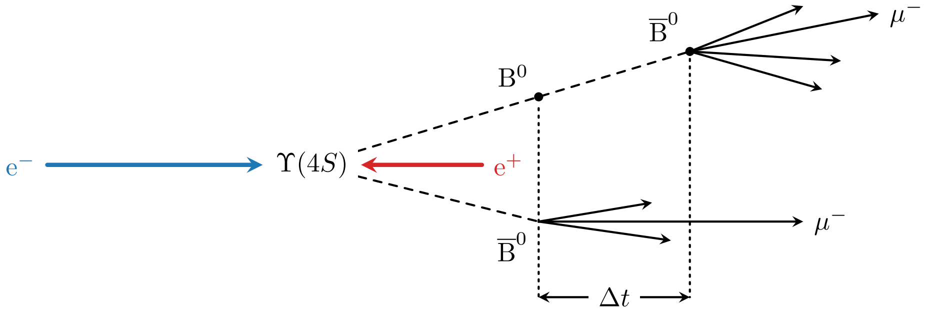

Figure 2.6: Schematic overview of $e^+e^- \to \Upsilon(4s) \to \mathrm{B}^0(\bar{\mathrm{b}}\mathrm{d})\overline{\mathrm{B}}^0(\mathrm{b}\bar{\mathrm{d}})$ production followed by two $\overline{\mathrm{B}}^0 \to \mathrm{D}^+\mu^-\overline{\nu}_\mu$ decays. In between decays, the B^0 oscillated into a $\overline{\mathrm{B}}^0$.

$\overline{A}_f$, and can be expressed by

$$\Gamma_{\mathrm{B}^0\to f}(t) = |A_f|^2 \frac{e^{-\Gamma t}}{2} \left[(|\lambda_f|^2 + 1) - (|\lambda_f|^2 + 1) \cos(\Delta m_d t) - 2\mathrm{Im}(\lambda_f) \sin(\Delta m_d t) \right], \tag{2.9}$$

where the second contribution enters via

$$\lambda_f = \frac{q}{p}\frac{\overline{A}_f}{A_f}. \tag{2.10}$$

Note that λ_f is a physical observable which does not depend on any phase conventions.

2.2.4 Measurement of the oscillation frequency

The measurement of the time-dependent oscillation of neutral B-mesons can very effectively be used to resolve the mass difference between the two mass eigenstates, Δm_d. According to Equation 2.5, such a measurement also determines the $|V_{\mathrm{td}}|$ element of the CKM matrix.

The $\mathrm{B}^0 \leftrightarrow \overline{\mathrm{B}}^0$ oscillations are, for example, studied based on the semi-leptonic decays to muons, $\mathrm{B}^0 \to \mathrm{D}^-\mu^+\nu_\mu$ and $\overline{\mathrm{B}}^0 \to \mathrm{D}^+\mu^-\overline{\nu}_\mu$, as illustrated in Figure 2.6. The main advantage of these decays is that the flavor state of a B-meson (B^0 or $\overline{\mathrm{B}}^0$) can be unambiguously identified, or *tagged*, by the charge of the final state lepton since B^0 can not decay to negative leptons and vice versa. The two B-mesons are produced and propagate in a quantum-entangled state in which they keep opposite flavors at all times. Therefore, if one of the mesons decays as a particular flavor eigenstate, the other meson necessarily has to be in the opposite flavor state at the time of the decay. The second meson then propagates according to Equation 2.7 and may freely oscillate between the two flavor states until it decays itself.

The time difference between the decays of the two B-mesons, Δt, can be obtained by precisely reconstructing their decay vertices and calculating it by $\Delta t = \Delta z/(c\beta\gamma)$. The distance between the two vertices in the laboratory frame, Δz, is dictated by the boost of the center-of-mass system and will be only about 150 µm at SuperKEKB. Resolving such vertices requires high resolution vertex detectors such as the PXD installed in Belle II (introduced in Section 4.1).

Using the decay rates given in Equation 2.9 (and assuming no CP violation in decay and mixing, $|q/p| = |\overline{A}_{\overline{f}}/A_f| = 1$, as discussed in the following section), it is possible to construct time-dependent oscillation asymmetry, $A_{mix}(\Delta t)$. For the case of semi-leptonic decays to muons or electrons this asymmetry can be written as

$$A_{mix}(\Delta t) = \frac{N_{\mathrm{OF}}(\Delta t) - N_{\mathrm{SF}}(\Delta t)}{N_{\mathrm{OF}}(\Delta t) + N_{\mathrm{SF}}(\Delta t)},$$

where a distinction is made between same flavor decays of the B-mesons (SF) indicated by two leptons with the same sign, $\mu^-\mu^-$ or $\mu^+\mu^+$, and opposite flavor decays (OF) given by leptons with different signs, $\mu^-\mu^+$. Figure 2.7 shows a measurement of $A_{mix}(\Delta t)$ as a function of the time difference between the two decays performed by the predecessor experiment Belle [33]. The mass difference, Δm_d, is deduced from the frequency with which $A_{mix}(t)$ oscillates:

$$A_{mix}(\Delta t) = \cos(\Delta m_d \Delta t).$$

As a result of different measurement related effects such as the misidentification of leptons, the experimental Δt resolution and, in particular, the presence of backgrounds, the curve is not following the form of a pure cosine. This further underlines the need for understanding the influence of beam backgrounds on measurements performed at Belle II.

The oscillations of B-mesons have been studied greatly at a number of different experiments, including Belle. The current world average of all measurements of Δm_d [32] is

$$\Delta m_d = 0.5065 \pm 0.0016(\mathrm{stat}) \pm 0.0011(\mathrm{sys})\ \mathrm{ps}^{-1}.$$

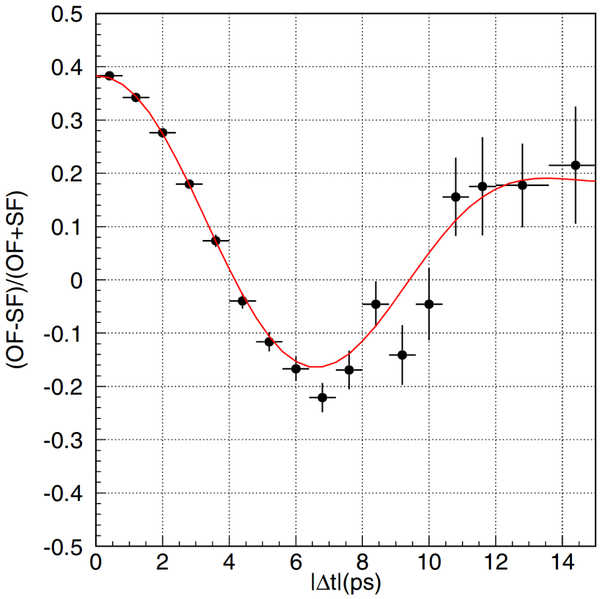

Figure 2.7: Measurement of the time-dependent flavor asymmetry for flavor-eigenstate decays, $A_{mix}(\Delta t) = \frac{N_{\mathrm{OF}}(\Delta t) - N_{\mathrm{SF}}(\Delta t)}{N_{\mathrm{OF}}(\Delta t) + N_{\mathrm{SF}}(\Delta t)}$, by the Belle experiment. The red line represents a fit of a combination of theoretical predictions and experimental effects. Figure taken from [33].

As mentioned earlier, through Equation 2.5 and by assuming that $V_{\mathrm{tb}} \approx 1$ the oscillation frequency also represents a measurement of $|V_{\mathrm{td}}|$:

$$|V_{\mathrm{td}}| = (8.1 \pm 0.5) \times 10^{-3},$$

where the given value is again the current world average [32].
Analogously to the measurements described here, it is also possible to observe the oscillation of B-mesons containing strange quarks, $\mathrm{B}^0_{\mathrm{s}}(\overline{\mathrm{b}}\mathrm{s}) \leftrightarrow \overline{\mathrm{B}}^0_{\mathrm{s}}(\mathrm{b}\overline{\mathrm{s}})$. Results obtained in this second B system lead to the following world averages for the mass difference, Δm_s [32], and the corresponding CKM matrix element, $|V_{\mathrm{ts}}|$ [32]:

$$\Delta m_s = 17.757 \pm 0.020(\mathrm{stat}) \pm 0.007(\mathrm{sys})\ \mathrm{ps}^{-1},$$
$$|V_{\mathrm{ts}}| = (39.4 \pm 23.0) \times 10^{-3}.$$

Note that Belle II will probably not be able to observe such oscillations of B-mesons containing strange quarks.

2.2.5 *CP* violation in the B system

In general, *CP* violation may be divided into three distinct categories:

(i) *CP* violation in decay or *direct CP* violation occurs when the decay rate of a process is different from the decay rate of its charge conjugated process. Experimentally, this is the case when

$$\left|\frac{\overline{A}_{\overline{f}}}{A_f}\right| \neq 1 \quad \rightarrow \quad \text{direct } CP \text{ violation,} \tag{2.11}$$

where A_f and $\overline{A}_{\overline{f}}$ are the corresponding decay amplitudes as defined by Equation 2.8. The ratio $|\overline{A}_{\overline{f}}/A_f|$ is a phase convention independent quantity which summarizes direct *CP* violation.

(ii) *CP violation* in mixing or *indirect CP* violation takes place in systems of neutral mesons where the mass eigenstates do not correspond to *CP* eigenstates. Such a discrepancy (see Equation 2.4) arises when

$$\left|\frac{q}{p}\right| \neq 1 \quad \rightarrow \quad \text{indirect } CP \text{ violation.} \tag{2.12}$$

This ratio is also a phase convention independent quantity and hence experimentally meaningful. A notable example of indirect *CP* violation is the decay of $\mathrm{K}_L \rightarrow \pi\pi$ described in Section 2.1.4.

(iii) CP violation in interference or *mixing induced CP* violation takes place when neutral mesons can decay to a common final state f with and without mixing, for example $\mathrm{B}^0 \rightarrow f$ and $\mathrm{B}^0 \rightarrow \overline{B}^0 \rightarrow f$. Again a phase convention independent quantity exists which is given by λ_f defined in Equation 2.10. It implies *CP* violation if

$$\lambda_f \neq \pm 1 \quad \rightarrow \quad \text{mixing induced } CP \text{ violation.}$$

Both Equations 2.11 and 2.12 immediately lead to $|\lambda| \neq 1$. By contrast, *CP* can still be violated through $\mathrm{Im}(\lambda) \neq 0$ even if $|q/p| = 1$ and $|\overline{A}_{\overline{f}}/A_f| = 1$.

Due to its relatively large effects in the B system, mixing induced *CP* violation is the type which is most relevant to Belle II. An important example for mixing induced *CP* violation is the decay $\mathrm{B} \rightarrow \mathrm{J}/\Psi\mathrm{K}_S$ (see Figure 2.8) which is also referred to as the “golden channel” due to its clear experimental signature and will be widely studied at Belle II.

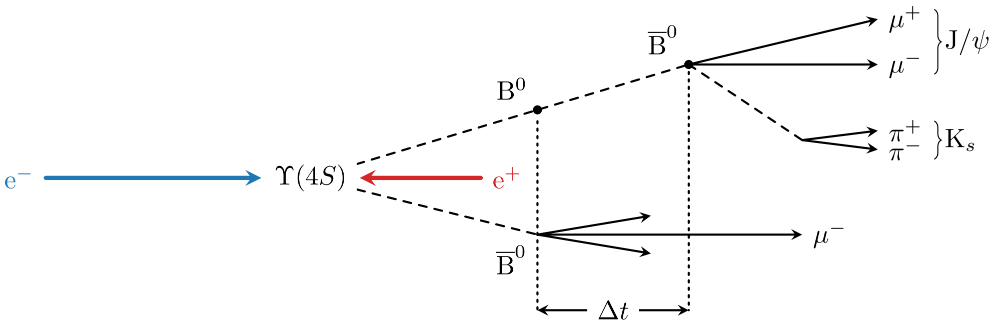

Figure 2.8: Schematic overview of $e^+e^- \to \Upsilon(4s) \to B^0(\overline{b}d)\overline{B}^0(b\overline{d})$ production followed by $\overline{B}^0 \to D^+\mu^-\overline{\nu}_\mu$ and $\overline{B}^0 \to J/\Psi K_S$ decays. In between decays, the B^0 oscillated into a $\overline{B}^0$.

Applying an analysis method similar to the one described in Section 2.2.4, this decay channel can be used to measure a non-zero value for the unitarity angle $\sin(2\phi_1)$ which is a direct demonstration of *CP* violation in the B system.

For B-mesons, the interference between the decays of the flavor eigenstates and therefore *CP* violation in mixing is relatively small implying that $|q/p| \approx 1$. Furthermore, the final state $J/\Psi K_S$ is accessible from the B^0, as well as the $\overline{B}^0$ and is a $CP = -1$ eigenstate. The leptonic decay of the $\overline{B}^0$ clearly tags the second meson as a B^0 at $t = 0$. It is then the interference between the amplitudes of the direct decay, $B^0 \to J/\Psi K_S$, and the decay after mixing, $B^0 \to \overline{B}^0 \to J/\Psi K_S$, which gives rise to *CP* violation.

The $B^0/\overline{B}^0 \to J/\Psi K_S$ decays are segmented into two subsequent parts. First the mesons decay to the corresponding flavor eigenstates of the kaons, $B^0 \to J/\Psi K^0$ and $\overline{B}^0 \to J/\Psi\overline{K}^0$. Then the kaons propagate as a linear combination of their mass eigenstates K_S and K_L and finally decay to the *CP* eigenstates $J/\Psi K_S$ and $J/\Psi K_L$.

It is possible to measure the *CP* violation in the interference between $B^0 \to J/\Psi K_S$ and $B^0 \to \overline{B}^0 \to J/\Psi K_S$ by deriving the time-dependent *CP* asymmetry:

$$A_{CP}(\Delta t) = \frac{\Gamma_{B^0 \to J/\Psi K_S} - \Gamma_{\overline{B}^0 \to J/\Psi K_S}}{\Gamma_{B^0 \to J/\Psi K_S} + \Gamma_{\overline{B}^0 \to J/\Psi K_S}} = \eta_{cp} \sin(\Delta m_d \Delta t) \sin(2\phi_1)$$

where $\eta_{cp} = -1$ is the *CP* eigenstate of the final state. The background subtracted data collected by the Belle experiment performing such a measurement is illustrated in Figure 2.9. This measurement also includes other channels with similar properties which are divided into $CP = -1$ decay modes, such as B→ $J/\Psi K_S$, (*left*) and $CP = +1$ decay modes, as for example B→ $J/\Psi K_L$, (*right*). The *top* part of the plots shows the number

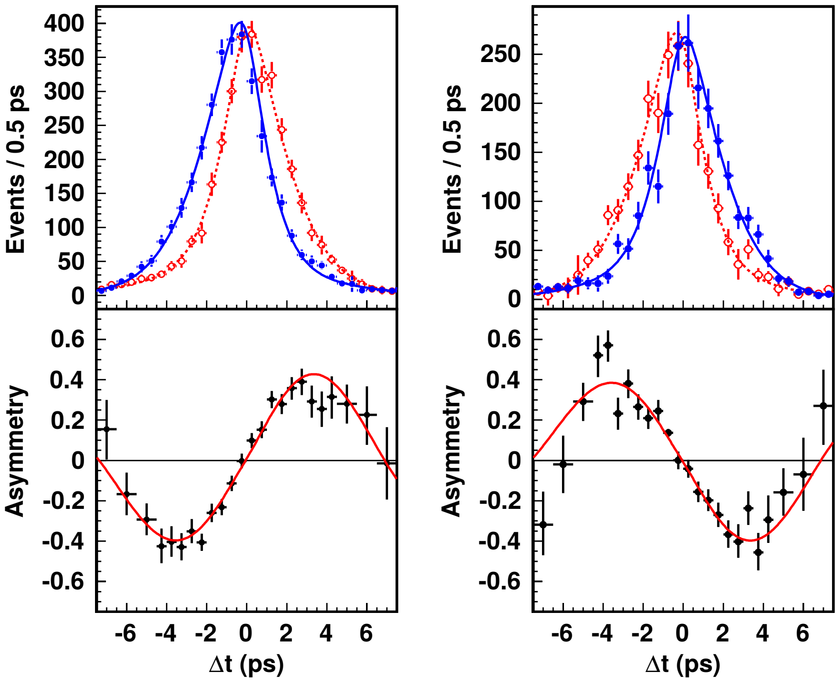

Figure 2.9: Background subtracted measurements of the time-dependent CP asymmetries for B→ J/ΨK$_S$ with $CP = -1$ (*left*) and B→ J/ΨK$_L$ with $CP = +1$ (*right*). The *top* part of the plots shows the number of events for mesons tagged as either B^0 (*red*) or $\overline{\mathrm{B}}^0$ (*blue*). The *bottom* part provides the asymmetry $A_{CP}(\Delta t)$. Note that the data includes additional decay modes. Figure taken from [34].

of events for mesons tagged as either B^0 (*red*) or $\overline{\mathrm{B}}^0$ (*blue*), whereas the *bottom* part presents the asymmetry, $A_{CP}(\Delta t)$. The Belle experiment obtained an angle $\sin(2\phi_1)$ [34] of

$$\sin(2\phi_1) = +0.667 \pm 0.023(stat) \pm 0.012(sys).$$

2.3 Physics prospects at Belle II

Building on the phenomenology described in the previous sections, the Belle II experiment will pursue a wide physics program at the intensity frontier. The objective of the BaBar and Belle experiments was to confirm the CKM mechanism for *CP* violation by demonstrating that measurements are consistent with CKM unitarity triangle expectations. For Belle II, the focus will be on high precision searches for deviations from predictions of the SM and for strongly suppressed flavor physics reactions. With the absence of clear signals for NP at the LHC, this approach has further gained in importance.

Existing SM decay amplitudes can potentially be modified by yet unknown diagrams in which NP interactions or particles contribute via additional box, loop (penguin) or even tree processes. The consequences of these modifications may be divided into two main categories. On the one hand, the new amplitudes can cause slight deviations from the SM predictions for the parameters of the CKM mechanism which can be revealed in precision measurements of various decays. On the other hand, they can also lead to explicit observations of rare decays which are originally “forbidden” or at least strongly suppressed in the SM.

Belle II’s sensitivity to such NP is defined by the strength of the new flavor violating couplings and has a potential reach[6] of up to $\mathcal{O}(100\,\mathrm{TeV})$ for new particles and processes. Historically, measurements of loop processes have often led to predictions of particles with masses far beyond the mass scale directly available for accelerators at that time. In that way, it was for example possible to observe evidences for the existence of the W, Z and Higgs bosons, as well as the top quark. Searching and potentially observing deviations from SM predictions will give hints at the underlying physics and will help to discriminate between the various proposed NP models.

Using the underlying concepts governing the production and decay of charged and neutral B-mesons, their various decays can be studied in order to probe different processes related to flavor changing CKM mechanisms. Besides B-mesons, SuperKEKB will also directly produce a significant number of τ lepton pairs via the process $e^+e^- \to \tau^+\tau^-$. In the following, we list several decays and observables which are in the focus of Belle II and describe the flavor physics questions addressed through them. Note that this is by no means a complete overview; a detailed description of the intended physics program can be found in [23].

- **Consistency tests of the CKM mechanism** Testing the consistency of the SM and the CKM mechanism requires that different measurements of various parameters are all compatible with each other such that they lead to a closed unitarity triangle (see Figure 2.3 in Section 2.1.5). A non-closing triangle, on the other hand, would imply that the examined processes have contributions from additional amplitudes clearly pointing to yet unknown NP phenomena.

  While current measurements of the sides and the angles of the triangle show a good

---

[6] This assumes that the new couplings are not suppressed as it is partially the case in the SM.

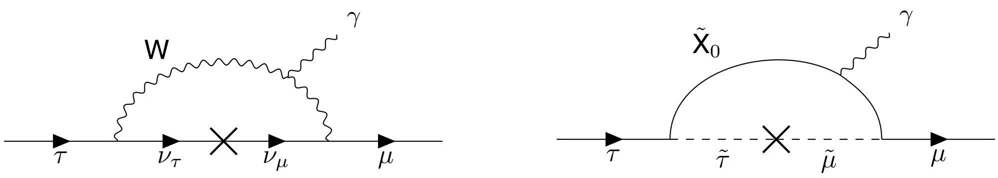

Figure 2.10: Feynman diagrams for the lepton flavor violating process $\tau \to \mu\gamma$ for Standard Model (including neutrino masses) only (*left*) and Beyond Standard Model (*right*) effects.

consistency of the CKM picture, the results still allow for NP contributions of order 10% of the size of the SM amplitudes. Belle II will be capable of performing highly precise measurements of all three angles of the triangle. The angles ϕ_1 and ϕ_2 can be obtained from time-dependent *CP* violation processes such as $\mathrm{B} \to \mathrm{J}/\Psi\mathrm{K}_S$ (ϕ_1, see Section 2.2.5) and $\mathrm{B} \to \rho^\pm\rho^0$ (ϕ_2), whereas ϕ_3 can be extracted from tree-level measurements of $\mathrm{B} \to \mathrm{D}^{(*)}\mathrm{K}^{(*)}$ decays. The expected uncertainties on ϕ_1, ϕ_2 and ϕ_3 are 0.4°, 1.0° and 1.0°, respectively. Additionally, the matrix elements $|V_{\mathrm{ub}}|$ and $|V_{\mathrm{cb}}|$ can be studied in various inclusive and exclusive semileptonic decays of the B-mesons, such as $\mathrm{B} \to \pi l \nu_l$ ($l \in \{e, \mu, \tau\}$, $|V_{\mathrm{ub}}|$) or $\mathrm{B} \to \mathrm{J}/\Psi\mathrm{K}_S$ ($|V_{\mathrm{cb}}|$).

Currently, the angle ϕ_3 is the least precisely known of the three unitarity angles. For quite some time, there are also $\mathcal{O}(3\sigma)$ inconsistencies between the inclusive and exclusive measurements of both $|V_{\mathrm{ub}}|$ and $|V_{\mathrm{cb}}|$. Possible explanations for these inconsistencies are extensions to the SM which predict additional charged Higgs bosons such as two-Higgs doublet models.

Belle II will be able to resolve these tensions and measure the elements of the CKM matrix with remarkable precision. In addition, comparing the rates of semileptonic B decays to various leptons will also be used to search for processes which violate lepton flavor universality such as charged Higgs-like coupling to tau leptons.

- **Lepton flavor violation in τ decays** In the SM, a distinct *lepton number*, L_l ($l \in \{e, \mu, \tau\}$), is assigned to the leptons of each generation which is conserved in all interactions. Decays such as $\tau \to \mu\gamma$ would violate this lepton number and are therefore forbidden. The only currently known mechanism which is capable of enabling lepton flavor violation (LFV) is the oscillation of neutrino flavors as illustrated in Figure 2.10 (*left*). The relatively small neutrino masses, however, lead to a strong suppression of such a decay (*e.g.* $\sim 10^{-45}$ for $\tau \to \mu\gamma$) effectively making their branching ratios unobservable in the SM.

  By contrast, LFV can be substantially increased through yet unknown NP contributions such as the processes shown in Figure 2.10 (*right*). Various NP scenarios like supersymmetric, little Higgs or leptoquark models predict such LFV processes which are in reach of upcoming experiments. In addition to radiative decays like the $\tau \to \mu\gamma$ discussed here, LFV will also be searched for in decays to three charged leptons, $\tau \to 3l$, lepton plus pseudo-scalar, $\tau \to lp^0$, and other processes without a tau neutrino in the final state. The current upper limits on the branching fractions are of $\mathcal{O}(10^{-8})$ at 90% confidence level. With an expected level of $\mathcal{O}(10^{-9})$-$\mathcal{O}(10^{-10})$, Belle II will reduce this limit significantly and facilitate the search of a larger parameter space in various NP scenarios.

- ***CP* violation in charm mixing** The SM mixing effects in heavy flavor systems are dominated by short range processes which are suppressed in the charm system. As observed by LHCb [35], the effects of *CP* violation in $\mathrm{D}^0 \leftrightarrow \overline{\mathrm{D}}^0$ mixing are therefore relatively small which makes them a promising probe for NP. Despite the challenging hadronic interactions, Belle II will measure final states containing neutral particles and contribute to the investigation of *CP* violation in the charm sector.

- **New *CP* violating phases** The *CP* violation processes included in the SM are orders of magnitude too small to explain the matter-antimatter asymmetry observed in the universe. Belle II will search for additional *CP* violating phases by comparing the decay rates of B^0 and $\overline{\mathrm{B}}^0$ in measurements of time-dependent *CP* violation in $\mathrm{b} \to \mathrm{d}$ and $\mathrm{b} \to \mathrm{s}$ penguin transitions (see Section 2.2.5). Important examples for such processes are the decays $\mathrm{B} \to \phi\mathrm{K}^0$ and $\mathrm{B} \to \eta'\mathrm{K}^0$.

The previous generation of B factories found tensions in a number of different measurements of CKM parameters. Belle II will help to resolve those tensions and will either contribute towards a consistent CKM picture or will find hints for the new sources of *CP* violation needed for the formation of a matter dominated universe.
As mentioned earlier, this will be achieved by precision measurements and searches for rare decays which both require enormous amounts of data. The unrivaled luminosity of SuperKEKB will put Belle II in the unique position to collect this data. However, the increased luminosity needed for such measurements also comes at the price of significantly elevated beam backgrounds. One of the big challenges for the operation of Belle II will therefore be to measure and understand these backgrounds and to find ways to limit them to tolerable levels.

Chapter 3

The SuperKEKB accelerator

In this chapter, we provide a description of the SuperKEKB accelerator. Due to their relevance for the work presented in this thesis, special emphasis is put on the dynamics of the beams and processes responsible for beam backgrounds.

The physics program discussed in the previous chapter imposes certain requirements on the design of the accelerator. Precision measurements based on well defined initial states and high statistics call for an e^+e^--collider capable of delivering extreme luminosities. Producing B-mesons at center-of-mass energies which correspond to the Υ resonances $(1S)$ through $(6S)$ necessitate precisely tunable electron and positron energies. In addition, boosting the center-of-mass system with respect to the laboratory frame in order to separate decay vertices of B-mesons is only possible with asymmetric beam energies. SuperKEKB is an asymmetric energy electron-positron collider that will mainly operate at a center-of-mass energy of 10.58 GeV. Its main components are a double storage ring, a linear accelerator (linac) which injects both types of particles at full energies, a damping ring to reduce positron emittance and dedicated electron and positron sources for initial generation of the beam particles. A schematic overview of the accelerator is shown in Figure 3.1, whereas the most important machine parameters are summarized in Table 3.1.

The electrons and positrons are directly accelerated up to their full design energies of 7 GeV (e^-) and 4 GeV (e^+) using the same multi stage linac. First, a high current low emittance electron bunch is generated by a pulsed laser beam hitting a photo cathode and then accelerated to 3.5 GeV. These electrons are either accelerated further or used to produce high current positron bunches by hitting an amorphous tungsten target. The positron bunches are accelerated to modest energies of 1.1 GeV before being directed into a newly constructed damping ring with a circumference of 135 m. As will be discussed

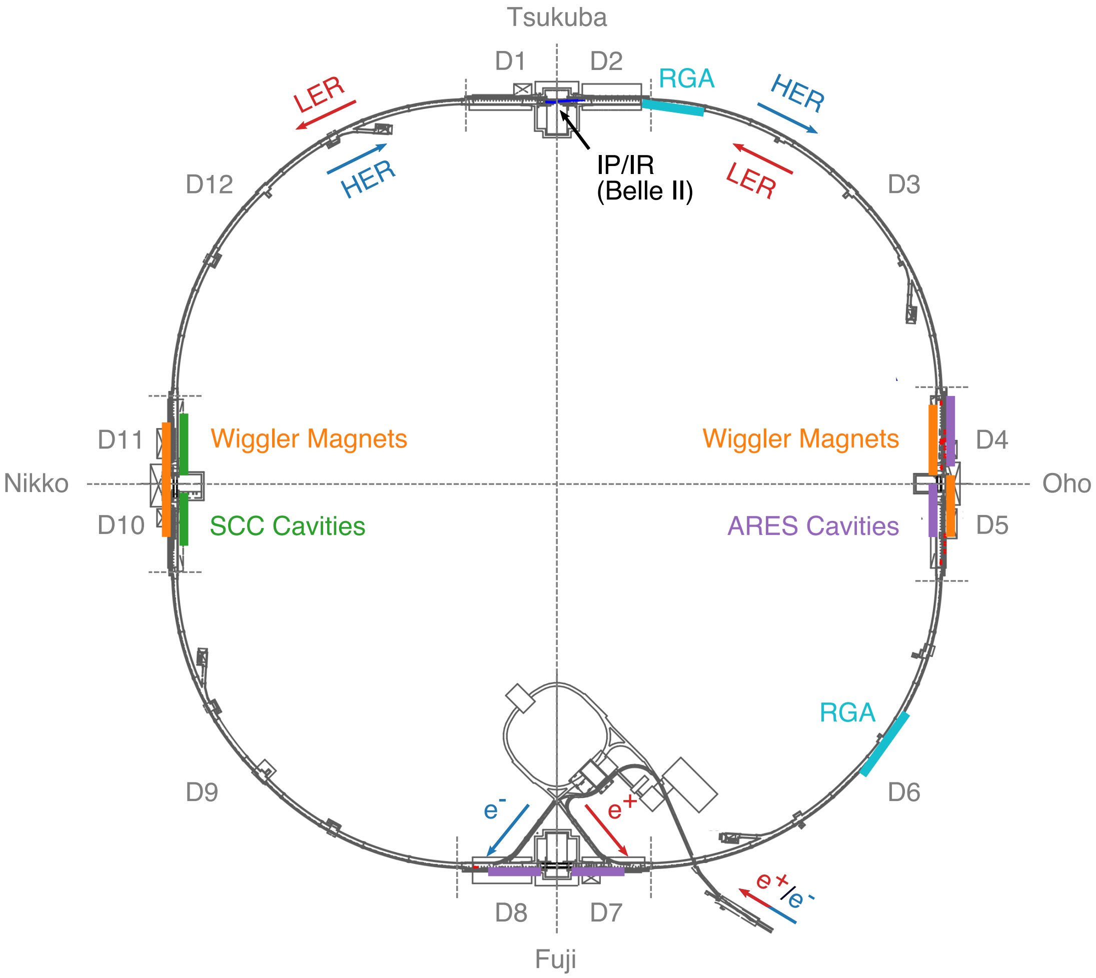

Figure 3.1: Schematic overview of the SuperKEKB accelerator with the dedicated storage rings for positrons (LER) and electrons (HER). Modified version of figure taken from [36].

in detail in Section 3.2, the damping ring uses synchrotron radiation damping to reduce the horizontal emittance from 1.4 µm to 42.9 nm and the vertical emittance from 1.4 µm to 3.12 nm within a damping time of 10.87 ms [37]. After the final acceleration stage, the electrons and positrons are injected into the main storage rings using a dedicated beam transfer line (see bottom part of Figure 3.1). The injection procedure is described in detail in Section 3.3.

The central part of SuperKEKB is the alternating gradient synchrotron which consists of two parallel but independent storage rings with a circumference of 3 km: the *high energy ring* (HER) containing the electrons and the *low energy ring* (LER) guiding the positrons. The beam lines in these rings essentially represent a distinct sequence of bending and

Table 3.1: Overview of machine parameters of SuperKEKB. The values listed in parentheses denote parameters at zero beam currents. Modified version of the table given in [16].

	Symbol	LER (e^+)	HER (e^-)	Units
Beam Energy	E	4	7	GeV
Half Crossing Angle	ϕ	41.5		mrad
Horizontal Emittance	ϵ_x	3.2(2.7)	2.4(2.3)	nm
Emittance Ratio	ϵ_y/ϵ_x	0.40	0.35	%
Beta Function at the IP	β_x^*/β_y^*	32/0.27	25/0.41	mm
Horizontal Beam Size	σ_x^*	10.2(10.1)	7.75(7.58)	µm
Vertical Beam Size	σ_y^*	59	59	nm
Betatron Tune	ν_x/ν_y	45.530/45.570	58.529/52.570	
Momentum Compaction	α_c	2.74×10^{-4}	1.88×10^{-4}	
Energy Spread	σ_ϵ	$8.14(7.96)10^{-4}$	$6.49(6.34)10^{-4}$	
Beam Current	I	3.60	2.62	A
Number of Bunches/Ring	n_b	2503		
Energy Loss/Turn	U_0	2.15	2.50	MeV
Total Cavity Voltage	V_c	8.4	6.7	MV
Synchrotron Tune	ν_s	-0.0213	-0.0117	
Bunch Length	σ_z	6.0(4.9)	5.0(4.9)	mm
Beam-Beam Parameter	ξ_y	0.0900	0.0875	
RF Bucket Size	T_{bucket}	1.965		ns
Revolution Period	T_{rev}	10.0614		µs
Luminosity	$\mathcal{L}$	8×10^{35}		$\mathrm{cm}^{-2}\mathrm{s}^{-1}$

focusing magnets, drift spaces and RF accelerating structures (referred to as *ARES* and *SCC* cavities in Figure 3.1) which is referred to as the *lattice* of the accelerator. The motion of the beam particles in the beam lines is discussed in detail in Section 3.1. The storage rings are also equipped with various beam instrumentation systems and condition monitors which are introduced in Section 3.5.

The electrons and positrons collide at the IP where the Belle II detector is located (see top part of Figure 3.1). For these collisions, the asymmetric beam energies lead to a center-of-mass energy of 10.58 GeV which corresponds to the mass of the $\Upsilon(4S)$ resonance. This also implies that the center-of-mass system is boosted with respect to the laboratory system by a factor of $\beta\gamma = 0.287$. While the majority of the runtime will be spent at this energy, the range of possible center-of-mass energies which can be provided by the injector linac covers the Υ resonances $(1S)$ through $(6S)$. The high design luminosity is achieved by two main elements: high beam currents of 3.2 A (electrons) and 2.6 A (positrons), and two superconducting final focusing quadruple systems (QCS) installed on either side of the IP which reduce the vertical beam size down to 50 nm (nano-beam scheme [38]). The region around the IP is referred to as the *interaction region* (IR) which is in particular relevant for Phase 1. The beam properties at the IP/IR are discussed in Section 3.2.

The ambitious design luminosity is expected to cause challenging levels of beam-induced backgrounds for the Belle II experiment. The different processes causing theses backgrounds are introduced in Section 3.4. At the time of writing, SuperKEKB and Belle II are undergoing their third and final commissioning phase. Finally, a brief overview of the three commissioning phases is given in Section 3.6.

3.1 Transverse and longitudinal beam dynamics

In this section, we introduce the underlying concepts of beam dynamics in the storage rings of SuperKEKB; that means in the context of an alternating gradient synchrotron which collides electrons and positrons in the high-energy limit, $v/c \approx 1$. Note that this is only a brief introduction; exhaustive reviews of the topics discussed in this and the following section can be found in [32, 39–41].

The dipole fields of the lattice define an ideal trajectory on which a reference particle with exactly the right energy and position repeatedly propagates through the machine. This trajectory is referred to as the *nominal* or *design orbit*. In reality, however, a distribution of particles always differs from the properties of the reference particle. For sufficiently small deviations, these particles perform stable oscillations around the nominal orbit in each of the three degrees of freedom. The oscillations transverse to the direction of their motion are referred to as *betatron oscillations*, whereas their longitudinal oscillations are denoted by *synchrotron oscillations*. As a consequence of their distinct time scales it is possible to examine the transverse and longitudinal motions separately. These oscillations play an important role in the analysis of injection backgrounds presented in Sections 7 and 8.

Betatron oscillations A description of the transverse motion of particles can be obtained by determining and solving their equations of motion in the presence of magnetic fields. For this purpose, the coordinate system depicted in Figure 3.2 is used where

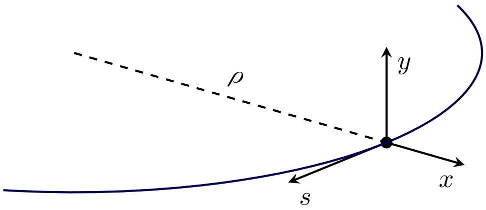

Figure 3.2: Coordinate system used for the description of particle motion in the presence of magnetic fields relative to a reference particle.

particle positions are stated relative to the design orbit. Here, ρ is the curvature of the reference orbit and x and y are the radial and vertical distances. Rather than time, the independent variable is given by the distance along the nominal trajectory, s. As such, the prime denotes d/ds. The trajectory of a real particle in horizontal or vertical transverse direction is then given by a pair of coordinates $(x(s), x'(s))$ or $(y(s), y(s)')$, respectively.

In this system, the propagation of a particle through an element of the accelerator in x or y direction can be described by a 2×2 matrix, $\boldsymbol{M}$. Such an element can be a single component like a dipole magnet or an arbitrarily complex sequence of components which are then connected by $\boldsymbol{M} = \boldsymbol{M}_n \cdots \boldsymbol{M}_1$. A common example of a joined matrix are the focus-drift-defocus-drift, or *FODO*, cells which serve as the standard quadrupole magnet configuration for strong focusing. Treating each of the individual components as a thin lens and using geometrical optics arguments yields the following matrices for the propagation through the cells:

$$\begin{pmatrix} x \\ x' \end{pmatrix}_{s_1} = \underbrace{\begin{pmatrix} 1 & 0 \\ -1/f & 1 \end{pmatrix}}_{\boldsymbol{F}} \underbrace{\begin{pmatrix} 1 & L \\ 0 & 1 \end{pmatrix}}_{\boldsymbol{O}} \underbrace{\begin{pmatrix} 1 & 0 \\ 1/f & 1 \end{pmatrix}}_{\boldsymbol{D}} \underbrace{\begin{pmatrix} 1 & L \\ 0 & 1 \end{pmatrix}}_{\boldsymbol{O}} \begin{pmatrix} x \\ x' \end{pmatrix}_{s_0}, \tag{3.1}$$

where L is the drift space between the cells, f is the focal length and $s_{0,1}$ are the position before and after the cell.

An analytic description of the propagation can be found by using the generic ansatz of the equations of motion in the presence of magnetic fields,

$$\frac{d\vec{p}}{dt} = e\vec{v} \times \vec{B}(\vec{r}).$$

From that it can then be shown that the linearized equations for a particle which deviates from the position of the reference particle are given by

$$\begin{aligned} x'' + K_x(s)x = 0 \qquad & \text{with} \qquad K_x(s) \equiv \frac{e}{p}\frac{\partial B_y(s)}{\partial x} + \frac{1}{\rho^2}, \\ y'' + K_y(s)y = 0 \qquad & \text{with} \qquad K_y(s) \equiv \frac{e}{p}\frac{\partial B_y(s)}{\partial x}. \end{aligned} \tag{3.2}$$

Here the magnetic field, $B(s)$, is assumed to have only a component in the y-direction, to include only dipole and quadrupole terms and to be treated as static. The terms $K_{x,y}(s)$ are responsible for the transverse focusing of the particles which is mainly caused by quadrupole fields; focusing in the dipole fields enters only via the centripetal term $1/\rho^2$. The equations are similar to the ones governing a harmonic oscillator only with the difference that the restoring forces given by $K_{x,y}(s)$ are functions of s.

Exploiting the fact that they are instances of *Hill's equation*, the general solution to Equation 3.2 for the motion in x can be written as

$$\begin{aligned} x(s) &= A\sqrt{\beta(s)}\cos\left(\psi(s) + \delta\right) \\ x'(s) &= -\frac{A}{\sqrt{\beta(s)}}\big[\alpha(s)\cos\left(\psi(s)+\delta\right) + \sin\left(\psi(s)+\delta\right)\big], \end{aligned} \tag{3.3}$$

where A and $+\delta$ are constants of integration, $\alpha(s) \equiv -\beta'(s)/2$ and the phase, $\psi(s)$, advances according to

$$\psi' = \frac{1}{\beta(s)}.$$

The term $\beta(s)$ is referred to as the *amplitude function* and defines the form of the envelope of the motion of the particles. A similar solution with an independent set of parameters can be obtained for the motion in y. For the sake of brevity, however, we focus on the motion in x from here on.

Solving the equations of motion for the transverse movement of particles leads to solutions, (x, x'), which are defined by two distinct quantities $\beta(s)$ and $\psi(s)$. These parameters are functions of the location along the nominal beam trajectory and are generally defined by lattice of the accelerator. The task of finding a description for the transverse motion of particles then reduces to computing $\beta(s)$ and $\psi(s)$. If the solutions to the equations of motion describe periodic propagations, which is the case for a circular collider, $\beta(s)$ has to be periodic as well. Given a periodicity C, this implies that $\beta(s_0 + C) = \beta(s_0)$. Using the matrix representation introduced in Equation 3.1 to express Equation 3.3 yields

$$\begin{pmatrix} x \\ x' \end{pmatrix}_{s_0+C} = \begin{pmatrix} \cos\Delta\psi_C + \alpha\sin\Delta\psi_C & \beta\sin\Delta\psi_C \\ -\gamma\sin\Delta\psi_C & \cos\Delta\psi_C - \alpha\sin\Delta\psi_C \end{pmatrix} \begin{pmatrix} x \\ x' \end{pmatrix}_{s_0}, \tag{3.4}$$

where the phase advance of a particle's propagation, $\Delta\psi_C$, is given by

$$\Delta\psi_C = \int_{s_0}^{s_0+C} \frac{ds}{\beta(s)}.$$

That means that if the transfer matrix of a period can be measured or calculated, like it is for example the case for a *FODO* cell, the amplitude function and the phase advance for this element can be obtained by comparing the matrix to Equation 3.4. It is possible to generalize this procedure in order to obtain the $\beta(s)$ and $\psi(s)$ for any two points in the lattice. Knowing the initial conditions and the lattice functions at both points it is then possible to determine any beam propagation.

In a large circular collider most of the lattice consists of a large number of *FODO* cells and the length of a period, thus, is considerably lower than a full turn. A real particle is, therefore, continuously redirected towards the ideal trajectory resulting in the previously mentioned betatron oscillations around the nominal orbit. The amplitude function represents the bounding envelope of the betatron oscillations and can, thus, be interpreted as the local wavenumber which determines the rate of the phase advance. The so called *betatron tune* is defined as the number of oscillations per turn in either horizontal or vertical direction:

$$\nu_{x,y} \equiv \frac{1}{2\pi} \oint \frac{ds}{\beta(s)}.$$

Note that if this tune assumes an integer or lower order rational number, imperfections or perturbations are amplified with each subsequent revolution. For SuperKEKB, the horizontal design tunes, ν_x, are 45.5 (LER) and 58.5 (HER) and the vertical design tunes, ν_y, correspond to 45.6 (LER) and 52.6 (HER) (see Table 3.1).

Momentum dispersion So far, we were concerned with particles which are only differing in transverse position and direction but have the same momentum as the reference particle. In practice particles are also deviating in momentum, which leads to changes of the deflection in the bending magnets. As a consequence, the off-momentum particles undergo betatron oscillations in the x direction around new closed orbits which are slightly different from the design trajectory.

The displacement of these orbits depends on a new type of lattice function referred to as *momentum dispersion function*, $D(p, s)$, which can be written as

$$x(s) = D(p, s)\frac{\Delta p}{p_0} \qquad \text{with} \qquad p = p_0 + \Delta p.$$

Taking this into account, it is possible to obtain a modified version of the equations of motion:

$$D'' + \Big(K_x(s)\frac{p_0}{p} - \frac{1}{\rho^2}\frac{\Delta p}{p}\Big)D = \frac{1}{\rho}\frac{p_0}{p}.$$

This equation is also an instance of a (inhomogeneous) Hill's equation and can be solved by adopting an analogous approach as used for Equation 3.2. Exploiting the periodicity of $D(p, s)$ then yields matrices for the propagation from an arbitrary point along the nominal orbit s_1 to a second point s_2. Here, the matrices and the vectors they operate on are supplemented by a third component:

$$\begin{pmatrix} x \\ x' \\ \frac{\Delta p}{p_0} \end{pmatrix}_{s_2} = \boldsymbol{M}(s_1 \to s_2) \begin{pmatrix} x \\ x' \\ \frac{\Delta p}{p_0} \end{pmatrix}_{s_1} .$$

This third component is responsible for the fact that the particles perform betatron oscillations around new orbits which differ from the design orbit. That means that deviations in momentum lead to transverse oscillations in x direction. It can further be shown that these deviations also lead to slight shifts in the betatron tune.

Synchrotron oscillations Besides betatron oscillations transverse to the direction of motion, beam particles also undergo synchrotron oscillations in the longitudinal direction due to differences in energy relative to the reference particle. These oscillations can be described by an additional set of equations of motion for the difference relative to the reference particle in energy, ΔE, and time, Δt.

In the high-energy limit it can be assumed that the speed of the electrons and positrons is approximately c and thus constant. For identical particles, a ΔE is then equivalent to a deviation in momentum which leads to a change of the orbit period, τ, due to the bending in the dipole magnets. This relationship is expressed by the *slip factor*, η:

$$\frac{\Delta\tau}{\tau} = \eta\frac{\Delta p}{p} = \eta\frac{\Delta E}{E}.$$

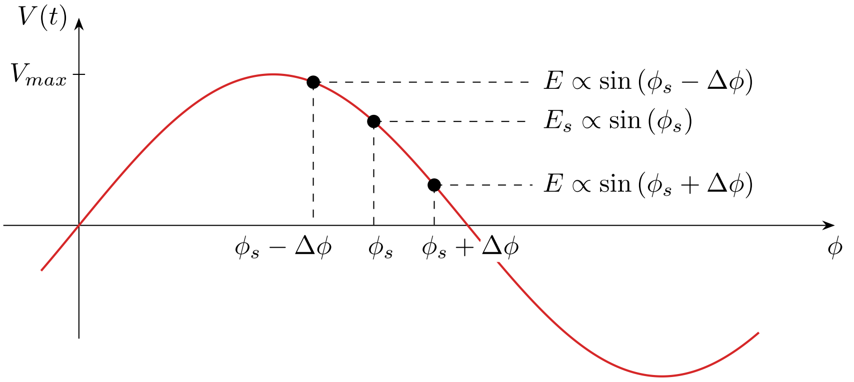

Figure 3.3: Energy gain in a RF acceleration element relative to the reference particle.

Note that for high energy synchrotrons such as SuperKEKB, η is generally positive.
The electrons and positrons are continuously provided with new energy when passing through one of the RF elements, as illustrated in Figure 3.3. The reference particle always passes the RF element with the synchronous phase, ϕ_s, for which the turn-wise gain in energy, $E_s = eV_{max} \sin \phi_s$, is exactly counteracting the losses due to synchrotron radiation. By calculating the turn-wise difference in energy and phase due to this RF acceleration it is then possible to determine the equation of motion in longitudinal direction relative to the reference particle:

$$\frac{d^2 \Delta t}{dn^2} = -(2\pi\nu_s)^2 \Delta t,$$

where the independent variable is the number of the turn, n, and we assumed that the oscillations are small. The equation of motion is similar to the one of a simple harmonic oscillator. Analogous to the betatron tune, this equation defines the so called *synchrotron tune*,

$$\nu_s = \sqrt{\frac{\eta h}{4\pi^2 E_s} eV_{max} \cos(\phi_s)},$$

which indicates the longitudinal synchrotron oscillations per turn. Generally, the RF frequency is a high multiple, h, of the orbit frequency and the synchrotron tune is considerable smaller than one. For SuperKEKB, the design tunes, ν_s, are 0.0213 (LER) and 0.0117 (HER) oscillations per turn (see Table 3.1). This implies that these oscillations takes place on considerably longer time scales than betatron oscillations.
Note that the particles undergo oscillations in longitudinal direction due to differences

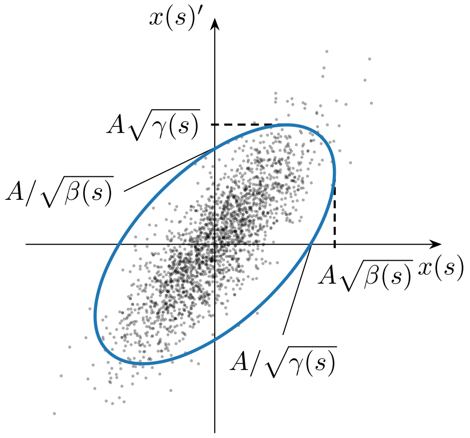

Figure 3.4: Phase space mapping in x direction relative to the design orbit for an arbitrary position in the accelerator.

in energy and thus also in momentum. As discussed before, a deviation in momentum also leads to transverse betatron oscillations.

3.2 Beam properties, damping and luminosity

Having discussed the dynamics of a single particle, we now turn to the properties of an ensemble of particles or, in other words, a particle beam.

Transverse and longitudinal beam emittance The transverse phase space which is occupied by the beam particles is defined by their betatron oscillations. Using Equation 3.3, the integration constant, A, can be expressed in terms of x and x':

$$A^2 = \gamma(s)x^2 + 2\alpha(s)x(s)x'(s) + \beta(s)x'(s)^2 \tag{3.5}$$

where $\gamma(s) \equiv (1+\alpha(s)^2)/\beta(s)$. Collectively, $\alpha(s)$, $\beta(s)$ and $\gamma(s)$ are referred to as the *Courant-Snyder parameters*. These parameters are functions of the location along the nominal beam trajectory and are generally defined by the lattice of the accelerator. The constant A^2 is denoted as the *Courant-Snyder invariant*.

It can be seen that Equation 3.5 corresponds to the equation of an ellipse such as the one illustrated in Figure 3.4. For each point in the accelerator the corresponding amplitude function defines a distinct ellipse. Whenever a single particle passes this point, its betatron oscillation coordinates (x, x') will then assume a point on this ellipse. For this particle, the area of the ellipse ($= \pi A^2$) is constant throughout the accelerator but its shape and orientation change with the position along the trajectory.

The area in transverse phase space which is occupied by the entire ensemble of particles is referred to as the *transverse emittance* of the beam, ϵ. Assuming that the transverse beam profiles follow a Gaussian distribution with width $\sigma_{x,y}$, the transverse emittance is defined as

$$\epsilon_{x,y} \equiv \frac{\sigma_{x,y}^2}{\beta_{x,y}},$$

and denotes the area which encloses 39% of the beam particles. Note that there are a number of different definitions of how much of the beam is covered by $\epsilon_{x,y}$.

Similar to $\epsilon_{x,y}$ in transverse phase space, the *longitudinal emittance*, ϵ_l, defines the area in ΔE-Δt space which is occupied by the particles. As such, ϵ_l is mainly determined by the synchrotron oscillations of the beam particles. In this phase space, the relative timing of the RF elements defines certain regions for which particle motion is stable. These regions are centered around multiples of the synchronous RF phase, ϕ_s, and are referred to as RF buckets. For SuperKEKB, the distance in time between two subsequent RF buckets is $T_{bucket} = 1.965\,\mathrm{ns}$.

According to *Liouville's theorem*, the local particle density in phase space of such an ensemble is constant in the absence of collisions and dissipation. That means, the transverse and longitudinal emittances of the beams are not altered by the magnetic focusing or bending which happens throughout the beam lines.

In addition it is possible to define the *admittance* as the area in phase space of the largest ellipse still accepted by the accelerator. As a consequence, particles which occupy a larger phase space collide with apertures leading to beam backgrounds.

Radiation dampening Liouville's theorem does not apply to intra-beam interactions which are responsible for beam backgrounds or the emission of synchrotron radiation where the beam particles emit parts of their own energy (both described in Section 3.4). Intra-beam interactions generally lead to a dilution of the emittance.

Synchrotron radiation is emitted in the direction of the tangent to the trajectory which reduces the magnitude of the momentum. The RF acceleration, on the other hand, increases only the longitudinal component of the momentum. The combination of continued synchrotron radiation and energy recovery therefore leads to a dampening of the transverse oscillation of the particles, which effectively reduces the transverse emittance of the beam. Furthermore, since the energy loss per turn is proportional to the particle energy squared, synchrotron radiation also dampens the longitudinal oscillation of the beam particles, reducing their longitudinal emittance. This means that oscillations in all three degrees of freedom are effectively reduced by continuous emission of synchrotron radiation. This technique is referred to as *synchrotron radiation damping* and is widely used in electron and positron synchrotrons. It offers an effective way to automatically achieve small beam emittances. At SuperKEKB, the positron damping ring and both main storage rings promote synchrotron radiation damping via bending and dedicated wiggler magnets and the corresponding RF acceleration structures.

Note that despite the damping effect, the emittances do not tend to zero. Instead the equilibrium emittances are primarily determined by an equilibrium between synchrotron radiation dampening and excitations from quantum fluctuations in the radiation rate. Generally, the emittance in the accelerator plane, ϵ_x, is significantly larger than the vertical emittance, ϵ_y.

Luminosity Besides the center-of-mass energy, the most important parameter for the performance of a collider is the instantaneous luminosity, $\mathcal{L}$. It represents a measure for the rate of collisions achieved by the machine and is closely related to the transverse emittance and the phase space occupied by the beam particles. At SuperKEKB, high precision measurements (see Section 2.3) will be enabled by increasing $\mathcal{L}$ by a factor of 40 compared to the peak luminosities of its predecessor KEKB.

For a collider with beams arranged in bunches of n_1 and n_2 particles which collide with a frequency, f_{coll} , $\mathcal{L}$ can be written as

$$\mathcal{L} = f_{coll} \frac{n_1 n_2}{4\pi\sqrt{\epsilon_x \beta_x^* \epsilon_y \beta_y^*}} \mathcal{F},$$

where β_x^* and β_y^* are the amplitude functions specifically at the IP and the factor $\mathcal{F} \leq 1$ accounts for crossing angles and other effects.

The essential elements for the increase in luminosity of SuperKEKB are a reduction of the horizontal beam emittances, an increase in beam currents and the nano-beam scheme (see Table 3.1). Modifications of the lattice of the accelerator and the newly installed damping ring for the positrons reduce ϵ_x by a factor 5 to 10 compared to KEKB . The doubling of the beam currents with respect to KEKB to 3.2 A (electrons) and 2.6 A (positrons) increases n_1 and n_2. Most importantly, the new final focusing magnets minimize β_y^* down to only 0.3 mm such that the vertical beam size is effectively reduced to approximately 60 nm. In that way, it will be possible to reach a so far unrivaled

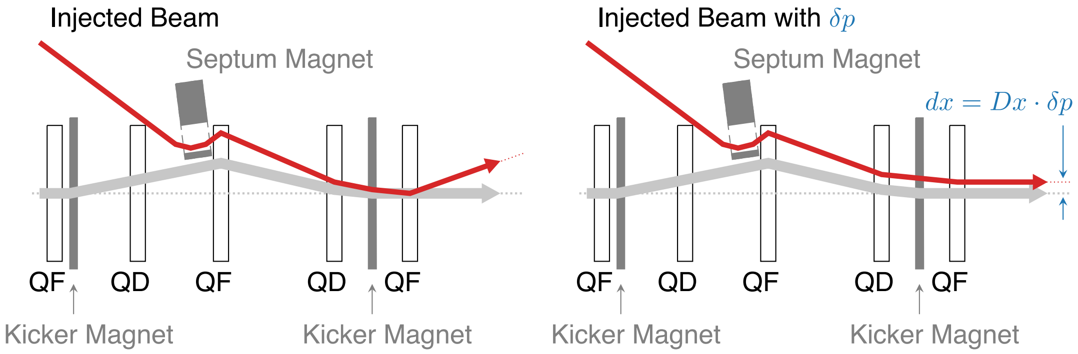

Figure 3.5: Schematic overview of top-up injections with an intentional orbit offset referred to as *betatron injections* (*left*). Schematic overview of top-up injections with an intentional momentum offset, δp, referred to as *synchrotron injections* (*right*).

instantaneous luminosity of

$$\mathcal{L} = 8 \cdot 10^{35}\,\mathrm{cm}^{-2}\mathrm{s}^{-1}.$$

3.3 Top-up injections and bunch structure

Similar to its predecessor, SuperKEKB uses *top-up injections* to compensate for particle losses due to background processes and collisions while maintaining constant luminosities. In such top-up injections, small numbers of new electrons and positrons are continuously injected into already circulating bunches. In general, the injection systems have to be capable of transferring the beams with sufficiently small losses while achieving the required beam parameters and a minimal dilution of the beam emittance. Due to Liouville's theorem (see previous section), however, the injected beam can not be incorporated into the phase space volume which is occupied by the circulating beam. For this purpose, SuperKEKB will mainly utilize the *betatron injection* scheme (deliberate space offset, see Figure 3.5 (*left*)). In order to be able to counteract possible beam blowups, however, the *synchrotron injection* scheme is adopted as a backup option (deliberate momentum offset, see Figure 3.5 (*right*)).

Both injection schemes generally employ the same hardware, namely a septum magnet and two kicker magnets, and exploit synchrotron radiation damping in order to maintain a low beam emittance. A septum is a special beam optics element which separates two field regions; septa design can make use of magnetic or electrostatic fields. The septum is used to deflect the injected beam into the accelerator aperture. The kicker magnets, on the other hand, introduce an orbit bump for the circulating beams which brings them to the vicinity of the septum and reduces the angle between the beams. Because the horizontal admittance is larger than the vertical admittance, the merger of the injected and the circulating beams takes place in the horizontal plane of the accelerator.

In the betatron scheme, the new beam particles are injected with certain deliberate betatron oscillation amplitudes what separates them from the circulating beams. As a consequence, the injected particles subsequently perform betatron oscillations around the closed orbit. These oscillations are then steadily reduced by synchrotron radiation damping until the injected beams have fully merged into the already circulating beams. Transverse dampening times for the LER and HER are 43 ms and 58 ms, respectively [42]. In general, it is possible to continue with collisions during injections. However, the major limitation of this injection scheme is that the betatron oscillation amplitudes can be significantly larger than the admittance of the accelerator. Nevertheless, betatron injections are the default injection scheme foreseen for the operation of SuperKEKB and have been almost exclusively used during Phase 1.

Alternatively, new particles are injected with a predefined momentum offset using the synchrotron injection scheme. Here, the positional offset between the injected and the stored beam, Δx, is defined by the dispersion at the position of the injection, D, and the momentum offset, δp:

$$\Delta x = \delta p \times D.$$

In that way, the betatron orbit of the injected particles matches their momentum and they only undergo synchrotron oscillations. Similar to betatron injections, the new beam particles are steadily damped by synchrotron radiation damping until they have fully merged into the already circulating beams.

Beam particles for which the betatron oscillation amplitudes either caused by transverse displacement or by synchrotron oscillations exceed the admittance of the accelerator collide with the beampipe or other accelerator elements, causing beam backgrounds. In particular, bunches which received new particles in injections and are in their cooling phase result in significantly increased background levels for the detectors whenever they pass by the IP. These bunches are therefore referred to as *injection bunches* or *noisy bunches*. Measurements conducted before the shutdown of KEKB suggest that such injection backgrounds persist for up to 4 ms after the injection before backgrounds return to regular levels [43]. Note that the time in which the detectors observe elevated background rates is smaller than the time which the newly injected particles require to

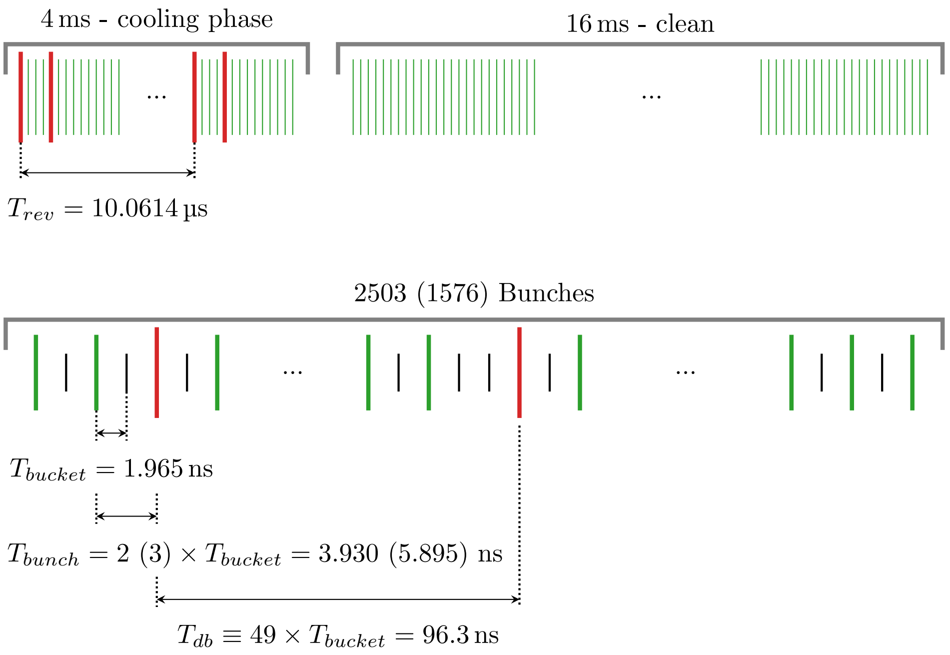

Figure 3.6: Schematic overview of the expected time structure of injections (*top*) and the bunch-by-bunch structure (*bottom*). The parentheses denote values used during Phase 1 operation.

fully merge with the circulating bunch. It is foreseen to perform alternating injections of electrons and positrons with a repetition rate of 25 Hz each, as illustrated in Figure 3.6 (*top*). That means an injection takes place every 20 ms of which the first 4 ms are hampered by the cool down of injection background. During this cooling phase, the injection bunch circulates in the rings and passes by the IP in intervals corresponding to the revolution period, $T_{rev} = 10.0614\,\mu\text{s}$.

As described in the previous section, the bunches are placed in RF buckets divided by fixed intervals defined by the bucket size, $T_{bucket} = 1.965\,\text{ns}$, as shown in Figure 3.6 (*bottom*). How many and which specific buckets are filled at runtime depends on the employed fill pattern. For the operation of SuperKEKB, it is foreseen to utilize every second bucket resulting in a bunch spacing of $T_{bunch} = 3.930\,\text{ns}$ with 2503 bunches in total. During Phase 1, on the other hand, the predominantly employed pattern specifies that only every third bucket is used and, therefore, $T_{bunch} = 5.895\,\text{ns}$ with 1576 bunches [44]. While it is possible to inject only into a single bunch, injections are generally performed for two bunches simultaneously in order to maximize injection efficiency. These bunches are separated by 49 RF buckets with a time difference of $T_{db} \equiv 49 \times T_{bucket} = 96.3\,\text{ns}$

between them. The injected bunches are selected based on the criterion of the lowest sum of bunch currents.

Comprehensive reviews of beam injections into circular electron-positron synchrotrons and light sources can be found in [45, 46]. More details on the SuperKEKB specific injection procedure are given in [16, 37, 47].

3.4 Sources of beam backgrounds

The term *beam backgrounds* generally refers to undesirable particles and can be divided into three main categories: backgrounds caused by the circulating beams, or *beam-induced backgrounds*; backgrounds as a byproduct of collisions, also referred to as *luminosity-dependent backgrounds*; and backgrounds due to the injection of new beam particles or so-called *injection backgrounds.* The background particles can be the beam particles themselves due to processes such as radiative Bhabha scattering or secondary particles generated by the beams. For example, single-beam processes such as beam-gas or Touschek scattering cause beam particles to depart from their nominal orbits leading to significantly increased oscillations and emittances. When these emittances exceed the admittance of the accelerator, the particles collide with the beampipe or other parts of the accelerator setup and cause secondary particle showers. Background processes generally reduce the beam currents and limit the beam lifetime in the accelerator. Background particles, in particular secondary ones, increase the occupancy in Belle II and thus hamper the performance of the reconstruction software. They can also lead to an elevated flux of neutrons and ionizing radiation dose which reduces the lifetimes of the materials and the electronics and enlarges their dead time.

In the following, we provide an overview of the six main sources for beam backgrounds at SuperKEKB. Since they will be of great importance for Phase 2, Phase 3 and the final operation, radiative Bhabha scattering and the production of two-photon events are also included in the overview. Due to the lack of collisions, however, these two luminosity dependent types of background are irrelevant for the study of Phase 1 data.

- **Touschek scattering** The term *Touschek effect* or simply *Touschek scattering* refers to an intra-bunch scattering process in which a single Coulomb scattering between two particles of the same bunch leads to a significant change of their energy. It affects the particles implicated in the interaction by increasing the energy of one and decreasing the energy of the other [48]. As discussed in [37], the probability of scattering can be calculated using Bruck's formula. The total scattering rate for the entire ring is then proportional to the number of filled bunches and the

second power of the bunch current, and inversely proportional to the beam size and the third power of the beam energy. As such, the higher beam currents and the dramatically reduced β_x^* and β_y^* due to the nano-beam scheme will promote beam loss by Touschek scattering. A simple scaling based on the beam size and the currents suggests that this type of background will increase approximately by a factor of 20 compared to KEKB. Due to the energy dependence, however, observed Touschek backgrounds will come mainly from the LER.
After such an interaction takes place, the affected particles are eventually lost at the inner wall of the beampipe. If the loss position is in the proximity of the IP, the resulting secondary particle showers can reach the detector.

- **Beam-gas scattering** The second source of beam backgrounds is *beam-gas scattering* which denotes scattering of beam particles with residual gas molecules in the vacuum chambers. Such an interaction can take place through two different processes: elastic Coulomb scattering and inelastic Bremsstrahlung. The first type of interaction changes the direction of beam particles and hence increases their transversal emittance. The second type of interaction, on the other hand, reduces their energy and expands their longitudinal emittance.
  The scattering rate due to beam-gas interactions is proportional to the beam current and the vacuum pressure in the rings. As a consequence of the reduced size of the beampipe with an inner radius of just 1 cm, the vacuum levels at the IP are expected to be 100 to 1000 times higher than at KEKB. Promoted by the increased vacuum levels and beam currents, the Beam-gas scattering rate will approximately be a factor 100 higher at SuperKEKB.

- **Synchrotron radiation** The third source of backgrounds is *synchrotron radiation* (SR), i.e. photons emitted by the beam particles while undergoing centripetal acceleration. The turn wise energy loss of the electrons and positrons is scaling according to

  $$\Delta E \propto \frac{E^4}{\rho},$$

  where ρ is the radius of the deflection in the bending magnets. As such, SR increases significantly with the energy of the particles and is the most severe limitation for circular e^+e^- colliders. As a consequence of this energy dependence, SR is predominantly caused by the HER beams.
  In the laboratory system, SR is strongly collimated in the direction of propagation

of the charged particle with an opening angle of only few mrad. The spectrum of the emitted radiation ranges from few keV up to tens of keV but falls of rapidly above a certain critical energy.
Note that synchrotron radiation plays a key role in the design of an electron-positron synchrotron such as SuperKEKB since it dampens oscillations in all three degrees of freedom and, therefore, enables stable propagation of the beams (see Section 3.2).

- **Radiative Bhabha process** The fourth source of backgrounds is *radiative Bhabha scattering.* The term *Bhabha scattering* refers to elastic scattering of electrons and positrons ($e^+e^- \to e^+e^-$) which dominates the e^+e^- cross section. Because it is a well understood process with clean experimental signatures, the rate of wide angle Bhabha scattering will be the primary method for monitoring the luminosity provided by the machine.
  However, for the majority of such interactions the deflection angle is small and the scattered particles continue propagating along the beam lines. If the changes in momentum and direction are sufficiently small, the scattered particles are able to maintain (temporarily) stable orbits. If they exceed the experimental aperture, the scattered particles collide with the beampipe or the accelerator magnets and the resulting showers of secondary particles can back-scatter towards the IP. Naturally, the rate of Bhabha scattering scales with the luminosity.
  Bhabha scattering is always accompanied by radiative effects which reduce the energy of the beam particles: $e^+e^- \to e^+e^-\gamma$. The produced photons propagate nearly parallel to the beam axis before they eventually collide with the accelerator elements. An interaction with the iron of the accelerator magnets then results in a larger number of low energy gamma rays and (via the giant photo-nuclear resonance) neutrons.

- **Two-photon process** The fifth source of backgrounds are very low momentum electron-positron pairs produced via the *two-photon process*: $e^+e^- \to e^+e^- + \gamma\gamma \to e^+e^-e^+e^-$. Guided by the field lines of the solenoid, such pairs then perform spiral movements and cause a large number of hits in the inner detector. A similar behavior can also be observed for primary electrons and positrons which took part in interactions where they lost large amounts of energy.

- **Injection background** The final source of background is *injection background.* As discussed in detail in the previous section, newly injected beam particles undergo extended oscillations before they fully merge with the injected bunch. These extended oscillations lead to a significantly elevated background rate whenever the bunch pass by the IP. Since the damping ring was only available from Phase 2 onwards, injection backgrounds of positrons are expected to be larger than for electrons during Phase 1.

Touschek scattering, beam-gas scattering and synchrotron radiation are types of beam-induced backgrounds. Radiative Bhabha and two-photon processes, on the other hand, are luminosity dependent backgrounds. Measurements performed during Phase 1 represent a unique opportunity to study beam-induced and injection backgrounds in a clean environment.

A comprehensive time resolved analysis of beam backgrounds during the first commissioning phase of SuperKEKB is presented in Chapters 7 and 8. A combined measurement of beam-gas and Touschek backgrounds in the interaction region and a method for disentangling the these two types of backgrounds is discussed in Chapter 9. A detailed investigation of luminosity dependent backgrounds will then be performed during Phase 2 and 3.

3.5 Beam and accelerator condition monitors

The following section will give a brief overview of the beam instrumentation and accelerator condition monitors installed at SuperKEKB which are used in the analysis of beam backgrounds presented in Chapters 7 through 9.

- **Beam size monitor** To measure the vertical size of the beams, σ_y, X-ray beam size monitors (XRM) are installed in each ring. The XRM measure the X-ray component of the synchrotron radiation emitted in the bending magnets using single-slit and multi-slit optical elements. The monitors are installed in the last arc-bends directly upstream of the straight sections in Fuji (LER) and Oho (HER) (see Figure 3.1).

  Several calibration studies on the performance of the XRM have been carried out during Phase 1. For the LER, the studies yield a vertical emittance of approximately 8 pm which is in reasonable agreement with an estimation based on beam optics. For the HER, however, they find a vertical emittance of approximately 41 pm what is a factor of four larger than the beam optics estimate. It is, therefore, foreseen to perform further studies, in particular to examine possible sources for smearing of the measured σ_y.

- **Pressure gauges** To monitor pressure throughout the beamlines, around 300 cold cathode gauges (CCGs) are installed in each ring at intervals of 10 m. Since the CCGs are located next to sputter ion pumps and separated from the beam line at the end of 1 m ducts, the pressure measured by the gauges is lower than the one seen by the beams. Based on simulations for SuperKEKB, it can be shown that the beam pressure, P_{beam}, can be reconstructed by

  $$P_{beam} = 3 \cdot P_{CCG} - 2 \cdot P_{base},$$

  where the base pressure, P_{base}, is defined as the minimum pressure recorded within the last multi-hour period without current in the respective ring. The base pressure is determined individually for each CCG.

  For the LER, the dynamic pressure is considerably larger than the base pressure and, therefore, $P_{beam} \approx 3 \cdot P_{CCG}$. For the HER, on the other hand, the base pressure has a significant influence on the pressure seen by the beam. In cases where the measured values are below the range of acceptance of the CCGs, we utilize their minimum reading of 18×10^{-8} Pa. From here onwards, the corrected pressure, P_{beam}, is used for all pressure readings.

- **Residual gas analyzer** To identify the individual components in the gas composition, two *residual gas analyzer* (RGA) are installed in the LER. One of the RGAs is located directly upstream of the IP, whereas the other one is placed approximately on the opposite side of the storage ring near the positron injection line (see Figure 3.1). The RGAs are mass spectrometers which yield the relative occurrences of ion fragments with mass-to-charge ratios m/Z in the range from 1 to 50.

  In particular for the study of beam-gas backgrounds, it is possible to determine an effective atomic number of the gas composition, Z_e. This Z_e corresponds to the atomic number of a pure gas for which the background levels caused by beam-gas interactions would be the same as for the gas mixture found in the beam lines. First, a list of possible gas species which could be present in the vacuum chambers is established. Second, the relative occurrence of each species in the residual gas is determined by fitting the measured spectra with the predefined list. These occurrences are used to calculate the number of atoms, n_i, of each element, Z_i. Finally, the Z_e can be expressed as the weighted average of all the Z_i^2:

$$Z_e = \sqrt{\frac{\sum_i Z_i^2 n_i}{\sum_i n_i}}.$$

Dedicated measurements performed during Phase 1 show good agreement between this model and the measured data [36].

A comprehensive description of this and additional beam instrumentation installed at SuperKEKB is given in [16]; a more detailed explanation of the condition monitors used, in particular for the study of beam backgrounds, can be found in [36].

3.6 The SuperKEKB commissioning campaign

In order to prime SuperKEKB and Belle II for physics operation and full luminosities an extensive commissioning campaign is performed. We complete the description of the accelerator by giving a brief overview of the three stages of this campaign which are simply referred to as *Phase 1*, *Phase 2* and *Phase 3*. Machine parameters attained during the operation of KEKB and SuperKEKB Phase 1, as well as the nominal machine parameters for SuperKEKB Phase 2 and 3 are summarized in Table 3.2. At the time of writing, SuperKEKB and Belle II are undergoing their third and final commissioning phase.

Phase 1 focused on the basic operation of the accelerator and, as such, the final focusing system and the Belle II detector have not yet been installed at the IP. Since the beams were unfocused, no intended collisions took place. The primary objectives for SuperKEKB were improving the vacuum conditions by *vacuum scrubbing* and performing basic machine studies. Examples for such studies are tuning of the feedback systems or low emittance optimization of the beam optics. During Phase 1, the BEAST II beam background detectors assumed the place of Belle II at the IP. Data taking for Phase 1 took place from February to June, 2016. The work presented in this thesis is based entirely on measurements performed during Phase 1 operations.

For Phase 2, the final focusing system and the positron damping ring were installed at SuperKEKB and the Belle II detector assumed its position at the IP. In that way, it was possible to focus both beams and perform the first collisions of the new machine. For beam background monitoring, however, the vertex detector of Belle II was replaced by a dedicated BEAST II Phase 2 detector system. Data taking for Phase 2 took place from March to July, 2018. Towards the end of the runtime, the accelerator achieved a peak

Table 3.2: Machine parameters during KEKB and SuperKEKB Phase 1 operation, and nominal machine parameters for SuperKEKB Phases 2 and 3. Table taken from [36].

	KEKB		Phase 1		Phase 2		Phase 3	
Ring	LER	HER	LER	HER	LER	HER	LER	HER
Beam current I [A]	1.64	1.19	1.01	0.87	1.0	0.8	3.6	2.6
Number of bunches N_b	1584	1584	1576	1576	1576	1576	2500	2500
Vertical beam size σ_y [μm]	0.94	0.94	110	59	0.25	0.39	0.048	0.062
Number of collimators	16	16	2	16	5	19	11	22
Luminosity [10^{34} cm^{-2}s^{-1}]	2.1		0		2		80	

instantaneous luminosity of $5.55 \times 10^{33}\,\mathrm{cm}^{-2}\mathrm{s}^{-1}$ [49].

Phase 3 represents the final stage of the commissioning campaign and, at the same time, the beginning of physics data taking. Here, the accelerator and the detector operate in their final configuration. Data taking for Phase 3 started in March, 2019 and will officially continue until the full design luminosity is reached.

Chapter 4

The Belle II and BEAST II experiments

In this chapter, we provide an overview of the detector systems installed at the SuperKEKB accelerator. In Section 4.1, we briefly introduce the Belle II experiment and discuss the difficulties for its operation which arise due to beam backgrounds. Section 4.2 then describes the BEAST II experiment which replaced Belle II during Phase 1 of the SuperKEKB commissioning campaign in order to perform first background measurements.

4.1 The Belle II experiment

Having introduced the SuperKEKB accelerator in the previous chapter, we now move on to describing the corresponding Belle II detector. Special emphasis is here placed on the impact of beam backgrounds since they will represent the primary challenge for the successful operation of the detector.

4.1.1 The Belle II detector

The physics program discussed in Chapter 2 also imposes certain requirements on the detector itself. In general, the detector has to have a high reconstruction efficiency for momenta and tracks of charged particles across the full kinematic range from 50 MeV up to 8 GeV. In particular, a vertex resolution of approximately 50 µm is needed in order to resolve the vertices from B-meson decays. It also needs to be able to determine the energy and direction of photons with such energies. Efficiently separating pions, kaons,

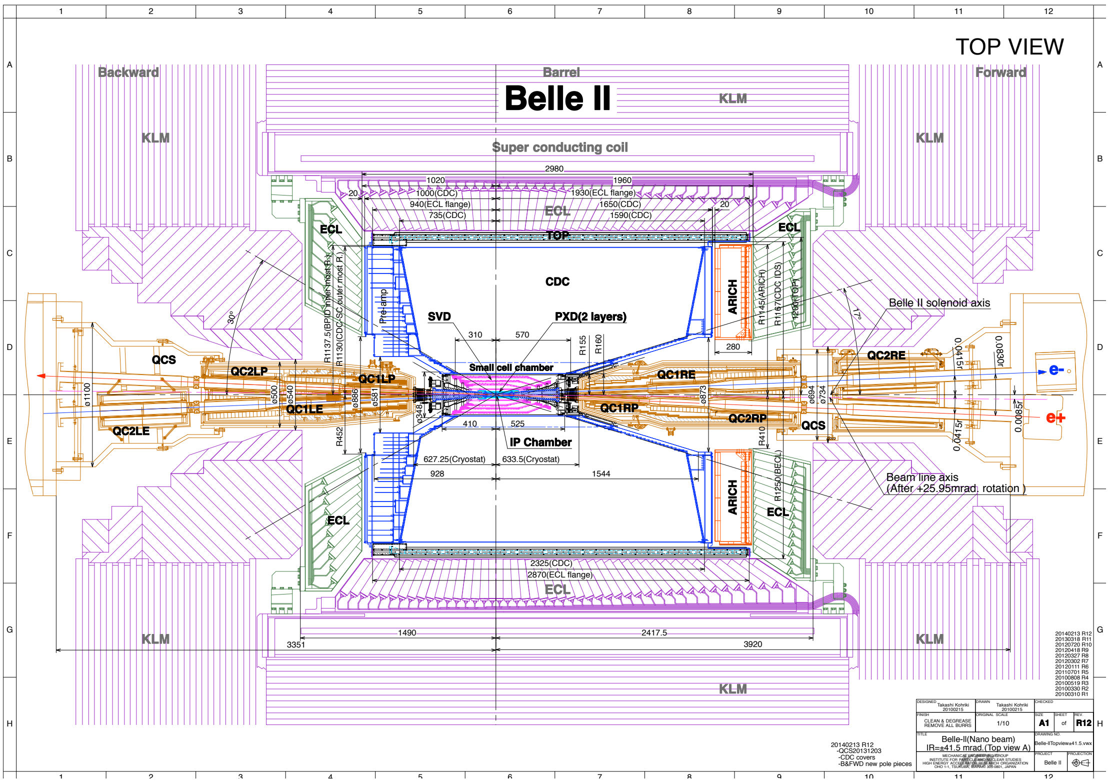

Figure 4.1: Technical overview of the Belle II detector shown from the top perspective. Figure taken from [23].

protons, electrons and muons from the various decay modes of the B-meson requires a highly capable particle identification system. The detector needs to cover almost the entire solid angle in order to be able to reconstruct final states with neutrinos and to have a fast and efficient triggering system to fully exploit the luminosity provided by the accelerator.

A technical overview of the Belle II detector shown from the top perspective is presented in Figure 4.1. The side of the detector on which the electrons enter (left side) is generally referred to as *backward* (BWD), whereas the other side (right side) is denoted by *forward* (FWD). In the following, the different subsystems of Belle II are introduced whereby the order commonly reflects their distance to the IP.

- **Vertex Detector** The Vertex Detector (VXD) consists of six layers of two different types of silicon sensors, namely the silicon Pixel Detector (PXD) and the Silicon Vertex Detector (SVD), and represents the inner tracker of Belle II. The hit information of all layers can be combined to reconstruct charged particle tracks

and vertices.
The two innermost layers at radial distances of only 14 mm and 22 mm are covered by the PXD, which is based on the so called DEPleted Field Effect Transistor (DEPFET) technology [50]. This technology offers high internal amplification and thus allows to reduce the sensor thickness to only 50 µm minimizing the material budget. For each pixel an individual field effect transistor is integrated onto a fully depleted silicon substrate. Electrons which are generated by incident particles are collected in a potential minimum until a "clear" voltage removes them. Switching on the transistor causes a resistivity which is proportional to the collected charge and, thus, represents a measurement of the energy deposited in the pixel. The PXD is read out row after row in a *rolling shutter mode*. First the resistivity at each pixel in a row is determined before the entire row is cleared. The readout of a full frame requires around 20 µs.
The continuous charge collection in the PXD means that the sensors also accumulate noise. If the charge collection capacity of a pixel is exceeded, it essentially becomes blind until readout. It is, however, possible to operate the PXD in an insensitive blind mode referred to as *gated mode*. In this gated mode, a large positive voltage is applied such that generated electrons are redirected and do not accumulate in the potential minimum. A major limitation of this approach is the fact that at least 2 µs are required for ramping up and down of this voltage.
In total, the PXD has around 10×10^6 readout channels. A detailed description of the PXD and its operations is given in [51].
The PXD is followed by the SVD which consists of four layers of double-sided silicon strip sensors located at radial distances of 39 mm, 80 mm, 115 mm and 140 mm from the z-axis. The top and bottom strips of each layer are orientated orthogonal to each other so that measurements can be combined into 2D hit information. In total, the SVD has around 14×10^3 readout channels.

- **Central Drift Chamber** The Central Drift Chamber (CDC) is the central tracking subsystem of Belle II. It has three main functions: reconstructing the tracks of charged particles in order to determine their momenta; identifying particles based on their energy loss within the gas volume, in particular low momentum particles which are not able to reach the outer systems, and serving as exclusive input for the *first level trigger* due to the insufficient readout time of the vertex detectors.
  The CDC is a cylindrical large volume drift chamber which covers radial distances from 160 mm to 1130 mm. With a 50:50 gas mixture of He and C_2H_6, average drift

velocities of 3.3 cm/µs and a maximum drift time of around 350 ns are achieved. Signals are read out by a total of 14 336 sense wires which are arranged parallel to the beam axis, referred to as *axial layers*, or slightly skewed, referred to as *stereo layers*. Combining the information of the axial and stereo layers enables the reconstruction of the full 3D helix track of a particle.
Offline, tracks and vertices are precisely reconstructed by combining measurements of the PXD, the SVD and the CDC.

- **Particle identification system** In particular to discriminate between kaons and pions, a particle identification system determines the velocity of charged particles based on a measurement of the Cherenkov angle. As a consequence of the elevated background levels and the tighter space constraints, two newly developed systems are used in Belle II. Together they cover polar angles from 17° to 120°.
  In the region of the forward endcaps, the aerogel ring-imaging Cherenkov detector is employed. An aerogel radiator with a thickness of 2 cm leads to the emission of a cone of Cherenkov photons which are subsequently detected by a dedicated photon sensor. The radius of the cone then yields the particle velocity.
  In the barrel region, on the other hand, a time-of-propagation (TOP) counter is used, which consists of long rectangular quartz radiator bars with 2.6 m length located directly on the outer wall of the CDC. The quartz bars are read out by photon sensors with a time resolution of around 100 ps which are located at one end of the bars. The time-of-flight of the photons depends on their propagation through the quartz bar and, thus, on the angle in which they are emitted. The Cherenkov angle can, therefore, be reconstructed from the impact position and the transition time (both have to be provided by other subsystems) of the incoming particle. The TOP detector system has the advantage of being extremely compact facilitating a larger tracker volume and deeper calorimeters within a same sized magnet.

- **Electromagnetic Calorimeter** The electromagnetic calorimeter (ECL) determines the energy of all particles and is the only subsystem capable of detecting neutral particles.[1] It therefore has several different tasks: detect photons with high efficiency; precisely measure their energy and direction; distinguish electrons from hadrons based on comparisons of momentum and energy; luminosity measurements; detection of K_L (together with the KLM discussed below), and the generation of a

---

[1] Neutral particles do not engage in electromagnetic interactions for example with the gas in the CDC or the silicon in the VXD.

first level trigger.
The ECL is divided into a barrel, a forward and a backward region (see Figure 4.1). Together they use 8736 identical thallium-doped caesium iodide, CsI(Tl), crystals which cover about 90% of the center-of-mass system and provide 0.8 nuclear interaction lengths. The crystals, preamplifiers and the support structure are not new systems but are reused from Belle. Not considering the increased background rates, the performance figures for the ECL, therefore, should be very similar to the predecessor: $\sigma_E/E = 1.6\%$ at 8 GeV and a π^0 mass resolution of 4.5 MeV/c^2.

- **Solenoid magnet** A superconducting solenoid provides a homogeneous 1.5 T magnetic field parallel to the direction of the beam axis. Charged particles flying perpendicular to this field are thus forced on a curved trajectory. The curvature of this track together with the strength of the magnetic field can then be used to retrieve the momentum of the particle. The solenoid covers a cylindrical volume with an inner radius of 1.7 m and a length of 4.4 m and encloses all subdetectors except the KLM discussed in the following.

- **K$_L$-Muon Detector** The solenoid is surrounded by the outermost subsystem of Belle II, the K$_L$ and muon detector (KLM). It consists of an alternating sandwich structure of 4.7 cm iron plates and active sensor layers which have a total thickness of 3.9 interaction lengths. Its main purpose is to identify muons leaving the detector and serve as an extended calorimeter for the rudimentary measurement of hadronic showers, in particular from long lived neutral hadrons such as K$_L$. Besides the detection of particles, the iron plates of the KLM simultaneously serve as a return yoke for the magnetic flux of the solenoid and provide mechanical support for the other subsystems of Belle II.
  In the barrel, the glass-electrode resistive plate chambers (RPC) of Belle are reused. For the FWD and BWD endcaps, however, the increased background levels require faster detectors. The RPCs in the endcaps, therefore, have been replaced by scintillator strips with wavelength shifting fibers and SiPM readout; a system which is very similar to CLAWS (see Section 5).

An in-depth description of the Belle II detector can be found in [16].

4.1.2 Impact of beam backgrounds

The Belle II detector will be taking data at an accelerator with a target luminosity of $8 \cdot 10^{35}\,\mathrm{cm}^{-2}\mathrm{s}^{-1}$, 40 times higher than for Belle. As such, the detector needs to be capable of operating at a 40 times higher event rate while being exposed to beam backgrounds for which the rates increase by a factor 10 to 20 [16]. These backgrounds significantly increase the occupancy, in particular in the inner detectors like the PXD, they cause fake hits, pile-up noise and neutron induced hits across a wide range of systems and they lead to potential radiation damages. Limiting and mitigating those background will be the primary challenge for the successful operation of the Belle II detector.

To counteract backgrounds, all of the systems are either extensively upgraded or entirely new developments. For the ECL for example, it is expected that the elevated background levels and the relative long decay time of CsI(Tl) lead to significant overlap between signal pulses of subsequent events (i.e. pile-up). To reduce the impact of this pile-up, the readout electronics have been modified in such a way that they continuously sample the waveforms similar to the signal processing of CLAWS (see Section 5). However, for the part of the detector which is located in the forward region close to the beam pipe the increased pile-up noise will still degrade the performance considerably.

Depending on the process, Belle II and SuperKEKB will employ several different countermeasures to mitigate beam backgrounds. Horizontal and vertical movable collimators and metal shields will be used to prevent particles which deviate from their nominal orbits, for example as a result of Touschek and beam-gas scattering, from reaching Belle II. While collimators will be installed at various positions throughout the beam lines, the ones located close to the IR play an important role in reducing such backgrounds. Furthermore, dedicated heavy-metal shields will be installed in the volume of the VXD and on the final focusing system for Phase 2 and Phase 3 in order to keep secondary shower particles from reaching the detectors. Synchrotron radiation and low angle Bhabha scattering will be tackled through the design of the final focusing system and the inner beampipe. The beampipe in the IR is made from beryllium and its inner surface is coated with a gold layer in order to absorb SR photons. The shape of the beampipe and separate quadrupoles for each outgoing beam will further prevent photons and Bhabha scattered electrons from reaching the detectors. High background levels during injections require an interruption of data recording in several subsystems of Belle II, in particular in the PXD. To lower the loss in integrated luminosity it is intended to gate data taking of the subsystems and stop recording only during transits of injection bunches.

The work presented in this thesis is part of a large effort to understand beam backgrounds and validate background simulations by first experimental results as early as possible.

4.2 The BEAST II experiment

As was pointed out in the introductory chapter, during Phase 1 of the SuperKEKB commissioning campaign the final focusing system and the Belle II detector have not yet been installed at the IP. Instead, a suite of eight dedicated beam background detectors, collectively referred to as the BEAST II experiment, was mounted in the IR. The main objectives of the BEAST II experiment are the following: verifying that radiation levels are safe for the installation of Belle II, validating beam background simulations and providing real time feedback to the operators of the accelerator on how machine parameters influence background levels at the IP. In this section, we introduce BEAST II and provide a technical description of the experiment and its subsystems.

Figure 4.2 presents a photograph of BEAST II (*top*) and a CAD rendering of the platform, the beampipe and the subsystems (*bottom*) both shown from the top perspective. The experiment sits on a dedicated platform made out of concrete which levels out the size difference compared to Belle II. The IR for Phase 1 ranges ±4 m from the IP covering essentially the area shown in Figure 4.2. The beams are crossing (not necessarily colliding) in a 40 cm long central beampipe made from aluminum with an inner radius of 4 cm and a thickness of 4 mm. This central beampipe was build specifically for Phase 1 and was installed exactly at the IP. Two additional pairs of aluminum beampipes with a dedicated cooling, vacuum and support structure connect the central beampipe with the two storage rings. The whole IR is covered by an additional rectangular concrete shell with a wall thickness of 75 cm (not shown in Figure 4.2) placed directly on the platform. Together, the platform and the shell, simply referred to as the *BEAST cave*, provide a shield against radiation and ambient light and lead to relatively stable temperatures during operation.

For BEAST II, a temporary support structure made from off-the-shelf fiberglass elements is mounted around the IR (see Figure 4.2 (*top*)). The sensors are then installed either electrically isolated directly on the beampipe or onto this structure. They are mounted with a position accuracy of better than 1 cm.

The BEAST II experiment includes eight different subsystems summarized in Table 4.1. The PIN diode system consists of 64 diodes in 32 different locations and monitors the ionization radiation dose throughout the IR. Four single-crystal diamond detectors, foreseen as a beam abort system for Belle II, measure the dose rates only at selected locations close to the IP but with fast timing characteristics. The Crystal system consists of units of inorganic scintillators read out by photomultiplier tubes which measure the rate and spectrum of electromagnetic backgrounds at different positions corresponding to the

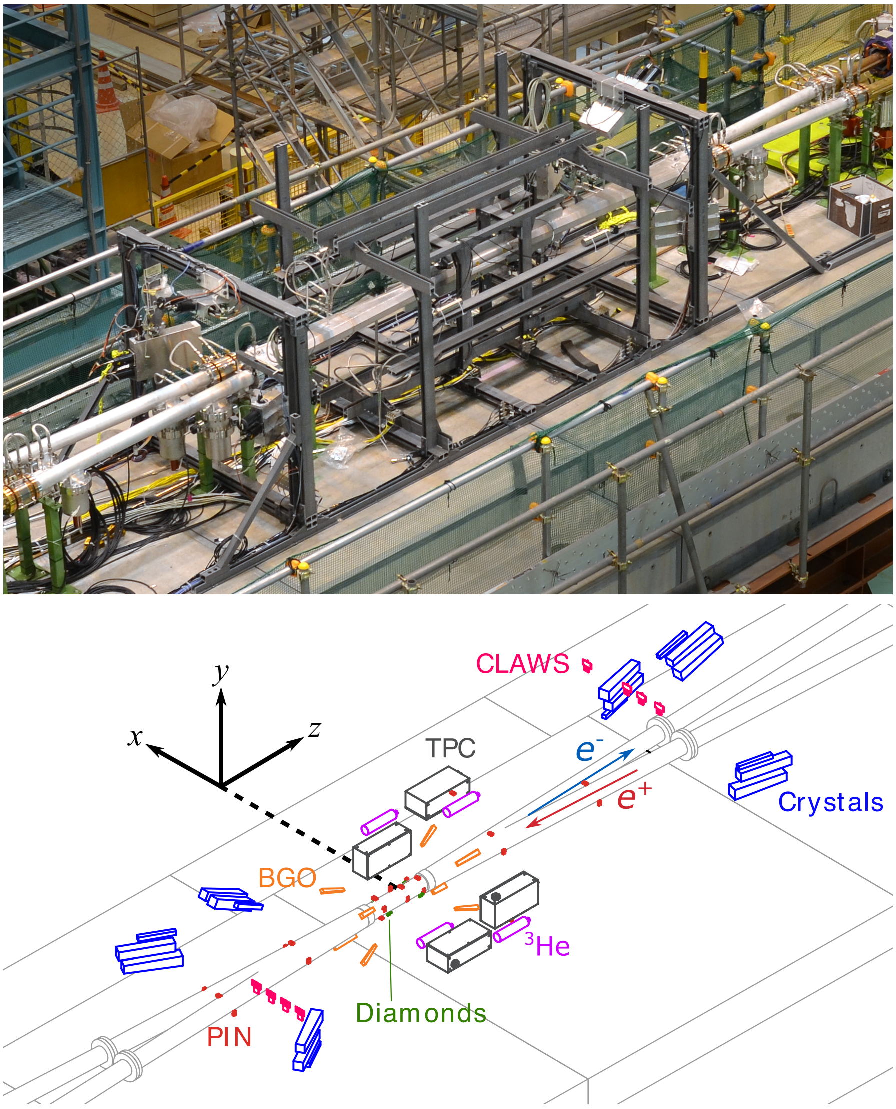

Figure 4.2: Photograph of the interaction region with the BEAST II detector system taken prior to the installation of a concrete shield (*top*). CAD rendering of the platform, beampipe and the subsystems of BEAST II shown from the same perspective (*bottom*). For clarity, the coordinate axis are shifted from their actual position which is the nominal interactions point. Figures taken from [36].

innermost part of the ECL. In addition, eight bismuth germanium oxide (BGO) detectors are reused from the Belle extreme forward calorimeter which also record electromagnetic backgrounds and are an intended prototype for a luminosity monitor via counting of Bhabha scattering. As the main topic of this thesis, CLAWS is described in detail in the

Table 4.1: Summary of BEAST II subsystems. Table taken from [36].

System Name	Detector Type	#	Unique Measurement or Capability
PIN	PIN diodes	64	Instantaneous dose rate at many positions
Diamond	Diamond Sensors	4	Near-IP fast dose rate, beam abort prototype
Crystal	CsI(Tl), CsI, LYSO crystals	$6+6+6$	Electromagnetic energy spectrum, injection backgrounds
BGO	BGO crystals	8	Electromagnetic dose rate
CLAWS	Plastic scintillators	8	Injection backgrounds
^{3}He	^{3}He tubes	4	Thermal neutron rate
TPC	Time Projection Chambers	4	Fast neutron flux and directionality
QCSS	Plastic scintillators	6	Charged particle rates, prototype for Phases 2,3

following chapter. Four ^{3}He tubes are installed in order to record the rate of thermal neutrons. Four micro time projection chambers (TPCs) measure the direction and energy loss of recoils from ‘fast’ or higher energy neutrons. Finally, six prototype background monitors based on plastic scintillators with SiPM readout referred to as QCSS are small enough to be installed between the QCS cryostat and the Belle II detector.

The readout electronics for the sensors is located in a radiation safe counting room below the beam line and is accessible during operation. Sensors and electronics are connected by cables with a length of around 37 m. Except for a number of front-end amplifiers and digitizers mounted directly on the sensors, all signal processing takes place in racks located in the counting room.

The time of the readout PCs of all BEAST II subsystems is synchronized via a dedicated time server which allows unified timestamps with a precision of up to 10 ms. In order to provide feedback to the operators of the accelerator, the BEAST II experiment is fully integrated into the accelerator slow control network via the Experimental Physics and Industrial Control System (EPICS) [52]. As it is the case for accelerator conditions, observables from BEAST II are shared in real-time via the network and with the control room of the machine. To be able to perform offline analysis of beam background measurements after runtime, 1 s summaries of these observables and accelerator conditions are used to generate a unified data set. For example, the analysis presented in Chapter 9 is based on this data set.

The BEAST II experiment was continuously monitoring beam backgrounds during the full five month of the first commissioning phase of SuperKEKB in Spring 2016. It performed a wide range of measurements including instantaneous and integrated dose rates, as well as, novel measurements of the bunch-by-bunch structure of charged particle backgrounds (which are discussed in detail in this thesis) or the direction and energy of neutrons. Towards the end of Phase 1, dedicated machine studies took place in which we systematically varied various beam parameters in order to determine their influence on backgrounds at the IP. In total, BEAST II examined instantaneous and integrated dose rates, beam-gas and Touschek scattering, beam-dust events and injection backgrounds. A comprehensive description of BEAST II, its subsystems and the studies performed is given in [36].

Chapter 5

CLAWS - Experimental setup

In this chapter, we provide a detailed description of the experimental setup of CLAWS installed during Phase 1 of the commissioning of SuperKEKB. Because of their significant impact on the data taking efficiency, the primary objective of CLAWS is the study of backgrounds caused by continuous top-up injections. Requirements for the measurement of injection backgrounds are mainly related to timing. In order to differentiate between energy deposits of individuals bunches, a time resolution comparable to or smaller than the time between consecutive bunches ($T_{bunch} = 3.930\,\text{ns}$) is needed. Capturing the full time evolution of injection backgrounds requires being able to monitor background rates over hundreds of turns in the accelerator or up to several milliseconds. To synchronize injections and data, the setup must be able to start recording by a dedicated trigger signal provided by the injector linear accelerator. Secondary objectives for CLAWS are the measurement of other beam-induced backgrounds as part of the overall BEAST effort. To infer the type of background particles and the responsible background process, a time and energy resolution small enough to resolve energy deposits of single particles is required. Studying beam-induced backgrounds also calls for the capability to self-trigger continuously. Furthermore, as demanded from all BEAST II subsystems CLAWS needs to be integrated into the SuperKEKB network and has to provide real-time feedback to shifters and operators. Also performing online and detailed offline analyses of the raw sensor data requires handling and storing extensive amounts of data. All of these considerations and requirements have been taken into account in the design and the setup of the CLAWS experiment.

First, we introduce the CLAWS sensor modules and their components in Section 5.1 and outline the overall setup installed at SuperKEKB in Section 5.2. In Section 5.3 we then describe different calibration measurements performed before and after the runtime of

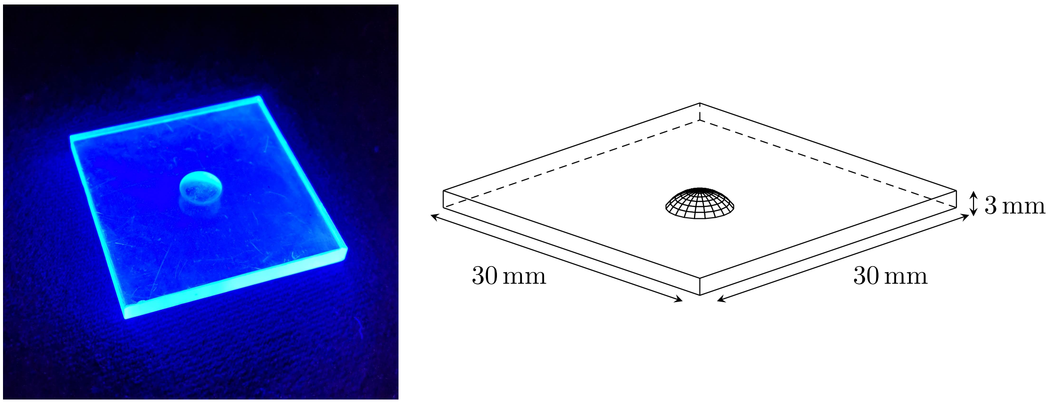

Figure 5.1: Picture taken under UV light (*left*) and technical drawing (*right*) of a scintillator tile used for the CLAWS sensor modules.

Phase 1. Finally, Section 5.4 presents the custom-made data acquisition software (DAQ) used to control the setup, read out the sensors and store the recorded waveforms for offline analysis.

5.1 Detector design

The CLAWS sensors use organic plastic scintillator tiles as their primary method of detecting particles. The light emitted by theses scintillators is then read out by SiPMs. Together, the scintillating tiles and the SiPMs are mounted on custom made PCB boards for signal transmission, power distribution and mechanical support. Collectively, we refer to these as the *CLAWS sensor modules*.

The design of the sensor modules is based on the CALICE-T3B experiment [53, 54] which examined the time structure of hadronic showers. To reduce intrinsic noise rates and enhance radiation hardness, a new type of SiPM and a different scintillator material is used in CLAWS. In the following, we provide a detailed description of the tiles, the SiPMs and the design of the sensor modules.

5.1.1 Plastic scintillators

Figure 5.1 shows a picture taken under UV light (*left*) and a technical drawing (*right*) of a CLAWS scintillator tile. The tiles are cuboid-shaped and have a size of $30 \times 30 \times 3\,\mathrm{mm}^3$. To accommodate the SiPM, a partial half sphere with a depth of 1.5 mm and a diameter of 6 mm (on the surface) is drilled in into the bottom side of the tile. This so-called *dimple* facilitates the coupling of the tile and the SiPM via a simple air gap and ensures a

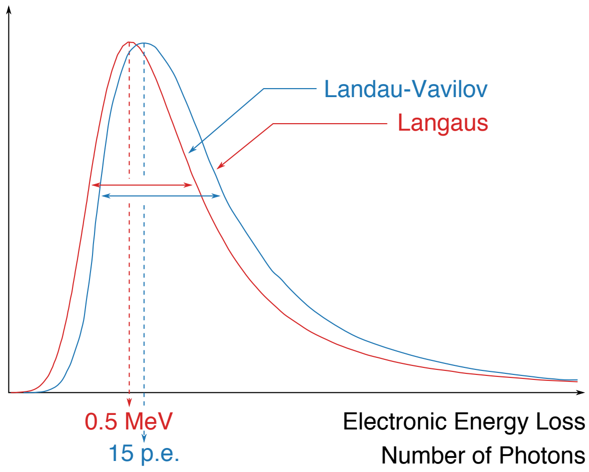

Figure 5.2: Illustration of the distribution of electronic energy deposits of a minimum ionizing particle passing through one of the CLAWS sensor modules.

uniform light yield irrespective of the position of the traversing particle. This design has been developed for surface-mounted photon sensors for the CALICE Analog Hadronic Calorimeter [55] and is a further development of the scintillator tiles used in the CALICE-T3B experiment which are based on SiPMs coupled to the side face of the scintillator [56].

Particle interactions The processes discussed in Section 3.4 primarily lead to three different types of background particles: electrons and positrons, photons, and neutrons. While passing through the detectors, charged particles such as electrons and positrons are subject to two different types of electromagnetic energy losses: ionization/excitation and bremsstrahlung. Through a number of collisions with the hull electrons, the incident particles excite or ionize the atoms and molecules of the scintillator. The mean rate of energy losses due to such interactions depends primarily on the material (atomic mass and number) and the $\beta\gamma$ of the incident particle and has a broad minimum around $\beta\gamma \approx 3-4$ (see *Bethe equation* [32]). A particle with an energy for which the mean loss rate in matter is close to this minimum is referred to as a minimum ionizing particle (MIP).
For thin absorbers like plastic scintillator tiles, the probability for such energy losses can be described by a Landau-Vavilov distribution (highly-skewed Landau distribution), as illustrated in Figure 5.2. This distribution has a long tail due to rare events in which extreme amounts of energy are transfered. As a consequence of the large weights of these rare events, the mean of experimental distributions with less than few hundred events is subject to notable fluctuations. Therefore, the most probable value (MPV)

of this distribution is generally used to characterize the response of detectors instead of the mean. Promoted by their low mass, electrons and positrons are also subject to radiative energy losses via bremsstrahlung. While the probability for a direct detection of bremsstrahlung photons is small, such an interaction can be observed through tertiary electrons and positrons generated via subsequent pair production processes.

In the scintillator, photons can interact via the photoelectric effect, Compton scattering or pair production. A photoelectric absorption or Compton scattering also leads to the ionization or excitation of the atoms and molecules and can take place for photons of up to few tens of MeV. Again, pair production causes the generation of detectable tertiary particles. Due to the large proportion of hydrogen in the scintillator, also neutrons with kinetic energies up to few MeV can be detected through collisions with protons. As a consequence of the momentum transfer, the protons get knocked out of the molecule and ionize the scintillator material. In the broad majority of the cases, however, CLAWS observes the transit of charged particles.

Scintillation process The scintillator material is the same as the one used for the Muon Veto Detector 1 (MUV1) of the NA62 experiment [57]. It is based on polystyrene (Styron 143E) with additional small admixtures of scintillating fluors (p-terphenyl, 2%) and POPOP (0.05%). It is primarily the molecules of the widespread base material which are excited in the particle interactions. The deposited energy is transfered from the base to the fluors and subsequently to the POPOP mainly by resonant dipole-dipole interactions. Finally, POPOP radiates the energy in the form of photons in the blue visible range from 380 nm to 500 nm with a peak emission of around 420 nm (see Figure 5.1 (*left*)). The energy which is required to excite the widespread base material is generally larger than the one of the emitted photons. This shift of the wavelength thus reduces the probability for a reabsorption of the photons significantly and effectively makes the scintillator self transparent. In general, the emission of the photons is not instantaneous but smeared in time with relatively short decay times of around 2 ns.

5.1.2 Silicon photomultipliers

SiPMs are a relatively new but by now widely used type of solid state photon sensor [58]. These sensors offer several features which make them the preferred choice for the use in the CLAWS detectors, such as a fast response, single photon detection capability and a high intrinsic amplification ($\mathcal{O}(10^6)$).

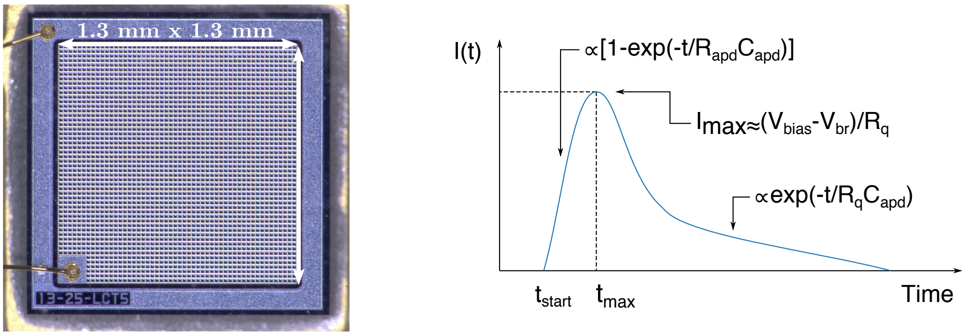

Figure 5.3: Close-up of a prototype for the Hamamatsu S13600-1325PE series SiPMs consisting of a large number of avalanche photo diodes (APDs) in a matrix structure which are used in the CLAWS sensor modules (*left*). Illustration of the typical signal pulse of an APD, more specifically of a single pixel of a SiPM (*right*).

Underlying concept As shown in Figure 5.3 (*left*), SiPMs consist of a large number of avalanche photo diodes (APDs) operated in Geiger mode. APDs themselves are based on regular photo diodes. In such a diode, an incident photon with an energy above the indirect bandgap gets absorbed in the depleted region of a pn-junction where it generates an electron-hole pair via the photoelectric effect. Since no amplification takes place in the diode, the amount of charge carriers generating the signal simply corresponds to the number of created electron-hole pairs.

In APDs, a large reverse-bias voltage, V_{bias}, is applied to the pn-junction. This voltage leads to an electric field which is sufficiently strong to accelerate the initial electron-hole pairs so that they generate secondary charge carriers via impact ionization. While this multiplication process is associated with the formation of a charge avalanche, the number of generated secondaries is proportional to the number of initial electron-hole pairs. It is also possible to operate the diodes in the so-called *Geiger mode* by applying a bias voltage above the breakdown voltage, V_{br}. In this regime, a single electron-hole pair is sufficient to generate a self sustaining charge avalanche. An operation in Geiger mode requires a dedicated quenching resistor, R_q ($\mathcal{O}(1\,\mathrm{M}\Omega)$), connected in series with the diode to limit and interrupt the signal. The current caused by the formation of an avalanche leads to a voltage drop at the quenching resistor resulting in a decrease of the bias voltage below the breakdown voltage. In Geiger mode, the signal amplitude depends only on the bias voltage and the properties of the diode and is not proportional to the number of initial charge carriers.

A SiPM represents a matrix of a large number of Geiger mode APDs which are connected in parallel and fabricated on a single monolithic silicon crystal (see Figure 5.3 (*left*)).

The individual APDs of a SiPM are, thus, called the *pixels* of the SiPM; pixel with an ongoing charge avalanche are referred to as *firing pixels.*

Signal shape and sensor properties Figure 5.3 (*right*) shows an illustration of the typical signal pulse of an APD operated in Geiger mode, more specifically of a single pixel of a SiPM. The shape of the pulse is characterized by three distinct features: a fast rise, a maximum current, I_{max}, and a slower exponential decay caused by the quenching of the avalanche. The rise time is determined by the intrinsic resistivity, R_{apd}, and capacity, C_{apd}, of the APD. The maximum is given by the difference between V_{bias} and V_{br} divided by R_q. Finally, the exponential decay taking place in the later part of the signal is defined by R_q and C_{apd}. In general, the intrinsic properties of the APD can be used to adjust its signal height and its timing characteristics. Since it is normally caused by an incident photon, such a signal pulse is referred to as a *photon equivalent* (p.e.).
The *photon detection efficiency* (PDE) of a SiPM denotes the probability that an incident photon leads to a Geiger discharge in the sensor. As such, it depends on the probability to create an electron-hole pair (*quantum efficiency*), the probability for an electron-hole pair to trigger an avalanche (*breakdown efficiency*), and the ratio of the active to the total area of the SiPM (*geometrical fill-factor*). The PDE is a function of the wavelength of the incident photon.
The multiplication factor between the electron-hole pair generated by a single photon and the amount of charge carriers in an avalanche for a single pixel is defined as the gain of the SiPM, G. It is determined by C_{apd} and the so-called overvoltage, $U_o \equiv U_{bias} - U_{br}$, and is not related to the number of initial charge carriers. That means the response of a single pixel is the same for a single or multiple photons and is approximately the same for each pixel. The U_{br} increases linearly with temperature and varies slightly between individual SiPMs of the same type due to fluctuations in the manufacturing process. Since the U_{bias} is usually kept constant, U_o and G decrease linearly with increasing temperature. The same is the case for the breakdown efficiency.
Normally the number of pixels of the SiPM is large compared to the number of incident photons, such that a pixel is hit only by a single photon. The response of the SiPM then is the superposition of the signals of the individual pixels and is scaling roughly linearly with the light intensity. Depending on the intensity, however, the finite number of pixels can lead to saturation effects and defines the maximum number of simultaneously detectable photons or in other words the dynamic range.

Noise effects As most semiconductor sensors, SiPMs are subject to unwanted side effects. The three most important of these effects are *thermal dark noise*, *afterpulsing* and *crosstalk*. All of these effects generate additional signal pulses which are indistinguishable from real signals.

- **Afterpulsing** Electrons generated in the discharge can get trapped due to crystal lattice defects in the silicon. If released after the recovery time of the pixel, this electron can cause an additional pulse in the same pixel, delayed with respect to the initial photon.
- **Crosstalk** During the development of an avalanche, an electron-hole pair generated in the Geiger discharge can recombine by emitting a photon. There is a certain probability that such a photon gets reabsorbed in a neighboring pixel where it triggers an additional discharge. This process results in additional pulses correlated with the original signal and takes place quasi-instantaneously.
- **Thermal dark noise** Rather than by incident photons, one p.e. pulses can also originate from electron-hole pairs generated by thermal excitation. The rate of such pulses depends on the temperature and varies between individual SiPMs of the same type due to fluctuations in the manufacturing process. Thermal dark noise occurs randomly and is not correlated with other signals. Due to crosstalk, it can also cause multi p.e. pulses.

Collectively, these effects hamper the determination of the exact arrival time of a traversing particle and the amount of energy it deposited in the scintillator (see Section 6.1.1).

Hamamatsu MPPCs All CLAWS sensor modules use Hamamatsu MPPC s13360-1325PE series SiPMs [59]. These SiPMs have 2668 pixels distributed over an active area of 1.3 mm × 1.3 mm integrated in a SMD packaging. The individual pixels have a size of 25 µm × 25 µm. Their spectral response ranges from 320 nm to 900 nm with a peak sensitivity at 450 nm, closely matching the emission spectrum of the scintillator (see previous section). The signal rise times are approximately 1.5 ns with total decay times of around 100 ns. To reduce the cross talk probability, the individual pixels are surrounded by an additional barrier called *trench* which captures inadvertently emitted photons. At 25°, the manufacturer states a breakdown voltage of $(53 \pm 5)\,\mathrm{V}$ and recommends an over voltage of 5 V. Under these conditions, the sensors offer a gain of 7.0×10^5, a peak photon detection efficiency of 25% and a thermal dark rate as low as 70 kHz.

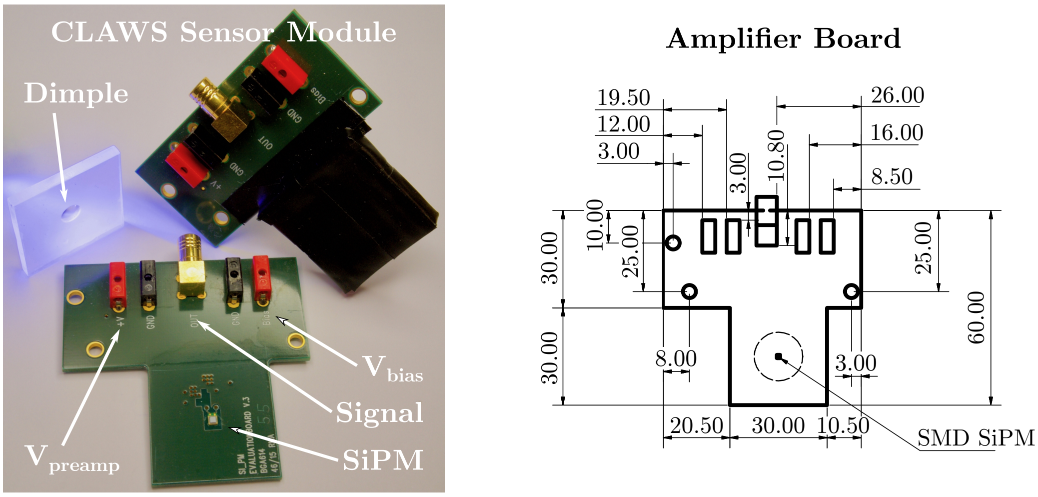

Figure 5.4: Photograph of an assembled CLAWS sensor module and its main components, a 30 mm × 30 mm × 3 mm scintillator tile and the PCB with photon sensor, preamplifier and connectors for power supply and signal transmission (*left*). Technical drawing of the readout boards used in the CLAWS sensor modules (*right*).

These SiPMs offer excellent timing characteristics and high detection efficiencies. Compared to the ones used in T3B, their pixel count and dynamic range is five times higher while their crosstalk probabilities and dark rates are significantly reduced.

5.1.3 Sensor modules

One of the fully assembled CLAWS sensor modules and its main components are shown in Figure 5.4 (*left*).

Module assembly The modules are assembled by mounting the scintillating tile and the SiPM on a custom made PCB readout board. A technical drawing of a readout board is shown in Figure 5.4 (*right*). Its design is essentially identical to the one used in T3B [56]. The SMD SiPM, an additional preamplifier and several other electronic components are soldered directly on the PCB. To prevent noise pickup, the preamplifier is located directly beneath the SiPM on the opposite side of the PCB. It matches the impedance to 50 Ω for further transmission and amplifies the signals by a factor of 8.9, significantly increasing the signal to noise ratio at the end of the readout chain. The second function of the readout board is to supply the electronics with power. Two separate power lines provide the SiPM with a bias voltage of 56 V and the preamplifier with 5 V. The third function of the readout board is to provide mechanical stability for the sensor modules and to allow for a mounting with precision better than 1 cm as demanded by the overall requirements of BEAST II. We use the five digit serial number of the SiPMs as an unique identification number for each sensor module.

Except at the dimple, the scintillator tiles are wrapped in a highly reflective *Daylighting Film DF2000MA* mirror foil produced by 3M [60]. For wavelengths in the range from 400 nm to 775 nm, the foil reaches a reflectivity of more than 99%. The wrapped tiles are glued on the readout board such that the photon sensor is fully submerged inside the dimple. This ensures an optimal coupling between scintillator and SiPM and a uniform response across the entire tile. Finally, all relevant areas of the tile and the board are covered in conventional black adhesive tape in order to shield the sensor from ambient light.

Detector response As mentioned earlier, the number of emitted scintillation photons is following a Landau-Vavilov distribution [32]. When traversing one of the scintillator tiles at perpendicular incidence, the most probable energy loss of a MIP is around 500 keV. Since the emission of a single photon requires approximately 100 eV [32], such a transit yields 5000 isotropically emitted scintillation photons. The SiPM, however, covers less than 0.1% of the surface of the tile and therefore the majority of these photons is lost. The fraction of photons, which is actually detected by the sensor, is relatively small and follows a Poisson distribution. Under typical operating conditions, we observe approximately 15 p.e. for a through-going MIP and thus approximate the fraction of photons by a Gaussian distribution. It is then possible to describe the number of photons detected after the transit of a MIP by the convolution of a Landau-Vavilov and a Gaussian (see Figure 5.2). Compared to a pure Landau-Vavilov, it has a slightly larger width and its MPV is shifted to higher values. We simply refer to this convolution by the name *Langaus*.

We define the light yield of a CLAWS sensor module, LY, as the MPV of the distribution of the number of observed p.e. for a large number of MIPs. Because it depends on the specific assembly (wrapping, coupling of tile and SiPM, etc.), the LY has to be determined individually for each module.

Radiation damage In particular, the SiPMs suffer from radiation damage which leads to significantly increased noise rates and depends on the integrated dose, the dose rate and certain environmental conditions. In addition, radiation damage also affects the other electronic components and the plastic scintillators, where it reduces the light yield and the attenuation length. The T3B experiment used a polyvinyl toluene based scintillator (Bicron BC 420) which has roughly a factor two higher light yield and a slightly faster decay time compared to the polystyrene based scintillator used in CLAWS. The main motivation for changing the type of scintillator was that it offers a notably higher radiation hardness.

As described in detail in [61], we found that the SiPMs of the sensor modules located closest to the beam pipe did suffer from radiation damage and show notably increased dark noise rates. For the scintillator tiles and other electronic components, on the other hand, we did not observe any signs for radiation damage during Phase 1.

5.2 Overall experimental setup

Having introduced the sensor design, we will now describe the overall experimental setup of CLAWS as it was installed during Phase 1. A schematic overview of the setup is illustrated in Figure 5.5.

Physical layout In total we installed eight CLAWS sensor modules arranged in two stations with four detectors each. To cover the full range of expected rates, the detectors of one station are installed in the region with the highest background rates predicted by simulations, on the forward side outside of the accelerator ring in the accelerator plane. The detectors of the other station are installed in the region with the lowest background prediction, on the backward inside of the accelerator ring. In both cases, the modules are mounted directly on the BEAST support structure (see Section 4.2) in a line roughly perpendicular to the beam with a spacing of around 10 cm between each detector (see Figure 5.6 for the backward station). Next to each sensor station, we installed a set of additional amplifiers to drive the signals over the long distance between sensors and readout electronics.

As it is the case for all BEAST systems, the readout electronics and the power supply (PSU) are located in a radiation safe counting room (DAQ room) below the beamline which is accessible during operation. Each sensor module is connected to the electronics by a 45 m power cable and a 45 m signal cable. Two additional 45 m power cables are used for supplying the amplifiers of both stations. All cabling used for CLAWS complies with low smoke zero halogen (LSZH) standards to reduce smoke formation when exposed to high sources of heat and to avoid activation of chloride which is usually included in cable sheaths.

Together with the ^{3}He system, the CLAWS system occupies one of the racks located in

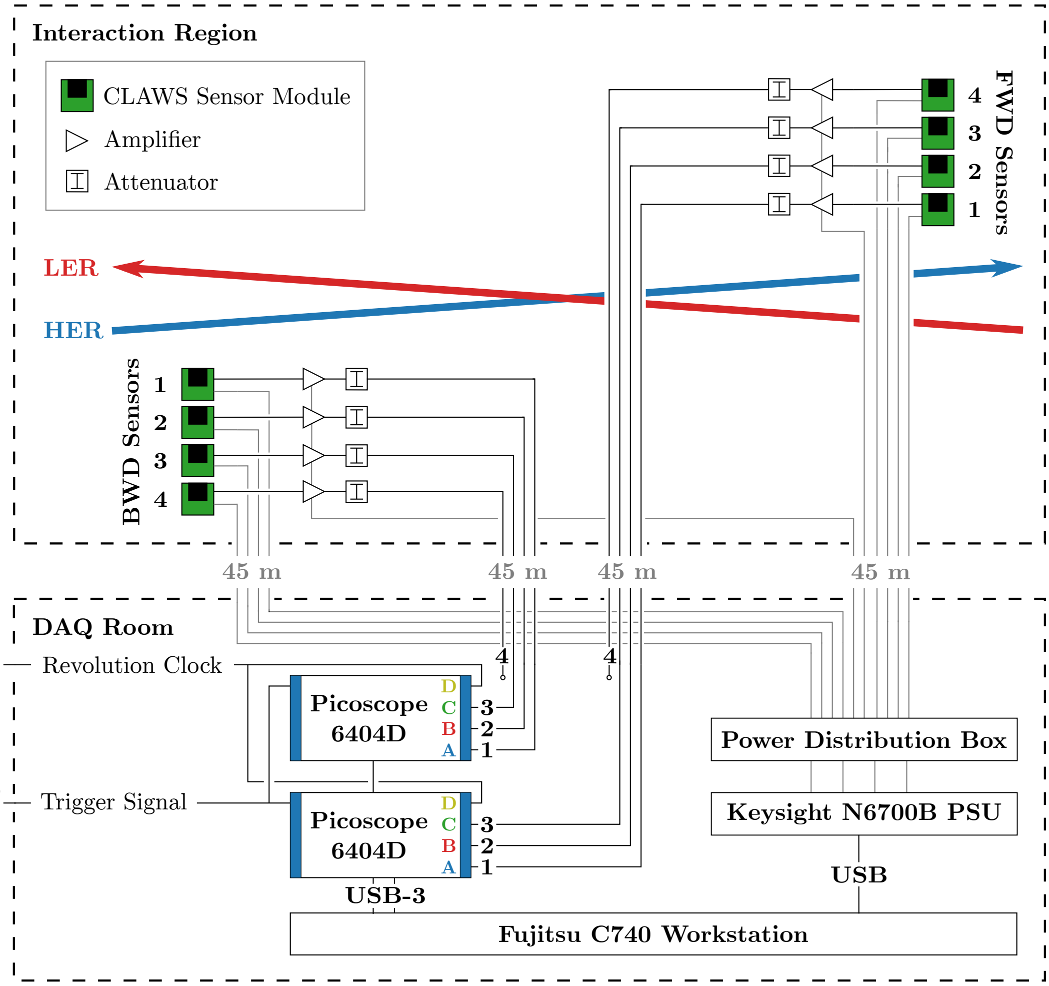

Figure 5.5: Schematic overview of the experimental setup of CLAWS.

the DAQ room. In this rack we installed a single PSU, a dedicated voltage distribution box, two oscilloscopes and a workstation running the CLAWS DAQ. A dedicate signal line running from the injector linac to the DAQ room provides the setup with an injection trigger signal and a duplication of the revolution clock.

Signal transmission, processing and trigger conditions In general, we use RG58 coax cables and BNC and SMB connectors for signal transmission from the modules to the amplifiers and then to the oscilloscopes in the DAQ room. The large cross sections of the cables ensure that signal amplitudes are not reduced by more than a factor of two. To drive the signals over the distance between the IR and the DAQ room we installed 20 dB amplifiers (Mini Circuits ZFL-500 [62]) which increase signal amplitudes approximately

Figure 5.6: Photograph of the CLAWS backward station taken from the position of the IP. Four sensor modules are mounted on the BEAST support structure in the plane of the accelerator with increasing radial distance from the beampipe (shown on the right).

by an additional factor of ten. Before the start of Phase 1, only rough estimates of the expected signal rates were available and it was foreseen to match rates and amplification during runtime by adding suitable attenuators; we had different versions in the range from 5 dB to 20 dB available. The signals encountered during runtime, however, were at the upper end of the estimates and it was therefore necessary to install the 20 dB attenuators (Mini Circuits HAT-20-75+ [63]) in front of the amplifiers to prevent saturation effects.

The signals are digitized with two 4-channel PC-based Picotech PicoScope 6404D oscilloscopes which sample each channel at 1.25 GHz (or every 0.8 ns) with 8 bit resolution [64]. Each scope has a shared internal buffer of 2 GS which is capable recording continuous waveforms of up to 400 ms. This allows uninterrupted monitoring of particle rates over up to around 40000 consecutive turns in SuperKEKB. In addition to the four regular channels, each scope has a dedicated trigger input. In general, we refer to the sampled sensor output recorded by the oscilloscopes by the name *waveforms*. The CLAWS DAQ runs on a Fujitsu C740 workstation [65] and controls the oscilloscopes, as well as records and stores the waveforms from the detectors. Workstation and oscilloscopes are connected via USB-3.

The CLAWS system uses two different trigger sources, an external and an internal one. For the injection trigger, a standard NIM pulse is send out by the SuperKEKB injector linac and distributed to the trigger input of both scopes. A simple threshold trigger set in the oscilloscopes detects the rise of this pulse and starts the recording of the data.

The data is thus time-stamped relative to the injection trigger, which has a fixed (but a priori not precisely known) time offset to the time of arrival of the injection bunches at the IP. This offset is determined from CLAWS data and used to define the time region of interest for the injection bunches in the data (see Section 7.3.1). We refer to this type of events as *injection* or *injection triggered* events. For the measurements of regular beam backgrounds, an automatic self-trigger is available, which starts the data acquisition once a pre-defined waiting time has elapsed. We refer to this type of events as *auto-triggered* events.

In dependence of their position relative to the beamline, we assign the channel names *FWD1-4* and *BWD1-4* to the sensors of the forward and the backward station, respectively. Due to radiation damage in the SiPMs, we observed significantly increased noise rates in the FWD1, BWD1 and BWD2 channels during runtime. We therefore replaced the sensor modules at these positions in the middle of Phase 1 in May, while having access to the IR. For debugging proposes, the fourth channel on both scopes was not used for the FWD4 and BWD4 sensors but for recording the revolution clock. Due to an error in the CLAWS DAQ only raw data for channels FWD1-3 has been written to disk and is available for offline analysis. Data for channels BWD1-3, however, was processed by the fast online analysis and available for real-time feedback through the online monitors.

Power distribution We use a single *Keysight 6700B* modular PSU, equipped with two *N6733B* and two *N6736B* DC power modules, for the entire CLAWS setup [66]. The PSU is connected to the workstation via USB and is operated primarily via the global CLAWS DAQ system. All power outputs of the PSU are fed into a custom made power distribution box for further allocation to the individual consumers. The box and the PSU are installed on top of each other in the CLAWS rack. From the box, each sensor module is supplied by a single four-core cable which utilizes two cores for the bias voltage and two cores for the voltage of the preamplifiers of the sensor modules. To account for the higher power requirements, the two amplifier stages are connected via similar cables only with bigger cross sections. Here, one of the cables supplies all four amplifiers of the FWD stations, whereas the other cable supplies the four amplifiers of the BWD station. To prevent pickup over such a long distance, the cables have twisted pairs and a copper mesh for shielding. Cable specifications and, in particular, cross sections are chosen such that notable voltage drops across the large distances are avoided.

Consumers supplied by the same module are generally connected in parallel. A single N6733B provides the 5 V supply voltage for all preamplifiers. As mentioned earlier, the required breakdown voltage varies between individual SiPMs due to differences in the manufacturing process. Based on the breakdown voltage specified by the manufacturer, the sensor modules are split in two groups installed in the FWD and BWD positions. One of the N6736B is then used to supply the bias voltage for the FWD section while the other one serves the BWD section. Due to the stable operating conditions and similar voltage specifications both sections are mainly operated at a bias voltage of 56 V, which is within the voltage range recommended by the manufacturer of the SiPMs. Finally, all amplifiers are supplied with 15 V from the remaining N6733B.

5.3 Detector calibration

A major part of the offline analysis is dedicated to reconstructing individual background particles from the sampled sensor output. For this purpose, we normalize the sensor signals to the response of cosmic muons via dedicated calibration measurements. We also use calibration measurements to ensure correct operation of the sensors and of the reconstruction procedure. In the following, we introduce four different types of calibration measurements which we performed before, during and after the runtime of Phase 1. A detailed description of the reconstruction procedure will then be given in Section 6.1.

Dark rate As discussed earlier, thermal excitation continuously generates fake single and multi p.e. pulses. During runtime, the sensor modules are not operated in the dark but at moderate ambient light. Due to residual light leakage in the wrapping of the modules, ambient light can reach the SiPMs and cause additional fake pulses. In a so-called *dark rate scan*, we determine the rate of fake pulses caused by thermal excitation or ambient light by counting the signals above a certain threshold voltage in a certain time interval.[1] Before Phase 1, we performed dark rate scans for each sensor module and rejected all modules with one p.e. noise rates above an arbitrary 600 kHz at full ambient light. A detailed description of the dark rate scans performed for the modules can be found in [61].

Temperature calibration The size of a one p.e. pulse, or in other words, the gain of the SiPM depends on the characteristics of the individual SiPM, the bias voltage and, most importantly, on the temperature which varies during runtime. The pulse size at the end of the readout chain is further modified by amplification and attenuation during signal transmission. In order to correct for temperature variations a precise estimate

---

[1] The dark rate in dependence of the number of p.e. is obtained by scanning through the threshold voltage and hence the name ‘scan’.

of the amplitude of one p.e. pulses must be available at all times. At fixed intervals during runtime, we therefore record a large number of one p.e. pulses caused by dark noise to which we refer to as *calibration waveforms.* By averaging these waveforms it is then possible to determine the average shape and amplitude of the signal of a single firing pixel. This so-called *average one p.e. waveform* automatically incorporates temperature variations, as well as amplification and attenuation of the readout. We use this information to reconstruct the number and exact timing of single firing pixels from the raw waveforms.

Light yield The light yield is a characteristic property of each sensor module which has to be determined in dedicated calibration measurements. For this purpose, we stack three sensor modules on top of each other and place them in a constant climate chamber located in the laboratory. We then use this setup to record the signals of a large number ($\mathcal{O}$(1000 events)) of cosmic muons. The upper and the lower modules serve as a coincidence trigger and ensure that the muons pass the sensors approximately perpendicularly. For data recorded in the middle sensor we then determine the number of p.e. in each event and use the MPV of a fit with a Langaus distribution as the specific LY for this sensor. This procedure is repeated individually for all sensor modules. In general, we use this LY to normalize the observed signals or more precisely the number of observed p.e. to the response of a MIP. Note that for these measurements we apply acquisition settings and an analysis method which is different from the one described in the following chapter. This increases the precision of the obtained LY but does not provide any timing information. A detailed description of these calibration measurements, as well as the light yields obtained for each module, are given in [61]. They have been performed after the runtime of Phase 1.

Muon telescope We perform an additional set of calibration measurements similar to the ones used to determine the LY. In contrast to the previous calibration, we stack the four sensors originally mounted in the forward station, use acquisition settings as close as possible to the ones during Phase 1 and apply the full CLAWS particle reconstruction (see in particular Section 6.1.3). In the following, this setup is referred to as the *muon telescope.* Again the trigger is provided by a coincidence in the upper and the lower modules and data of all four sensors is stored for offline analysis. We use data from these measurements to ensure the correct operation of the particle reconstruction and to fine tune and validate the procedure. These measurements have also been performed after the runtime of Phase 1 in the climate controlled chamber in the laboratory.

5.4 Data acquisition software

The CLAWS experiment is operated by an entirely new data acquisition software developed specifically for the requirements of Phase 1. This DAQ simultaneously controls both oscilloscopes and the PSU and handles storage of all data. To provide real-time feedback to shifters and operators of BEAST and SuperKEKB, it is fully integrated into the accelerator slow control network. We used the DAQ for the entire runtime of Phase 1 and the calibration measurements with the muon telescope.

Design principle At the time of development, the manufacturer of the oscilloscopes provided drivers and software development kits (SDKs) for C++ and LabVIEW which all required Windows 7 as an operating system for stable operation. Since it is widely used in already existing readout software running in the laboratory, LabVIEW was chosen as a base for the CLAWS DAQ.

As customary in LabVIEW, user interaction takes place entirely via a graphical user interface (GUI). The GUI of the CLAWS DAQ allows to start and stop data taking, fully configure the scopes and the PSU and to visualize the recorded data. The actual operation of the DAQ is based on the concept of an *event-driven producer-consumer state machine*. Figure 5.7 shows a state diagram of its overall design. The code is split into three parts, a so-called *producer loop* and two *consumer loops* which each consist of an individual finite-state machine. The central tasks of the producer loop are handling input/output operations of the GUI and instructing the two consumer loops accordingly. Each GUI interaction promotes the execution of another state which then initiates state changes in the two consumer loops.

The data consumer loop is responsible for the interaction with both oscilloscopes and handles the data processing. As such it relies on the LabVIEW SDK provided by the manufacturer of the oscilloscopes. It applies settings to the oscilloscopes, issues the command to wait for a new trigger and record data and reads the raw waveforms from the scope buffers. Subsequently, a fast online analysis is performed for each recorded waveform which determines time-dependent particle rates and signal decay times and makes them available to the user. A comprehensive description of the online data processing is given in [61]. Due to the significant data load it is not feasible to continuously store the raw data for later offline analysis. It is, therefore, possible to run either as a pure *online monitor* or to also write the data to disk during phases of interest. The data processing loop is (by far) the most complex part of the DAQ.

The PSU consumer loop handles the operation of the PSU. As such, it opens and closes

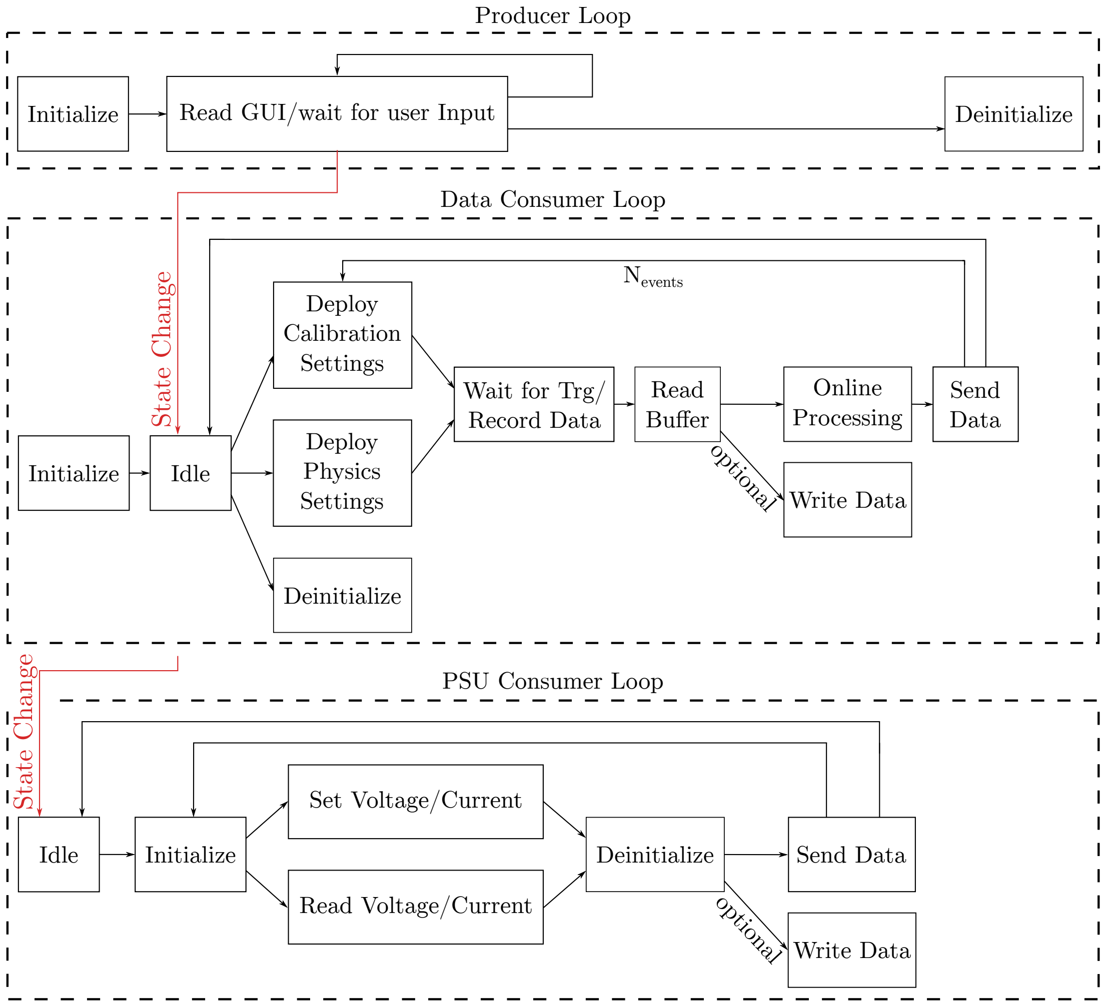

Figure 5.7: State diagram of the work flow of the CLAWS data acquisition software.

connections to the device, applies new settings and reads back actual voltages and currents. The secondary task of this part is the continuous monitoring of voltages and currents in order to prevent damages of the hardware.

To ensure optimal utilization of the computing hardware, the execution of the CLAWS DAQ makes use of parallelism and multi threading. As such, the operation of the producer loop and the PSU loop, as well as handling of both oscilloscopes and the corresponding data processing are performed in an individual thread. Nevertheless, as a consequence of the choice of LabVIEW and the complex processing of large waveforms, the total time required for recording a single event was around 30 s. Since injections usually take place with a rate of 25 Hz, it was only possible to record a small fraction of the injection

triggers.
In general, the CLAWS DAQ was working highly reliably and required only minimal user input over the entire course of Phase 1. However, using a graphical programming language such as LabVIEW for a program with the complexity of the DAQ made the code hard to maintain and difficult to extend further. The relatively low rate of processed events also offers room for improvement.

Network integration and online monitor As BEAST in general, CLAWS uses EPICS to share observables and other information with the other subsystem and SuperKEKB. In addition to the DAQ, we run a custom-made EPICS server implemented in Python and based on PCASpy [67] on the workstation which hosts different variables. Updated data is sent locally from the LabVIEW DAQ to the server which then publishes it via the network. In that way, the system is fully integrated into the accelerator slow control network.
The quantities shared by CLAWS are retrieved by a dedicated online monitor based on Control System Studio [68]. This monitor was running in the SuperKEKB control and visualized relevant quantities like the observed waveforms, particles rates or decay times.

Data transfer and storage In order to make the recorded waveforms available for detailed offline analysis, the CLAWS DAQ is required to transfer and store substantial amounts of raw data. The typical length of the recorded waveforms was 2.4 ms sampled at a rate of 1.25 GHz with 8 bit vertical resolution (i.e. 32 bit integers). A single event with eight waveforms thus occupies approximately 100 MB in memory and on disk. To reduce potential bottlenecks, we use a dedicated plugin card with four additional USB-3 controllers for data transfer from both oscilloscopes and write the data directly to a solid state disk. The data is then transfered manually to conventional hard disks for long term storage in periods where data is not recorded. The workstation supported simultaneous operation of three hot swappable 1 TB hard disks.
The raw waveforms are saved in the *NI Technical Data Management* (NI-TDMS) format. NI-TDMS is a open but LabVIEW specific data format which offers an effective way to efficiently store the large waveforms in a binary format while being fully integrated into the LabVIEW environment. After the raw data is transferred from the oscilloscopes and before it is processed, we also record the timestamp from the operating system which is time synchronized with the other BEAST II systems (see Section 4.2). We use additional files in the conventional human readable INI format to save this timestamp and additional meta information such as the settings used for the acquisition.

In general we distinguish two types of events: *physics events* and *calibration events*. Physics events are triggered by injection or auto trigger and contain long waveforms with measurements of beam backgrounds. Calibration events contain short waveforms with measurements of single p.e. pulses caused by thermal excitation. CLAWS data is recorded and stored as runs which typically contain 10 to 300 physics events and 1000 calibration events. For each physics event, a NI-TDMS file is created which contains the eight waveforms as independent arrays of integers. The meta information is saved in an identically named INI file. To facilitate code development for offline analysis, we also use this file division for calibration waveforms by combining arbitrary waveforms (one for each channel) into calibration events. Runs are distinguished by assigning them an ascending six digit run number. Events are named accordingly by adding a three digit event number to the run number. In addition, oscilloscope acquisition settings, PSU settings and other meta information are saved in a run wide INI file.

Finally, we use custom made Python scripts to compress/decompress entire runs by roughly a factor of ten to reduce data volume needed for long term storage and to convert waveforms from NI-TDMS files to ROOT files for offline analysis. In total, we recorded approximately 8 TB of raw data over the course of Phase 1.

Chapter 6

CLAWS - Data reconstruction and analysis framework

Over the course of Phase 1, the CLAWS experiment recorded a total of 8 TB of raw data which primarily consists of sensor output read out by the oscilloscopes. In this chapter, we describe the data processing and calibration procedures which are applied to the raw data in order to be able to perform the analyses of beam backgrounds presented in Chapters 7, 8 and 9. These processing and calibration procedures are performed by a dedicated software framework developed within the scope of this thesis. It is implemented in C++ and integrates the *ROOT Data Analysis Framework* [69] for visualization and analysis capabilities, the *GNU Scientific Library* [70] for scientific algorithms and the *OpenMP API* [71] for parallelization.

The processing and calibration procedures are divided into two stages which are performed sequentially. In Section 6.1, we describe the first stage of processing referred to as the *particle reconstruction.* During the particle reconstruction we apply different calibration steps to the raw data in order to reconstruct the interaction time and the energy deposited by individual background particles. In that way, the remnants of effects of the sensors and of the setup are removed and temperature dependencies are calibrated out. The reconstruction also unifies the background measurements recorded on many different dates throughout Phase 1. The particle reconstruction is a generic processing of the data that is applied in the same way to every run. Section 6.2 describes the second stage of data processing referred to as the *analysis framework.* It retrieves the output of the particle reconstruction, combines it and relates it to specific accelerator conditions. The output of the framework provides the foundation for the analysis of backgrounds presented in the subsequent chapters. The exact procedure performed to process the data, therefore, is adapted to the requirements of the respective analysis. Finally, we briefly discuss the uncertainties on the output of both processing stages in Section 6.3.

6.1 First-stage data processing - particle reconstruction

As introduced in Section 5.4, the raw data primarily consists of waveforms which capture the output of the sensors. Here, we differentiate between two different types of raw waveforms: *raw calibration waveforms* and *raw physics waveforms*. The calibration waveforms capture the pulses of single firing pixels and are used to obtain the average response to a single photon emitted by the scintillator. This average response incorporates all temperature effects and the majority of readout effects. The particle reconstruction is build around the so called *waveform decomposition*, in which the average response is iteratively subtracted from a raw physics waveform in order to determine the time distribution of photons. From the time distribution of photons, we finally derive the time distribution of background particles along with the amount of energy they deposit. This time distribution of background particles assumes the sampled form of the raw waveforms, but its amplitude denotes the energy deposited within the period of a sample (0.8 ns) instead of a voltage; the energy thereby is normalized to the response of a through-going MIP. This approach was first used by Simon, Soldner and Weuste in the T3B experiment [53] and offers an effective way to disentangle information about background particles from detector effects and external influences. We hence refer to the output of the particle reconstruction as the *reconstructed waveforms*.

In this section, we give a comprehensive description of the operation of the particle reconstruction. In Section 6.1.1, we first review the characteristic features of both types of raw waveforms. Subsequently, Section 6.1.2 discusses the actual particle reconstruction and its individual processing steps in detail. Finally, we validate the reconstruction procedure in Section 6.1.3 by applying it to calibration measurements with cosmic muons recorded in the laboratory. This muon data is also used to optimize the values of several steering parameters of the particle reconstruction. We refer to this method of optimization as a *parameter scan*. For greater clarity, the results of the scan, i.e. the values of the optimized steering parameters, are discussed along with the description of the respective processing step in Section 6.1.2. Section 6.1.3 only describes the implementation of the parameter scan itself.

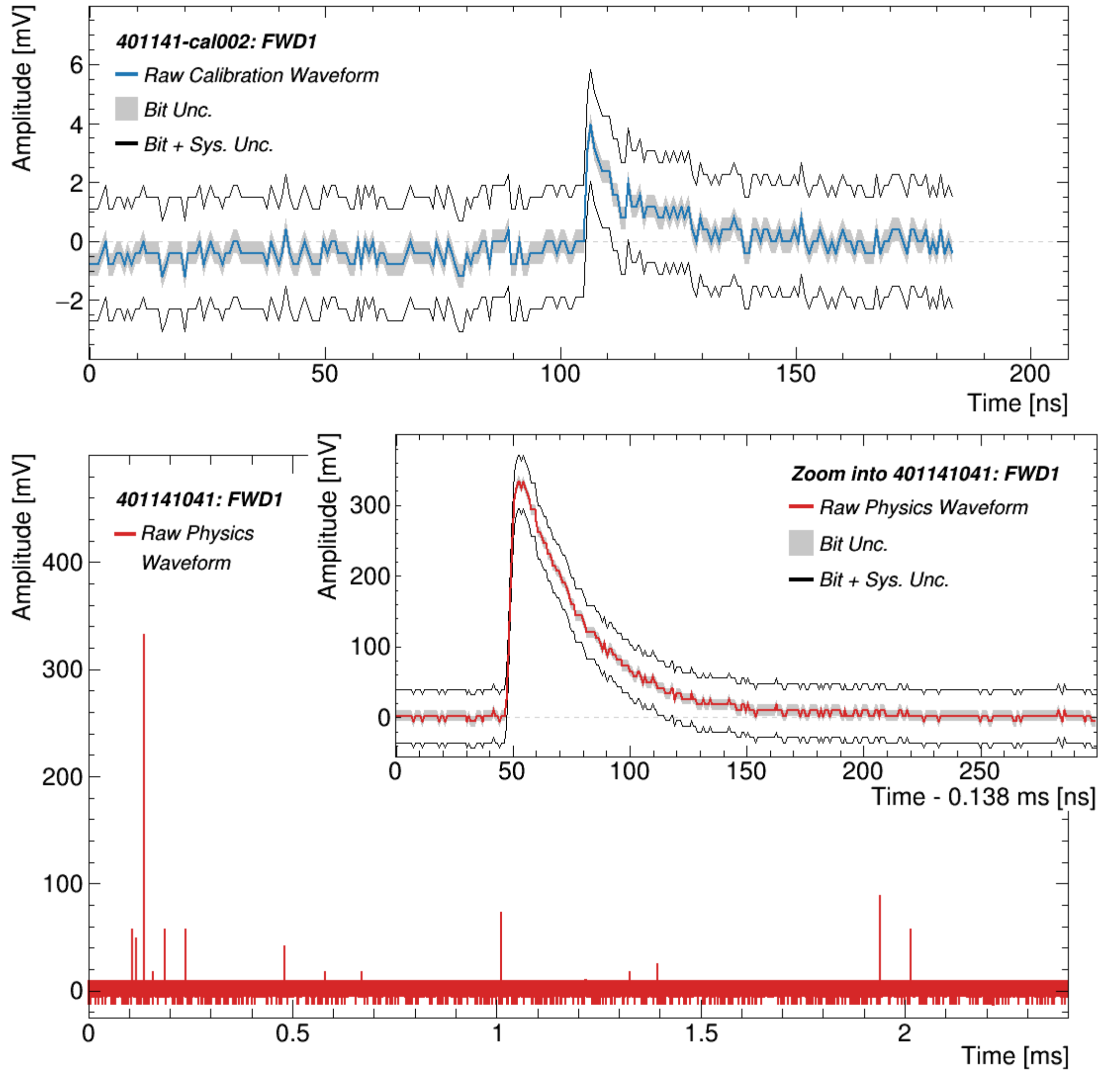

Figure 6.1: Illustration of a typical raw calibration waveform (*top*) and a typical injection triggered raw physics waveform (*bottom*) recorded during regular operation of Phase 1. For greater clarity, the waveforms are already converted from ADC counts to millivolts.

6.1.1 Input data

The form of the raw waveforms is determined by different properties of the experimental setup, in particular the SiPMs and the oscilloscopes (see Section 5.1). The waveforms are also affected by external influences like temperature variations, ambient light or radiation damage, all encountered frequently over the course of five months of data taking. Figure 6.1 shows typical examples of a raw calibration waveform (*top*) and an injection triggered raw physics waveform (*bottom*) taken during regular operation of Phase 1. Since the length of the physics waveforms masks details, a cutout illustrates one of the signal pulses and its features with higher resolution in time.

For both types of waveforms, we used the highest available sampling rate of the oscilloscopes of 1.25 GHz (one sample every 0.8 ns) throughout data taking. The vertical range, on the other hand, varied and was set according to the respective requirements. The manufacturer of the oscilloscopes states that the voltage measurement is limited by two types of uncertainties [64]: a systematic uncertainty and a bit uncertainty. The systematic uncertainty is specified to be 3% of the applied vertical range and can, for example, be caused by an imperfect calibration of the device. It can be assumed that such an uncertainty is constant over time and can be corrected by a dedicated subtraction (see following section). The bit uncertainty, on the other hand, is given by the size of a single bit due to the finite vertical spacing and determines the size of features in a waveform, which can still be resolved. The remainder of this section will discuss the individual characteristics of both types of waveforms in more detail.

Raw calibration waveforms Calibration waveforms capture the signals of single pixels firing as a result of thermal dark noise. It is worth noting that a pulse from a single pixel is the same regardless of whether it occurs due to thermal noise or is triggered by a real photon. The aim is to constantly record such pulses during run time in order to calibrate out the temperature dependence of the SiPMs and to account for amplification and attenuation during signal transmission (see Sections 5.1 and 5.3). Based on the assumption that the temperature does not change notable over the course of a single run, all calibration events were recorded at the end of a run.

As pointed out in Section 5.2, the SiPMs of all channels in the forward station are supplied with the same bias voltage of 56 V which is within the voltage range recommended by the manufacturer; the voltage is chosen such that the maximum of the amplitude of a one p.e. pulse in the channels FWD1-3 is around 4.5 mV. The smallest vertical range of 50 mV is, therefore, sufficient to capture all pulses while giving the best available precision; this range corresponds to a bit uncertainty of only 0.39 mV what is considerably smaller than the expected signal amplitudes. The pulses captured by the calibration waveforms are characterized by a fast rise and a subsequent exponential decay, as expected for signals of SiPMs. Their recording is triggered individually for each channel by a simple threshold trigger which requires a minimum voltage of 3 mV. This threshold level is arbitrarily chosen so that it is well above the ambient noise, but still sufficiently smaller than the amplitude of a single p.e.

The oscilloscopes have been set to record 132 pre-trigger samples, used to determine the pedestal, and 98 post-trigger samples, meant to cover the signal pulse. In the pre-trigger part, the baseline of the waveform is shifted to negative values, demonstrating the need for a pedestal subtraction. In the post-trigger part, on the other hand, the signal fails to fully decay back to this baseline since the number of post-trigger samples is not sufficient to cover the whole pulse. As will be described in the following section, it is possible to recover the final part of the waveform by a suitable correction. Nevertheless, future versions of the CLAWS experiment should increase the sample size of the calibration waveforms in order to capture the entire signal pulse.

With a low probability, thermal noise, afterpulsing or crosstalk can cause secondary p.e. pulses in the calibration waveforms. However, the gain, which is reflected by the integral of the waveform, is a reliable indicator for such multi p.e. signals and can be used as a veto criterion (see following section).

Raw physics waveforms As a result of the transit of a background particle, the scintillators in the sensors emit photons which then lead to a certain number of firing pixels in the SiPM. The signal pulses in the raw physics waveforms are, therefore, a superposition of several of the one p.e. pulses captured by the calibration waveforms. Hence they also show a fast rise time followed by an exponential decay. In general, however, the observed pulses do not occur fully simultaneously and their time of detection is delayed with respect to the transit time of the particle. The p.e. appear to be smeared in time as a consequence of the following effects: decay time of the light emission, crosstalk, afterpulsing, thermal noise and ambient light. The light emission of the scintillator is not instant but smeared over several nanoseconds causing delayed pulses. Crosstalk and afterpulsing, both occurring in the SiPM, cause additional fake pulses which are correlated with the background particle. The fake pulses from afterpulsing, however, appear several tens to hundreds of nanoseconds after the transit. Eventually, thermal noise and ambient light lead to signals which are not correlated with actual particles and are randomly distributed over the whole waveform. If close to a real signal, these can mimic early photons and lead to an improper assessment of the detection time of the corresponding particle. The goal of the physics waveforms is to record the time structure of backgrounds over several milliseconds. They are, therefore, a very long sequence of such multi p.e. signal pulses and capture the interactions of numerous background particles.

To be able to cover the full time evolution, the physics waveforms are significantly longer than the calibration waveforms. While the number of samples varied throughout Phase 1 and waveforms with up to 20 ms (2.5×10^7 samples) have been recorded, we mostly used settings with a length of 2.4 ms (3×10^6 samples). The signals observed, especially during injection periods, can be as large as 1.8 V, corresponding to 450 simultaneous p.e. or roughly 30 background particles. In order to entirely cover such signals, we used a sizable vertical range of ±1000 mV with an additional analog offset of −900 mV. The evident downside side of such a large dynamic range is the loss of precision for small amplitudes since the corresponding bit uncertainty of ±7.87 mV is already considerably larger than the amplitude of a single p.e. This loss of precision compromises both the ability to determine the detection time of a background particle and to resolve the number of photons and, in that way, the total deposited energy. These large amplitudes do not only force a larger vertical range, they also impact the amplifiers in the readout chain. Large signals lead to an undershoot which temporarily shifts the baseline for subsequent signals and lasts for up to 20 µs after the initial pulse. It is, however, possible to recover the baseline by applying a dedicated correction to the physics waveforms (see following section).

6.1.2 Reconstruction procedure

Having discussed the shape of the signals, we will now move on to describing the particle reconstruction itself. Figure 6.2 provides an overview of the individual processing steps and, running from top to bottom, the order in which they are performed. First, the calibration waveforms are processed to establish the mean response of a single firing pixel. Then this mean response is used as an input to the processing of the physics waveforms. The reconstruction is structured in such a way that it processes the data of individual runs in a step-by-step manner. Each of the steps yields the modified data and different summary plots. The modified data then functions as the input for the subsequent step which allows to perform each of them independently. The summary plots, on the other hand, are used to monitor the stability and the performance of the sensors and the reconstruction procedure. In the following, only the most relevant summary plots will be shown along the description of the respective processing steps. The computation time required to fully process a single run primarily depends on the number of physics events and the length of their waveforms but may take up to several hours on a normal CPU. In the following, we will describe each of the individual processing steps in detail.

- **Calibration waveform pedestal subtraction** In order to correct for constant offsets in the baseline, we first apply a pedestal subtraction to each calibration waveform. Such offsets can, for example, be related to systematic uncertainties

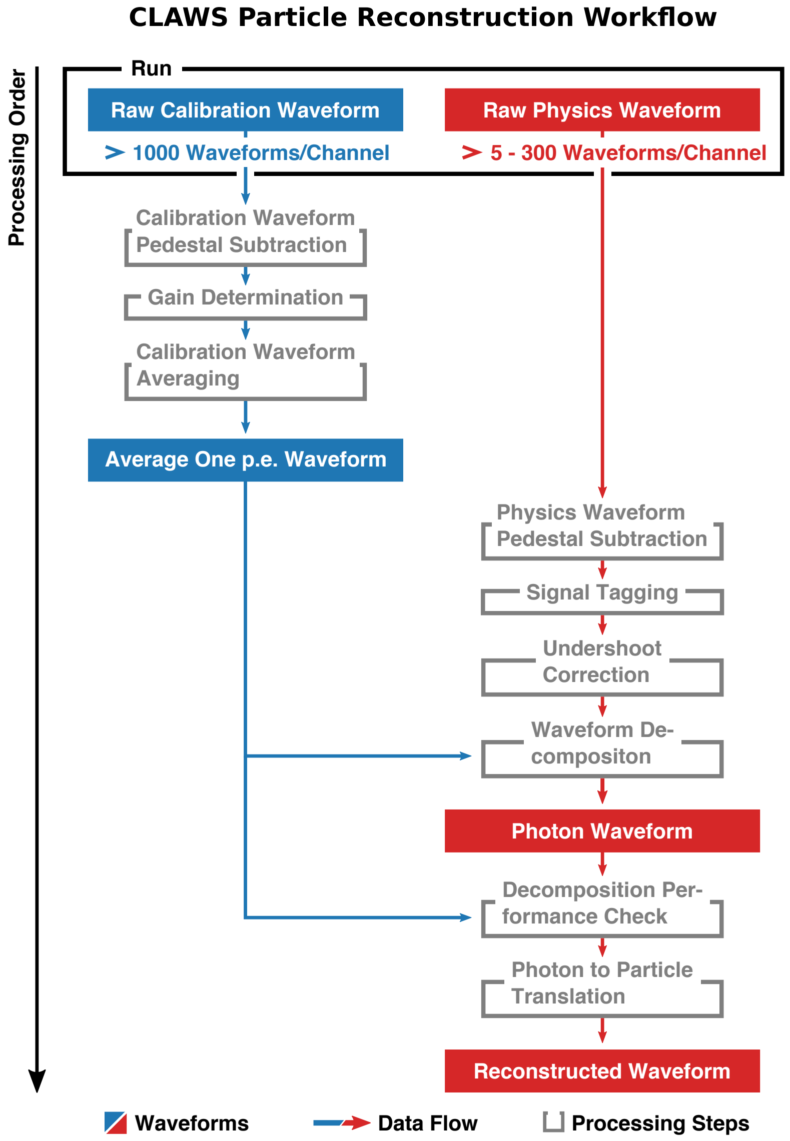

Figure 6.2: Graphical illustration of the work flow of the first stage of data processing referred to as the particle reconstruction.

of the oscilloscope or be caused by external electrical sources. To establish an initial estimate, which is needed to properly veto signals in case of unusually large pedestals, the sample mean of all samples in the waveform is calculated. Subsequently, signal pulses are identified by requiring that three consecutive samples are larger than 0.98 mV plus the previously calculated mean.[1] Figure 6.3 (*left*)

---

[1] For a range of ±50 mV, used for the calibration waveforms, 0.98 mV corresponds to 2.5 bit.

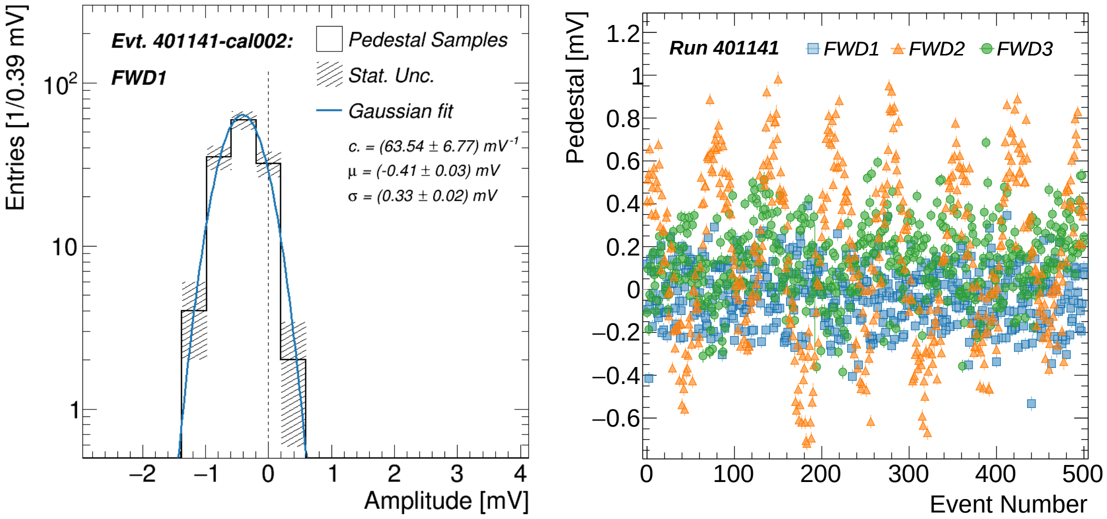

Figure 6.3: Distribution of amplitudes of non-signal samples for a typical raw calibration waveform (*left*). The mean of a fit with a Gaussian is utilized as the pedestal for the respective event; stated parameters and corresponding uncertainties are adopted from the fit. Calibration pedestals for the first 500 events of the corresponding run (*right*).

illustrates the distribution of the amplitudes of the remaining non-signal samples for a typical waveform. Here, the pedestal is determined by fitting a Gaussian to the distribution;[2] the mean of this fit is then subtracted from the full waveform. Signal samples, which are not properly excluded, or admixtures of additional pulses can give rise to a deformation of the distribution and compromise the determination of the pedestal. To ensure a correct operation of the pedestal subtraction, all waveforms with a fit result showing a p-value smaller than 5% are excluded from further processing.

Figure 6.3 (*right*) shows the pedestals for the first 500 events of the corresponding run for all three channels. Here, all channels indicate a sinusoidal fluctuation of the pedestal, which is particularly evident in FWD2 and observed across a wide range of runs. The most likely causes of this fluctuation are electronic noise in the hardware or pickup in the long signal and power cables. Since its period is ∼2.1 ms,[3] the effect of the pickup on a single calibration waveform (184 ns) is approximately constant. It can therefore be assumed that determining and subtracting the pedestals on an

---

[2] We apply a maximum likelihood fit in the range of ±1.18 mV relative to the maximum of the distribution; uncertainties on the parameters are adopted from the fit.

[3] With a signal rate of 50 kHz [59] and a minimum time between acquisitions required by the scope [64] of ∼1 µs, the estimated period of ∼100 events corresponds to ∼2.1 ms.

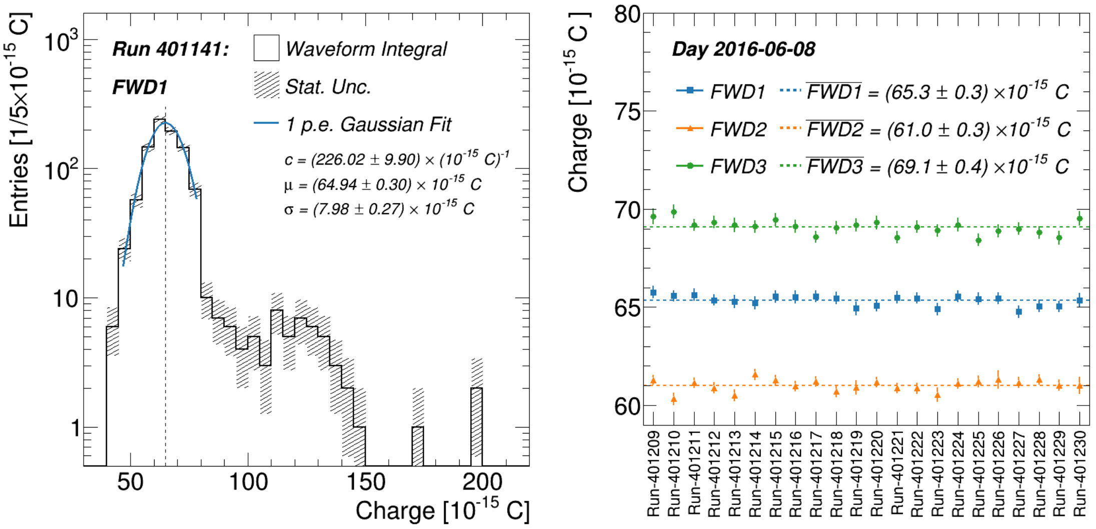

Figure 6.4: Distribution of the integrals of the calibration waveforms multiplied by the 50 Ω input impedance of the oscilloscopes for a typical run (*left*). The mean of a fit with a Gaussian is utilized as the average gain for the respective run; stated parameters and corresponding uncertainties are adopted from the fit. Average gain for all runs of the corresponding day during run time (*right*). Dotted lines indicate the sample mean and corrected sample standard deviation for the full day.

event-by-event basis corrects for the observed fluctuations.

The pedestal subtraction is working highly reliably and, as expected by the nature of the cut, only around 5% of the events are excluded.

- **Gain determination** As mentioned earlier, the gain of a calibration waveform can be used to distinguish pulses caused by a single or multiple firing pixels. Usually, the gain is defined as the amount of charge multiplication in the SiPM as a result of a single detected photon. For practical purposes, however, we interpret the gain as the charge observed by the oscilloscope after the full readout chain. It is determined by multiplying the integral of a one p.e. waveform, i.e. a calibration waveform, with the 50 Ω input impedance of our oscilloscopes. Figure 6.4 (*left*) shows the distribution of gain values for a single channel for a typical run. The first and, by far, largest peak stems from one p.e. pulses, whereas the second, considerably smaller, peak is caused by events in which two pixels fire simultaneously due to optical cross talk, afterpulsing or coincidental signals. The mean of a Gaussian fit

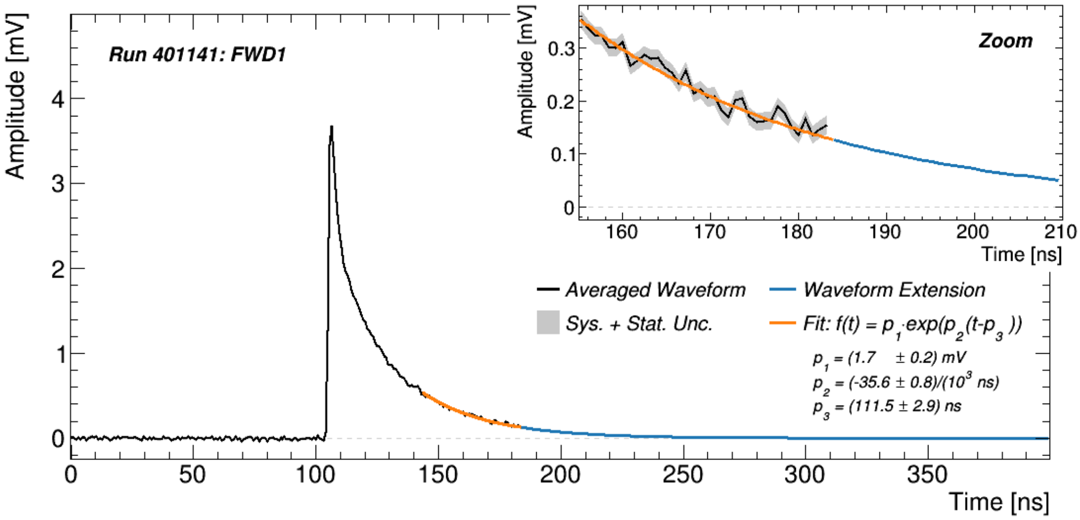

Figure 6.5: Average one p.e. waveform for a typical run. The cutout illustrates the transition region between averaged waveform and extension in more detail. The error band represents the errors after averaging. Stated parameters and their uncertainties are adopted from the fit.

to the first peak defines the *average gain* for the respective run.[4]
Figure 6.4 (*right*) compares the values of the average gain for all three channels for a typical day during run time. The run-by-run fluctuations are minimal during the day; all other days show a similar performance, which can be attributed to the stable operating conditions inside the BEAST cave (see Section 4.2). The gain determination is working highly reliably and is successful for all runs.

- **Calibration waveform averaging** In the final processing step of the calibration waveforms, we determine the average signal pulse of a single firing pixel. The previously determined gain is used to select all calibration waveforms with a single p.e. pulse by requiring a waveform integral which is within an arbitrarily chosen $\pm 10\,\%$ of the average gain; all other waveforms are excluded from further processing. This limit typically accepts around half of the 1000 calibration waveforms per run and channel which is more than sufficient. The remaining waveforms are then averaged sample-by-sample. Figure 6.5 illustrates a typical example of such an averaged waveform. The stated uncertainties are given by $\pm 1\,\mathrm{bit}/\sqrt{N}$, where N is

---

[4] We apply a maximum likelihood fit in the range of ±25% relative to the maximum of the distribution; uncertainties on the parameters are adopted from the fit.

the number of waveforms averaged;[5] for the given example the uncertainties are within ±1.7 µV.

As was pointed out in the previous section, the length of the calibration waveforms is not sufficient to completely capture the signal pulses. The averaged waveform, thus, ends abruptly at 184 µs before the pulse entirely levels out. Subtracting it repeatedly in the waveform decomposition would cause remaining artifacts in the physics waveforms which are identified incorrectly as additional signal pulses. To recover the absent tail, we fit an exponential (see Section 5.1.2) to the late part of the waveform and, subsequently, extend this fit up to a length of 400 ns.[6] Within this window, the extension drops for all fits below a value of 1 µV which is smaller than the typical uncertainty associated with the averaging.

We refer to the merger of the averaged waveform and the extension as the *average one p.e. waveform.* These waveforms represent an accurate description of the response to a single photon and incorporate temperature dependence and applied amplification and attenuation. One of these waveforms is obtained for each channel and run; it works highly reliably and succeeds for all runs.

- **Physics waveform pedestal subtraction** As for the calibration waveforms, we first apply a pedestal subtraction to the raw physics waveforms to correct for constant offsets in the baseline. If four consecutive samples all exceed an arbitrarily chosen threshold of 11.8 mV (1.5 bit) the following 400 ns are identified as a signal pulse and are rejected. Analogously, if four consecutive samples all undercut a threshold of −11.8 mV (-1.5 bit) the following 30 µs are identified as an undershoot and are also rejected. As a consequence of the large bit uncertainty, it is inevitable that one and two p.e. pulses pass the rejection of signal samples. Such signals, however, are primarily caused by thermal dark noise; they are few in numbers and their impact is negligible (see Section 5.1.2).[7] Figure 6.6 (*left*) illustrates the distribution of the amplitudes of the remaining non-signal and non-undershoot samples for a typical waveform. Again the mean of a Gaussian fit is utilized as the pedestal for the respective event and subsequently subtracted from the full waveform.[8]

---

[5] Here, we assume that the uncertainties of a single waveform are fully covered by the bit uncertainty, that uncertainties in different waveforms are independent of each other and that they are normally distributed.

[6] We apply a χ^2-fit in the range from 36 ns after the maximum of the waveform up to its end.

[7] A rate of thermal one p.e. pulses of around 50 kHz [59] and a waveform length of 2.4 ms suggest that only around 100 of such pulses occur in a full physics waveform which each only affects $\mathcal{O}(1)$ samples.

[8] We apply a maximum likelihood fit in the range of ±24.7 mV relative to the maximum of the distribution; uncertainties on the parameters are adopted from the fit.

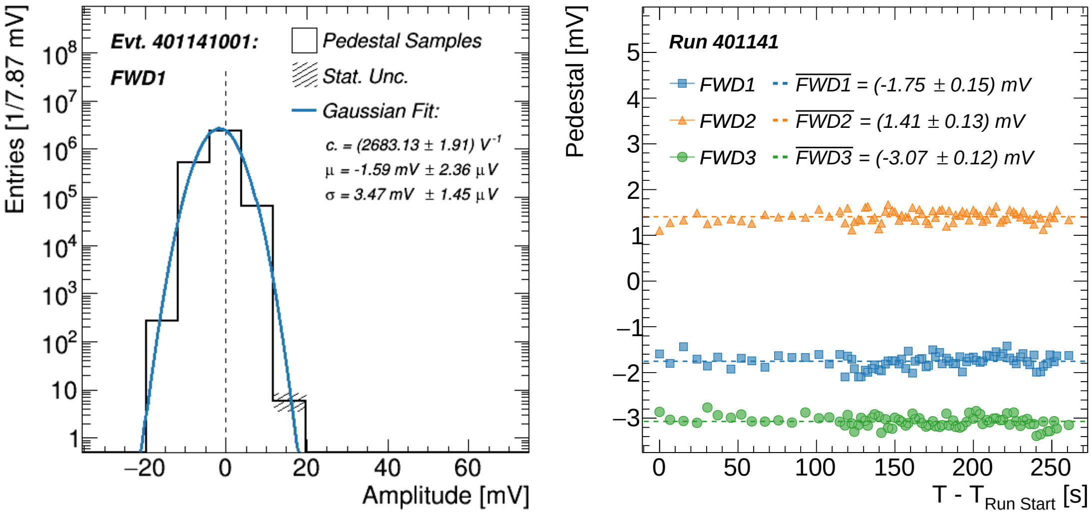

Figure 6.6: Distribution of the amplitudes of non-signal, non-undershoot samples for a typical raw physics waveform (*left*). The mean of a fit with a Gaussian is utilized as the pedestal for the respective event; stated parameters and corresponding uncertainties are adopted from the fit. Physics pedestals for all events of the same run over the corresponding event time relative to the start of the run (*right*). Early events are auto triggered; later events are injection triggered. Sample mean and corrected sample standard deviation for all events are indicated by dotted lines.

Because of the low vertical resolution and the resulting admixture of positive signals, it can not be assumed that the distribution is entirely Gaussian shaped and no rejection based on the p-value is applied. Instead, we ensure the validity of the processed events by rejecting all events where the fit failed in general or the fit parameters showed unphysical results ($const. < 0$ or $\sigma < 0$). It is assumed, and empirically confirmed, that the measures described above are sufficient for a correct operation of the pedestal subtraction.

Figure 6.6 (*right*) shows the pedestal for all events of a typical run over the event time relative to the start of the run. Here the earlier events are auto triggered, whereas the later events are injection triggered with a higher repetition rate. Unlike for the calibration waveforms, the pedestals show a uniform distribution with a minimal spread.[9] The most likely cause for this difference is the significantly larger vertical range. It can therefore be assumed that the previously observed sinusoidal pickup is negligible for physics waveforms. The pedestal subtraction works highly reliably for the majority of runs and only an insignificant number of events is

---

[9] The corrected sample standard deviations is only few microvolts.

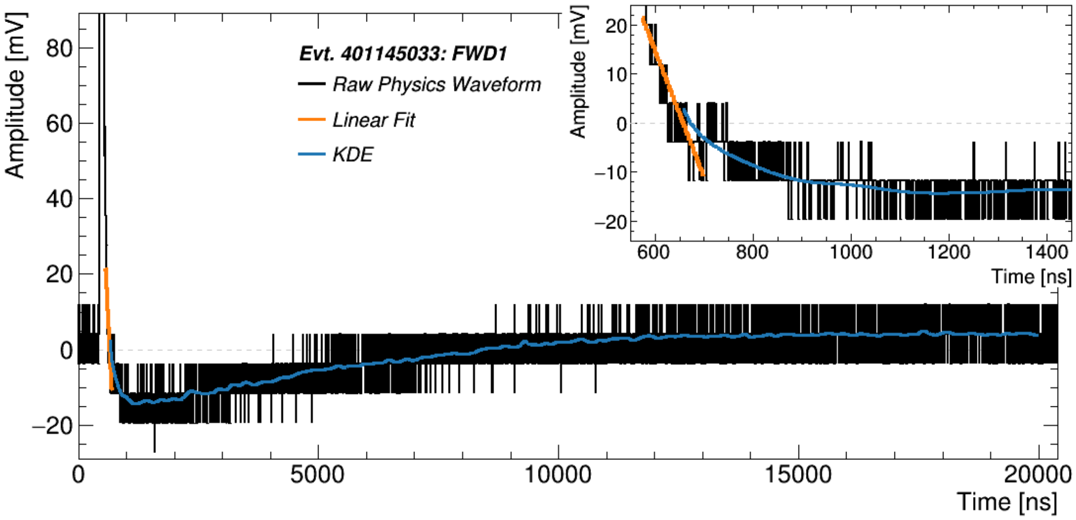

Figure 6.7: Illustration of a typical raw physics waveform which suffers from an undershoot of the amplifiers as a consequence of a large signal pulse. Also shown are fits with a straight and a template function obtained by a Kernel Density Estimation which are used to correct for the undershoot.

excluded from further processing.

- **Undershoot correction** As was pointed out in in the previous section, signals with amplitudes larger than 400 mV (approximately six simultaneous charged particles) lead to a noticeable undershoot of the amplifiers after the initial pulse. A typical example of such an undershoot is illustrated in Figure 6.7. It can be clearly seen that after the signal pulse causing the undershoot, the baseline is shifted to the negative for a duration of up to 20 µs. As will be described shortly, additional signal pulses which occur in the shifted region can hamper the correct operation of the waveform decomposition. This affects in particular the measurement of injection backgrounds, since, firstly, such large signals are almost exclusively caused by injections and, secondly, the injection bunch recurs after around 10 µs (one full turn).

  As it is not possible to describe the undershoot analytically, the only viable method we found is to approximate it with a Kernel Density Estimation (KDE) [69]. It is assumed that the rise and decay times of the undershoot are defined by properties of the electronic components in the amplifiers and are, therefore, constant. Hence, only the amplitude varies between events. We take an arbitrary event with no apparent trailing pulses and apply the KDE to the undershoot region over a range of 20 µs. The result of the KDE, multiplied by a vertical scaling parameter, is then used as a template. If a signal pulse is larger than an, empirically motivated, threshold of 400 mV, the template is fitted to the undershoot after the signal.[10] Thereby, the start of the template fit is determined by the zero crossing of a linear fit to the falling flank of the initiating pulse.[11] Subsequently, the adjusted template is subtracted from the physics waveform. Note that signals with such large amplitudes are encountered almost exclusively during injections and, even in this case, a correction is only necessary in a fraction of the events. In principle, signals below this threshold are also affected. Here however the amplitude of the undershoot is so small that it gets overshadowed by the bit uncertainty rendering a correction impossible and unnecessary.

- **Signal tagging** As preparation for the waveform decomposition, we identify all signal regions in the raw physics waveforms by requiring that three consecutive samples each exceed a threshold of 11.8 mV. The range from 4 ns before the first sample until 300 ns after it is then categorized as a signal. Note that this approach is similar to the one used in the respective pedestal subtraction. Subsequently, all samples in non-signal regions are identified as noise and set to zero. In that way, these noise regions can not be misinterpreted as signal pulses later in the decomposition and smaller signals, caused predominantly by dark noise or ambient light, are rejected.
  Lower thresholds increase the probability that noise pulses pass the rejection, whereas greater thresholds decrease the sensitivity to backgrounds with smaller energy deposits. Results obtained by the parameter scan show that the thresholds and the number of consecutive samples used represent the best compromise between noise rejection and sensitivity and yield the optimal results with respect to determining the detection time and the deposited energy of the background particle. They also suggests that the influence of the number of samples is relatively small. In addition to the noise rejection, the signal tagging also serves as an intermediate visualization and control step.

- **Waveform decomposition** The core of the particle reconstruction is the waveform decomposition. It determines the number and the precise detection time of individual photons by repeatedly subtracting the response of a single firing pixel, i.e. the average one p.e. waveform. Figure 6.8 illustrates the principle of the

---

[10] We apply a χ^2-fit with a total length of 19.5 µs.

[11] We apply a χ^2-fit in the range of around 100 ns to 500 ns after the time at which the threshold is crossed.

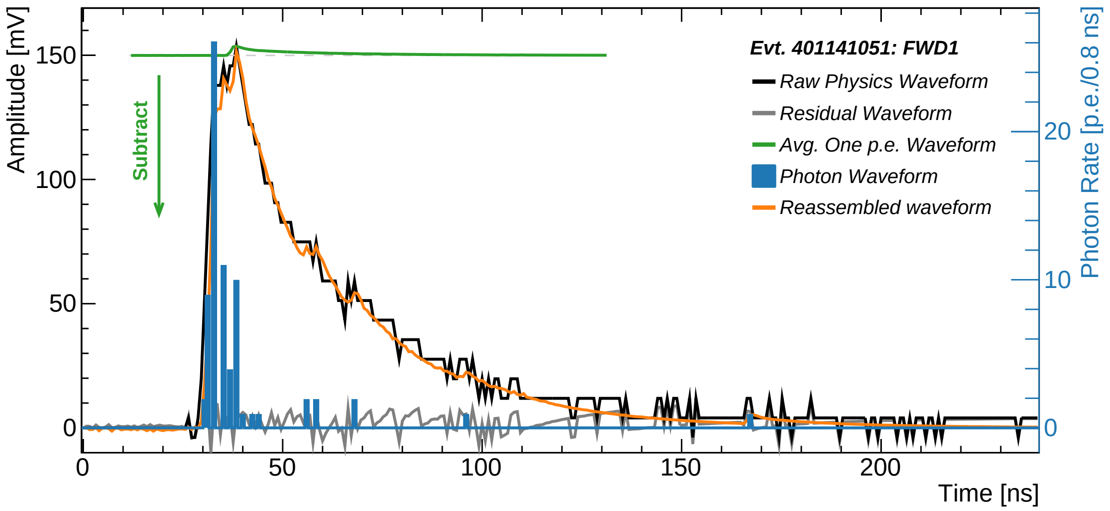

Figure 6.8: Illustration of the operation of the waveform decomposition processing a section of a typical physics waveform. The same signal pulse as reassembled by the decomposition performance check is also shown for comparison.

operation of the decomposition based on a section of a typical physics waveform. First, signal pulses in the raw physics waveforms are identified by searching the signal regions defined by the tagging for the sample with the global maximum. The time of this maximum is matched with the time of the maximum of the average one p.e. waveform. Then the amplitude of the one p.e. waveform is subtracted sample-by-sample from the physics waveform. We define the time of the global maximum as the time at which the respective pixel fired and, thus, use it as the detection time of the initial photon. In order to reconstruct the time distribution of all detected photons, this process is repeated iteratively until it is no longer possible to distinguish signal pulses from noise.

The particular challenge lies in correctly identifying all one p.e. pulses despite the limited vertical precision which fails to resolve single one p.e. pulses.[12] When searching for a new global maximum in the physics waveforms, only samples which fulfill three criteria are considered:

(i) The average of the amplitudes of all samples in the range of ±4 ns of the respective sample has to be positive in order to prevent the creation of artifacts like negative spikes.

(ii) The amplitude of the sample itself must be at least twice as larger as the

---

[12] The bit uncertainty is ±7.8 mV, whereas the amplitude of a one p.e. pulse is only $\sim 4.5\,\mathrm{mV}$.

average of the amplitudes of all samples in the range of ±2 samples. It that way it is possible to avoid falsely identifying single samples which are subject to large noise.

(iii) The amplitude in the respective sample has to exceed a threshold of 2.5 times the maximum of the average one p.e. waveform to reject noise in general.

If it is not possible to find a new maximum which passes all three criteria, the decomposition is terminated.

In order to optimize the decomposition, we examine the values for the ranges, used in the first two criteria, and the threshold, used in the third criterion, in the parameter scan. While the specific values of the ranges only have a limited influence, the exact value of the threshold has considerable impact on the performance of the particle reconstruction. Higher thresholds, necessary for the rejection of noise, leave behind a waveform with noticeable residuals. This causes a systematic underestimation of the number of observed photons, since it is not possible to distinguish the remaining signal pulses from fluctuations. Lower thresholds, however, lead to noise being incorrectly classified as real signals and, in that way, a significant overestimation of the number of photons. The parameter scan showed that the values used yield the best results for the detection time and the reconstructed energies of the background particles.

The output of the waveform decomposition is the time distribution of reconstructed photons to which we refer as the *photon waveform*. This photon waveform assumes the sampled structure of the raw waveforms, but instead of a voltage their amplitude indicates the number of observed photons (per 0.8 ns, the period of a sample).

- **Decomposition performance check** As pointed out previously, during the waveform decomposition it is possible that noise is falsely identified as signal pulses and subtracted. To monitor the accurate execution of the decomposition, we reassemble the raw waveform based on the photon and the average one p.e. waveforms and compare it to the initial one. The reassembled waveform for the respective event is also shown in Figure 6.8 for comparison. The procedure of reassembling the waveform is essentially the inversion of the decomposition (apart from the residual waveform). For each entry in the photon waveform, the average one p.e. waveform is added to an initially empty waveform so that the position of the maximum matches the one of the photon. Subsequently, this procedure is repeated iteratively for every photon. As a consequence of the thresholds leading to the termination of the decomposition, the overall amplitude of the reassembled waveforms is prone

to be lower than the one from the original waveform. In general however, the sample-wise difference is below the bit uncertainty.
In order to quantify the level of agreement between the initial and the reassembled waveforms we calculate a quasi-χ^2:

$$\chi^2 = \sum_{samples \neq 0} \frac{(A_{inital} - A_{reco})^2}{\sigma^2_{bit\ unc.}}$$

$$\chi^2/ndf = \frac{\chi^2}{N_{samples \neq 0}},$$

where A_{inital} and A_{reco} are the sample-wise amplitudes in the waveforms and $\sigma_{bit\ unc.}$ is the bit uncertainty. In order to ensure that all significant features of the original waveform are captured, the differences are summed for all samples in which the amplitude of the original waveform is unequal to zero; the number of these samples is also used as the degrees of freedom, *ndf*. Across all runs, the obtained values of the normalized χ^2 are remarkably consistent indicating no significant failures of the waveform decomposition. We therefore waive any type of event rejection based on a χ^2-cut.

- **Photon to particle translation** The principle of operation of the photon to particle translation is illustrated in Figure 6.9. The entries in the photon waveform primarily show groups of photons caused by the transits of the respective background particles. As explained in the previous section, these photons are smeared in time and delayed with respect to the transits due to the light emission of the scintillator. The real photons are mixed with fake photons caused by afterpulsing and crosstalk (correlated with background particles) or caused by dark noise or ambient light (uniformly distributed over the full waveform).
  The main challenge lies in translating this distribution of photons (photon waveform) into a distribution which indicates the transit times and energies of the initial particles (reconstructed waveform). For this purpose, we first cluster the photons in such a way that each cluster represents the response to a single background particle or to a number of background particles which originate from the same bunch and pass the sensors simultaneously. We treat both types in the same way and refer to such a cluster as a *hit*. Subsequently, we infer the energy deposited by a background particle in the scintillator from the number of photons and assign each hit a characteristic interaction time. This energy and interaction time are

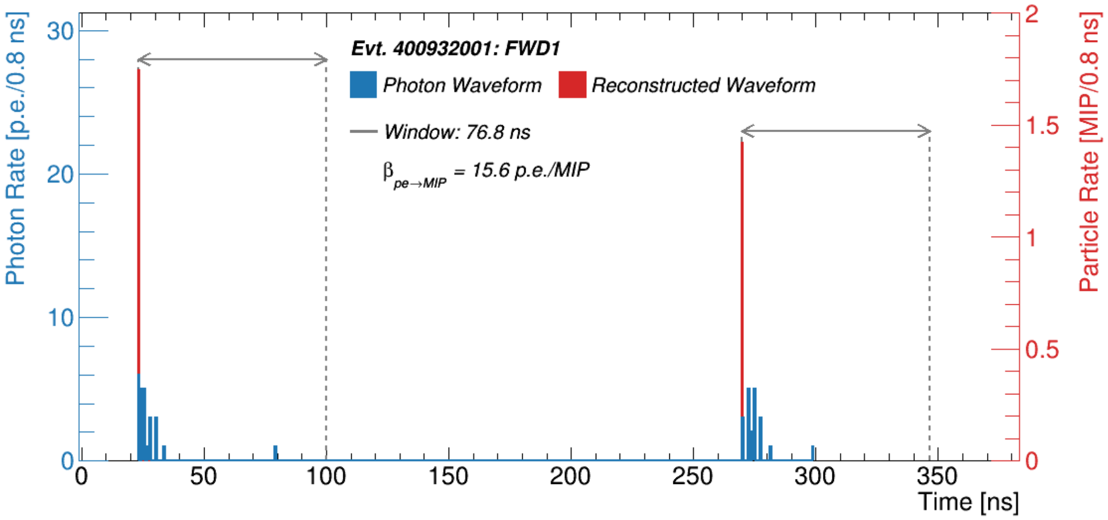

Figure 6.9: Illustration of the operation of the photon to particle translation processing a section of a typical photon waveform. The photon waveforms shows two characteristic photon clusters which are the response to the transits of two background particles separated by approximately 250 ns.

referred to as *hit energy* and *hit time*, respectively. Recall that the photon waveforms and the reconstructed waveforms are discrete time signals which adopt the same sampling rate of the raw waveforms. In technically terms, this means that a hit corresponds to a specific sample in the reconstructed waveform. The amplitude of this sample is given by the hit energy, whereas its position in the waveform, or in other words its sample index, represents the hit time.

The photon waveform is searched sample-by-sample until an entry is found. To create a cluster, we sum all entries within a predefined integration window starting with this first photon. The probability to accidentally include photons caused by afterpulsing or dark noise increases with the length of the integration window. Shorter windows, on the other hand, risk missing real photons which are delayed. Using a similar setup (plastic scintillators based on BC 408), the T3B experiment applied an integration window of just 9.6 ns [53]. To account for the longer relaxation times of the polystyrene scintillators of the CLAWS sensors, we deploy a larger window with a length of 76.8 ns. Examining the value in the parameter scan showed that this length represents the best compromise between missing delayed photons and accidentally including fake signals.

The number of photons observed by the SiPM is (on average) proportional to the number of scintillation photons and, thus, to the energy deposited in the scintillator.

The hit energy, E^{hit}, can, therefore, be calculated by

$$E^{hit} = \frac{N_{pe}}{LY} + \rho_c, \tag{6.1}$$

where N_{pe} is the total number of entries found in the integration window and LY is the light yield of the sensor module obtained from calibration measurements in the laboratory, as described in Sections 5.1.3 and 5.3. Recall that the LY is a calibration constant and normalizes the hit energy to the response of a MIP; from here onwards we use this response as a measure for the deposited energy, i.e. we state energies in the unit "MIP". In that way, the energy also acts as a measure for the mean number of particles involved in the hit. As pointed out earlier, the waveform decomposition systematically underestimates the number of reconstructed photons. To correct for this effect, a correction term, ρ_c, is added to every deposit; it will be described in detail in Section 6.1.3.

Finally, we can determine the hit time of the transit of the initial particle. Since the amplitude of a signal also affects the probability to observe prompt photons, it is necessary to account for time walk effects. The hit time, therefore, is determined with respect to the total number of photons within the integration window, N_{pe}. We select the nth photon, n_{pe}, in the window according to

$$n_{pe} = N_{pe} \cdot \alpha_{cf},$$

where α_{cf} is a steering parameter which determines the constant fraction of photons and n_{pe} is rounded to the nearest integer. The detection time of this nth photon is assigned as the hit time. In that way the index of the nth photon is utilized as the sample index i of the hit. Note that the shift between the assigned hit time and the actual transit is irrelevant since it applies in the same way for all hits and we are only interested in relative time differences between backgrounds. As mentioned earlier, each hit represents a specific sample in the reconstructed waveform where the amplitude corresponds to the hit energy and the index of the sample represents the hit time. In the following, we therefore combine the E^{hit} and i and denote hits by E_i^{hit}. Subsequently, this determination procedure is repeated for every cluster in the photon waveform.

The parameter scan showed that $\alpha_{cf} = 0.1$ minimizes the time resolution (see following section). In the scan, we also examined a second method in which the detection time of the first photon in the integration window is used as the hit time.

This alternative approach, however, results in a slightly higher time resolution. The translation of the full photon waveform represents the final processing step of the particle reconstruction and yields the reconstructed waveforms which depict the time distribution of background particles.

In summary, the particle reconstruction processes the raw data recorded by CLAWS and effectively disentangles the time of the transit of a background particle and the energy it deposits from detector effects. It also accounts for temperature variations and external influences and unifies the response. The outputs of the particle reconstruction are the reconstructed waveforms.

6.1.3 Validation and optimization

The following section presents the methodology used to confirm the correct operation of the reconstruction and optimize several of its steering parameters. For this purpose, we apply the particle reconstruction to muon data recorded in the laboratory in order to retrieve the hit times and the hit energies of the muons. Since the response to muons is known from other high-resolution laboratory measurements, we then compare these times and energies to evaluate the operation of the reconstruction.
We use a data set of more than 7000 cosmic muon events recorded with the muon telescope as described in Section 5.3. Recall that in this setup, the four sensors originally mounted in the FWD1-3 positions of the CLAWS setup are stacked on top of each other.[13] The acquisition of the muon events is self-triggered requiring that a threshold of 20 mV is exceeded simultaneously in the lower and the upper most sensors. To mimic the length of the raw physics waveforms, the muon waveforms are significantly longer than the signal pulses and consist of 3×10^4 (24 µs) samples. For the same reason, we also adopt the vertical range and similar settings from Phase 1 operation.

Hit time confirmation and time resolution To asses how well the reconstruction is able to retrieve the transit times of particles, we examine the differences in the hit times in the two center sensors. In that way, it is also possible to determine the time resolution of the sensor modules together with the particle reconstruction. Note that the two center sensors are not implicated in the trigger condition and that we can neglect the time of flight of the muons since it is merely 70 ps. The distribution of differences obtained by processing the muon data with the final set of steering parameters for the

---

[13] The sensor originally mounted in FWD1 position was switched during runtime to counteract radiation damage; we therefore have two sensors mounted in the FWD1 position.

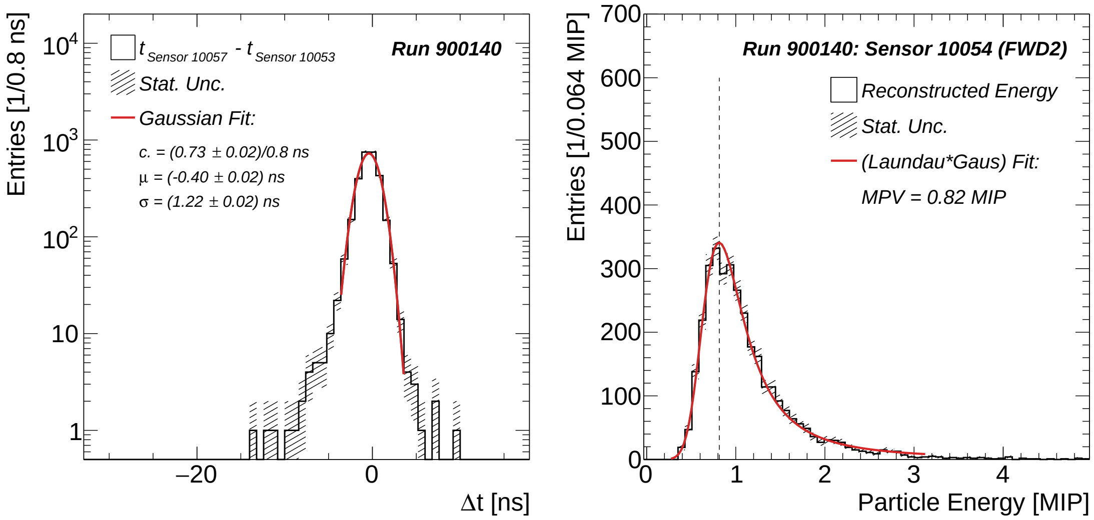

Figure 6.10: Distribution of differences in hit times obtained by applying the particle reconstruction to recordings of cosmic muons taken in the laboratory after runtime of Phase 1 (*left*). Distribution of hit energies for an exemplary sensor for the same recordings (*right*).

reconstruction is shown in Figure 6.10 (*left*). Here, we utilize the width of a Gaussian fit, σ_{fit}, as a measure for the time resolution and its mean value, μ_{fit}, as an indicator for unintended differences in the treatment of the two channels.[14] This width represents not the resolution of a single sensor, but the width of the sum of the hit times. In the case that the reconstruction operates correctly, the time resolution of a single sensor combined with the reconstruction procedure itself is then given by[15]

$$\sigma_t = \frac{\sigma_{fit}}{\sqrt{2}} = 0.86\,\mathrm{ns}.$$

With respect to the sampling rate (1/0.8 ns), this result suggests that the time resolution is primarily determined by the capabilities of the hardware. The value for $\mu_{fit} = (-0.40 \pm 0.02)\,\mathrm{ns}$, on the other hand, indicates a minor preference for one of the sensors which can be considered insignificant with respect to the time resolution. Together σ_{hit} and μ_{fit} summarize the capability of the particle reconstruction to retrieve the transit times of individual background particles.

These results are consistent with previous laboratory measurements with technically

---

[14] We apply a maximum likelihood fit in the range of $\pm 3.2\,\mathrm{ns}$ around zero; uncertainties on the parameters are adopted from the fit.

[15] This assumes that the hit times in both sensors are normally distributed and independent.

identical sensors which obtained a slightly lower time resolution, $\sigma_{hit} = 0.47\,\text{ns}$ [72]. This study employed a more conventional analysis method based on the signal height of the raw SiPM pulses, including a correction for time walk effects. The differences in the time resolution, however, can be attributed to the considerably higher vertical precision which was used by the earlier measurements. Comparing the two results, it can be seen that the hit times reconstructed by the particle reconstruction are correct and that the obtained precision is in line with the previous results.

Hit energy confirmation and correction factor Apart from the hit time, the particle reconstruction also retrieves the energy deposited in a hit. Since it is already normalized to the response of a MIP by the reconstruction, the distribution of hit energies for the muon data should follow a characteristic Langaus form (i.e. convolution of a Landau-Vavilov and a Gaussian, see Section 5.1.3) with a maximum at an energy of 1 MIP. To asses the capability of the reconstruction to retrieve these deposited energies, we fit the distribution of hit energies of each sensor with a Langaus function and utilize the most probable value (MPV) of the fit as a measure.[16]

Figure 6.10 (*right*) shows this distribution of reconstructed muon energies together with the corresponding fit for one of the sensors; the distribution for the other sensors can be found in Appendix A. The distributions for all four sensors are following the expected Langaus form. Contrary to expectations however, the position of the MPVs is shifted slightly to energies smaller than 1 MIP. This inconsistency can be attributed to the sizable thresholds required for the rejection of noise which are applied in the waveform decomposition (see description of the waveform decomposition in Section 6.1.2). These thresholds cause a systematic underestimation of the number of reconstructed p.e. and, thus, the hit energy. It can therefore be assumed that this effect is constant and does not scale with the deposited energy.

As pointed out earlier, we correct for this underestimation by adding a predefined correction factor, ρ_c, to the energy of every hit (see description of the photon to particle translation in Section 6.1.2). This correction factor is determined on the basis of the hit energy distributions of the muon data and simply compensates for the shift of the MPVs:

$$\rho_c = 1 - MPV.$$

---

[16] We apply a maximum likelihood fit with the convolution of a Landau and a Gaussian in the range from around 0.25 MIP, to reject noise, to the energy which corresponds to four times the location of the maximum of the distribution.

Table 6.1: Correction factors for the systematic underestimation of the number of reconstructed p.e. for all four sensors used during Phase 1.

Position	Sensor	MPV [MIP]	ρ_c [MIP]
FWD1	10053	1.15	-0.15
FWD1	10057	0.86	0.13
FWD2	10054	0.82	0.18
FWD3	10074	0.77	0.23

Since the factors are sensor dependent, we obtain four different values which are summarized in Table 6.1. We estimate the systematic uncertainty on these correction factors by the corrected sample standard deviation of all factors. In that way, we obtain a value of $\sigma_\rho = 0.17\,\mathrm{MIP}$.

Surprisingly, the MPV for the first sensor is larger than 1 MIP resulting in a negative correction factor. This inconsistency can be related to the radiation damage the innermost sensors suffered during runtime, as described in Section 5.1.3. As a consequence of the radiation damage, the SiPMs exhibit a significantly higher noise rate which leads to a large number of additional one p.e. pulses and can explain the observed excess in energy. Since the deviation in this sensor is still smaller than the attributed uncertainty, we simply do not apply any correction for the hit energy based on muon data in this sensor. This approach is further corroborated by the results which will be presented in section 7.2.2.

Optimization by parameter scan So far the muon data was used to verify that the particle reconstruction processes the raw data correctly. In the following, we will describe how this muon data can also be utilized to optimize the values of several steering parameters employed by the particle reconstruction. An example for such a steering parameter is the threshold terminating the waveform decomposition. As mentioned earlier, we refer to this method as a parameter scan.

The parameter scan examines the steering parameters which we found to either have the strongest influence on the performance of the reconstruction or to be difficult to determine by other means. For each of these parameters, the particle reconstruction processes the muon data with a number of predefined values. After processing of each iteration, we generate the distributions of the differences of the hit times and the hit energies, as described above, and extract the values of σ_{fit}, μ_{fit} and the four MPVs as benchmarks.

The values of the set of steering parameters together with these six benchmark quantities are then saved. This procedure is repeated for any possible combination of predefined parameter values. In that way, the effect on the time resolution and the distribution of hit energies of a variation of each parameter is determined.
The number of scanned parameters and parameter values determines the number of iterations, N_{itr}, required for the execution of the scan:

$$N_{itr} \propto \prod_{parameters} n_k,$$

where n_k is the number of predefined values for a respective parameter. Since performing the particle reconstructing is computationally intensive, N_{itr} is limited. In total, the final parameter scan examined eight different parameters in 5670 iterations and determined their leverage on the operation of the particle reconstruction. For clarity, the effects of the individual parameters have already been described in detail along with the respective processing step (see previous section). In general, the findings obtained show that the parameter with the largest impact on all of the benchmark quantities is the threshold employed in the waveform decomposition. Other parameters with notable influence are, in that order, the threshold used in the signal tagging and the window length used in the photon to particle translation. The effects of the remaining parameters are limited. For each of the parameters we chose the value which demonstrates a minimal σ_{fit} and μ_{fit}, as well as, MPVs as close as possible to an energy of 1 MIP. For most parameters, this optimal value represents a compromise between several of the benchmark quantities.

6.2 Second-stage data processing - analysis framework

The particle reconstruction is a generic processing of the data that is applied in the same way to every run. It disentangles the information about background particles from effects of the sensors and the setup and returns it in the form of the reconstructed waveforms. The analysis framework then retrieves these waveforms and their information and relates them to accelerator conditions. Figure 6.11 provides an overview of its individual processing steps and, running from top to bottom, the order in which they are performed. The output of the framework provides the foundation for the analyses of backgrounds presented in the subsequent chapters. Thus, the processing procedure performed by the framework depends on the requirements of the respective analysis. In order to meet these requirements, it selects and combines events and links them to measurements of the SuperKEKB conditions monitors and other BEAST II subsystems.

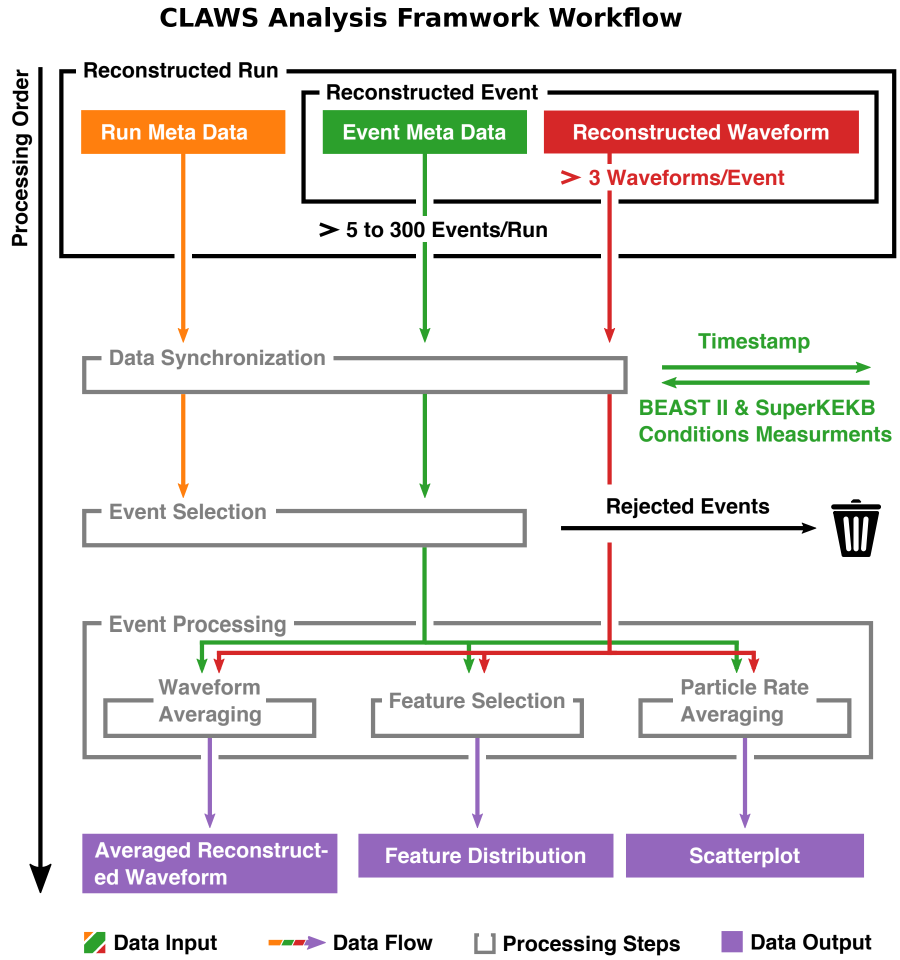

Figure 6.11: Graphical illustration of the work flow of the second stage of data processing referred to as the analysis framework.

In the following, the different processing steps are described in detail.

- **Data synchronization** The *data synchronization* first surveys the full CLAWS data and creates a list of all available runs which match the dates of interest for the respective analysis. For all selected runs, it confirms that all relevant files are accessible. If this is not the case, the run is rejected from further processing. Subsequently, the synchronization routine loads the meta data associated with each event and the run itself. This meta data consists of the settings applied by the DAQ to record the respective run and, for each event, summaries of the individual steps of the particle reconstruction. It also includes a unique timestamp which specifies the time at which each of the events was recorded.

As described in section 4.2, during runtime the BEAST II subsystems and the SuperKEKB accelerator conditions monitors continuously generated 1 s summaries of their measurements and shared them via EPICS. Besides providing real-time feedback to shifters and operators, these summaries have been used to generate a dedicated data set for offline analyses which comprises of selected measurements of BEAST II subsystems and specific accelerator conditions. It encompasses, for example, measurements of the beam currents and the pressures in the rings or the settings defining the injection of new electrons and positrons. In this unified data set, measurements of different quantities are synchronized by a timestamp corresponding to the time of the summary. In the same way, this timestamp is also used to make these quantities available for the offline analysis of CLAWS data. For each event, the data set is searched for entries matching the CLAWS timestamp. Subsequently, the corresponding quantities of interest are retrieved and added to the collection of meta information for the respective event.

- **Event selection** In the second processing step, we apply an event selection based on the aforementioned quantities in order to be able to relate measurements of backgrounds to accelerator conditions. The selection first examines the results of the individual steps of the particle reconstruction. If an event failed due to one of the control mechanisms described in the previous section or if it is not possible to locate the file with the reconstructed waveforms, the event is rejected and excluded from further processing.

  In principle, the selection operates in such a way that it is possible to select events based on any available information, including characteristics of the reconstructed waveforms. In practice however, we only use the following four quantities which are included in the meta information or retrieved from the data set of accelerator conditions and BEAST II measurements:

  (i) The number of samples of the recorded waveforms, i.e. their length, in order to have a unified set of events in particular for the study of the time structure of backgrounds.

  (ii) A machine state published by the accelerator which indicates a certain type of operation, as for example “BEAST studies”.

  (iii) The beam currents measured by the beam and accelerator condition monitors of the accelerator (see Section 3.5) where we set a minimum and a maximum current for each ring. In that way, it is possible to select events with contributions form a single ring to independently examine backgrounds in the HER or the LER.

(iv) To distinguish events with injection backgrounds from the ones with regular beam backgrounds, we utilize the beam gate in the injector which needs to be opened when particles are injected into the main rings.

Events which do not match the specific selection criteria for the respective analysis are rejected and excluded from further processing.

- **Event Processing** For the actual processing, we first generate a list of all events which pass the selection. Subsequently, the reconstructed waveforms are loaded for all the events. Depending on the type of analysis, the framework is able to process and combine the reconstructed waveforms in three different ways: by averaging a number of waveforms, extracting certain features from the waveforms or determining an average rate of background particles for each waveform.

(i) The first way of processing is directed at the study of the time structure of backgrounds. The measurements of backgrounds observed during Phase 1 suffer from significant event-by-event fluctuations. We therefore average the reconstructed waveforms of all events in the list. Recall that each hit, E_i^{hit}, is represented by specific sample in the reconstructed waveforms where the hit energy, E^{hit}, is given by the amplitude and the hit time is represented by the index of the sample i (see description of the photon to particle translation in Section 6.1.2). The averaging is then performed by calculating the average hit energy, $\overline{E_i^{hit}}$, for a given sample with index i:

$$\overline{E_i^{hit}} = \frac{1}{N_{wf}} \sum_{j=1}^{N_{wf}} E_{ij}^{hit}, \tag{6.2}$$

where N_{wf} is the number of waveforms being averaged.
We refer to this averaged time series of backgrounds as the *averaged reconstructed waveform*. It serves as the input for the analyses of the time structure of backgrounds presented in Chapters 7 and 8.

(ii) The second way of processing targets specific features included in the time structure of backgrounds. These features are represented by certain quantities of interest which are extracted individually from the reconstructed waveforms of each event and are subsequently filled into a histogram. The output of the analysis framework for this type of processing then is the distribution of the respective quantity of interest. An example for such a feature distribution are the spectra of hit energies examined in Sections 7.2.2 and 7.3.2.

(iii) The third way of processing tackles the study of backgrounds which resolve on longer timescales where a detailed picture of the time structure is not required. For such backgrounds, we can summarize each reconstructed waveform by an average rate of particles, R. This rate R is determined by summing all the hit energies of the respective waveform and normalizing them its length:

$$R = \frac{1}{N_s T_s} \sum_{i=1}^{N_s} E_i^{hit}, \tag{6.3}$$

where N_s is the number of samples of each waveform and T_s is the sampling period (0.8 ns).

This average particle rate is then related to measurements of the beam and accelerator condition monitors and combined into a scatterplot. On the time scale of a single waveform (few milliseconds), non-injection backgrounds are approximately uniformly distributed and their underlying background levels do not change notably (see Section 7.2). This type of analysis is therefore used for the study of such non-injection backgrounds with respect to certain accelerator conditions, in particular together with the other BEAST II subsystems. A corresponding analysis building on this type of processing and an example for such a scatterplot are presented in Chapter 9.

The analyses presented in the following chapters are based directly on the output of the analysis framework.

6.3 Estimation of uncertainties

Having described how the particle reconstruction and the analysis framework process the data, the final section of this chapter addresses the estimation of uncertainties on the corresponding outputs. This section focuses solely on the uncertainties on the measurement of deposited energies and particle rates. The uncertainties on the detection time of particles obtained from cosmic muon data recorded in the laboratory for the sensors and the reconstruction procedure are given in Section 6.1.3. In addition, we also determine the uncertainties on the detection time from data taken during runtime for the full CLAWS setup in Section 7.3.1.

In the following, we first determine the uncertainties on the output of the particle reconstruction, namely the reconstructed waveforms. The analysis framework uses these waveforms to generate three different types of output: the averaged reconstructed waveforms, feature distributions and scatterplots showing the averaged particle rate. Subsequently, the uncertainties on the reconstructed waveforms are propagated to these outputs of the framework. In each case, we separately determine the statistical and systematic uncertainties and combine them for an estimate of the total uncertainty.
For this discussion, we assume that uncertainties can be propagated in the following ways. Suppose that $x, \ldots, z$ are measured variables which are used to calculate a function $q(x, \ldots, z)$. If the statistical uncertainties on these measured variables, $\sigma_x^{stat}, \ldots, \sigma_z^{stat}$, are uncorrelated then the statistical uncertainty, σ_q^{stat}, is given by

$$\sigma_q^{stat} = \sqrt{\left(\frac{\partial q}{\partial x}\right)^2 (\sigma_x^{stat})^2 + \cdots + \left(\frac{\partial q}{\partial z}\right)^2 (\sigma_z^{stat})^2}. \tag{6.4}$$

By contrast, for the treatment of systematic uncertainties, σ_q^{sys}, we adopt a more conservative approach and add them linearly:

$$\sigma_q^{sys} = \left|\frac{\partial q}{\partial x}\right| \sigma_x^{sys} + \cdots + \left|\frac{\partial q}{\partial z}\right| \sigma_z^{sys}. \tag{6.5}$$

This assessment always holds, even if the uncertainties are maximally correlated and lean in the same direction. In that way, it rather represents an upper estimate of the systematic uncertainties. As described shortly, this treatment is sufficient since in most cases $\sigma^{stat} > \sigma^{sys}$ and, thus, the uncertainties are mainly determined by statistics. To be able to quote a common uncertainty, σ_q^{tot} , we assume that the statistical and systematic uncertainties are uncorrelated and normally distributed and that they, therefore, can be combined by adding them in quadrature:

$$\sigma_q^{tot} = \sqrt{(\sigma_q^{stat})^2 + (\sigma_q^{sys})^2}. \tag{6.6}$$

A more detailed discussion of the treatment of uncertainties and their propagation can be found in [73].

Uncertainties on the reconstructed waveforms With respect to the reconstructed waveforms, we first establish the uncertainties on the hit energy for a given position i, E_i^{hit}, calculated in Equation 6.1. Here, both LY and ρ_c are constants whose values are determined once and remain unchanged during usage. The only source of random uncertainties are fluctuations in N_{pe}, or in other words, the photon count. It can therefore be assumed that N_{pe} is following a Poissonian distribution with a standard deviation $\sigma_{pe} = \sqrt{N_{pe}}$.[17] Using Equation 6.4, the statistical uncertainty on the hit energy, σ^{stat}, for the sample with index i (or in other words the position in the reconstructed waveform) can be obtained by

$$\sigma_i^{stat} = \sqrt{\left(\frac{\partial E^{hit}}{\partial N_{pe}}\right)^2 \sigma_{pe}^2} = \left|\frac{\sigma_{pe}}{LY}\right| = \frac{\sqrt{N_{pe}}}{LY}.$$

Since systematic uncertainties on N_{pe} are subsumed into ρ_c, the remaining sources for systematics are LY and ρ_c. The uncertainties on LY, σ_{LY}, are adopted from [61], whereas uncertainties on ρ_c, σ_ρ, are estimated by the corrected sample standard deviation of the four correction factors (see Section 6.1.3). With Equation 6.5, the systematic uncertainties on the hit energy, σ^{sys}, are similarly given by

$$\sigma_i^{sys} = \left|\frac{\partial E^{hit}}{\partial LY}\sigma_{LY}\right| + \left|\frac{\partial E^{hit}}{\partial \rho_c}\sigma_\rho\right| = \left|-\frac{N_{pe}}{LY^2}\sigma_{LY}\right| + \left|\sigma_\rho\right|.$$

Finally, the total uncertainty on the hit energy, σ_i^{tot}, is calculated by adding the statistical and the systematic uncertainties in quadrature as described in Equation 6.6.

The uncertainties are functions only of N_{pe} or rather of E^{hit} which are also sensor dependent due to LY and ρ_c. Statistical, systematic and total uncertainties for one of the sensors are compared in Figure 6.12. It can be seen that for small hit energies below approximately 0.4 MIP, the σ^{tot} is mainly determined by systematic uncertainties, in particular by σ_ρ. For all other energies, however, it is dominated by statistical uncertainties.

The uncertainties calculated for the reconstructed waveforms provide the starting point for the calculation of the uncertainties on the output of the analysis framework discussed in the following.

Uncertainties on the averaged reconstructed waveform With respect to the averaged reconstructed waveforms, we determine the uncertainties on the averaged hit energy, $\overline{E}^{\,hit}$, defined in Equation 6.2. For greater clarity, we refer to the uncertainties on $\overline{E}^{\,hit}$ by the letter η rather than the previously used σ. Since the averaging covers events which are recorded over a wide range of different accelerator conditions, it can not be assumed that the hit energies, E_i^{hit}, in the individual waveforms are measurements

---

[17] According to the principle of maximum likelihood, N_{pe} is the best estimate for the average number of counts and, therefore, $\sigma_{pe} = \sqrt{N_{pe}}$.

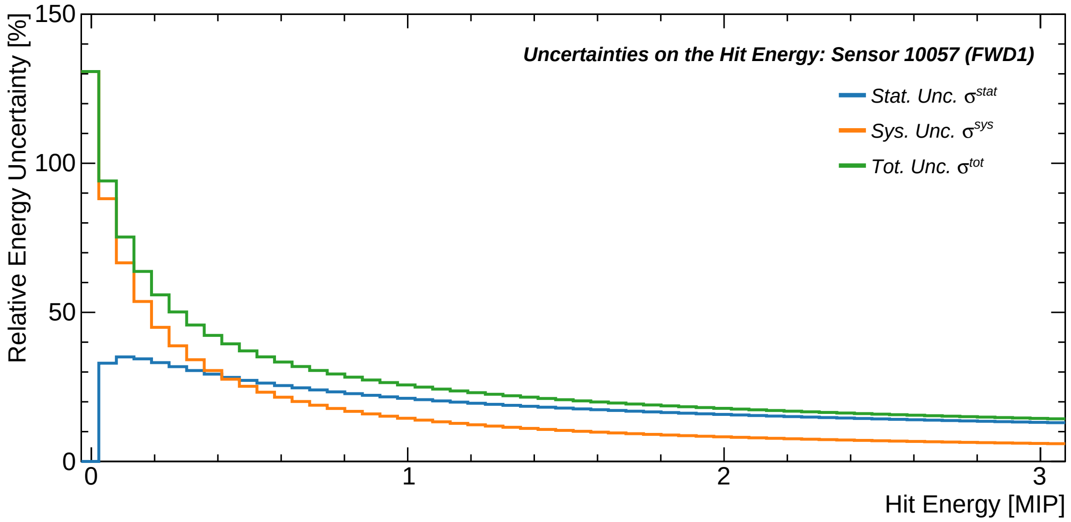

Figure 6.12: Relative statistical, systematic and total uncertainties of the hit energy for one of the sensors used during Phase 1.

of the same quantity with the same uncertainty. Instead, we calculate the uncertainties by propagating the uncertainties on the individual E_i^{hit} using Equations 6.4, 6.5 and 6.6. The statistical uncertainty, η_i^{stat}, for a given position in the waveform i is then given by

$$\eta_i^{stat} = \sqrt{\sum_{j=1}^{N_{wf}} \left(\frac{\partial E_i^{avg\ hit}}{\partial E_{ij}^{hit}} \right)^2 (\sigma_{ij}^{stat})^2} = \frac{1}{N_{wf}} \sqrt{\sum_{j=1}^{N_{wf}} (\sigma_{ij}^{stat})^2},$$

where the index j indicates the respective reconstructed waveform. In the same way, the systematic uncertainties, η_i^{sys}, are determined by

$$\eta_j^{sys} = \sum_{j=1}^{N_{wf}} \left| \frac{\partial E_i^{avg\ hit}}{\partial E_{ij}^{hit}} \right| \sigma_{ij}^{sys} = \frac{1}{N_{wf}} \sum_{j=1}^{N_{wf}} \sigma_{ij}^{sys}.$$

The total uncertainty, η^{tot}, can again be obtained by adding in quadrature.

The uncertainties η_i^{stat}, η_i^{sys} and η_i^{tot} are functions of the various hit energies of the waveforms being averaged (σ_{ij}) and are therefore not following a strict analytical function. In general, they show a similar behavior as the regular hit energies meaning that the uncertainties for averaged hit energies smaller than 0.4 MIP are dominated by systematic uncertainties, whereas larger energies are dominated by statistical uncertainties.

Feature distribution Another output type of the analysis framework are feature distributions summarizing quantities of interest. These distributions count the number of events for which the quantity of interest falls into a certain category or rather a certain bin. The statistical uncertainty on the number of counts for each bin can, therefore, be described by Poissonian uncertainties. According to the principle of maximum likelihood, the best estimate for the average number of entries is the observed number of counts, N. The statistical uncertainty, δ^{stat}, is then simply given by

$$\delta^{stat} = \sqrt{N}.$$

For the sake of simplicity, we forgo to state systematic uncertainties on the feature distributions and only show statistical uncertainties.

Uncertainties on the averaged particle rate The third type of output of the analysis framework are scatterplots based on accelerator conditions provided by SuperKEKB and the averaged particle rate, R (see Equation 6.3). Since examining uncertainties on the SuperKEKB conditions monitors is beyond the scope of this thesis, we assume that these quantities are known well enough that their statistical and systematic uncertainties can be neglected with respect to the ones on the averaged particle rate. Nevertheless, we briefly revisit the discussion of uncertainties on the measurements of the condition monitors when discussing results of the respective analysis in Chapter 9.
For greater clarity, we refer to the uncertainties on the averaged particle rate by the letter θ rather than the previously used σ, η or δ. The values for N_s and T_s are assumed to be well known and, therefore, do not carry any uncertainties. The statistical uncertainty on R , θ^{stat}, is then determined analogously by

$$\theta^{stat} = \sqrt{\sum_{i=1}^{N_s} \left(\frac{\partial R}{\partial E_i^{hit}} \right)^2 (\sigma_i^{stat})^2} = \frac{1}{N_s T_s} \sqrt{\sum_{i=1}^{N_s} (\sigma_i^{stat})^2},$$

where the summation is performed over all samples in a single reconstructed waveform. We obtain the systematic uncertainty on R , θ^{sys}, in a similar way:

$$\theta^{sys} = \sum_{i=1}^{N_s} \left| \frac{\partial R}{\partial E_i^{hit}} \right| \sigma_i^{sys} = \frac{1}{N_s T_s} \sum_{i=1}^{N_s} \sigma_i^{sys}$$

Again these uncertainties are functions of the respective hit energies and can not be described strictly analytically. As expected from the uncertainties on the hit energies, however, they are dominated by statistical uncertainties and the systematic uncertainties generally play no role.

Chapter 7

Time resolved analysis of backgrounds

In this chapter we present a comprehensive time resolved analysis of beam backgrounds during the first commissioning phase of SuperKEKB. It offers the unique possibility to study beam backgrounds cleanly and independently of collisions and final focusing. A time resolved analysis here implies three things: the achieved time and energy resolutions are sufficient to resolve energy deposits of single particles which allows us to infer the type of background particles and the responsible background process. Second, the achieved time resolution is well below the expected maximum rate of signals given by the bunch spacing and thus we are able to map energy deposits to single bunches. And third, the length of the measurement covers several milliseconds which is sufficient to study the time evolution of backgrounds over hundreds of revolutions in the rings. The last two capabilities are imperative for the investigation of injection backgrounds introduced in Sections 3.3 and 3.4.

The different sources of regular beam backgrounds at SuperKEKB are also described in Section 3.4. Because of its significance for the future operation of Belle II, however, the presented analysis focuses especially on backgrounds caused by continuous top-up injections. Such injections lead to background levels which require an interruption of data recording in several subsystems of Belle II, in particular in the PXD (see Section 4.1). Measurements conducted before the shutdown of KEKB suggest damping times of up to 4 ms after injection before backgrounds return to regular levels [43]. With a foreseen injection rate of 50 Hz together for both rings this would potentially reduce the integrated luminosity by as much as 20% and would therefore have a considerable impact on the Belle II physics program. To lower the loss in integrated luminosity it is intended to gate data taking of the subsystems and stop recording only during transits of injection bunches. Despite their precise description of the regular operations of SuperKEKB, simulations fail to predict the time evolution of injection backgrounds with sufficient accuracy. The shape of veto windows therefore has to be determined by direct measurements.

Performance studies for the operation of the PXD have shown that gating is required if the occupancy is exceeding a limit of 3% [43]. If converted to a particle flux in the CLAWS sensors, this limit would correspond to more than 9000 particles recorded within a period of 20 µs.[1] By contrast, the backgrounds observed by CLAWS during the first commissioning phase are two orders of magnitude below this limit. The fundamentally different conditions prevailing during the final operation of Belle II and Phase 1, however, make an exact prediction of injection backgrounds based on Phase 1 measurements difficult. Instead the main purpose of this study is to serve as a prototype for understanding the time structure of injection backgrounds. Additional goals are to verify that the beam background levels are safe for installation of the detector and to determine the delay between the trigger signal and the arrival of newly injected particles at the IP. Note that the analysis presented within this thesis is a more comprehensive version of the one described in [36] and thus there is some overlap.

This chapter is structured as follows: In Section 7.1, we give an introduction to the examined data sets. In the presented analysis we study backgrounds based on two scenarios, backgrounds originating purely from regular circulating bunches (non-injection background) and combined backgrounds of circulating bunches together with injection bunches (injection background). In Section 7.2, we first discuss results for the case of non-injection backgrounds. Here, we focus on their time structure and their composition in terms of particle species and energies. Building on this, in Section 7.3 we present results of a comprehensive analysis of injection backgrounds. We again scrutinize the general time structure and the background composition but also demonstrate a method for quantifying the decay behavior of injection background and for developing a gating scheme for the future operation of Belle II.

7.1 Overview of examined data sets

We begin by giving an overview of the data sets studied in the presented analysis. The data sets together with relevant quantities provided by the SuperKEKB beam and condi-

---

[1] This conversion considers only the active area of the innermost layer in the PXD [51] and the area for which the normal vector is parallel to the direction of propagation of the beams in the CLAWS sensors (see Section 5.1).

Table 7.1: Summary of data sets examined for the time resolved analysis of backgrounds. Injection parameters changed with respect to their nominal values (HER-REF and LER-REF) in a dedicated injection study are highlighted in bold red. Beam currents are stated by the range, whereas the injection efficiency is given by the sample mean and corresponding sample standard deviation.

Data Set	*BG*	I_{HER} [mA]	I_{LER} [mA]	PS [°]	$VS1$ [µrad]	$VS2$ [µrad]	SA [mrad]	Θ_{inj} [pC]	N_{evts} [%]
NI-ALL	-	29 - 788	9 - 852						2676
NI-HER	-	38 - 705	0						1806
NI-LER	-	0	4 - 974						4057
NI-VACS	-	452 - 706	105 - 752						792
HER-ALL	HER	1 - 706	0		-465 -(-265)	80 - 220		57 ± 60	2401
LER-ALL	LER	0	1 - 999		-378 -(-234)	-39 - 153		71 ± 38	7936
LER-VACS	LER	0	1 - 875		-378 -(-330)	83 - 153		72 ± 28	1238
HER-REF	HER	3 - 149	0	258	-385	80	2.35	65 ± 28	62
HER-PS	HER	286 - 449	0	**305**	-385	80	2.35	96 ± 169	190
HER-VS1	HER	216 - 300	0	258	**-465**	80	2.35	15 ± 12	265
HER-VS2	HER	301 - 400	0	258	**-435**	80	2.35	39 ± 17	162
LER-REF	LER	0	3 - 398	1	-378	123	5.51	90 ± 14	220
LER-PS	LER	0	185 - 486	**31**	-378	123	5.51	81 ± 20	617
LER-VS	LER	0	272 - 350	1	-378	**43**	5.51	73 ± 9	97
LER-SA	LER	0	2 - 185	1	-378	123	**5.39**	75 ± 14	239

tion monitors (see Section 3.5) are summarized in Table 7.1. CLAWS data taken during the runtime of Phase 1 is partitioned into events which consist of a single waveform for each of the three channels. Each data set represents a selection of such events based on certain accelerator conditions (see Section 6.2). The first half of a name of a set refers to the type of injection required in the selection. The second half indicates a certain property of the selection and helps to differentiate the sets. If not stated differently, the findings presented in this chapter are discussed based on the results for specific data sets and the innermost channel, FWD1, which offers the highest signal rates. Figures for the channels FWD2 and FWD3, as well as figures for other data sets can generally be found in Appendix B. Although longer waveforms have been recorded, all data sets studied here consist of waveforms with a length of 2.4 ms (3×10^6 samples). In the following, we first introduce the relevant quantities and then describe the data sets and their selection criteria in more detail.

The beam gate, BG, indicates the type of injection where we differentiate between the following three cases: events are triggered exclusively by injections into the HER, denoted by "HER"; by injections into the LER, denoted by "LER"; or specifically without injections, denoted by "-" in the table or a NI (short for *non-injection*) in the name of the respective data set. The beam currents in the HER, I_{HER}, and the LER, I_{LER}, are given as the range of values among events in the data set after selection. The remaining quantities in Table 7.1, except N_{evts}, are related to injections. The injection of new particles into the circulating bunches are largely determined by four parameters: the phase with which particles are injected, PS; the two vertical incidence angles, $VS1$ and $VS2$; and the incidence angel in the horizontal plane or septum angle, SA. Depending on whether one or different values were used, $VS1$ and $VS2$ are denoted by a range or a single value. Also given is the injection efficiency, Θ_{inj}, which represents the percentage of the injection charge that actually reaches the rings. It is stated by the sample mean and the corresponding sample standard deviation of all events in the respective data set. Quantities related to injections are omitted when not relevant or not available for the analysis.[2] Finally, N_{evts} denotes the total number of events in the respective data set after the selection.

We use BG to select only events with a certain type of injection, as indicated by the first part of the name. Additionally, a cut on beam currents is applied to study backgrounds of the HER and the LER independently or explicitly combined. A beam current above 1 mA in one ring and below 1 mA in the other is required for single ring data sets, whereas a beam current above 1 mA in both rings is required for joint data sets.

NI-ALL, NI-HER, NI-LER and NI-VACS are non-injection data sets selected for the study of the structure of backgrounds of regular bunches. As described in Section 3.3, the distance between consecutive bunches in SuperKEKB is given by multiples of the size of an RF bucket, T_{bucket} (1.965 ns), and, like the total number of bunches, depends on the exact fill pattern adopted by the accelerator. The pattern mostly used during Phase 1 specifies a bunch spacing of three buckets or 5.995 ns (169.6 MHz) with a total of 1576 bunches circulating in the rings [44]. Non-injection events are recorded by auto-trigger at random without any time correlation to processes in the machine. In order to realign these events with the bunch spacing in the rings, the reconstructed waveforms of all

---

[2] For NI-ALL, NI-HER, NI-LER and NI-VACS, the injection parameters are irrelevant; for HER-ALL, LER-ALL and LER-VACS, the values of PS and SA are not available for the analysis.

non-injection data sets are shifted by the time of the occurrence of the first hit. NI-ALL includes all respective events with beams in both rings taken during run-time,[3] and thus covers a wide range of partly very different accelerator conditions. The equivalents for events with beams in a single ring are NI-HER and NI-LER.

The term *vacuum scrubbing* describes the outgassing of impurities in the vacuum system of a particle collider which is accelerated by the circulating beams via electron-induced desorption and photon-induced desorption. In electron-positron colliders such as SuperKEKB, the former process is more common and is caused by machine-induced electron multipacting [74]. The latter process can result from synchrotron photons emitted in interactions of the beams with the material of the vacuum chambers [75]. During vacuum scrubbing very high beam currents and artificially inflated beam sizes are used to promote desorption reactions which also maximizes the backgrounds of ordinary circulating bunches. NI-VACS includes all non-injection events with beams in both rings taken (only) during periods of vacuum scrubbing in both rings. As such, it is a subset of NI-ALL.

Injection events are triggered by an external signal provided by SuperKEKB and are, therefore, aligned in time with respect to the injection process and the circulating beams. HER-ALL and LER-ALL are collections of all injection triggered events with beams only in the respective ring. LER-VACS is a subset of LER-ALL consisting of events taken during periods of vacuum scrubbing.

For the regular physics operation of SuperKEKB it is foreseen for both rings to simultaneously inject new particles into two bunches separated by 49 RF buckets (96.3 ns). During Phase 1, however, double bunch injection was only employed for the LER and even here only in specific cases. One of these cases is vacuum scrubbing for which it was the default injection scheme. Thus, LER-VACS exclusively and LER-ALL partially consist of events with double bunch injections. All other injection data sets are solely based on events with single bunch injections. The HER-ALL, LER-ALL and LER-VACS data sets consist of a large number of events but are taken over a wide range of accelerator conditions.

During Phase 1, SuperKEKB and BEAST II performed a dedicated injection background study to measure background levels and time structures under controlled conditions and to assess the effect of variations in the injection parameters. The study was conducted separately for HER and LER injections and collated in four data sets each. First, a reference run with nominal injection parameters was taken as a baseline for both rings;

---

[3] Events containing all information necessary for a full time resolved analysis have been taken from the 15th of May, 2016 onwards.

the data sets for the reference injection runs are labeled HER-REF and LER-REF. For each of the other given data sets one injection parameter, marked red in the table, was changed from nominal settings to the value yielding the minimal injection efficiency in order to study its effect on the time structure and the background levels.[4] All of the data sets from the injection study consist of relatively few events but are each taken under very specific and homogeneous accelerator conditions.

In summary, of the 15 data sets studied in the presented analysis four sets examine non-injection backgrounds of ordinary circulating bunches, five sets examine HER injection backgrounds and six sets examine LER injection backgrounds. For each ring, four of these sets have been taken during a dedicated injection background study which assessed the effects of variations in the injection parameters.

7.2 Time resolved analysis of non-injection backgrounds

New particles are injected into already circulating bunches and therefore injection backgrounds are always accompanied by regular beam backgrounds. In order to understand the former it is essential to first understand the latter on the same level. In this section, we perform a time resolved analysis of backgrounds measured during periods without injections. An analogous but more extended analysis of injection backgrounds is presented in the next section.

Different sources of beam backgrounds at SuperKEKB are introduced in Section 3.4. From these sources only synchrotron radiation (SR), both types of beam-gas scattering and Touschek scattering are relevant for the presented analysis. For beam-gas and Touschek scattering, simulations for Phase 1 predict particle loss rates (for the full IR region for a single ring) of a few MHz each. Photons caused by SR, on the other hand, are mainly absorbed by the beam pipe and simulations can only estimate an upper limit of a moderate 500 Hz [36]. It can therefore be assumed that SR is of no relevance. In general, the total signal rate is expected to be significantly smaller than the bunch crossing frequency. These signals are caused by single photons or charged particles and are uniformly distributed in time. Their energy deposits in the CLAWS sensors are similar to the ones from charged particles observed in laboratory measurements (see Section 5.3). In Section 7.2.1, we first describe the time structure of non-injection backgrounds. Section 7.2.2 then examines the composition of non-injection backgrounds, where the focus

---

[4] Here we assumed that the minimum in injection efficiency would correspond to the maximum in injection background at the IP. The injection efficiency, however, was limited by the elevated radiation exposure of parts of the accelerator due to the increased particle loss.

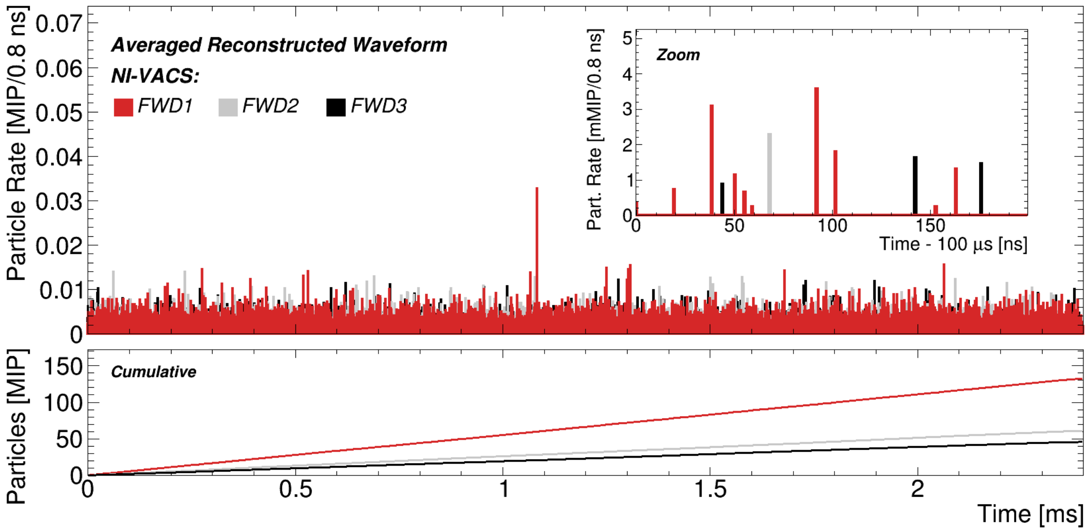

Figure 7.1: Background time distribution for the NI-VACS data set for all three channels stacked on top of each other (*top*) and their cumulatives separately for each channel (*bottom*).

is on the hit energy distribution which is used to derive the type of background particles and the responsible background processes. It also discusses if backgrounds are distributed uniformly or if there is a preference for particular noisy bunches. Finally, we briefly summarize the key findings from the time resolved analysis of non-injection backgrounds in Section 7.2.3.

7.2.1 Time structure

Backgrounds fluctuate significantly between events what is in particular affecting the analysis of data sets with a small number of events. In order to understand common features in the time evolution, it is necessary to study backgrounds based on averaged time distributions. The part of the analysis presented in this section thus examines the averaged reconstructed waveforms, as introduced in Section 6.2.

Figure 7.1 shows the averaged reconstructed waveform for all channels stacked on top of each other for the NI-VACS data set (*top*). As expected, signals are distributed uniformly over the whole waveform. A cutout illustrates an arbitrary part with higher resolution and shows that there are considerably less signals than the number of bunch crossings in the given range. Furthermore, the overall signal level of few mMIPs/0.8 ns suggests that the entries in the waveform originate from energy deposits in single events.[5] In contrast to injections, for regular beam backgrounds we typically do not observe the sum of signals by time-wise correlated sources but single particles.

Figure 7.1 (*bottom*) shows the cumulatives separately for each channel for the same data set. Here, the uniformity of the distribution of signals is reflected by the linearity of the increase, whereas the overall number of particles detected in the full time window is given by the endpoint. Both the inclination and the endpoint are larger the closer the respective sensor is to the beam lines and therefore to the source of backgrounds. Due to the artificially wide beams and high currents during vacuum scrubbing we record up to 140 MIPs over the length of the waveform, which are the largest overall backgrounds we observe among the non-injection data sets.

7.2.2 Background composition

We study the composition of backgrounds by examining individual energy deposits obtained from the reconstructed waveforms before averaging (see Section 6.2). We refer to the distribution of such energies as a hit energy distribution or a hit energy spectrum. Figure 7.2 (*left*) compares these hit energy spectra of the NI-HER, NI-LER and NI-ALL data sets. The distributions are normalized to the number of events, the length of the waveforms and the area of the sensors for which the normal vector is parallel to the direction of propagation of the beams (see Section 5.2). Different quantities describing these distributions for the stated data sets and channels are summarized in Table 7.2. In the following, we discuss findings from the obtained hit energy spectra based on the distributions and quantities and thus infer the sources responsible for the measured non-injection backgrounds.

Particle flux The integral of the distributions corresponds to the number of observed hits, N_{hits}, and represents the particle flux in the respective sensor. Note that the flux for the individual rings (NI-HER and NI-LER) should only add up to the combined flux (NI-ALL) if the events would be taken under the exact same accelerator conditions. For the given data sets, however, this is only partially the case and hence the excess of the NI-ALL distribution relative to the sum of the other two is not unexpected. In general, the particle flux is decreasing with the distance from the beams and is the largest in the innermost sensor (FWD1) and vice versa.

To estimate the average signal rate due to non-injection backgrounds for a single bunch

---

[5] Recall that NI-VACS comprises of 792 events and that we are expecting signals of approximately 1 MIP per particle, so 1 MIP in a single event would translate to a rate of 1.3 mMIP/0.8 ns at its time position.

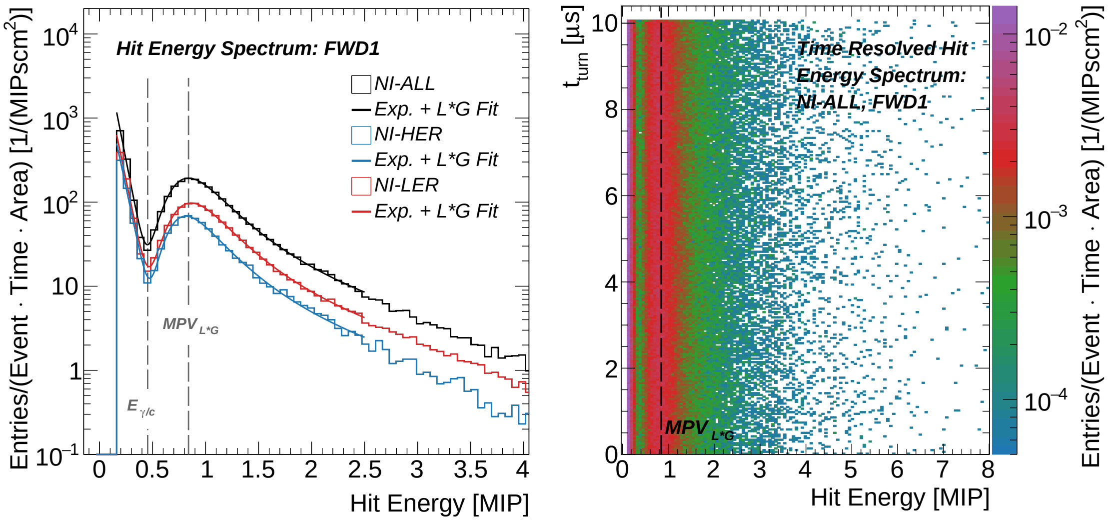

Figure 7.2: Distributions of hit energies for given non-injection data sets for the channel FWD1 (*left*). The distribution of the time in turn versus the hit energy, or time resolved hit energy distribution, for NI-ALL for channel FWD1 (*right*). All distributions are normalized to the number of events, the length of the waveforms and the area of the sensors.

and to assess if the observed energy deposits are caused by a single or multiple particles, we calculate the number of hits per bunch:

$$N_{hits}/Bunch = N_{hits} \cdot A \cdot 3 \cdot T_{bucket},$$

where A is the area of the CLAWS sensors and $3 \cdot T_{bucket}$ represents the time between two consecutive bunches. From these numbers it becomes apparent that the probability to observe a particle from a bunch is generally less than one in ten thousand. We conclude that the observed signals are caused almost exclusively by single particles and that we indeed can approximate the particle flux by N_{hits} since the probability for an accidental “pile-up” is negligible.

Description of hit energy spectra The different background sources determine firstly the type of particles and secondly the particle energies. Note that thermal noise or imperfectly shielded ambient light are generally excluded as sources for the observed signals since pedestal runs, taken at the end of the runtime, show no noticeable number of hits. In the following, we first divide the respective hit energy spectrum in three energy ranges and examine each of these ranges separately. Subsequently, we then describe the

Table 7.2: Key quantities summarizing the hit energy distributions for the stated data sets and sensors. The particle type, *pt*, differentiates between photons, γ, and charged particles, c.

Data Set	N_{hits}	$\frac{N_{hits}}{Bunch}$	MPV_{L*G}	$E_{\gamma/c}$	$P_{pt}(E < E_{\gamma/c})$		$P_{pt}(E > E_{\gamma/c})$		N_{pt}/N_{hits}	
					$pt \hat{=} \gamma$	$pt \hat{=} c$	$pt \hat{=} \gamma$	$pt \hat{=} c$	$pt \hat{=} \gamma$	$pt \hat{=} c$
	$[\frac{1}{\mathrm{s\,cm^2}}]$		[MIP]	[MIP]	[%]	[%]	[%]	[%]	[%]	[%]
FWD1										
NI-ALL	3454	1.8e-4	0.84	0.45	98.9	1.1	0.8	99.2	34.6	65.4
NI-HER	1274	6.8e-5	0.81	0.48	99.2	0.8	1.0	99.0	43.3	56.7
NI-LER	1826	9.7e-5	0.86	0.47	98.9	1.1	0.9	99.1	37.3	62.7
FWD2										
NI-ALL	1228	6.5e-5	1.02	0.64	98.9	1.1	1.3	98.7	32.9	67.1
NI-HER	441	2.3e-5	1.03	0.57	98.9	1.1	0.5	99.5	16.3	83.7
NI-LER	578	3.1e-5	1.06	0.71	99.2	0.8	2.4	97.6	48.7	51.3
FWD3										
NI-ALL	1050	5.6e-5	0.95	0.50	97.5	2.5	1.2	98.8	34.3	65.7
NI-HER	396	2.1e-5	0.97	0.49	96.7	3.3	0.8	99.2	18.5	81.5
NI-LER	345	1.8e-5	0.97	0.51	97.3	2.7	1.3	98.7	33.2	66.8

entire distribution by a combined parameterization.

As expected, there are no entries up to the energy which corresponds to the correction factor ρ_c (see Section 6.1.3). The hits in the region from ρ_c up to a local minimum located at around half of a MIP are attributed primarily to photons. Relevant background processes producing such photons are only bremsstrahlung and SR, the latter being excluded by simulation. An additional reason to reject SR is that we do not observe significantly higher background rates in NI-HER compared to NI-LER, as would be expected due to the higher beam energy in the HER (see Section 3.4). In principle, such low energy hits can also originate from delayed photons which are caused by afterpulsing or late light emission and exceed the integration window (see Section 6.1.2). These photons, however, would follow larger initial signals, especially in the case of injection backgrounds. As will be shown in Section 7.3.1, delayed photons can be excluded since we do not observe such secondary pulses in the time structure of injection backgrounds. This means that the photons are either created directly by beam-gas bremsstrahlung or by bremsstrahlung of off-orbit particles in the experimental setup and the vacuum chambers. The latter can be caused by Touschek or beam-gas Coulomb scattering. While it is expected that the energy spectrum of bremsstrahlung photons is proportional to their inverse energy ($\propto 1/E$), we find that a fit with an exponential function

$$f(E) = p_1 \cdot e^{-p_2 \cdot E}$$

yields considerable lower normalized χ^2. In the following, this part of the hit energy spectra is therefore described by $f(E)$.[6]

Hits in the region from the local minimum up to 2.5 MIP are primarily attributed to charged particles. Relevant sources for charged particle backgrounds are Touschek scattering and the Coulomb component of beam-gas scattering. The distributions here clearly reflect the functional form expected for charged particles and observed in the calibration measurements with muons (see Sections 5.1.3 and 6.1.3). We therefore describe this part of the hit energy spectra by the convolution of a Landau and a Gaussian distribution, or Langaus:

$$g(E) = (Landau * Gaussian)(E).$$

For energies above 2.5 MIP, the distributions follow a power-law behavior up to an end-point of around 8 MIP where they begin to be limited by statistics. Hits in this range are solely attributed to charged particles.

Having discussed the individual regions, we finally describe the entire hit energy distribution by a fit with a joint parameterization, $h(E)$, which combines the photon and the charged particle components:

$$h(E) = f(E) + g(E).$$

Due to the calibration with cosmic muons (see Section 6.1.3), the most probable value of the charged particle component of the fit, from here on referred to as MPV_{L*G}, should correspond to an energy of 1 MIP. In general, the values obtained for MPV_{L*G} are consistent across all three data sets and agree on the percent level with each other. The values for FWD2 and FWD3 practically match the expectation of 1 MIP and deviate only

---

[6] This assumes that the cross section for the detection of photons is approximately constant for energies up to 2.5 MIP.

by as much as 6%. Results for FWD1, however, underestimate the response to charged particles by approximately 20%. Since it is observed across all three sets, this appears to be a systematic effect, which is still within the systematic uncertainties obtained for ρ_c. The level of agreement between the data recorded during runtime and the calibration validates the reconstruction of particles and the applied corrections.

Background composition The different components of the combined parameterization can be interpreted as the likelihoods for the respective particle species. The point where $f(E)$ and $g(E)$ intersect, from here on referred to as $E_{\gamma/c}$, thus corresponds to the energy at which hits are equally likely to be caused by a photon or a charged particle. For all data sets and channels, the values for $E_{\gamma/c}$ obtained from the fit are located at energies of approximately 0.5 MIP and are in good agreement with each other. Using both components then allows us to calculate the probability that a hit with an energy smaller than $E_{\gamma/c}$ is caused by a photon:

$$P_\gamma(E < E_{\gamma/c}) = \frac{\int_{\rho_c}^{E_{\gamma/c}} f(E)dE}{\int_{\rho_c}^{E_{\gamma/c}} h(E)dE}.$$

Probabilities for charged particles and energies in the range between $E_{\gamma/c}$ and 2.5 MIP are calculated accordingly. Across all sensors and data sets, we find that for low energies hits are primarily caused by photons with probabilities of 96% and more. For higher energies, on the other hand, the majority of hits originates from charged particle interactions with similarly unambiguous probabilities. For energies above 2.5 MIP, hits are then attributed exclusively to charged particles.

From the consistency of the probabilities in a given energy range, we conclude that a hit energy above or below $E_{\gamma/c}$ is a sufficient criterion to distinguish hits of photons from the ones of charged particles. These results might be used to separately measure beam-gas and Touschek backgrounds in the future. Combining the probabilities for the different ranges with the total particle flux yields the proportion of photons and charged particles observed across the full energy range. Here, we find that both types of particles occur in approximately the same proportion.

Time in turn and time resolved hit energy distribution To examine time patterns which repeat at every turn, we introduce a new quantity referred to as time in turn, t_{turn}. Recall that the beam revolution period is given by $T_{rev} = 10.0614\,\mu s$ (see Section 3.3). We first point to the time at which an arbitrary bunch passes by the IP.

Then the time of the transit of a second bunch relative to the first transit is well defined by the bunch structure and does not change if we move our point of reference by T_{rev}. Instead of the transit of an arbitrary bunch, we can also define the start of the waveform as our point of reference and denote the turn-wise distance between the point of reference and the transit of the second bunch by t_{turn}:

$$t_{turn} = t \bmod T_{rev},$$

where t is the absolute time after the start of the waveform. This means that for a particular bunch all transits correspond to the same t_{turn}. This quantity can thus be used to apply dedicated timing cuts in order to select only signals of specific bunches (i.e. the injected bunch). The t_{turn} is widely used in the analyses of injection backgrounds presented in the following sections.

Here, however, we adopt the t_{turn} to address the question if non-injection backgrounds are distributed uniformly or if there is a preference for particular noisy bunches which cause above average hit energies or number of hits. Figure 7.2 (*right*) shows the distribution of the t_{turn} versus the hit energy for NI-ALL, from here on also referred to as a *time resolved hit energy distribution*. We do not observe any structures with respect to the t_{turn}. Instead, the spectrum shown in Figure 7.2 (*left*) holds for all t_{turn}.

7.2.3 Summary and key findings

In this section, we presented a time resolved analysis of non-injection backgrounds in which we studied their time structure and their particle composition. The averaged time distributions showed that energy deposits are distributed uniformly in time without an apparent preference for specific bunches. Relating the observed particle flux to the number of bunch transits suggested that hits are caused almost exclusively by single particles. We also found a radial dependence of the background rates which matches the distance of the sensors from the beam lines.

We described the hit energy distributions with a combined parameterization which allowed separating their photon and charged particle components. The level of agreement between the parameterization and the calibration validated the reconstruction procedure and the corrections described in Section 6.1. The parameterization showed that backgrounds consist of roughly equal parts of photons and charged particles. The findings also allowed us to conclude that the hit energy is a sufficient criterion to distinguish hits of photons from the ones of charged particles. This a feature might be used to separately measure beam-gas and Touschek backgrounds in the future.

7.3 Time resolved analysis of injection backgrounds

Having discussed regular beam backgrounds, we now move on to examining backgrounds measured during periods with injections. As explained in detail in Sections 3.3 and 3.4, when additional particles are injected into a circulating bunch, this bunch is perturbed, causing a drastically elevated particle loss rate. It is expected that detectors observe considerably higher background levels during transits of these bunches. Data taking during periods of injections is triggered by an external trigger signal send out by the injector linac. The transit times of the injection bunches are therefore fixed with respect to the start of the waveform and their signals occur at the same times in every event. The positron damping ring, which will be indispensable for low-emittance injections of positrons into the main ring, was not yet installed during Phase 1 data taking. It is thus expected that injection backgrounds in the LER are significantly higher than in the HER.

The injection bunches are generally accompanied by other regular bunches which also circulated in the rings. These bunches continuously undergo beam-gas and Touschek scattering, as discussed in the previous section. Compared to injection backgrounds, however, these regular beam backgrounds are negligible due to three reasons: firstly, the per bunch probability for a hit in the sensors is significantly smaller; secondly, hits originate almost exclusively from single particles; and, thirdly, they are not correlated in time in the same way as the injection backgrounds.

In this section, we perform a time resolved analysis of backgrounds measured during periods with injections. This analysis is an extended version of the one presented in Section 7.2 which also examines additional aspects specific to injection backgrounds. In Section 7.3.1, we first study the time structure of injection backgrounds before we focus on their hit energy spectra in Section 7.3.2. Here we also verify that radiation levels are safe for the installation of the inner detector in Phase 2. Subsequently, Section 7.3.3 demonstrates a method for quantifying deposited energies and decay behavior of injection backgrounds with respect to accelerator conditions. This method offers an effective way to develop a gating scheme for the future operation of Belle II. Finally, we briefly summarize the key findings from the time resolved analysis of injection backgrounds in Section 7.3.4.

7.3.1 Time structure

As for non-injection backgrounds, we begin by examining the time structure of backgrounds observed during injections. Due to the significant event-by-event fluctuations, the time evolution is again studied based on averaged time distributions. This section is

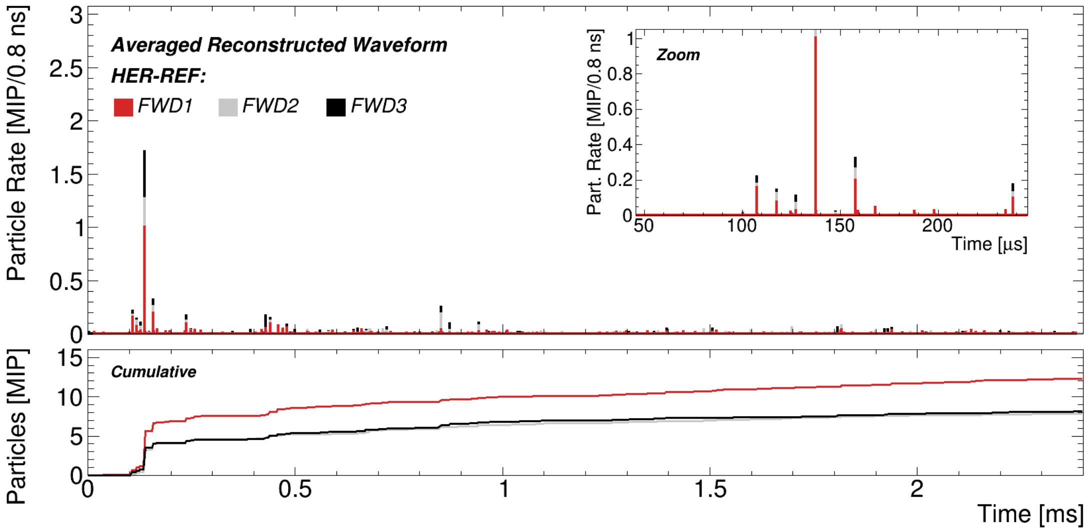

Figure 7.3: Background time distribution for the HER-REF data set for all three channels stacked on top of each other (*top*) and their cumulatives separately for each channel (*bottom*).

divided into three parts. The first part discusses the levels and the overall time structure of injection backgrounds. Here, we also motivate how the decay behavior of injection background is determined by the propagation of the newly injected particles along the beam lines of the accelerator and introduce a number of timing patterns observed in the time structure. As introduced in the previous section, bunches such as the injection bunch have a characteristic time in turn, t_{turn}. In the second part, we determine this t_{turn} for injection bunches of both rings and confirm the time resolution of the complete CLAWS systems based on data taken during runtime. We also describe how a cut on the t_{turn} can be used to separate energy deposits caused by the injection bunch from the ones of regular beam backgrounds. The trigger signal is send out by the injector linac in advance to the injection and, more importantly, the first transit of the injection bunch. We refer to this time difference as the trigger delay, T_{trg}. The objective of the third part is to determine the exact values of the T_{trg} for the HER and the LER.

HER background time distribution Since they reflect the nominal operation of the accelerator, we first examine the time structure of both reference data sets. Figure 7.3 shows the averaged reconstructed waveform for the HER-REF set for all three channels stacked on top of each other (*top*) and their cumulatives separately for each channel (*bottom*). We find several large peaks of significantly elevated background rates. These peaks are caused by the repeated transit of a single bunch which received new particles in a top-up injection. The distance between the peaks thus corresponds to multiples of the beam revolution period, T_{rev}; this is further highlighted in the zoom in the upper right corner. The first signals of the injection bunches are delayed with respect to the start of the waveform by a T_{trg} of around 107 µs. Across all data sets, we observe several slightly different values for T_{trg} which vary by less than 150 ns; these are determined later in this section. In general, the injection backgrounds are declining over time until they return to the levels of regular beam backgrounds and are mostly confined to the first 500 µs. The most striking aspect of the observed distribution is that they are not decreasing monotonically, or, in other words, constantly with every turn. Instead, the time structure is largely determined by the propagation of the newly injected particles along the beam lines and thus connected to properties of the accelerator. The decay behavior therefore can not be described analytically and has important implications for the development of a gating scheme for the operation of Belle II.

The background levels observed during transits of the injection bunch are significantly higher than the signals of regular beam backgrounds which are distributed uniformly over the whole waveform (see Section 7.2). In the cumulatives in Figure 7.3 (*bottom*) these large energy deposits appear as steps, whereas regular backgrounds are reflected by steady increases with moderate incline. Here, the total number of observed particles is driven by injection backgrounds and, due to the low beam currents in the reference data sets, contributions from Touschek and beam-gas play only a minor role. Note that, for example non-injection backgrounds recorded during vacuum scrubbing in NI-VACS (see Figure 7.1) surpass these by an order of magnitude. Injections primarily cause large instantaneous backgrounds which do not necessarily drive the overall level. As expected, FWD1 shows the largest overall background levels. The distributions for FWD2 and FWD3, on the other hand, are smaller and almost identical.

Observation of timing patterns In general, we find that three distinct timing patterns occur in the sequence of injection backgrounds: signals occurring every other turn resulting in a period of 2 turns (20 µs), from here on referred to as *on/off-pattern*; groups of signals recurring with a period of 9 to 11 turns (∼100 µs), from here on referred to as *long betatron pattern*; and groups of signals recurring with a period of 40 (HER) or 50 (LER) turns, from here on referred to as *synchrotron pattern.* To different extents, these timing patterns are observed across all injection data sets. We will demonstrate two methods for quantifying their frequencies from detector data in Chapter 8. Taken together, the patterns suggest that the time structure of injection backgrounds is strongly

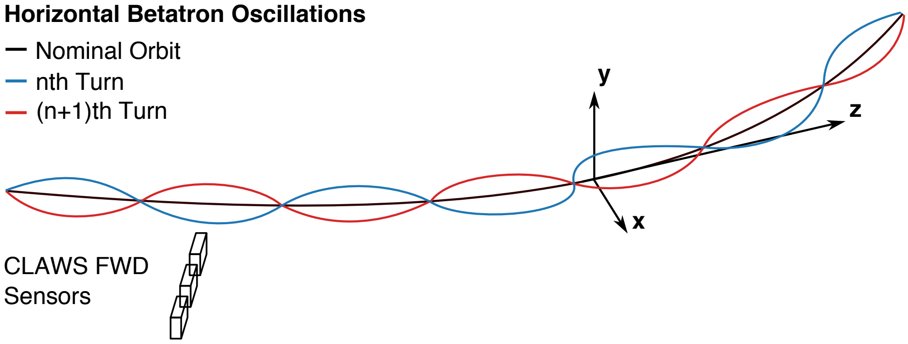

Figure 7.4: Illustration of the horizontal betatron oscillations of the beam particles relative to the position of the CLAWS FWD sensors.

affected by betatron and synchrotron oscillations performed by the newly injected beam particles.

As described in detail in Section 3.1, the trajectories of real beam particles differ from the nominal orbit defined by the lattice of the accelerator. For deviations transverse to the primary direction of motion, the particles perform stable horizontal and vertical betatron oscillations around the nominal orbit. Furthermore, SuperKEKB uses the betatron injection scheme in which new particles are deliberately injected with such a horizontal offset (see Section 3.3). Thus, in particular the newly injected particles undergo horizontal betatron oscillations with large amplitudes. Due to these injections and the fact that the CLAWS sensors are mounted in the horizontal plane, it can be assumed that vertical betatron oscillations do not affect the rate of backgrounds observed by the sensors. Horizontal oscillations, on the other hand, can explain two of the observed time patterns. Figure 7.4 illustrates the position of the beam particles which are undergoing such oscillations with respect to the CLAWS FWD sensors. Their trajectory is temporarily shifted from the nominal orbit, what effectively causes an asymmetry of the physical aperture. This increases the probability that beam particles collide with the accelerator beam pipe at positions of large amplitudes. If maxima in the amplitude of the oscillation coincide with the location of the sensors, the higher loss rate results in elevated background rates.

A tracking simulation of beam orbits in the HER, which was performed using the same machine parameters as applied during the reference injections, predicts horizontal and vertical betatron tunes of 45.53 and 43.57 oscillations per turn, respectively [42]. Depending on the conditions of the machine, however, the values of the tunes slightly deviate in practice. Since we observe the injection backgrounds from a fixed point and only once per turn, the integer part of the tune is of no relevance for the following discussion and will be disregarded. The fact that the betatron tune is approximately half-integer, on the other hand, can explain the observed 20 µs on/off-pattern. If in the nth turn the maximum is located at the sensors it will be shifted strongly to the side opposite of CLAWS in the $(n+1)$th transit and vice versa. A notable example of the on/off-pattern in Figure 7.3 are the signals of the fourth (∼137 µs), fifth (∼147 µs) and sixth (∼157 µs) transit. Here we observe two large signals separated by 20 µs which are interleaved by a transit without noticeable backgrounds. On closer inspection, the tune differs slightly from the half-integer value by 0.03 oscillations per turn. As mentioned earlier, the tune and thus this divergence depend in practice on the conditions of the accelerator. We attribute the long betatron pattern to this deviation of the tune from an half-integer value. Notable examples are the peaks at 137 µs and 237 µs which are around 100 µs, or ten turns, apart.

In addition to betatron oscillations, beam particles also undergo synchrotron oscillations, as again described in Section 3.1. Recall that synchrotron oscillations refer to oscillations parallel to the primary direction of motion which are caused by deviations in the energy of the beam particles. The difference in energy leads to an altered beam orbit period due to the deflection in the dipole magnets. Particles deviating in energy therefore also undergo transverse oscillations which affects the background rates observed by the sensors. Compared to betatron oscillations, synchrotron oscillations resolve on somewhat longer time scales with periods of several turns. For nominal accelerator parameters, beam orbit simulations for the HER for Phase 1 predict a period of 40.6 turns (409 µs) which in practice again varies by few turns [36, 42]. This is also reflected in the time distribution since peaks are roughly arranged in three groups separated by around 400 µs: one between 100 µs and 200 µs following the first transit of the injection bunch, one between 400 µs and 500 µs and one between 800 µs and 900 µs.

LER background time distribution Having discussed the time structure in the case of the HER, we now move on to nominal injections into the LER. Figure 7.5 shows the averaged reconstructed waveform for the LER-REF data set for all three channels stacked on top of each other (*top*) and their cumulatives separately for each channel (*bottom*). Similar to HER-REF, we observe several large peaks which are caused by the repeated transit of the injection bunch. The distances between these signals correspond again to multiples of the T_{rev}, what is particular evident in the zoom in the upper right corner. The time structure for LER-REF, however, is different from the one for HER-REF in a

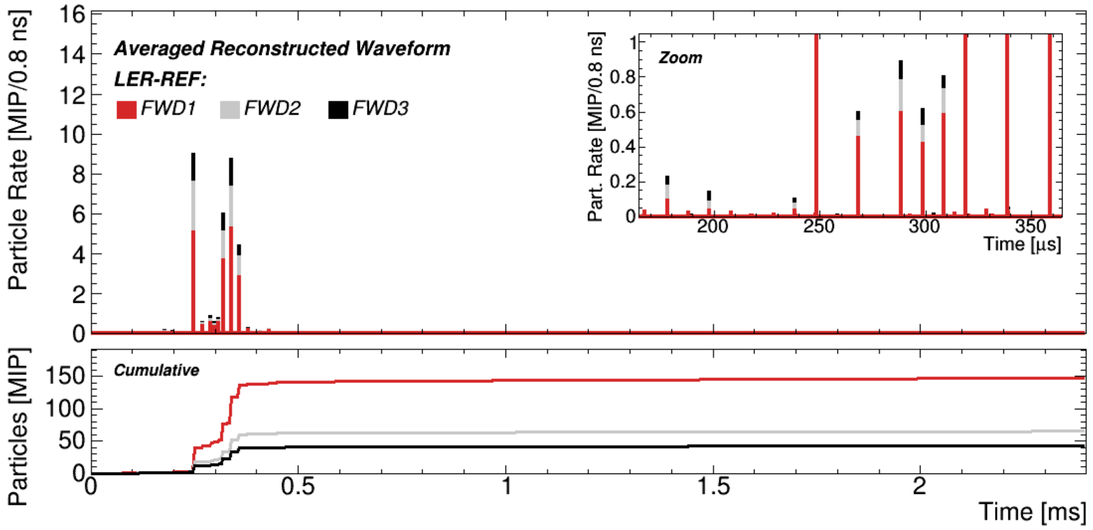

Figure 7.5: Background time distribution for the LER-REF data set for all three channels stacked on top of each other (*top*) and their cumulatives separately for each channel (*bottom*).

number of respects. The signals are considerably larger and much more concentrated in time. The T_{trg} for LER injections is approximately the same as for the HER, yet the first significant signals only appear $\sim$180 µs after the start of the recording (i.e. seven full turns after the first transit). And, instead of a single dominant peak there are four similar sized peaks, which surpass the rest of the waveform, and no significant energy deposits beyond 500 µs. The most likely explanation for this behavior is the absence of the damping ring for positrons which leads to higher loss rates and a faster merging of the newly injected particles. Shorter time patterns such as the on/off-pattern are therefore more pronounced in the LER, whereas longer patterns like synchrotron oscillations are less evident.

For nominal accelerator parameters, beam orbit simulations for the LER for Phase 1 predict horizontal and vertical betatron tunes of 44.53 and 46.57 oscillation per turn, as well as a synchrotron oscillation period of 52.3 turns (526 µs) [36, 42]. Again, these values somewhat diverge in practice. Note that the non-integer part of the betatron tunes is identical to the prediction for the HER. We observe multiple instances of the on/off-pattern, most clearly seen in the zoom where the distances between signals is mostly 20 µs. The distance between the two largest peaks corresponds to 90 µs which is a consequence of the long betatron pattern. For the LER-REF data set, however, we observe no conclusive evidence for synchrotron oscillations.

As explained earlier, the absence of the damping ring for positrons leads to larger injection backgrounds in the LER than in the HER. Instantaneous background levels here are as much as five times higher. The radial dependence, in contrast, is comparable to the one observed for HER injections: FWD1 is larger than FWD2 which is larger than FWD3. The background from regular circulating bunches is similar to the one observed in HER injection and non-injection events; it is uniformly distributed and the overall height is negligible compared to the signals from the injected bunch. The overall background levels in the cumulatives are dominated by injection backgrounds which appear as steps of large energy deposits. In that way, the total number of particles is an order of magnitude larger than in the HER and driven almost entirely by injection backgrounds.

The averaged reconstructed waveforms for the other injection data sets generally show a background time structure with similar features and overall background levels (see Appendix B.1).

HER Rate in turn As described in Section 7.2.2, the time in turn, t_{turn}, offers an effective way to examine time patterns which repeat every turn. The times at which we observe injection backgrounds are defined, firstly, by the T_{trg} which determines the time of the first transit and, secondly, by the T_{rev} which establishes the time between two consecutive transits. For a given data set, both of these quantities are fixed. As a consequence, signals caused by injection bunches have a characteristic t_{turn}, which distinguishes them from regular beam backgrounds.

Figure 7.6 (*left*) shows the averaged particle rate as a function of the t_{turn} for the HER-REF data set. We refer to this type of plot as the *rate in turn*. Here and in the following, all distributions of this type are normalized to the ratio of the length of the waveforms to T_{rev} (i.e. the number of turns) and to the number of events. The rate in turn is uniformly distributed over the whole range, except for a single large peak located at around 6.8 µs. This peak is caused by the superimposed signals of the injection bunch. Compared to the full time distribution shown earlier, the maximum particle rate decreases considerable since the rate in turn is averaged over all transits of the injection bunch of which only the earlier ones cause large energy deposits. The rest of the distribution shows only sporadic entries of comparable amplitude which are caused by regular beam backgrounds. These entries, however, are clearly limited by statistics due to the small number of events in the studied data set.

Figure 7.6 (*right*) shows a zoom into the region around the peak associated with the injection bunch for the same channel and data set. This peak is significant in at least three major respects: its width represents the time resolution achieved by the full CLAWS

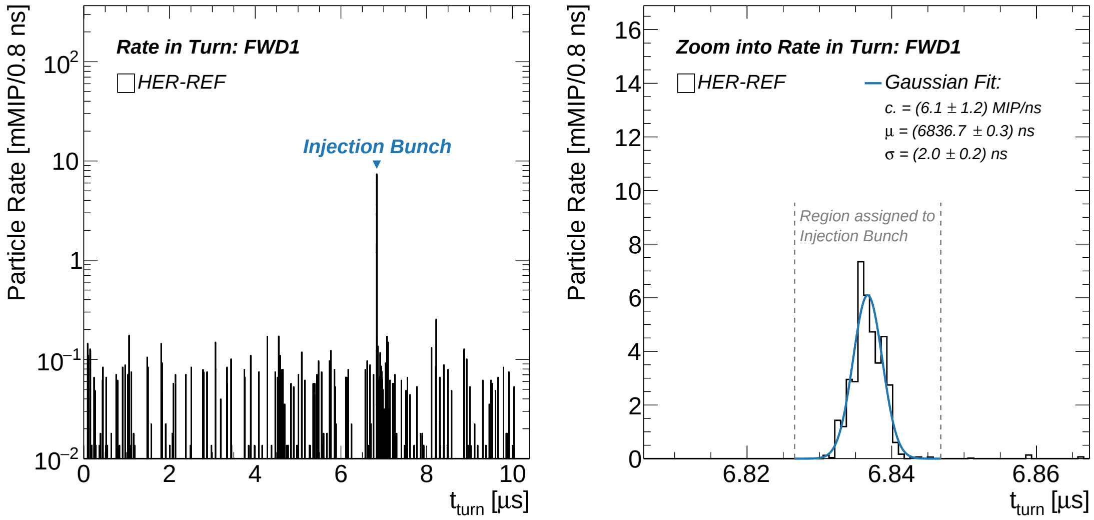

Figure 7.6: Averaged particle rate as a function of the time in turn for the HER-REF data set and channel FWD1 (*left*). Cutout highlighting the part associated with signals of the injection bunch (*right*). The distribution is normalized to the ratio of the length of the waveforms to T_{rev} (i.e. the number of turns) and to the number of events. Stated parameters and corresponding uncertainties are obtain by a maximum likelihood fit with a Gaussian.

setup; its form confirms that measurements are stable over several milliseconds; and its mean corresponds to the characteristic t_{turn} of the injection bunch. To determine the two quantities, we fit the peak with a Gaussian distribution.[7] For the time resolution for the given data set we find a value of (2.0 ± 0.2) ns. The time resolution obtained from muon measurements in the laboratory, discussed in Section 6.1.3, takes only the sensors and the data processing into account and does not consider uncertainties from the trigger system or the longer signal transmission. The width of the distribution obtained here, on the other hand, demonstrates the time resolution of the complete CLAWS system during data taking. The values for the time resolution obtained from all injection data sets and channels (see Appendix B.3) agree within the uncertainties and are approximately twice as large as for the laboratory measurements. A skewed distribution would indicate either a wrong value for the T_{rev} or a non-uniform sampling rate of the oscilloscope. A wider or non-Gaussian shaped peak, on the other hand, could be caused by fluctuations or jitter of the trigger signal. From the form and width, we conclude that our results are valid and that we can indeed measure backgrounds with the required nanosecond time

---

[7] We apply a two-stage maximum likelihood fit in the range of $\pm 5\,\sigma$ of the mean; uncertainties on the parameters are adopted from the fit.

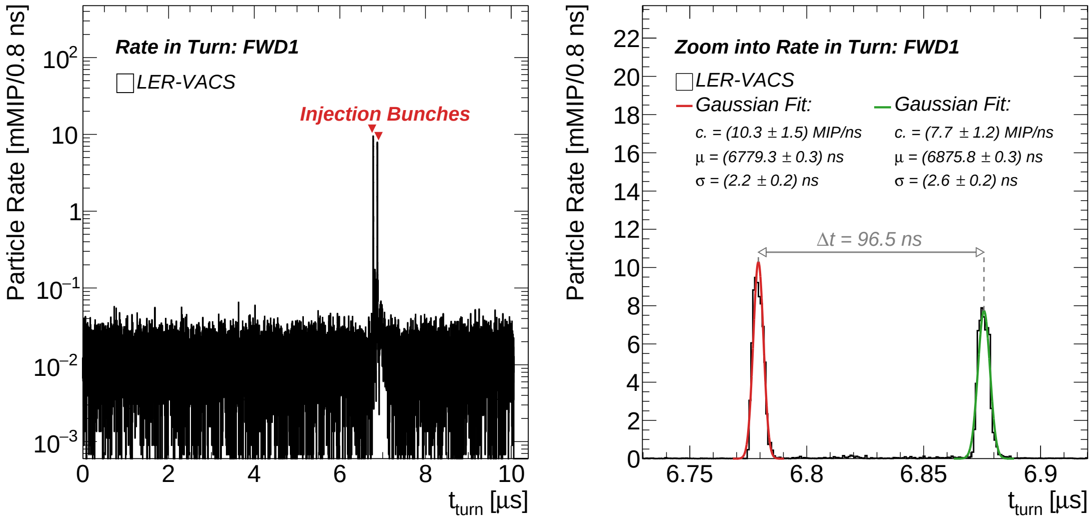

Figure 7.7: Averaged particle rate as a function of the time in turn for the LER-VACS data set for channel FWD1 (*left*). Cutout highlighting the part associated with signals of the injection bunches (*right*). The distribution is normalized to the ratio of the length of the waveforms to T_{rev} (i.e. the number of turns) and to the number of events. Stated parameters and corresponding uncertainties are obtain by maximum likelihood fits with Gaussians.

resolution over the full length of our waveforms.

For the t_{turn} for the given data set we find a value of (6836.7 ± 0.3) ns. Having determined the value which corresponds to the injection bunch, a dedicated timing cut in the t_{turn} can be used to separate injection and regular beam backgrounds. We classify all hits with a t_{turn} which lies within $\pm 5\,\sigma$ of the previously obtained mean as injection backgrounds. This width is somewhat arbitrarily chosen since the probability of having a hit due to an ordinary circulating bunch within two or more additional σ is small (see Table 7.2). It must only ensure that it covers all deposits by the injection bunch.

LER rate in turn As mentioned earlier, for a given data set the characteristic t_{turn} is defined by T_{rev} and T_{trg}. The former is of course dictated by the circumference of the rings and, in that way, constant. The latter, on the other hand, depends on the injection settings of the accelerator and varies between data sets. It has to be determined individually for each setting. This is particularly evident in the case of double bunch injections into the LER where we observe different values for the time in turn for each of the two bunches.

Figure 7.7 (*left*) shows the averaged particle rate as a function of the t_{turn} for the LER-

VACS data set. Signals of regular beam backgrounds are again distributed uniformly over the whole range. Instead of a single peak, we find two distinct peaks located in close proximity to each other. These are caused by the two bunches which received new particles in an injection. The section with the peaks is illustrated in more detail in Figure 7.7 (*right*). Fits, analogous to the one for HER-REF, are applied to both peaks. They yield time resolutions of (2.2 ± 0.2) ns and (2.6 ± 0.2) ns, which agree within the uncertainties with each other and with the previously obtained value. Again we observe no skewness or non-Gaussian shape. Apart from that, the peak-to-peak distance of the two bunches is (96.5 ± 0.4) ns agreeing with the expected value of 96.3 ns (49 RF buckets).[8]

In principle, delayed photons, which are caused by afterpulsing or late light emission, can exceed the integration window and lead to additional signals correlated with the initial energy deposits (see Section 6.1.2). Such signals would especially be caused by the large injection backgrounds in the LER and occur as additional broader peaks, which are located 76.8 ns (the length of the integration window) and more after the initial peaks. While the rate in turn shows few of such hits, their overall number is small and we conclude that afterpulsing and late light emission can be neglected.

The t_{turn} allows to separate not only injection bunches from regular beam bunches, but also the contributions of the two bunches. In the following we distinguish between three different cuts: only hits of the first or second injection bunch indicated by indexes *ib1* or *ib2*, respectively, or hits of both injection bunches, indicated by an index *ib*. Note that for single bunch injections *ib1* and *ib* are equivalent.

Trigger delay In the future, gating of the PXD will be triggered by the same injection trigger signal as used by CLAWS. To be able to adapt the start of the gating window to the first transit of the injection bunch, the trigger delay, T_{trg}, has to be established. We determine the delay between the arrival of the signal and the transit with two complementary methods: extracting it directly from the averaged reconstructed waveform and calculating it from the T_{rev} and the t_{turn} associated with the injection bunch. In the first method, we fit the peak of the first transit of the injection bunch with a Gaussian distribution and extract the mean. Due to the complex time structure of injection backgrounds, however, the probability to observe a signal already with the first transit is small. Data sets with only a hundred events or less typically make a precise determination challenging. This particularly hampers the determination of T_{trg} for injections into the

---

[8] The distance is calculated by the difference of the two mean values; uncertainties are obtained by quadratic addition of the individual components.

LER.

Alternatively, the T_{trg} can also be calculated from the T_{rev} and the t_{turn} of the injection bunch:

$$T_{trg} = n \cdot T_{rev} + t_{turn}, \tag{7.1}$$

where n is an integer which is determined by the first approach. Due to the larger statistics, the results we obtain from the second method are more precise and reliable and the method is applicable to all injection data sets. Findings stated in the following are obtained by this approach.

For both rings and all data sets we find that $n = 10$. Depending on the particular injection settings of the accelerator, the exact values for T_{trg} varied by few nanoseconds during runtime. The data sets HER-ALL and LER-ALL are the supersets of all other data sets and contain all events for a respective ring taken during Phase 1. Here, the different T_{trg} appear as independent peaks in the averaged reconstructed waveform and the rate in turn. For the HER, we find three different values for T_{trg} which are approximately 10 ns apart: $(107\,429.3 \pm 0.8)$ ns, $(107\,438.4 \pm 0.6)$ ns and $(107\,451.3 \pm 1.0)$ ns.[9] For injections into the LER, we find two different values for the first bunch: $(107\,371.8 \pm 1.2)$ ns and $(107\,393.9 \pm 0.4)$ ns. In addition, we also obtain two different values for the second bunch: $(107\,468.2 \pm 1.2)$ ns and $(107\,490.6 \pm 0.5)$ ns. An implication of the variation in the values of T_{trg} is that the t_{turn} for the injection bunches and the corresponding timing cuts varies in the same way. For all data sets except HER-ALL and LER-ALL, the t_{turn} is constant across all events of the respective data set and the values can be determined individually for each of them. HER-ALL and LER-ALL, on the other hand, consist of events taken with different injection settings. For these data sets, we apply t_{turn} cuts which included hits in any one of the signal regions associated with the injection bunches.

7.3.2 Background composition

Having discussed the time structure of injection backgrounds, we now move on to studying their particle composition. This section begins by examining the hit energy spectra of backgrounds recorded during injections. These spectra are used to establish the maximum background levels observed during Phase 1 and to confirm that radiation levels are safe for the installation of the inner detector of Belle II in Phase 2. In the second part of this section we then scrutinize the time resolved hit energy spectrum of these backgrounds.

---

[9] For these results and the ones stated in the following uncertainties are given by the uncertainties on t_{turn} since T_{rev} and n are assumed to be exactly known.

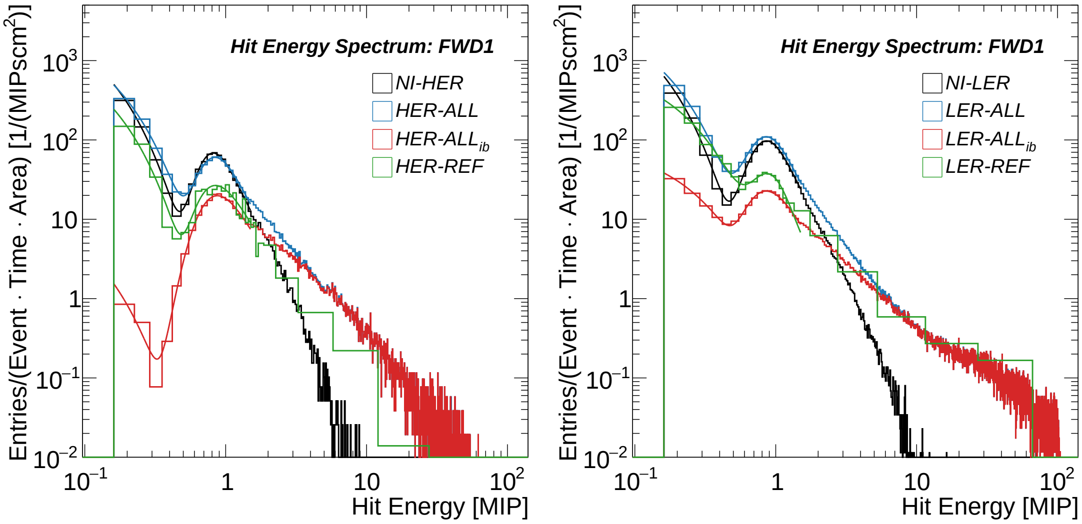

Figure 7.8: Distributions of hit energies for the given HER (*left*) and LER (*right*) injection data sets for channel FWD1. The distributions are normalized to the length of the waveforms, the area of the sensors and the number of events. For the HER-REF and LER-REF data sets, the bin size for higher energies is logarithmic due to limited statistics.

HER background composition Figure 7.8 (*left*) compares the hit energy spectra of different HER injection data sets to the corresponding non-injection data set NI-HER (see Section 7.2.2). For HER-ALL, the figure also shows the distribution of hits caused only by the injection bunch selected by a cut on the t_{turn}, as described in the previous section. We refer to this subset as HER-ALL$_{\mathrm{ib}}$. For HER-REF, we use logarithmic bin sizes for higher energies due to the small number of hits in this range. All four distributions are normalized to the length of the waveforms, the area of the sensors and the number of events such that their integral represents the particle flux through the CLAWS sensors.

For hit energies up to 2 MIP, the shape of the distributions for NI-ALL, HER-ALL and HER-REF are comparable. This suggests that hits are caused by similar proportions of photons and charged particles which are generated by beam-gas or Touschek scattering of regular circulating bunches (see Section 7.2.2). The reduced number of hits of HER-REF can thus be explained by the notable lower beam current during the recording of the data set (1 mA to 150 mA). Injection backgrounds are expected to be caused primarily by charged particles with only minor contributions from photons. As such, the pure injection background data set, HER-ALL$_{\mathrm{ib}}$, reveals a notably different spectrum with a distinct Langaus peak and a negligible photon component. The reduced overall number of hits of this set can be attributed to the fact that it only includes hits caused by one of the 1576 bunches. Nevertheless, it contributes around 10% of the charged particle backgrounds we observe.

At energies of approximately 2 MIP, the distributions for NI-HER and HER-ALL are beginning to diverge. From here on it is more likely for hits to be caused by injection backgrounds than by beam-gas or Touschek scattering. The distribution for NI-HER shows a power law behavior with a steady decrease which is cutting off at around 10 MIP. The distribution for HER-ALL is following a similar power law, but its decline is less steep and it reaches considerably higher energies of 62 MIP. While HER-REF shows less hits at lower energies, it almost matches the shape of the other injection data sets for higher energies. The most striking result to emerge from the data, however, is that HER-ALL$_{\mathrm{ib}}$ is rapidly merging with HER-ALL and that the two distributions are almost identical for energies above 3 MIP. It can therefore be assumed that large instantaneous background levels are caused exclusively by injection backgrounds.

For the channels FWD2 and FWD3 and other HER injection data sets, we find similar distributions which lead to the same results (see Appendix B.2). In general, the overall number of hits decreases with the distance from the beams (FWD1 $>$ FWD2 $>$ FWD3).

LER background composition In analogy to the distributions for the HER, Figure 7.8 (*right*) compares the hit energy spectra of different LER data sets. Note that LER-ALL partly consists of events with double bunch injections and that LER-ALL$_{\mathrm{ib}}$ covers the contributions of both bunches. The distributions are normalized in the same way as for the HER. For hit energies up to 2 MIP, the shape and the magnitude of the hit energy spectra for the LER are comparable to the ones for the HER with two exceptions. Firstly, we observe an increased rate of photon hits for LER-REF. Since this data set was recorded over a rather short period of less than 30 minutes, possible explanations for this finding are irregularities in the partial pressures at the IP or sudden desorptions of gas molecules leading to an increased rate of beam-gas scattering. Secondly, the photon contribution for LER-ALL$_{\mathrm{ib}}$ is considerably smaller than in the other LER data sets. These differences, however, are not as large as the ones observed between HER-ALL and HER-ALL$_{\mathrm{ib}}$. It is unclear what causes this effect, but it might be related to the fact that the LER partly uses double bunch injections and that the timing cuts for the LER-ALL data set are notably wider.

Again, distributions are beginning to diverge at approximately 2 MIP where injection backgrounds become dominant. For higher energies, all distributions show the expected power law behavior. For injection data sets, however, we observe a small ankle at around

10 MIP for which the slope of the decline becomes slightly larger. The spectra are cutting off at 112 MIP where CLAWS reaches the end of its dynamic range.

We find signs for saturation effects which are connected to this endpoint of the dynamic range. For energies above 100 MIP, the distributions show a small number of additional hits which form a Gaussian on top of the power law and are caused by backgrounds which exceed the dynamic range. For LER-PS, the data set with the largest overall background levels, this effect is more pronounced but still small. Due to the power law behavior of the spectra we generally assume that the end of our dynamic range approximately matches the largest signal amplitudes observed and that the impact of these saturation effects are negligible. We thus do not apply any type of saturation correction for the analysis of Phase 1 data. Again, the overall number of particles decreases with distance from the beams (FWD1>FWD2>FWD3).

Across all injection data sets, we observe significantly larger instantaneous background levels during transits of the injection bunch. During the first turns theses backgrounds are so high that the assumption that hits are caused by single particles is no longer valid and that the setup is on the verge of saturation. On the other hand, the setup is capable of still resolving energies which are deposited by single photons. These findings confirm that the dynamic range of CLAWS was optimally exploited. The highest instantaneous background levels we observed during Phase 1 do not exceed the levels of regular beam backgrounds by more than an order of magnitude. As such, they are two orders of magnitude below the occupancy limit for the PXD. Based on the backgrounds observed by CLAWS during the first commissioning phase, it can therefore be assumed that the radiation levels are safe for the installation of Belle II in the second commissioning phase.

Time resolved hit energy distribution Figure 7.9 (*left*) shows the distribution of hits for the time in turn versus the hit energy for the HER-ALL data set. In comparison with the equivalent distribution for the NI-All data set discussed in the previous section (see Figure 7.2 (*right*)), we observe a distinct line of hits which all have the same t_{turn} and are caused by the repeated transit of the injection bunches. Here, two findings stand out. First, the rate of charged particles for energies up to 2 MIP is significantly larger at the distinct line than for the surrounding regular beam backgrounds. And, second, hit energies above 2 MIP can be attributed almost exclusively to injection backgrounds. These observations are expected from the hit energy spectra discussed previously. By contrast, all hits with a t_{turn} not related to the injection bunch are following a distribution comparable to the one found for the non-injection data sets, such as NI-ALL.

With respect to injections into the LER, Figure 7.9 (*right*) provides the distribution

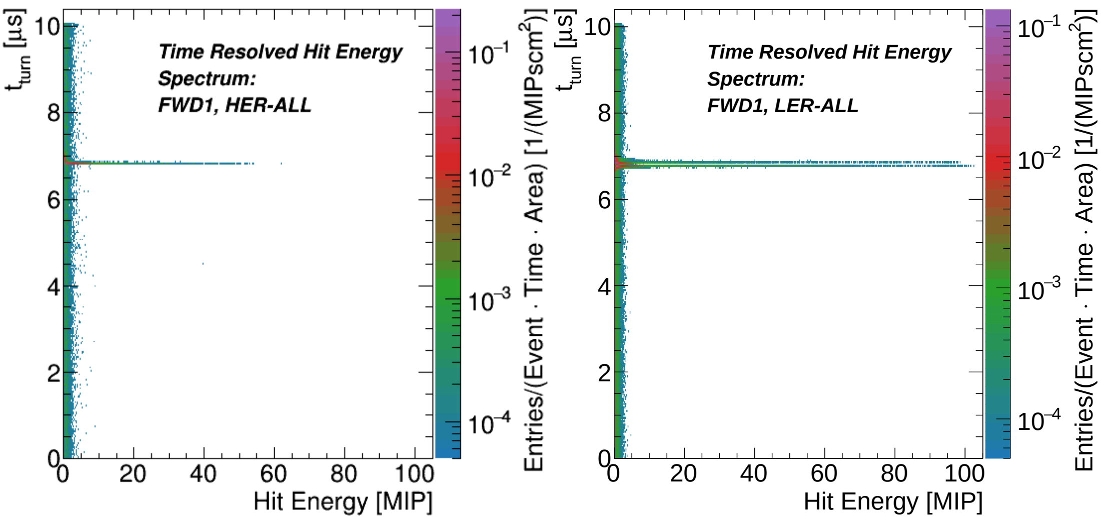

Figure 7.9: The distributions of hits for the time in turn, t_{turn}, versus the hit energy for HER-ALL (*left*) and LER-ALL (*right*) for channel FWD1. Both distributions are normalized to the length of the waveforms, the area of the sensors and the number of events.

of hits for the t_{turn} versus the hit energy for the LER-ALL data set. The distribution shows the same characteristics as the one for HER-ALL with two differences. Instead of a single line, we here observe two lines, each of which is caused by one of the injection bunches. There is no significant difference between the hits of the two bunches. The maximum hit energies for LER injections, however, are surpassing the ones for HER injections significantly, as already discussed previously.

FWD2 and FWD3 show comparable distributions with a reduced overall number of hits which reflects their positions (see Appendix B.2). All findings are in agreement with previous results and further validate the insights which have been acquired so far.

7.3.3 Injection background decay behavior

The purpose of this section is to demonstrate a method for quantifying deposited energies and decay behavior of injection backgrounds with respect to accelerator conditions. As discussed in the previous two sections, three main features of injection backgrounds are: the time evolution does not follow a well defined functional form; the background levels and the time structures fluctuate substantially between individual events of a data set; and the background levels and the time structures also fluctuate substantially for different accelerator conditions represented by the different data sets.

Since they can not be described analytically, we instead propose to characterize the behavior of injection backgrounds based on the following quantities: the total energy deposited in a single event, including regular beam backgrounds, E; the energy deposited only by the injection bunch or bunch energy, E_{ib}, which is selected by a cut on the t_{turn} (see Section 7.3.1); their ratios, E_{ib}/E; the proportion of the energy of the injection bunch which is deposited within 500 µs after the first transit, [10] $E_{ib}(t < 500\,\mu\text{s})/E_{ib}$; and the time of the last transit in which the E_{ib} per transit was larger than 2 MIP, $t(E_{ib} > 2\ \text{MIP})$. Here, E_{ib} of the first and, in case of double bunch injections, the second injection bunch are listed separately. Because of the large fluctuations, the quantities are determined independently for each event. For the HER-ALL and LER-ALL data sets, the large number of events allows to determine meaningful distributions of the quantities. For all other sets, the quantities are stated only by the sample mean and the corresponding sample standard deviation. The values obtained for the quantities for all injection data sets are summarized in Table 7.3. In the following, we introduce the quantities based on the distributions before we then discuss the findings for all data sets.

Overall energy proportions We first focus on the overall backgrounds and the fraction of the energies deposited by the injection bunch. Absolute (E_{ib}) and relative bunch energies (E_{ib}/E) can be used to assess the impact of injection backgrounds on a subsystem and motivate a need for a gating scheme.

As expected, the values obtained for the E for LER-ALL are considerably larger than the ones for HER-ALL. Comparing the E_{ib} with the E suggests that for HER-ALL the majority of the observed backgrounds is caused by the injection bunch. As a superset of LER-VACS and others, LER-ALL also partly consists of double bunch injections. Note that E_{ib2} is an average which is calculated from single and double bunch injection events and therefore only has a limited significance. Nonetheless, also the sum of E_{ib1} and E_{ib2} for LER-ALL suggests that the majority of backgrounds is caused by injections.

The proportions of injection backgrounds are further clarified by turning to the fraction of E_{ib}/E shown in Figure 7.10 (*left*). The peaks at zero are attributed to events in which the injection bunch did not cause a hit during any of its transits. There are several possible explanations for these peaks. The particle losses might be so sever that they completely take place before the first transit, or they might be located entirely at locations other than the IP. They could also be caused by events which are falsely classified as injection

---

[10] We use this range since the time structure shows that injection backgrounds are mostly confined to the first 500 µs.

Table 7.3: Key quantities summarizing injection background energy levels and decay behavior for all injection data sets for channel FWD1.

Data Set	E	E_{ib}		E_{ib}/E		$E_{ib}(t < 0.5\,\mathrm{ms})/E_{ib}$		$t(E_{ib} < 2\,\mathrm{MIP})$	
		$1st$	$2nd$	$1st$	$2nd$	$1st$	$2nd$	$1st$	$2nd$
	[MIP]	[MIP]	[MIP]	[%]	[%]	[%]	[%]	[µs]	[µs]
HER-ALL	56 ± 58	40 ± 58		48 ± 37		56 ± 34		750 ± 808	
LER-ALL	161 ± 116	86 ± 81	42 ± 68	46 ± 34	19 ± 22	92 ± 18	90 ± 21	430 ± 358	287 ± 416
LER-VACS	71 ± 73	17 ± 36	15 ± 38	15 ± 21	10 ± 17	84 ± 31	84 ± 32	131 ± 242	109 ± 255
HER-REF	12 ± 8	9 ± 6		73 ± 21		71 ± 29		266 ± 424	
HER-PS	59 ± 17	33 ± 14		55 ± 14		70 ± 20		801 ± 542	
HER-VS1	21 ± 10	6 ± 7		24 ± 22		67 ± 35		191 ± 348	
HER-VS2	32 ± 11	10 ± 8		27 ± 18		60 ± 37		172 ± 252	
LER-REF	147 ± 23	133 ± 20		90 ± 7		99.6 ± 0.8		412 ± 93	
LER-PS	248 ± 60	221 ± 52		89 ± 5		98 ± 1		605 ± 186	
LER-VS	184 ± 25	163 ± 23		88 ± 8		98 ± 10		456 ± 123	
LER-SA	186 ± 15	156 ± 13		84 ± 3		97 ± 2		595 ± 179	

events in the event selection (see *BG* in Section 7.1). The ratios for HER-ALL are distributed approximately uniformly except for a rise and a subsequent peak at values above 0.9. The ratios for LER-ALL, on the other hand, show distinct peaks at around 0.1, 0.45 and 0.95. The first two peaks are caused by double bunch injections in which only parts of the energy are deposited by the first bunch. Ratios for the sum of the energies of both injection bunches for the same data set show a distribution similar to the one for HER-ALL. The peaks around 0.95 in both sets are caused by events with low regular beam backgrounds and/or large injection backgrounds.

Injection background decay time Having scrutinized the proportion of injection backgrounds in the overall backgrounds, we now focus exclusively on the former. The fraction of the energy of the injection bunch which is deposited within a given time interval can be used to determine the optimal length of gating windows and assess the potential impact of an insufficient extension of these windows. Figure 7.10 (*right*) compares the fraction of $E_{ib}(t < 500\,\mu\mathrm{s})$ for the HER-ALL and LER-ALL data sets. Both sets again show a large number of events in which the injection bunch did not cause any hits within the first 500 µs. Neglecting the boundaries, the distribution for

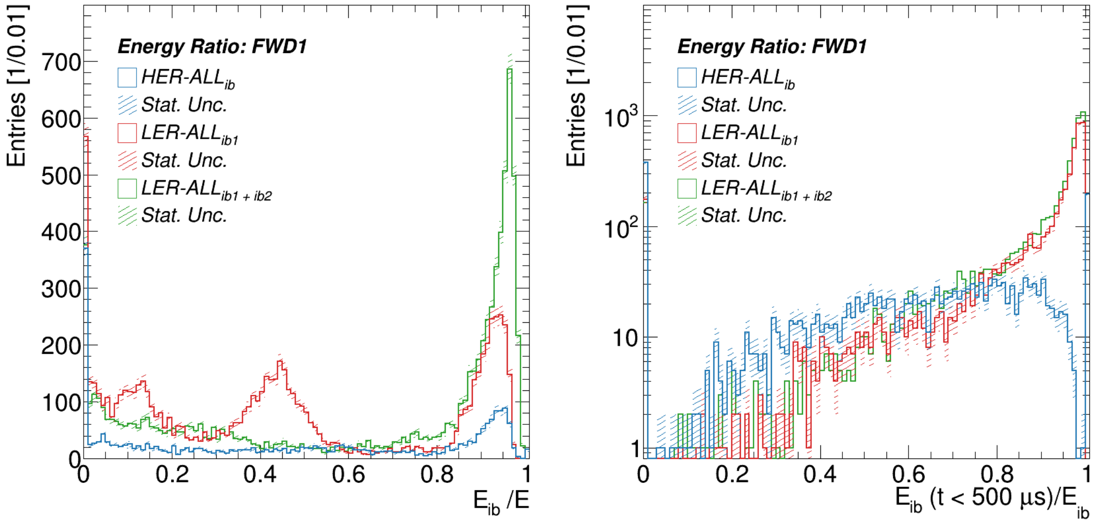

Figure 7.10: Distributions of ratios of energy deposited only by the injected bunch, E_{ib}, to the total energy, E, for channel FWD1 (*left*). Distributions of ratios of energy deposited by the injected bunch within the first 500 µs after the first transit, $E_{ib}(t < 0.5\,\mu\text{s})$, to the full bunch energy, E_{ib} for channel FWD1 (*right*).

the HER-ALL set is somewhat uniformly distributed with a skewness to larger ratios. This clearly shows that injection background in the HER is only partially confined to the first 500 µs. Both distributions for the LER-ALL set, on the other hand, are peaking at one and steeply decline to smaller ratios. Injection backgrounds in the LER are thus decaying faster and are mostly confined to the fist 50 turns.

Time of the last hit As an input for the determination of the time interval after which gating of the subsystems can be suspended, we establish the time of the last transit in which the energy deposited by the injection bunch is above a certain predefined limit. In general, this limit can be adapted to the requirements of the respective subsystem such as limits on the occupancy in the PXD. For the analysis of Phase 1 data, however, 2 MIP are chosen as a limit since it is the energy at which the hit energy spectra of injection and non-injection backgrounds begin to diverge (see previous section). Thus, the $t(E_{ib} < 2\,\text{MIP})$ indicates the time after which injection backgrounds are comparable to regular beam backgrounds. In principle, it is possible that a hit, which is recorded during a transit and exceeds the limit, is caused by regular beam backgrounds and not by injection backgrounds. The hit energy spectra for non-injection backgrounds, however, suggest that such a hit occurs in less than 1.1% of the events.

Figure 7.11 shows the distributions of the time of the last transit for the HER-ALL (*left*)

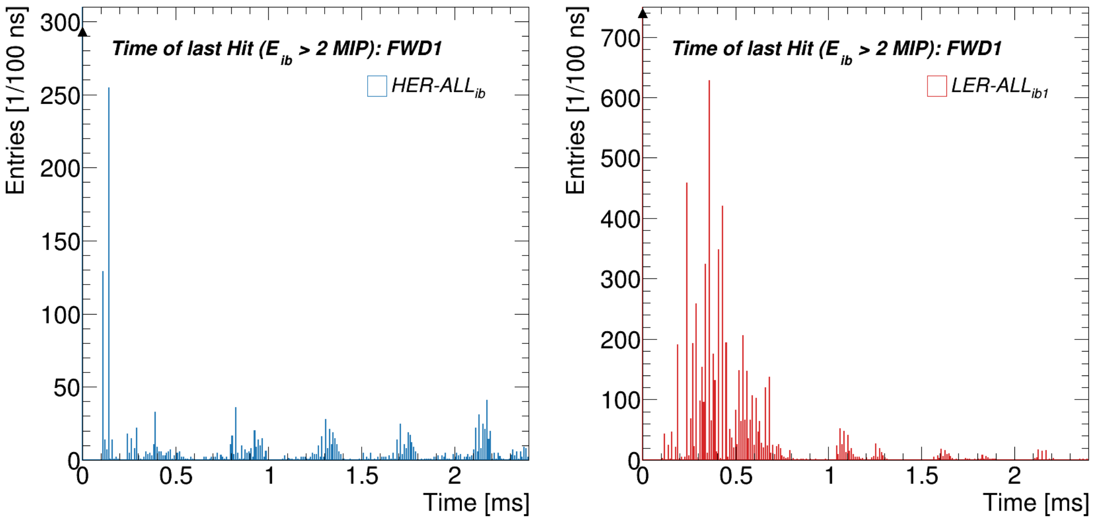

Figure 7.11: Distributions of the time of the last transit in which the energy per transit was larger than 2 MIP for channel FWD1 for HER-ALL (*left*) and LER-ALL (*right*).

and LER-ALL (*right*) data sets. The peaks at zero in both distributions are attributed to events in which no transit with energies above the limit occurred. The two largest peaks for the HER-ALL set are located directly at the first and fourth transit of the injected bunch. Apart from that, the distribution is stretching across the full 2.4 ms with periodically repeating patterns attributed to the synchrotron oscillations of the beam particles. This indicates that the timescale of injection backgrounds in the HER are fluctuating strongly between events and that in a significant fraction of the events a full decay requires at least 2.4 ms. For the LER-ALL set, on the other hand, in the majority of the events the decay is taking place entirely within the first 700 µs after the first transit. In a small number of events, however, injection backgrounds are also long lasting, showing influences of synchrotron oscillations. Analogous distributions which only consider hits caused by the second bunch or hits caused by any of the two bunches are similar to the ones shown here.

In general, observations for the time of the last hit are in agreement with the findings from the fractions of $E_{ib}(t < 500\,\mu\text{s})$.

Overall results and injection studies Finally, we can compare the quantities obtained for all injection data sets (see Table 7.3), especially the ones which are part of the dedicated injection studies. The values determined for the overall background, E, range from 12 to 248 MIP, with LER data sets showing significantly higher energies than

HER sets. The corresponding spread, however, indicates large event-by-event fluctuations across all data sets, which reach up to 100% of the total energy. In all data sets, injections account for a major part of these overall backgrounds. This is for example evident in the case of HER-ALL where the ratios of E_{ib}/E suggest equal shares of both kinds of backgrounds. In contrast to LER-ALL, LER-VACS consists entirely of double bunch injection events. As a consequence of the vacuum scrubbing and the associated large regular beam backgrounds, the fractions of injection backgrounds here drop to around 15% and 10% for the first and the second bunch, respectively. Due to the insignificant differences between the two bunches in LER-VACS, we conclude that there is no inequality between the behavior of bunches in double bunch injections.

For all data sets of the dedicated injection studies, the beam currents and thus the regular beam backgrounds are relatively low. For three of the four HER sets of the study, injection and regular beam background levels are similar and small. HER-PS, on the other hand, shows levels for both types of backgrounds which are comparable to HER-ALL. The ratios of E_{ib}/E for all four sets are subject to fluctuations and vary between 24% and 73% which reflects the different levels of injection backgrounds for the different injection settings. By contrast, the four LER injection study sets clearly show overall background levels comparable or exceeding the ones for LER-ALL and are dominated by injection backgrounds. This can be seen in the ratios of E_{ib}/E, where the sets show values of 84% and above.

Across all injection study data sets, the proportion of E_{ib} which is deposited within the first 500 µs is relatively stable for a respective ring. As mentioned earlier, injection backgrounds in the LER tend to be more localized and show larger fractions of E_{ib}/E. Compared to the reference injections, in both rings variations in the phase shift (as given by HER-PS and LER-PS) are found to have the largest impact on the injection backgrounds. For HER-PS and LER-PS, the bunch energies are significantly larger than in the other sets for the respective ring. A larger overall background level also increases the probability for later hits which are above the predefined 2 MIP limit. As a consequence, the $t(E_{ib} < 2\,\mathrm{MIP})$ for these two sets is also longer what implies that gating windows need to be larger and therefore have a higher impact on the integrated luminosity.

We observe no significant increase in the energy levels or decay times for variations in the vertical steering (HER-VS1, HER-VS2 and LER-VS). A possible explanation for this finding may be related to the nature of the betatron injections. A variation of the septum angle in the LER shows no increases in the overall energy level but extends the $t(E_{ib} < 2\,\mathrm{MIP})$. This suggests that the septum angle has a limited impact on the layout of a gating scheme.

7.3.4 Summary and key findings

In this section, we presented a time resolved analysis of injection backgrounds in which we studied their time structure, their background composition and their decay behavior. The averaged time distributions observed during injection periods clearly showed peaks of significantly elevated background rates which we associated with the recurring transits of the injection bunches. The time structure of these injection backgrounds suggested that their evolution is determined by the propagation of the newly injected particles along the beam lines of the rings, which is affected by several different recurring timing patterns connected to properties of the accelerator. We also used the time structure to demonstrate the time resolution of the complete CLAWS systems based on data taken during runtime and to determine the delay between the arrival of a dedicated injection trigger signal and the first transit of the injection bunch. For the time resolution, we obtained consistent values of around 2 ns. The precise knowledge of this trigger delay is required to adapt the start of the gating window in the PXD of Belle II to the first transit.

Comparing the hit energy distributions of regular and injection backgrounds showed that hits with energies below 2 MIP are mainly caused by regular backgrounds while hits with higher energies predominantly originate from injection backgrounds. The highest instantaneous background levels observed during injections in Phase 1 did not exceed regular beam backgrounds by more than an order of magnitude and fell short of the occupancy limit of the PXD by two orders of magnitude. In that way, backgrounds observed by CLAWS confirmed that the radiation levels were safe for the installation of Belle II in the second commissioning phase in 2018.

We also introduced a method which uses dedicated timing cuts to separate regular and injection backgrounds. In order to characterize the deposited energies and the decay behavior of injection backgrounds, we introduced different quantities which we determined on an event-by-event basis utilizing these timing cuts. In general, injection backgrounds accounted for a significant part of the overall backgrounds. During regular operation (i.e. HER-ALL and LER-ALL), for example, backgrounds caused by the single injection bunch were responsible for around half of the total observed backgrounds. We also found that LER injections result in higher backgrounds than HER injections, which can be explained by the lack of the positron damping ring in Phase 1. For both rings, the majority of the Injection backgrounds were typically observed within the first 500 µs after the injection. Individual decay times, however, were fluctuating strongly on an event-by-event basis and depended on the exact injection parameters used, in particular the phase shift. These quantities offer an effective way to develop a gating scheme for the future operation of Belle II.

Chapter 8

Fast varying backgrounds as a probe for machine timing patterns

Gating reduces the impact of injection backgrounds on the integrated luminosity considerably. Nevertheless, in the PXD it requires at least 2 µs during every transit of the injection bunch (see Section 4.1.1) and therefore reduces data taking by as much as 20% while injection backgrounds are cooling down. Adapting gating times precisely to the time structure of injection backgrounds, potentially even on an event-by-event basis, could further improve data taking efficiency. As discussed in Section 7.3, injection background is not decaying monotonically and its time evolution can not be described analytically. Instead, its time structure is largely determined by the propagation of the newly injected particles along the beam lines of the rings, which is affected by several different recurring timing patterns connected to properties of the accelerator. Since signal rates are significantly larger during transits of the injection bunch, it can be considered as a quasi-sole bunch or, in another way, as a probe for the study of timing patterns which determine the propagation of the beam particles.

In this chapter, we describe a program of measurements of the timing patterns which we found to affect the propagation of the beam particles, in particular of the injected bunch (see Section 7.3.1). The presented findings are obtained by two largely complementary analyses. Both analyses build on the time distribution of injection backgrounds, as given by the averaged reconstruct waveforms introduced in Section 6.2, and examine the same data sets as the analysis presented in the previous chapter and described in Section 7.1. Again the findings are discussed based on the results for the innermost channel, FWD1,

which offers the highest signal rates; corresponding figures for the channels FWD2 and FWD3 can generally be found in Appendix C.
In Section 8.1, we first describe an analysis based on the weighted time distance between two signals which examines the following timing patterns: the distance between bunches in double bunch injections; the beam revolution period, T_{rev}; the on/off-pattern; the long betatron pattern; and synchrotron oscillations. In Section 8.2, we then discuss an analysis of the frequency components based on a Fourier transform of the waveforms. This analysis focuses on the following timing patterns: the time distance between two consecutive bunches (the bunch spacing); the distance between bunches in double bunch injections; the beam revolution period, T_{rev}; the on/off-pattern and the long betatron pattern. Finally, we briefly summarize the key findings from these analyses in Section 8.3. Together the presented results provide important insights into the dynamics of beam particles and can be used to validate SAD simulations [76] for the future operation of SuperKEKB with first experimental results.

8.1 Weighted peak distance analysis

We first present an analysis of timing patterns based on the weighted distance between peaks, from here on also referred to as *PEAK analysis*. This type of analysis offers an effective way to determine the intervals in which large backgrounds recur. This section begins by introducing the analysis methodology before it will then go on to presenting experimental results for different timing patterns.

Analysis methodology To promote distances in time that represent prominent patterns, we weight every distance by the product of the corresponding signal amplitudes. The distance between two samples d_{ij} can be calculated simply by

$$d_{ij} = t_j - t_i,$$

where i and j are the indices of the respective samples and $t_{i,j}$ denote the corresponding times. The distances are then multiplied by the corresponding weight, w_{ij}, which is given by

$$w_{ij} = rate_i \cdot rate_j,$$

where $rate_{i,j}$ are the background particle rates for the respective samples ($\widehat{=}\ \overline{E_{i,j}^{hit}}$, see Section 6.2) Note that the index i runs from 1 to $N_{samples}$, whereas j runs only from $i+1$

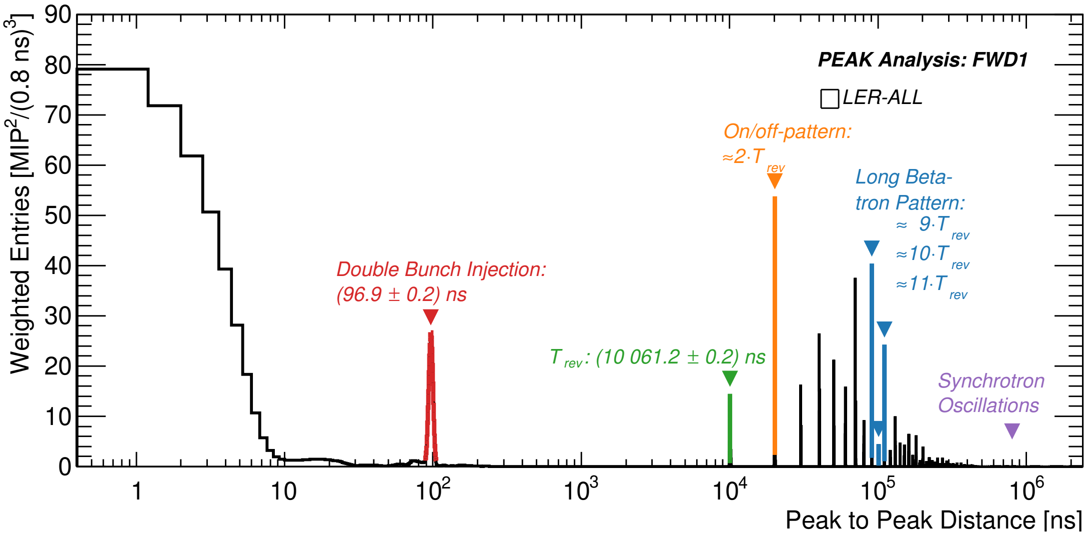

Figure 8.1: Distribution of weighted distances between signals for the LER-ALL data set for channel FWD1. Colored Gaussian fits and corresponding labels indicate responses of specific timing patterns connected to properties of the accelerator.

to $N_{samples}$ to avoid double counting of distances. The outcome of a PEAK analysis is a spectrum of distances between signals with their corresponding magnitudes similar to the result of a Fourier analysis, only as a function of distances instead of frequencies. In this spectrum, the distances which are particularly common or are separating large signals appear as peaks. These peaks are connected to certain properties of the accelerator which can be studied in that way. In theory, the PEAK analysis can probe distances from the difference between two samples (0.8 ns) up to the length of the waveform (2.4 ms).

Overall spectrum Figure 8.1 shows the distribution of weighted distances for a PEAK analysis applied to the LER-ALL data set. On a semi-logarithmic scale in time, the spectrum ranges from time patterns which take place on the time scale of several nanoseconds up to patterns that extend over milliseconds. The first structure is a continuum stretching up to around 10 ns which is observed across all data sets. It is not related to a specific timing pattern. Results delivered by a PEAK analysis are thus only meaningful for distances greater than the range of the continuum.

In the following, the results and the corresponding uncertainties for the respective patterns are given by the mean of a fit with a Gaussian distribution.[1] The first peak is attributed to the distance between the two bunches which simultaneously received new

---

[1] We apply a two stage maximum likelihood fit in the range of $\pm 2\,\sigma$ of the mean; uncertainties on the parameters are adopted from the fit.

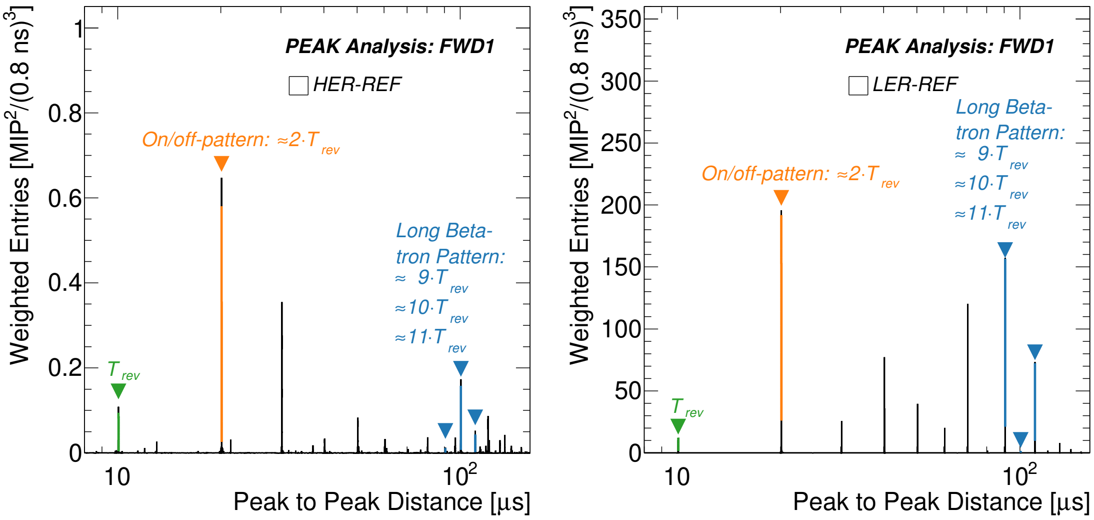

Figure 8.2: Sections of the distributions of weighted distances between signals for the HER-REF (*left*) and the LER-REF (*right*) data sets for channel FWD1. Colored Gaussian fits and corresponding labels indicate response of specific timing patterns connected to properties of the accelerator.

particles via double bunch injections. The mean of the fit is (96.8 ± 0.2) ns and is in reasonable agreement with the machine prediction (96.3 ns) and the result obtained by the rate in turn ((96.5 ± 0.4) ns). The second peak is attributed to the beam revolution period, T_{rev} (10 061.4 ns). Here, we obtain a mean value of $(10\,061.2 \pm 0.3)$ ns, which is, again, in good agreement with the prediction by the machine. Results for all other data sets generally show a similar level of agreement. The rest of the spectrum is shaped by multiples of T_{rev} and, in that way, by the propagation of the injected bunches along the beam lines. The timing patterns here affect the variation of backgrounds between consecutive transits of the injected bunches.

On/off-pattern and long betatron pattern So far, a data set which consists of a large number of events with a wide range of conditions has been studied. In the following, we discuss the effects of the on/off-pattern and the long betatron pattern based on the reference injections for both rings which are taken under more uniform machine conditions. Figure 8.2 shows the corresponding ranges of weighted distance distributions for the HER-REF (*left*) and the LER-REF (*right*) data sets. For both rings, we clearly observed peaks corresponding to the beam revolution period (T_{rev}). For backgrounds recurring with every transit of the injected bunch, the distance corresponding to a full turn in the ring should be the most abundant and therefore the dominant signal in the

PEAK spectrum. However, for both data sets this is not the case. Instead, we observe a dominant peak at the distance of two consecutive turns, i.e. $2 \cdot T_{rev}$, and several other larger peaks at distances from nine to eleven turns. The former is an instance of the on/off-pattern, whereas the latter is attributed to the long betatron pattern. As such, they are both caused by the betatron oscillations of the newly injected particles, as discussed in Section 7.3.1. Qualitatively, we observe that this behavior appears to be more pronounced for injections into the LER than into the HER, which is consistent with previous findings. Interestingly, we also find that the on/off-pattern gets amplified for both sets with a non-optimal phase shift (given by HER-PS and LER-PS). In future studies, it might be possible to quantify the amplitude of betatron oscillations by the ratio of these peaks.

With respect to the long betatron pattern, the HER-REF data set shows that the responses for distances larger than three turns are relatively small except for a distinct peak at ten turns (∼100 µs). This suggests, that the non-integer part of the vertical betatron tune (see Section 7.3.1) is deviating from a strict half-integer value by around 0.1 oscillations per turn. This interpretation differs from the 0.03 oscillations per turn predicted by simulations, but could explain why the signals we observe are recurring with a period of ten turns. For the LER-REF set, on the other hand, distances which correspond to nine and, to a smaller extent, to eleven turns show larger peaks, whereas there is no response for ten turns. This observation may be explained by a similar deviation of the betatron tune which is convolved with the on/off-pattern, what is in agreement with the previous findings.

Synchrotron oscillations At last, we examine the synchrotron oscillations of the beam particles. From the timing patterns accessible by the PEAK analysis, these patterns are the ones taking place on the longest time scales. As discussed in Section 7.3.1, in the majority of the events injection backgrounds return to the levels of regular beam backgrounds within 500 µs (∼50 turns). Therefore, only a small proportion of the events exhibit synchrotron oscillations beyond more than one period. Note that although these are only few events they are the ones which are ultimately determining the length of the gating windows. We therefore study synchrotron oscillations based on a PEAK analysis of the data sets with the highest statistics available given by HER-ALL and LER-ALL. Figure 8.3 (*left*) shows the full PEAK spectrum for the HER-ALL set. Here, all peaks are fitted with a Gaussian distribution;[2] the maximum of each Gaussian fit then reflects a multiple of the beam revolution period (as indicated by the colored markers). To

---

[2] We apply a maximum likelihood fit with a range of ±3 ns around the local maxima of the distribution.

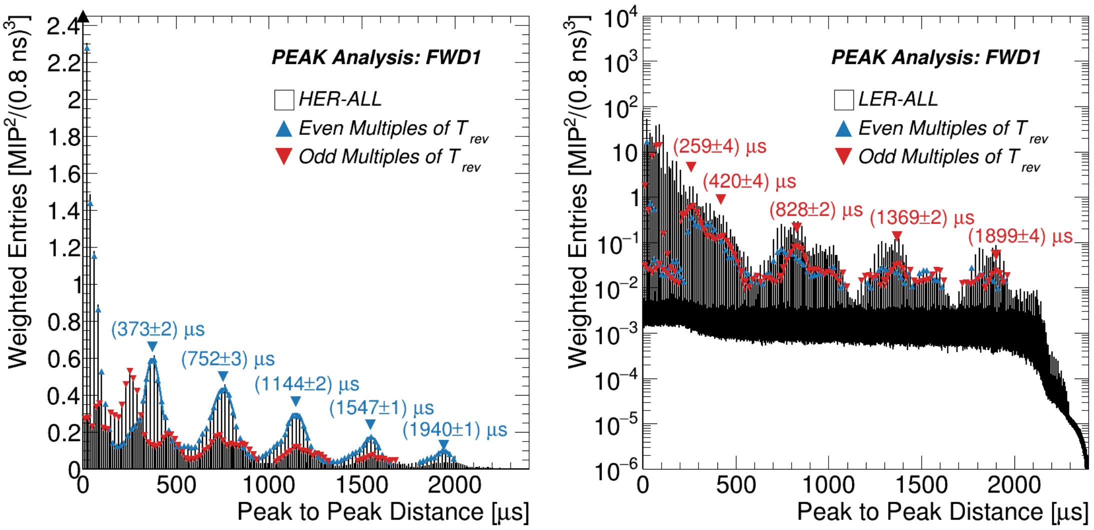

Figure 8.3: Distributions of weighted peak distances for HER-ALL (*left*) and LER-ALL (*right*) data sets for channel FWD1. Colors and markers indicate responses attributed to odd and even numbered transits of the injected bunch at the IP.

disentangle the effects of the on/off-pattern, these maxima are divided into even and odd multiples and, in that way, form two new distributions. The even multiples reveal a structure of several seemingly normal distributed peaks. We again fit the distribution of even multiples with Gaussians and state their mean values, as shown in the figure.[3] Now the value of the first mean, $(373 \pm 2)\,\mu\mathrm{s}$, represents a concrete measurement of the period of the synchrotron oscillations of particles in the beam lines; the other mean values are multiples of the synchrotron oscillation period. This result is in approximate agreement with the simulation prediction of an oscillation period of $409\,\mu\mathrm{s}$ (40.6 turns, see Sections 3.1 and 7.3.1). This finding, however, must be interpreted with some caution since the studied data set covers a wide range of accelerator conditions.

Injection backgrounds in the LER show considerably higher particle loss rates early on and are more localized to time scales below $500\,\mu\mathrm{s}$ after the injection. As a result, long lasting effects like synchrotron oscillations are less pronounced in the data sets making a measurement of the synchrotron oscillation period challenging. Figure 8.3 (*right*) shows the full PEAK spectrum for LER-ALL. Analogously to the HER, we try to disentangle the effects of the on/off-pattern by splitting the peaks into even and odd multiples of the beam revolution period. Here, however, odd multiples seem to better

---

[3] We apply a maximum likelihood fit with an arbitrary range; uncertainties on the mean are adopted from the fit.

reflect the oscillations of the beam particles. These differences might be related to the fact that the on/off-pattern is more pronounced in the LER. The structure which we observe here is significantly less conclusive than the one for the HER making it practically impossible to determine the period of synchrotron oscillations. The most likely candidate for a response is a peak at a distance of $(420 \pm 2)\,\mu\mathrm{s}$, what differs notable from the simulation prediction of $526\,\mu\mathrm{s}$ (52.6 turns, see Sections 3.1 and 7.3.1). By contrast, the differences between the following multiples are $(541 \pm 3)\,\mu\mathrm{s}$ and $(530 \pm 4)\,\mu\mathrm{s}$ which is in approximate agreement with the simulation.[4] Nonetheless, further data collection is required for reliable measurements of the synchrotron oscillation periods in the HER and the LER.

8.2 Frequency component analysis

In this section, we present an alternative analysis of the timing patterns based on the decomposition of the time distribution into its frequency components by a discrete Fourier transform (DFT). In such an analysis, the frequency components reflect the periods with which larger backgrounds recur and are, in that way, connected to properties of the accelerator. In the following, we first give a brief introduction to the analysis methodology before we show measurements of different timing patterns.

Analysis methodology The range and the resolution of the discrete frequency spectrum of a DFT depends on the sampling frequency and the sample count of the discrete time-domain signal. The averaged reconstructed waveforms have the same structure as the raw physics waveforms, as described in Sections 6.1.1 and 6.2. That means these waveforms have a total length of N_s (3×10^6) samples which are sampled with a frequency F_s (1.25 GHz or 1/0.8 ns). Consequently, the observed frequency spectra range from

$$0\,\mathrm{Hz} \text{ to } \frac{F_s}{2} = 0.6125\,\mathrm{GHz}, \tag{8.1}$$

with a frequency resolution of

$$\Delta f = \frac{F_s}{N_s} = 417\,\mathrm{Hz}. \tag{8.2}$$

---

[4] The distance is calculated by the difference of the two mean values; uncertainties are obtained by quadratic addition of the individual components.

Here, we took advantage of the fact that transforms of real signals are symmetrical around $f = 0$ and that the negative frequency information thus is redundant. According to the Nyquist criterion, only signals with a frequency smaller than $F_s/2$ can be sufficiently sampled. Signals with higher frequencies lead to aliasing making their responses in the Fourier spectrum indistinguishable from a fictitious lower-frequency component. The response of the time difference between two consecutive bunches is expected to have the highest frequency of all signals caused by beam backgrounds. Its frequency is 169.6 MHz, which is well below half of the F_s. We therefore do not expect any aliasing and do not apply measures against it.

The technical implementation of the DFT is based on a mixed-radix Fast Fourier Transform algorithm taken from the GNU Scientific Library [70]. A more detailed introduction to the operation of the Fourier transform can be found in [77]. In order to show relative magnitudes of the respective frequencies, the spectra in the following are normalized to unity.

This method of analysis, however, has a number of limitations. Firstly, signals in the averaged reconstructed waveforms are not sinusoids, but delta peaks. Secondly, signals of injection backgrounds start abruptly with the first transit and predominantly decay before the end of the waveform, which has a similar effect as applying a window function. And thirdly, while the sensor signals are sampled at a frequency of 1.25 GHz the amplitude of the injection backgrounds is only measured every time the injection bunch pass by the IP what corresponds to a frequency of around 100 kHz. That means variations of the injection backgrounds, which change with frequencies higher than 100 kHz/2, can in theory lead to aliasing, as explained earlier. Due to these reasons, results obtained by this method have to be interpreted with caution and statements of uncertainties are omitted. Nevertheless, as we will see in the following, a Fourier transform establishes concrete measurements of several quantities related to the time evolution of backgrounds.

Fourier transform of non-injection backgrounds We first discuss the case of a Fourier spectrum of regular beam backgrounds in the absence of injections. Figure 8.4 shows the frequency spectrum as a result of a DFT applied to the NI-VACS data set. We find a uniform response across the whole frequency range with the exception of two distinct peaks. The first peak is located at 0 Hz and is the response to the fact that signals are always non-negative. In that way, it is equivalent to the response of a constant DC offset in the case of signals which indicate a voltage over time. The frequency component of the second peak is attributed to the time difference between consecutive bunches of ∼6.0 ns (169.6 MHz). The peak is fitted with a Gaussian distribution and is centered

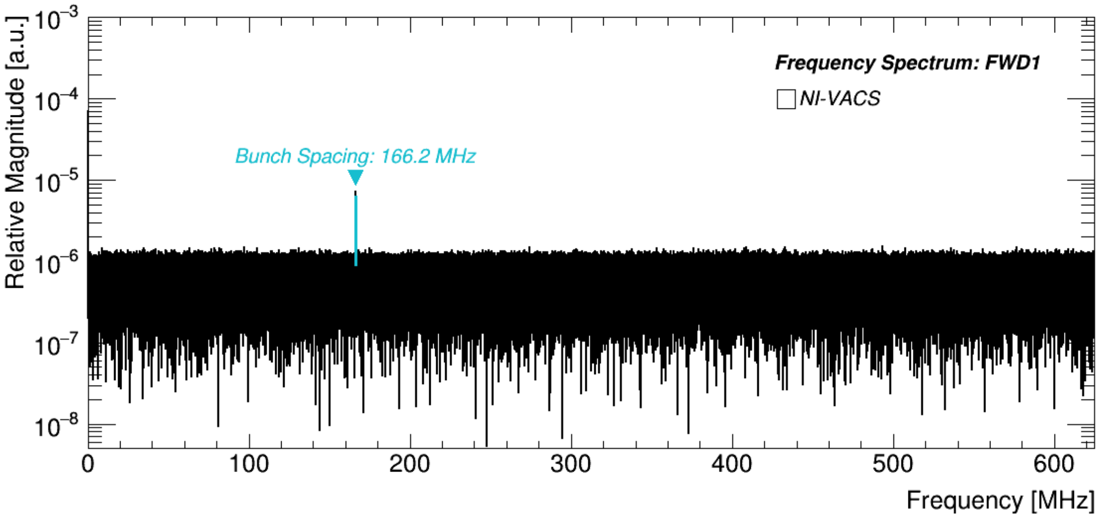

Figure 8.4: Frequency spectrum as a result of a discrete Fourier transform of the NI-VACS data set for channel FWD1. Spectrum is normalized to unity in order to show relative magnitudes of the respective frequencies.

at a frequency of 166.2 MHz.[5] Thus, measurement and expectation are in reasonable agreement. This Fourier spectrum of the non-injection data set NI-VACS establishes the baseline of signals of regular beam backgrounds.

Fourier transform of injection backgrounds With respect to injection backgrounds, we observe significantly different spectra which are dominated by several large peaks related to the time structure of injection backgrounds. Figure 8.5 presents the frequency spectrum obtained from a DFT applied to the LER-ALL data set. The fact that signals are always positive causes a widespread peak which is centered at 0 Hz and stretches up to approximately 6 kHz. The first peak related to the propagation of the injection bunch is located at 10.9 kHz (91.7 µs) and is attributed to the long betatron pattern. This finding is in agreement with results of the PEAK analysis which favors a long betatron pattern with a period of 90.6 µs (nine turns) for the same data set. We find two additional peaks located in close proximity of each other and centered at 44.4 kHz (22.5 µs) and 54.9 kHz (18.2 µs) which we attribute to the on/off-pattern. It is unclear why we observe two peaks. A possible explanation might be differing accelerator settings between events of the data set leading to two marginally different vertical betatron tunes.

The following larger peak is attributed to the beam revolution period, T_{rev}. We obtain

---

[5] We apply a maximum likelihood fit with an arbitrary range; the mean of the Gaussian determines the quoted frequency.

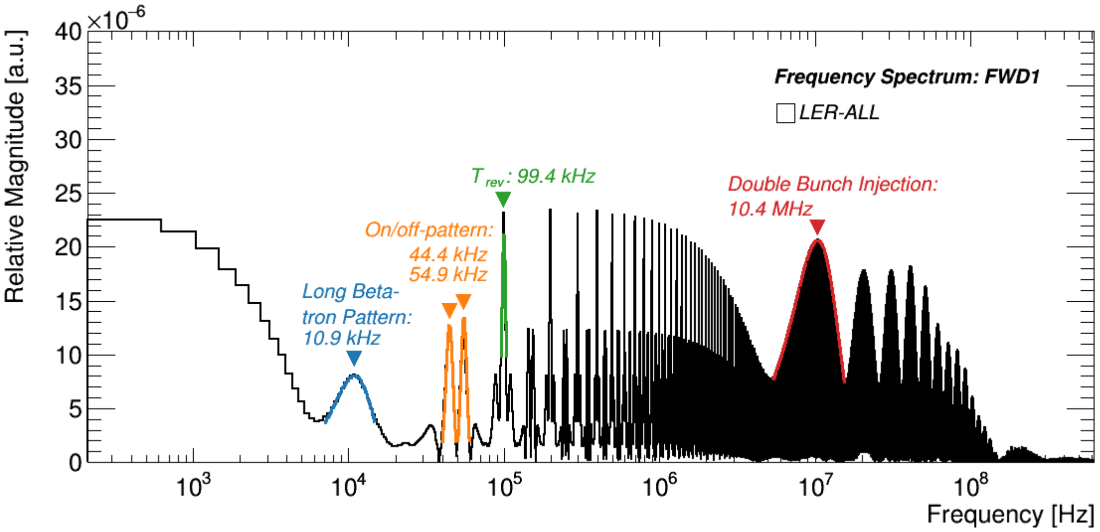

Figure 8.5: Frequency spectrum as a result of a discrete Fourier transform of the LER-ALL data set for channel FWD1. Spectrum is normalized to unity in order to show relative magnitudes of the respective frequencies.

a frequency of 99.4 kHz (10.06 µs) which is in agreement with the expectation by the machine of 10.0614 µs. The rest of the spectrum is determined by multiples of the responses of the on/off-pattern and the beam revolution period. Additional timing patterns in that region occur as superstructures on top of these multiples. This is for example the case for the distance between two bunches in double bunch injections. To average out the underlying structure of multiples and to determine the frequency of the double bunch injections, we first rebin the frequency spectrum by a factor of 200. A fit to the rebined distribution then yields a frequency of 10.4 MHz, which corresponds to a period of 96.2 ns and is comparable to the machine value (96.3 ns) and to the results obtained by the PEAK analysis ((96.8 ± 0.2) ns). Note that the corresponding Gaussian in Figure 8.5 is only an illustration of the fit applied to the rebined spectrum.

8.3 Summary and key findings

The time resolved analysis of injection backgrounds demonstrated that its time structure is determined by the propagation of the newly injected particles along the beam lines of the rings, which is affected by several different recurring timing patterns connected to properties of the accelerator. In this chapter, we presented a program of measurements of these timing patterns which used two complementary analyses, one based on a Fourier transform and one novel technique based on the weighted time distance between two signals also referred to as *PEAK analysis*. While the PEAK analysis is more suitable for longer time patterns like synchrotron oscillations, the Fourier transform is able to also probe shorter periods such as the bunch spacing. Together, these analyses examined the following timing patterns: the bunch spacing, the bunches distance in double bunch injections and the beam revolution period, as well as patterns related to betatron and synchrotron oscillations. In that way, it was possible to directly determine the frequencies of these patterns from detector data, mostly with sub-nanosecond precision.

Although it suffers from a number of limitations, the majority of the results of the Fourier transform are confirmed by the measurements obtained with the PEAK analysis. Further experiments with higher statistics are required to reliably determine the synchrotron oscillation periods of the newly injected particles and to refine the approach of using a Fourier transform.

Chapter 9

Beam-gas and Touschek backgrounds

As part of BEAST II, CLAWS also participated in a comprehensive program of non-injection background measurements. Collectively, these measurements and their findings are described in detail in [36]. Since reviewing all of these studies is beyond the scope of this work, we focus here on a single measurement which is discussed solely on the basis of CLAWS data. This is the combined measurement of beam-gas and Touschek backgrounds in the interaction region and a method for disentangling these two types of backgrounds.

As described in Sections 3.4 and 4.1.2, beam-gas and Touschek scattering are luminosity independent beam backgrounds which are expected to increase significantly for SuperKEKB. Beam-gas scattering refers to both bremsstrahlung and Coulomb interactions of beam particles with residual gas molecules in the vacuum chambers and depends on the pressure in the beam pipe and the beam current. It changes the energy and the direction of the beam particles and leads to the emission of photons. As a consequence of the larger beam currents and the new vacuum chambers, beam-gas backgrounds are expected to increase by a factor of two compared to KEKB. By contrast, Touschek backgrounds are caused by intra-bunch Coulomb scattering of two beam particles and lead to a deviation from the nominal beam energy. The Touschek scattering rate depends on the particle density in the bunches and thus on the beam current and the beam size. Promoted largely by the nano-beam scheme, they are expected to be around 20 times higher than at KEKB. Together, these two processes will lead to significantly elevated background rates and a higher occupancy of the detector systems of Belle II, in particular in the inner detector.

While it is not possible to simulate injection backgrounds, great efforts are made to predict and assess the impact of non-injection backgrounds on the physics program of Belle II by simulations. These efforts include the simulation of the beam backgrounds during Phase 1. A detailed description of the structure and performance of this simulation is given in [36]. It is imperative to understand the accuracy of these predictions using first experimental results as early as possible. One of the main goals of the BEAST II experiment, therefore, is the validation of these simulations and the different background models employed.

In Section 9.1, we first introduce a combined parameterization of beam-gas and Touschek backgrounds. This parameterization allows to relate the observed rate of background particles to accelerator conditions. Subsequently, Section 9.2 describes the data set recorded during a dedicated beam study performed by BEAST II and SuperKEKB. In Section 9.3, we then apply the combined parameterization to this data set in order to obtain independent measurements of beam-gas and Touschek backgrounds. The obtained results are used to directly compare experimental background rates with rates predicted by simulation in Section 9.4. Finally, we briefly summarize the key findings from the presented study in Section 9.5.

9.1 Background parameterization

With the aim of relating observed backgrounds to accelerator and beam conditions, we describe beam-gas and Touschek backgrounds by a combined parameterization as defined in the following.

Beam-gas parameterization Beam-gas scattering refers to both bremsstrahlung and Coulomb interactions of the beam particles with residual gas molecules. We simultaneously account for these two processes by describing them by

$$R_{bg} = S_{bg} \cdot IPZ_e^2, \tag{9.1}$$

where R_{bg} is the observed rate of background particles which can be assigned to beam-gas scattering (bremsstrahlung and Coulomb), S_{bg} is a constant of proportionality we refer to by *beam-gas sensitivity*, I is the beam current, P is the vacuum pressure and Z_e is the effective atomic number of the residual gas mixture, as introduced in Section 3.5. While the theoretical dependencies on Z are more complex, the scattering rate is approximately proportional to Z^2 for the gas mixtures encounter in practice.

The parameterization of beam-gas backgrounds by Equation 9.1 is accurate if P and Z_e reflect the gas pressure and gas mixture at the scattering location. The exact scattering location, however, is unknown and gas properties vary significantly throughout the rings. As a consequence, using average gas pressure and mixture in the description of beam-gas backgrounds does not yield correct results and a more precise parameterization is required.

A more precise beam-gas parameterization The overall pressure in the rings, P, is driven by dynamic pressure as a result of the desorption of gas molecules from the walls of the beam pipe. This desorption is promoted by radiation emitted by the beam particles or collisions of off-orbit particles (see description of vacuum scrubbing in Section 7.1). Due to the entirely new beam pipe, this is especially the case in the LER. The position of collisions of off-orbit beam-particles depends greatly on their propagation along the beam lines and the specific geometry of the vacuum chambers. The pressures recorded in two neighboring gauges (separated by around 10 m, see Section 3.5) usually disagree by factors of two to five, but can differ by as much as two orders of magnitude. Similarly, the localized desorption promoted by photons or electrons affects the composition of the gas mixture described by Z_e. The values of Z_e determined in the two residual gas analyzers (RGAs) (separated approximately by one kilometer, see Section 3.5) thus differ by $5 - 25\%$ on the time scale of several minutes.

If the local pressure and gas composition would be known throughout the beam lines these could be weighted by the distribution of scattering locations in order to account for these variations. However, such a weighting is not feasible since Z_e is only measured at two positions and pressure readings are more frequent but still coarse. For the parameterization, we therefore utilize an *effective pressure*, P_e:

$$P_e = \frac{\sum_i^{CCG} P_i w_i}{\sum_i^{CCG} w_i}, \tag{9.2}$$

where the weights w_i are the relative likelihoods of scattering in the region of the ith cold cathode gauge (CCG) causing detectable backgrounds at the IP. The Z_e, on the other hand, has to be interpolated or estimated in order to make up for the absence of a measurement at each CCG. The rate of observed backgrounds which can be attributed to beam-gas scattering, R_{bg}, can hence be described by

$$R_{bg} = S_{bg} \cdot IP_eZ_e^2.$$

This reduces the parameterization of beam-gas backgrounds to the task of finding the suitable weights. As will be demonstrated based on measurements in Section 9.3, adequate results can be obtained by using only the pressure in the CCG which yields the best agreement between the parameterization and the data, or, in other words, the most-predictive CCG.

Touschek parameterization Among other things, Touschek scattering depends on the number of particles per bunch, the number of bunches in general and the beam energy. Under regular operating conditions, however, these quantities do not change. It can therefore be assumed that the rate of backgrounds which can be attributed to Touschek scattering is proportional to the beam current squared, I^2, and the vertical beam size, σ_y, and can be parameterized in a similar way by

$$R_T = S_T \cdot \frac{I^2}{\sigma_y}, \tag{9.3}$$

where S_T is the equivalent constant of proportionality we refer to as *Touschek sensitivity.*

The combined beam-gas and Touschek parameterization Finally, the terms for the two background types can be subsumed into a combined parameterization:

$$R = S_{bg} \cdot IP_eZ_e^2 + S_T \cdot \frac{I^2}{\sigma_y}, \tag{9.4}$$

where R reflects the total rate of both types. This parameterization is expected to describe the vast majority of non-injection backgrounds with respect to accelerator conditions, which are observed during Phase 1. For each ring, we assign each channel a set of characteristic values for the beam-gas and Touschek sensitivities, S_{bg} and S_T. These values reflect how "sensitive" the respective channel is for the particular background type due to its individual position. If all accelerator conditions except the ones stated in Equation 9.4 are fixed, these values should be constant.

To visualize this parameterization in a more intuitive way, Equation 9.4 can by rewritten as

$$\frac{R}{IP_eZ_e^2} = S_{bg} + S_T \cdot \frac{I}{P_eZ_e^2\sigma_y}. \tag{9.5}$$

If $R/(IP_eZ_e^2)$ is shown as a function of $I/(P_eZ_e^2\sigma_y)$, then the sensitivities reflect the intercept and the slope of this linear dependence. In the following, we refer to Equation 9.5 simply as the *combined parameterization.*

9.2 Dedicated beam studies

In order to study beam-gas and Touschek backgrounds with respect to varying beam sizes and currents and to validate the parameterization, SuperKEKB and Beast II performed a so-called *size sweep scan.* In this size sweep scan, we measured the rate of backgrounds at several different predefined and fixed beam currents and vertical beam sizes. A breakdown of the data set recorded for the size sweep scan and its segmentation is presented in Table 9.1. For each of these runs, the beam current in the respective ring was topped off to a specific level. A run then consists of five different subruns each targeted at a specific vertical beam size.

In the HER, the beam size was manipulated by shifting the beam orbit in an isolated position in the vertical direction by a pair of bending magnets what caused vertical dispersion. For the LER an alternative method was used. Here, the strength of a skew quadrupole magnet was altered in order to promote a strong x-y coupling. In that way, it was possible to manipulate the beam size over the whole ring without affecting the beam orbit itself.

The rate R in Equation 9.5 is given by the averaged particle rate introduced in Section 6.2. For the other quantities, measurements from the various SuperKEKB conditions monitors are used, as described in Section 3.5. Since the RGAs are installed only in the LER, we utilize the average of the readings during the LER size sweep scan in the RGA located in the intermediate-upstream LER arc section as Z_e for runs of both rings. Approximating Z_e in such a way does not affect the accuracy of the fits as described shortly. The local pressure readings, P_i, are obtained from different CCGs as also described shortly. We exclude all events for which the readings of the beam size are outside of a range of $35\,\mu\text{m} < \sigma_y < 400\,\mu\text{m}$ or, in other words, are physically unplausible, as well as events recorded during injections (see Sections 6.3 and 7.1).

9.3 Analysis procedure and experiment results

We now describe how beam-gas and Touschek backgrounds are determined by applying the combined parameterization to the data set recorded during the size sweep scans. We first plot the data of the scan with the quantities described in the previous section

Table 9.1: Summary of the runs used in the size sweep study of the HER (*left*) and the LER (*right*). Values for the beam sizes are obtained by measurements with a X-ray monitor. In practice, beam sizes varied from the stated values throughout the subruns due to an imperfect control.

Ring	I [mA]	Subrun	σ_y [µm]	Marker
HER	320	1	85	△
		2	68	△
		3	39	△
		4	44	△
		5	45	△
	480	1	91	○
		2	66	○
		3	47	○
		4	32	○
		5	41	○
	640	1	121	□
		2	74	□
		3	46	□
		4	40	□
		5	56	□

Ring	I [mA]	Subrun	σ_y [µm]	Marker
LER	360	1	81	△
		2	65	△
		3	51	△
		4	38	△
		5	32	△
	540	1	95	○
		2	72	○
		3	67	○
		4	58	○
		5	51	○
	720	1	148	□
		2	147	□
		3	141	□
		4	145	□
		5	146	□

and then apply a χ^2-fit with Equation 9.5 to it. Examples of such a fit are shown in Figure 9.1; findings from these figures, however, are discussed later in this section. In this scatterplot, every point represents a single event recorded in the size sweep scan together with the corresponding measurements of the SuperKEKB condition monitors. The shapes reflect the different beam currents, whereas colors correspond to the various beam sizes stated in Table 9.1. Note that the uncertainties on the data points are based only on statistical uncertainties of the measured rate of background particles (see Section 6.3). The agreement between the parameterization and the data is then evaluated based on the normalized-χ^2 of the fit result. We perform such a fit independently for each channel and each ring in order to determine the individual sensitivities, S_{bg} and S_T, As described shortly, these fits can also be used to find the most predictive CCG by comparing the normalized-χ^2 of the respective fits. Following Equation 9.4, the obtained sensitivities and the respective CCG can then be used to predict the experimental beam-gas and Touschek background rates for any beam size, current, pressure and gas composition.

CCG selection procedure As discussed in Section 9.1, the rate of backgrounds caused by beam-gas scattering highly depends on the weights in Equation 9.2 used to determine the effective gas pressure. The true distribution of scattering locations reflected by the weights, however, is unknown. We therefore circumvent determining all weights and try to find a single CCG which yields the most accurate results for the fits in the size sweep scan. The identity of the most predictive CCG is unique to each channel and has to be determined individually. Note that the most accurate CCG does not necessarily represent the dominant scattering location.

The simulation of Touschek and beam-gas backgrounds for Phase 1 predicts that scattering in the LER is almost entirely taking place in the vicinity of the IP. It can therefore be assumed that the nearest-upstream CCG is the most suitable choice for the most predictive CCG and we, therefore, use it for all channels.

For the HER, on the other hand, the simulation predicts that the observed backgrounds are sensitive to scattering at different locations and that they vary between channels. The simulation identifies 75 different CCGs located upstream of the IP which are responsible for a significant part of the beam-gas scattering in the HER. For pressure readings of each of these CCGs, we fit the combined parameterization to the data from the HER size sweep scan. For each channel it is possible to find a CCG for which the parameterization and the data are in sufficient agreement as indicated by the normalized-χ^2 and a respective p-value larger than 25%. We therefore conclude, that there is no advantage in searching for possible linear combinations of CCG weights. For the HER, we thus use pressure readings of the CCG for which the the normalized-χ^2 is the smallest.

CCG selection results and beam-gas and Touschek sensitivities Finally, we use the fit with pressure readings in the most predictive CCG to determine the unique beam-gas and Touschek sensitivities for each channel. Figure 9.1 shows these final fits using the most-predictive CCG for the size sweep runs in the HER (*left*) and the LER (*right*) for FWD1; similar fits for FWD2 and FWD3 are given in the appendix in Figures D.1 and D.2, respectively.

In the LER, the fit of the combined parameterization to data from FWD1 using pressure readings of the closest upstream CCG yields a p-value of almost 100%. A possible explanation of this extraordinary large p-value might be that the assessment of uncertainties (see Section 6.3) overestimates the statistical uncertainties on the averaged particle rate.

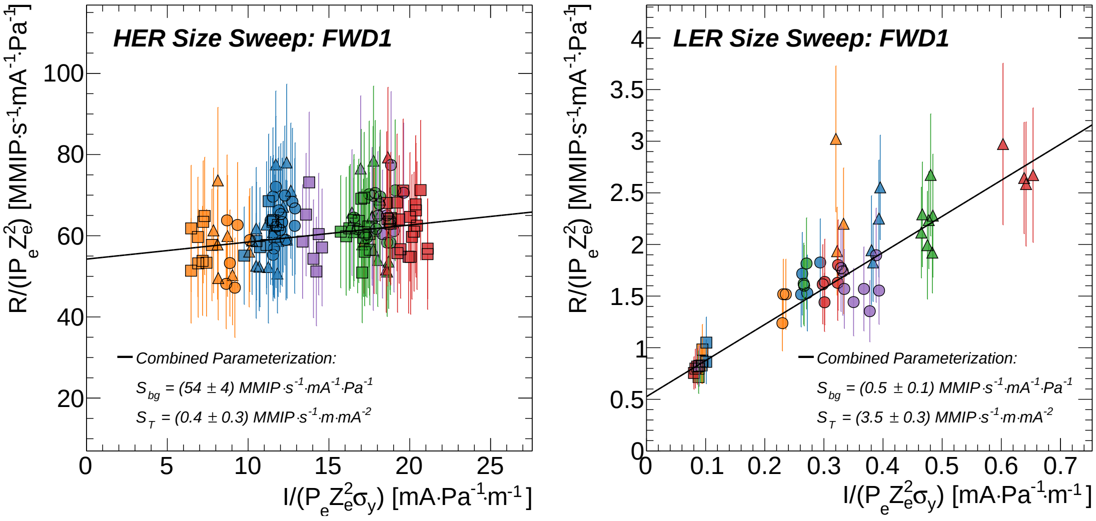

Figure 9.1: Fit of the combined parameterization of beam-gas and Touschek backgrounds given by Equation 9.5 to data obtained in size-sweep scans for the HER (*left*) and the LER (*right*) for channel FWD1. Shapes reflect different beam currents, whereas colors indicate vertical beam sizes. Uncertainties on the data are solely statistical; uncertainties on the parameters are adopted from the fit.

By contrast, for FWD2 and FWD3 we obtain p-values close to zero. This discrepancy could be attributed to the significantly smaller signal rates in the sensors located further away from the beam lines.

As mentioned previously, in the HER it is for all channels possible to find a CCG for which the p-value of the respective fit is larger than 25%. FWD1 and FWD3 converge on the same CCG located approximately 190 m upstream of the IP, while for FWD2 the most accurate CCG is the one next to it located approximately 180 m upstream of the IP. For each channel and ring, these fits yield the identity of the most predictive CCG and a pair of unique sensitivities S_{bg} and S_T. Uncertainties on the sensitivities are adopted from the fits.

9.4 Comparison of simulation and data

Having determined the sensitivities, we can now use the parameterization to directly compare background rates measured by the sensors to rates predicted by simulation. In that way, it is possible to probe the accuracy of the simulation of beam-gas and Touschek backgrounds for Phase 1.

Simulated background rates The simulation of beam-gas and Touschek backgrounds is based on tracking regular and scattered beam particles in the *Strategic Accelerator Design* (SAD) software framework [76]. Detector effects are then simulated by handing the loss positions and momenta of scattered particles over to the *Geant4* toolkit [78]. As a consequence of the significant computation time required, it is not possible to simulate beam-gas and Touschek loss rates over a wide range of accelerator conditions. Instead, the simulation is performed with fixed and uniform pressure, P^{SAD}, current, I^{SAD}, gas composition, Z^{SAD}, and vertical beam size, σ_y^{SAD}. In the 2D space of Figure 9.1, these simulated conditions and the corresponding background rates represent a single point. The specific conditions at which the simulation is performed are the following: $I^{SAD} = 1.0\,\mathrm{A}$, $Z^{SAD} = 7$, $\sigma_y^{SAD} = 59\,\mu\mathrm{m}$ (HER) and $\sigma_y^{SAD} = 110\,\mu\mathrm{m}$ (LER) with $P^{SAD} = 1.33 \times 10^{-6}\,\mathrm{Pa}$. The simulation predicts the rate of beam-gas backgrounds, R_{bg}^{MC}, and the rate of Touschek backgrounds, R_T^{MC}, separately. As for the parameterization, beam-gas Coloumb and bremsstrahlung scattering are combined into R_{bg}^{MC}. The dependence of the beam-gas component on the Z of the gas mixture assumed by SAD is different from the simplistic Z_e^2 scaling used by the parameterization (see Section 9.1). To account for these differences, the rates predicted by the simulation are in situ rescaled by a constant parameter which only depends on Z_e.
In total, we obtain a pair of simulated background rates, R_{bg}^{MC} and , R_T^{MC}, for the HER and for the LER for each channel, corresponding to six pairs in total.

Experimental background rates We can use the parameterization and the sensitivities obtained in the size-sweep scans to determine the background rates expected for experimental data for the same conditions as used in the simulation. The corresponding experimental beam-gas rate, R_{bg}^{Data}, is then given by

$$R_{bg}^{Data} = S_{bg} I^{SAD} P_e^{SAD} Z_e^2. \tag{9.6}$$

As mentioned earlier, the simulation is performed at a fixed and uniform pressure P^{SAD}. During runtime, however, the average pressure in the rings does not comply with the pressure in the most-predictive CCG used in the study of the size-sweep scan. We therefore first compare average pressures in the respective ring and the readings in the most-predictive CCG across a wide range of pressures. We then use this comparison to find a pressure P_e^{SAD} which corresponds to the pressure expected in the CCG when the ring average pressure is equal to P^{SAD} and utilize it in Equation 9.6. With respect to Z_e, simulated background rates are already rescaled to account for the differences between

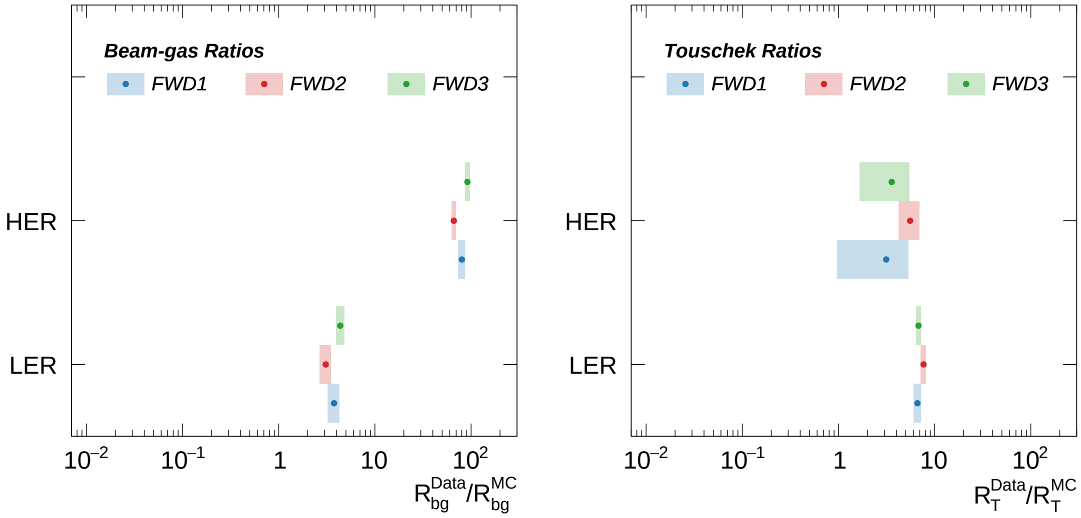

Figure 9.2: Ratios of background rates expected for the accelerator conditions at which the simulation is performed to rates predicted by simulation for beam-gas (*left*) and Touschek (*right*) scattering in the HER and the LER. Uncertainties are derived from uncertainties of the sensitives obtained in the size-sweep scan and are solely statistical.

Z_e and Z^{SAD}. In Equation 9.6, we therefore use Z_e instead of Z_{SAD} employed by the simulation.

Using equation 9.3, the experimental Touschek rate, R_T^{Data}, is obtained analogously. As for the simulated background rates, in total we obtain six pairs of background rates, one for each ring and channel.

Ratios of experimental and simulated background rates So far we have determined directly comparable experimental and simulated background rates which reflect the same accelerator conditions. With the aim of examining the level of agreement between data and simulation, we calculate the ratios of these rates. Figure 9.2 compares the ratios obtained separately for beam-gas (*left*) and Touschek (*right*) backgrounds. The error bars on the ratios are derived from the fit uncertainties on the respective sensitivities as obtained by the size-sweep scans. Estimating uncertainties in that way, however, does not account for variations due to the choice of the best CCG. It also examines only statistical uncertainties and does not consider uncertainties of any kind on the simulation or the readings of the beam and accelerator condition monitors.

The channel-by-channel variations for all ratios are relatively small. The ratios for Touschek scattering in both rings and the ratios for beam-gas scattering in the LER agree for all channels within $1.5\,\sigma$ of each other. The HER beam-gas ratios for the all channels, on the other hand, agree on the level of $3\,\sigma$. From the ratios of all channels it is apparent that there is a distinct excess in data over simulation. For HER Touschek for FWD1 and FWD3, this excess is small and still within $1.5\,\sigma$. For all beam-gas ratios in the HER and for the Touschek ratios in the LER in FWD2 and FWD3, the ratios exceed unity by more than $10\,\sigma$. For all other ratios, the excess is between $3\,\sigma$ to $10\,\sigma$. Except for HER beam-gas, the absolute excess irrespective of the uncertainties is relatively consistent and background rates in data are between 3 to 10 times larger than the rates predicted by simulation. For HER beam-gas, on the other hand, experimental background rates are up to two orders of magnitude larger.

The distinct overall excess of experimental background rates indicates additional unknown systematic uncertainties in the simulation, the detector calibration or the analysis procedure. Other BEAST II systems generally observe similar excesses but few channels also show deficits in data over simulation; the magnitude of the excesses and deficits is comparable in size [36]. It is difficult to explain these findings, but they might be related to the highly local nature of the gas conditions. The conditions affect the experimental rates since we only have rather course pressure readings due to the lack of instrumentation. They also influence the rates predicted by simulation because they assume uniform gas conditions throughout the rings. The results of this study do not allow to conclude whether the observed differences are caused by detector-level systematics or if they stem from a real disagreement between experiment and simulation. Further research is required to determine the variations of the gas conditions throughout the rings.

9.5 Summary and key findings

As part of the overall BEAST II effort, CLAWS also participated in a comprehensive program of non-injection background studies. In this chapter, we presented one of these studies, a combined measurement of beam-gas and Touschek backgrounds, based solely on CLAWS data. To be able to disentangle the two types of backgrounds, we developed a combined parameterization and applied it to data of a dedicated beam study in which we scanned LER and HER beam sizes and beam currents. We used this parameterization to calculate the ratios of background rates measured by the sensors to rates predicted by simulation. For the ratios of the experimental to the simulated background rates, we found a distinct excess in data over simulation which ranges from a factor three up to two orders of magnitude. Other BEAST II systems generally observed similar excesses but few channels also showed deficits in data over simulation; the magnitude of the excesses and the deficits was comparable in size [36]. It is not yet clear what causes these deviations, but they might be related to the strong location dependence of residual gas concentrations and of vacuum conditions for which we only had rather course readings available. Further research is required to determine the variations of the gas conditions throughout the rings.

Chapter 10

Summary, conclusions and outlook

In this thesis, we described the sensor technology and the overall installation of the CLAWS detector system. We explained how the recorded data was processed and presented the measurements CLAWS performed during the first phase of the commissioning of SuperKEKB, referred to as Phase 1.

The ambitious design luminosity of SuperKEKB is expected to cause challenging levels of beam backgrounds for various subsystems of the corresponding Belle II experiment, in particular for its pixel vertex detector. Understanding and mitigating these beam backgrounds early on is critical for the successful operation of the accelerator and the detector. In particular, backgrounds related to continuous top-up injections of new particles can not be simulated with sufficient accuracy and have to be determined by direct measurements. Phase 1 in 2016 focused on the basic operation of the accelerator and thus the detector and the final focusing systems were not installed and no collisions took place. To study beam-induced backgrounds in this collision-free environment, we placed a suite of dedicated beam background detectors collectively referred to as BEAST II at the IP. One of these detectors is the CLAWS experiment.

The CLAWS detector system consisted of eight plastic scintillator tiles with directly coupled SiPMs. The sub-nanosecond time resolution and single particle energy resolution of the sensors allowed novel bunch-by-bunch measurements of beam backgrounds and made the system uniquely suited for the study of injection backgrounds. The sensor signals were read out by a custom DAQ and electronics capable of continuously recording data over periods up to several milliseconds. We applied different calibration procedures to this raw sensor data in order to reconstruct the time distribution of background particles which was used in high level analyses of beam backgrounds. In these analyses, we studied various aspects of beam-induced backgrounds. We performed a time resolved analysis of backgrounds, examined different timing patterns related to properties of the accelerator and conducted a combined study of beam-gas and Touschek backgrounds.

The time resolved analysis showed that energy deposits of non-injection beam backgrounds were uniformly distributed in time and that we observed $\mathcal{O}(10^{-5})$ background particles per bunch. The distribution of hit energies suggested that backgrounds from photons and charged particles can be distinguished by the energy they deposit. This feature might be used to separately measure beam-gas and Touschek backgrounds in the future. The time structure observed during injection periods clearly showed peaks of significantly elevated background rates which we associated with the recurring transits of injection bunches. Comparing the hit energy distributions of regular and injection backgrounds revealed that injections predominantly lead to singular hits with exceptionally high energy deposits. However, the instantaneous background levels observed during injections in Phase 1 did not exceed regular beam backgrounds by more than an order of magnitude and fell short of the occupancy limit of the PXD by two orders of magnitude. In that way, backgrounds observed by CLAWS confirmed that the radiation levels were safe for the installation of Belle II in the second commissioning phase in 2018. We also demonstrated a method for separating energy deposits of regular and injection bunches by applying specific timing cuts. These timing cuts were utilized to quantify the decay behavior and overall proportion of injection backgrounds. We found that LER injections generally result in significantly higher backgrounds than HER injections, which can be explained by the lack of the positron damping ring in Phase 1. For both rings, the majority of the Injection backgrounds were typically observed withing the first 500 µs after the injection. Individual decay times, however, were fluctuating strongly on an event-by-event basis and depended on the exact injection parameters used, in particular the phase shift.

The time resolved analysis of injection backgrounds revealed that its time structure is determined by the propagation of the newly injected particles along the beam lines of the rings, which is affected by several different recurring timing patterns connected to properties of the accelerator. In order to quantify these patterns we performed two complementary analyses, one novel technique based on the weighted time distance between two signals and one based on a Fourier transform. These analyses examined the following timing patterns: the bunch spacing, the bunches distance in double bunch injections and the beam revolution period, as well as patterns related to betatron and synchrotron oscillations. In that way, it was possible to directly determine the frequencies of these patterns from detector data, mostly with sub-nanosecond precision.

In Phase 1, CLAWS also participated in a comprehensive program of non-injection background studies as part of the overall BEAST II effort. Here, we presented one of these studies, a combined measurement of beam-gas and Touschek backgrounds, based solely on CLAWS data. To be able to disentangle the two types of backgrounds, we developed a combined parameterization and applied it to data of a dedicated beam study in which we scanned LER and HER beam sizes and beam currents. We used this parameterization to calculate the ratios of background rates measured by the sensors to rates predicted by simulation. For all ratios, we found a distinct excess in data over simulation which ranges from a factor three up to two orders of magnitude. It is not yet clear what causes these deviations, but they might be related to the strong location dependence of residual gas concentrations and vacuum conditions for which we only have rather course readings available.

Together, the presented studies, including a novel time resolved analysis of backgrounds, make several noteworthy contributions to advancing the understanding of beam-induced backgrounds and injection mechanisms in high luminosity flavor factories. The measurements performed by the CLAWS experiment provide important insights into the dynamics of beam particles and can be used to validate beam dynamic simulations for the future operation of SuperKEKB by first experimental results. The methods used to quantify the decay behavior of injection backgrounds offer an effective way for developing a gating scheme for the PXD based on corresponding measurements in Phases 2 and 3.

Current simulations, which already incorporate several improvements based on Phase 1 results, predict that at full luminosities all of the sub-detectors of Belle II except the SVD and the KLM will be critically affected by beam backgrounds [36]. According to these simulations, in particular the CDC and the TOP will be close to the limits of significant performance degradation. The dominant background process in all detectors except the PXD is predicted to be radiative Bhabha scattering followed by either two-photon or Touschek backgrounds. For the PXD, on the other hand, the dominant background comes from the two-photon process followed by synchrotron radiation. Bhabha scattering and two-photon processes are luminosity dependent backgrounds. The predictions of the simulations for these background types, therefore, have to be validated based on background measurements performed during Phases 2 and 3. Based on Phase 1 results, the simulated Touschek scattering rate was already confirmed to be within one order of magnitude of the experimentally measured rates. As such, they are not expected to be a mayor concern for Phase 3 and onwards. The predictions also imply that none of the subsystems will be significantly impacted by the expected beam-gas scattering rates. However, at the time of writing beam background measurements performed during Phase 3 suggest that rates of several types of backgrounds are considerably higher than the simulation estimates. In particular, beam-gas backgrounds are so high that they threaten the operation of Belle II at full luminosities.

These discrepancies between simulations and measurements, which were already emerging in Phase 1 and have been measured by CLAWS, emphasize the requirement for a further investigation of beam backgrounds by dedicated beam background monitors in Phases 2 and 3. Furthermore, the simulations do not include injection backgrounds which will potentially reduce data taking in the PXD and other subsystems by as much as 20%. As a consequence of the differences in the IP chamber, as well as the installation of the final focusing QCS magnets and the damping ring, the injection background rates measured during Phase 1 are not directly comparable to the rates which will be observed in Phases 2 and 3. A priority of the second commissioning phase has therefore been to measure these beam backgrounds and to constrain their impact on the data taking efficiency.

Following its success in Phase 1, the sensor technology and the analysis methodology described in this thesis serve as the basis for new versions of the CLAWS detector system for the second and third commissioning phase of SuperKEKB in 2018 and 2019 onwards. To study injection backgrounds during Phase 2, we installed a fully redesigned system inside the inner part of the Belle II detector. Instead of separate sensor modules we utilized two sensor ladders, each equipped with eight preamplifiers, SiPMs and slightly smaller scintillating tiles located roughly at the position of first layer SVD modules. Based on experiences during Phase 1, we used the same type of preamplifiers, amplifiers and SiPMs but shifted to polyvinyl toluene based scintillator tiles with less radiation hardness but a higher light yield. Phase 1 measurements revealed that especially the background rates during injections are so high that they partially lead to saturation effects in the electronics. To adopt to the even higher background rates expected due to the position very close to the beam pipe and to further increase the dynamic range, the Phase 2 sensors were equipped with a remotely switchable bypass of the preamplifiers. To overcome another shortcoming of Phase 1, namely the high processing time and the insufficient maintainability and extendability, the experimental setup was operated by an entirely new Phase 2 CLAWS DAQ. At the time of writing, the offline analysis of data recorded during Phase 2 is still ongoing. Background studies performed with this data will be natural progressions of the ones presented in this thesis.

The Phase 3 version of the CLAWS system is no longer part of the Belle II detector but is installed around both QCS final focusing magnets. This system represents a permanent installation which will monitor beam backgrounds throughout the entire data taking of SuperKEKB and Belle II. It consists of 32 extensively modified versions of the sensor modules which incorporate a Phase 1 sensor, a Phase 2 like switchable preamplifier bypass and an additional amplifier on a single PCB board. In addition, the modules are connected via a single cable which is simultaneously responsible for signal transmission and power supply. At the time of writing, the system is taking part in the Phase 3 commissioning effort where it provides real time feedback to the operators of the accelerator and the detector. In the future, it is foreseen to upgrade the CLAWS system to a dedicated beam abort system which will protect Belle II from damages due to diverted beams caused by quenches of the QCS magnets.

Appendix A

Distribution of hit energies for cosmic muons

Figures A.1 and A.2 show the distribution of hit energies from cosmic muons recorded with the muon telescope (see Section 5.3) for the remainin three sensors. Results from these measurements are used to validate and optimize the operation of the first part of the data processing, or particle reconstruction (see Section 6.1).

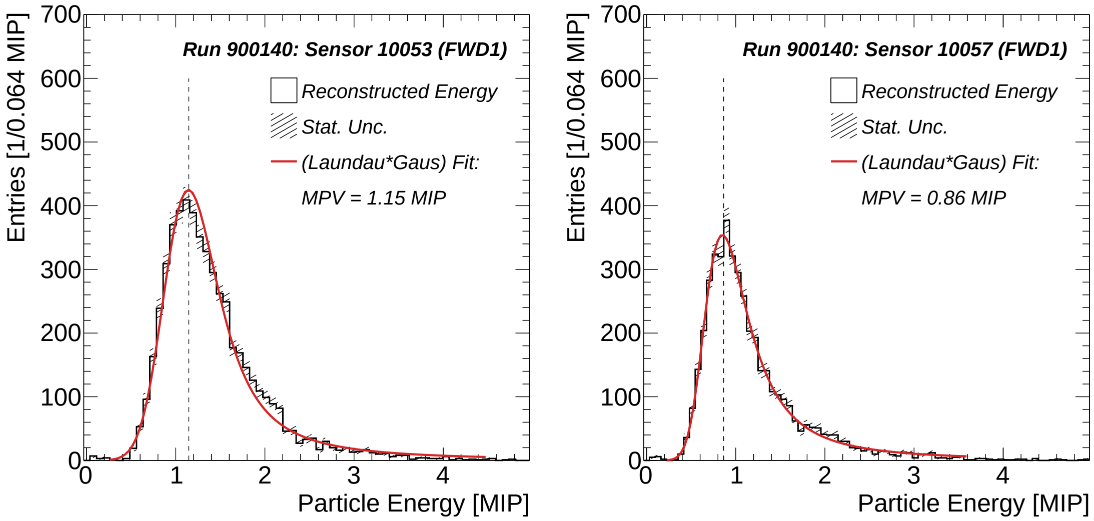

Figure A.1: Distribution of hit energies obtained by applying the particle reconstruction to recordings of cosmic muons taken in the laboratory after runtime of Phase 1 for sensor installed at FWD1 position in the first half (*left*) and second half (*right*) of Phase 1.

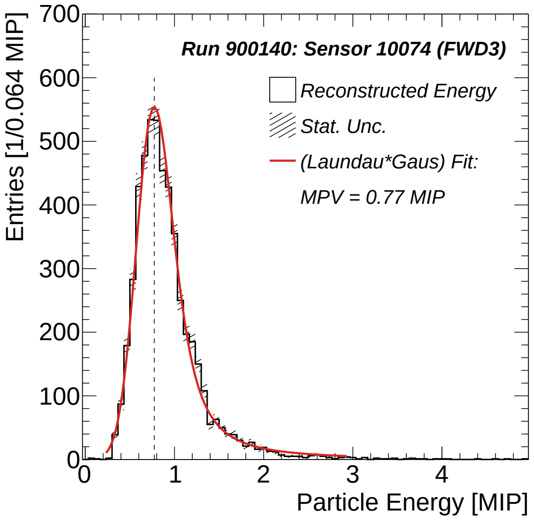

Figure A.2: Distribution of hit energies obtained by applying the particle reconstruction to recordings of cosmic muons taken in the laboratory after runtime of Phase 1 for sensor installed at FWD3.

Appendix B

Additional figures for the time resolved analysis of backgrounds

In this appendix, we provide additional figures from the time resolved analysis of beam backgrounds presented in Chapter 7.

B.1 Averaged reconstructed waveforms

Figures B.1, B.2 and B.3 show the averaged reconstructed waveforms for all three channels stacked on top of each other (*top*) and their cumulatives separately for each channel (*bottom*) for the NI-ALL, NI-HER and NI-LER non-injection data sets, respectively (see Section 7.2.1). Figures B.4, B.5 and B.6 show the averaged reconstructed waveforms for all three channels stacked on top of each other (*top*) and their cumulatives separately for each channel (*bottom*) for the HER-ALL, LER-ALL and LER-VACS injection data sets, respectively (see Section 7.3.1). Figures B.7, B.8 and B.9 show the averaged reconstructed waveforms for all three channels stacked on top of each other (*top*) and their cumulatives separately for each channel (*bottom*) for the HER-PS, HER-VS1 and HER-VS2 data sets from the HER injection study, respectively (see Section 7.3.1). Figures B.10, B.11 and B.12 show the averaged reconstructed waveforms for all three channels stacked on top of each other (*top*) and their cumulatives separately for each channel (*bottom*) for the LER-PS, LER-VS and LER-SA data sets from the LER injection study, respectively (see Section 7.3.1).

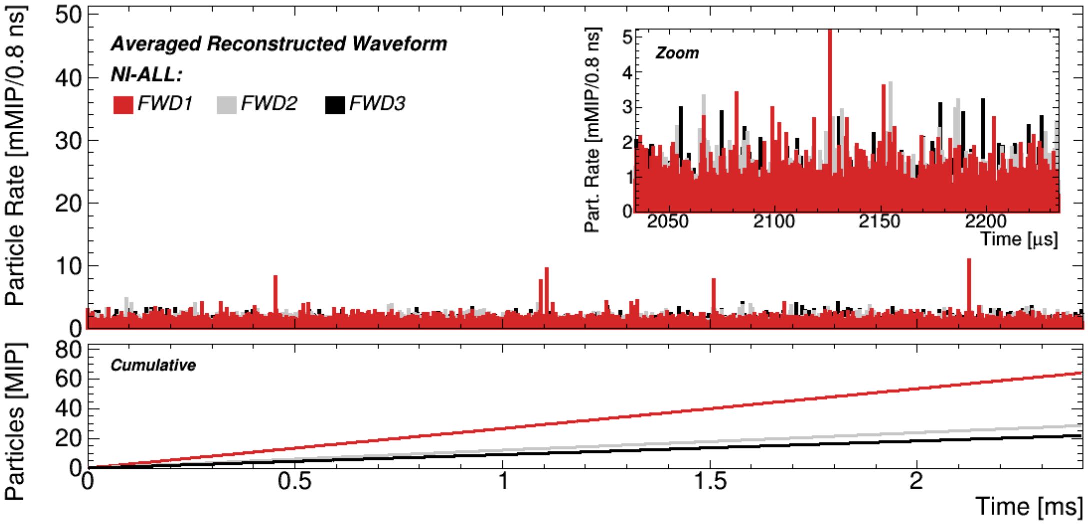

Figure B.1: Background time distribution for the NI-ALL data set for all three channels stacked on top of each other (*top*) and their cumulatives separately for each channel (*bottom*).

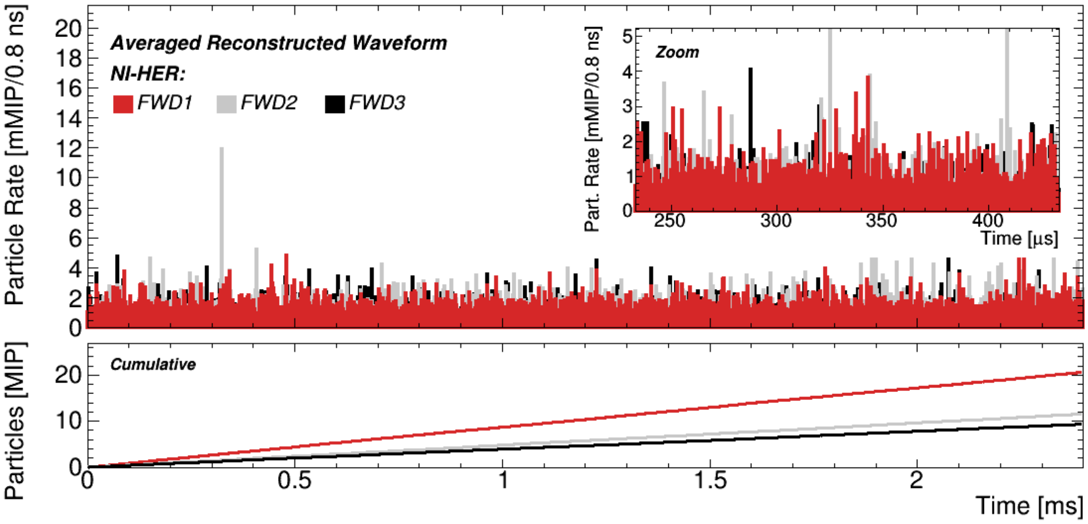

Figure B.2: Background time distribution for the NI-HER data set for all three channels stacked on top of each other (*top*) and their cumulatives separately for each channel (*bottom*).

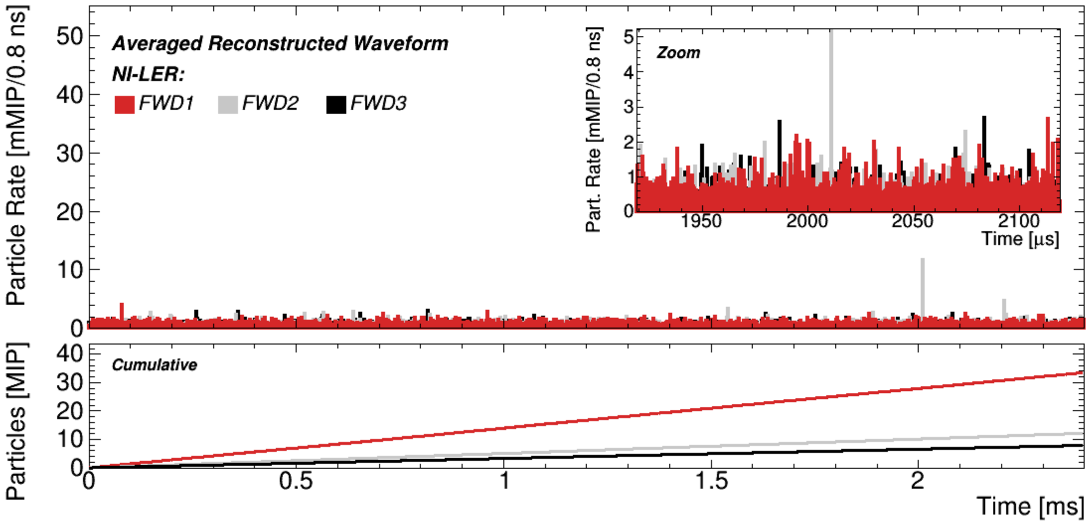

Figure B.3: Background time distribution for the NI-LER data set for all three channels stacked on top of each other (*top*) and their cumulatives separately for each channel (*bottom*).

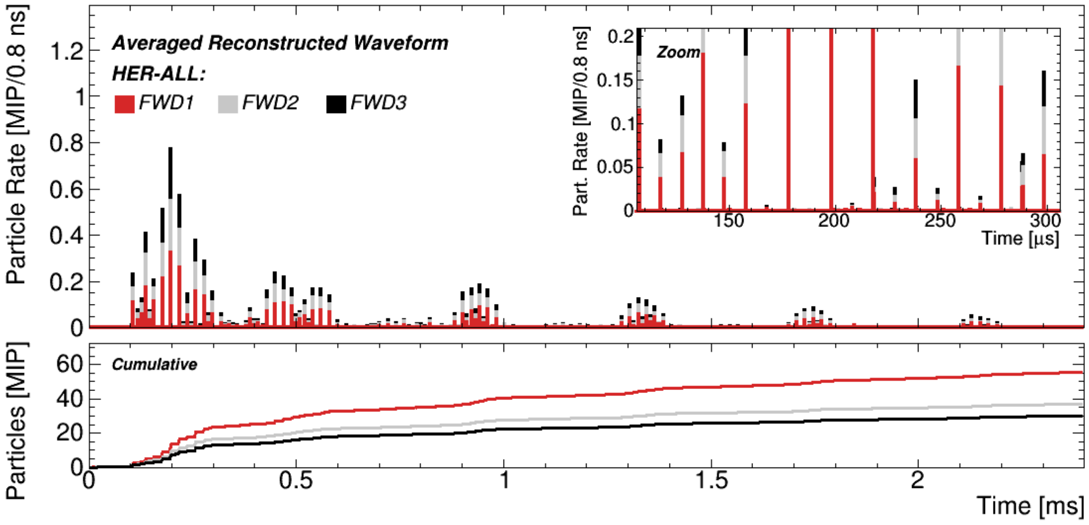

Figure B.4: Background time distribution for the HER-ALL data set for all three channels stacked on top of each other (*top*) and their cumulatives separately for each channel (*bottom*).

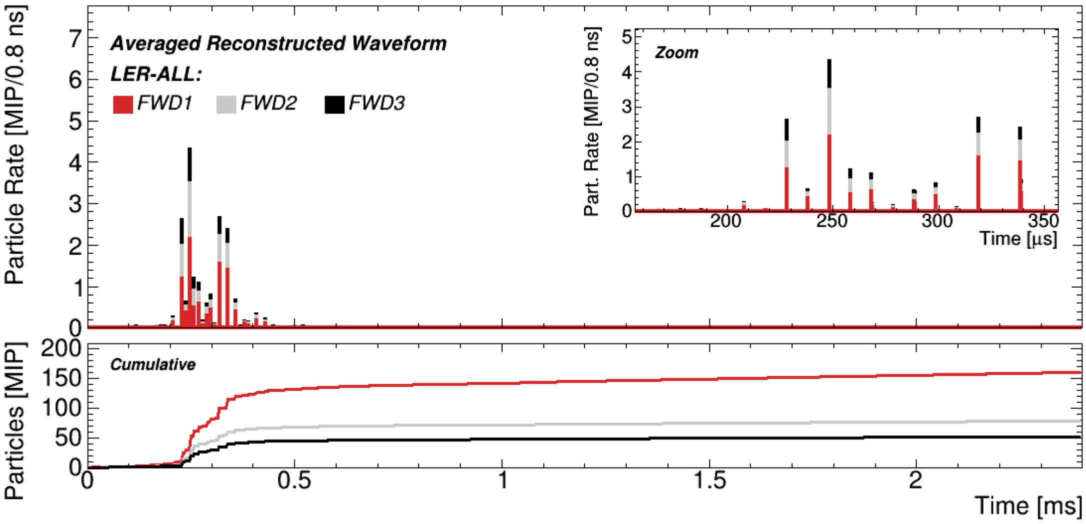

Figure B.5: Background time distribution for the LER-ALL data set for all three channels stacked on top of each other (*top*) and their cumulatives separately for each channel (*bottom*).

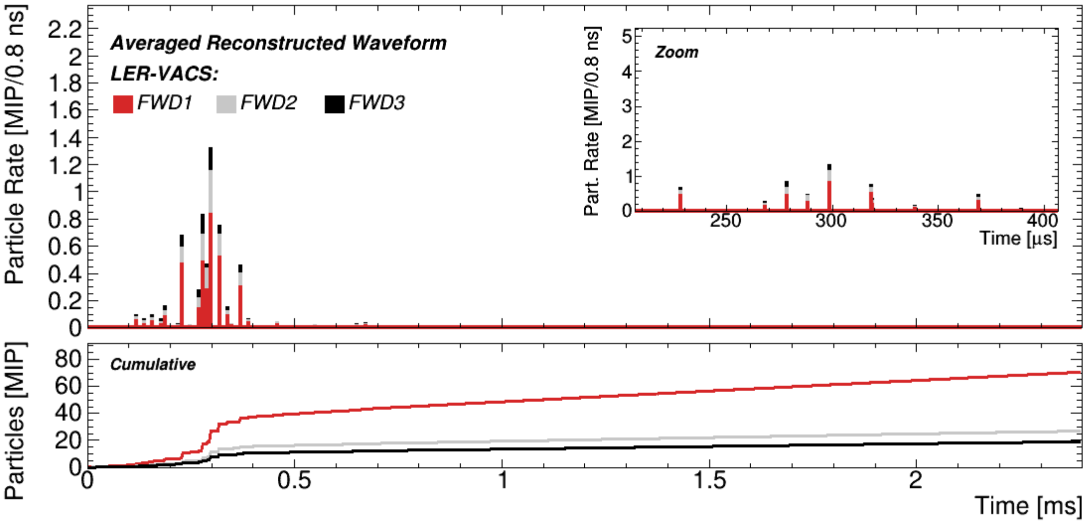

Figure B.6: Background time distribution for the LER-VACS data set for all three channels stacked on top of each other (*top*) and their cumulatives separately for each channel (*bottom*).

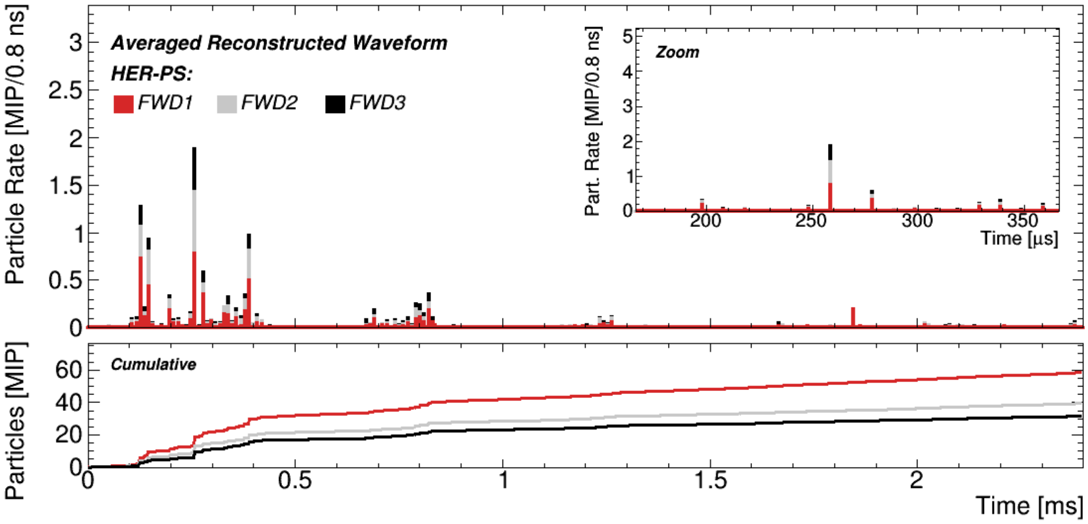

Figure B.7: Background time distribution for the HER-PS data set for all three channels stacked on top of each other (*top*) and their cumulatives separately for each channel (*bottom*).

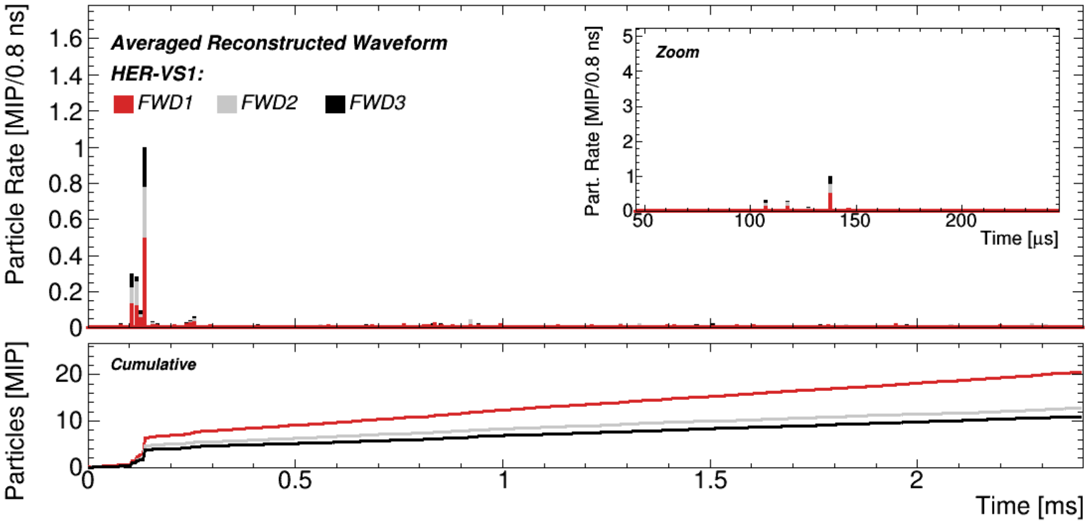

Figure B.8: Background time distribution for the HER-VS1 data set for all three channels stacked on top of each other (*top*) and their cumulatives separately for each channel (*bottom*).

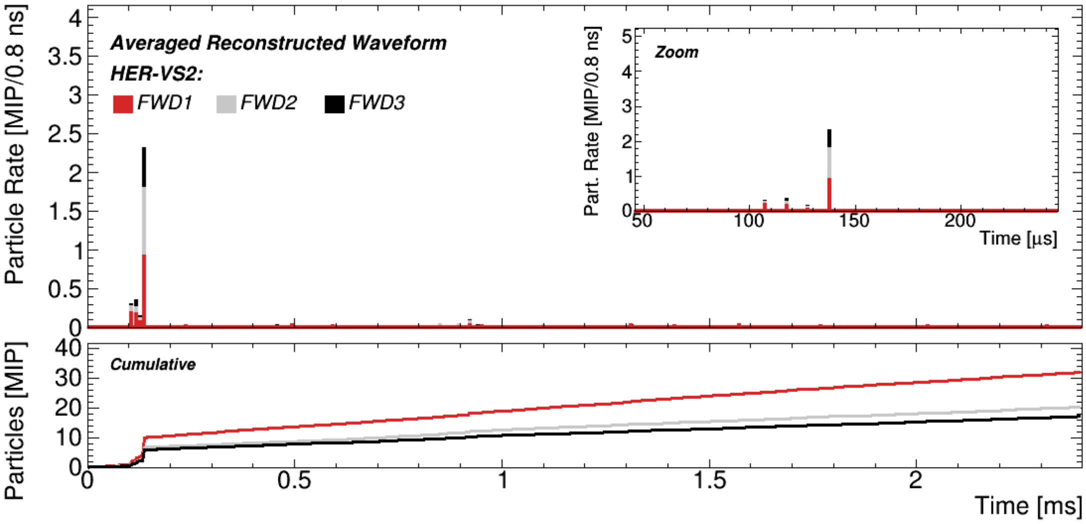

Figure B.9: Background time distribution for the HER-VS2 data set for all three channels stacked on top of each other (*top*) and their cumulatives separately for each channel (*bottom*).

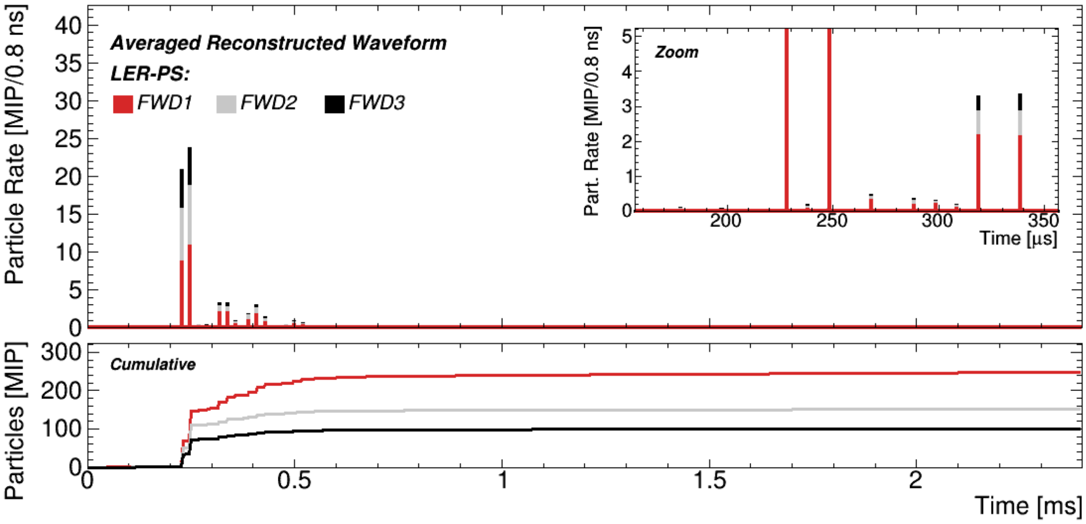

Figure B.10: Background time distribution for the LER-PS data set for all three channels stacked on top of each other (*top*) and their cumulatives separately for each channel (*bottom*).

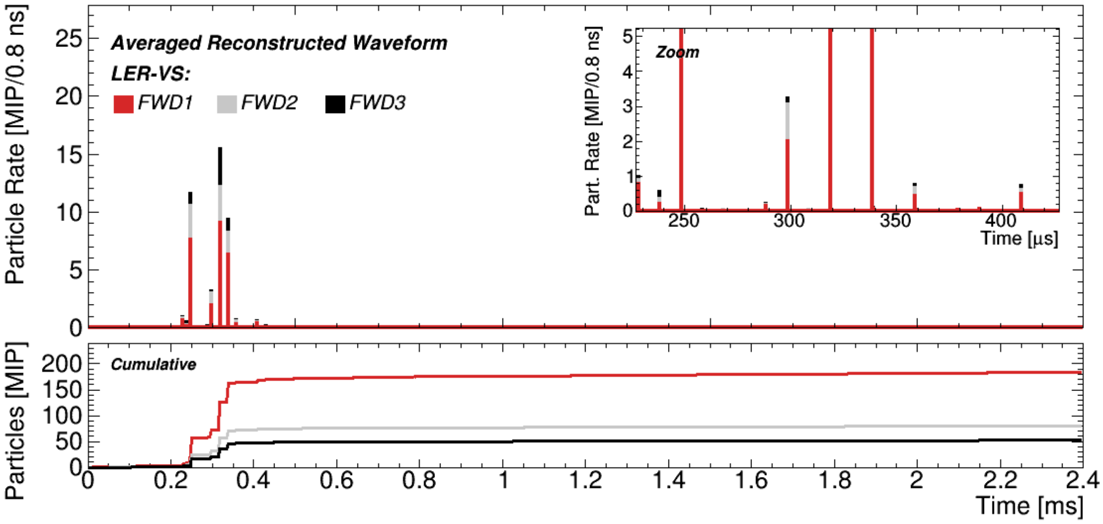

Figure B.11: Background time distribution for the LER-VS data set for all three channels stacked on top of each other (*top*) and their cumulatives separately for each channel (*bottom*).

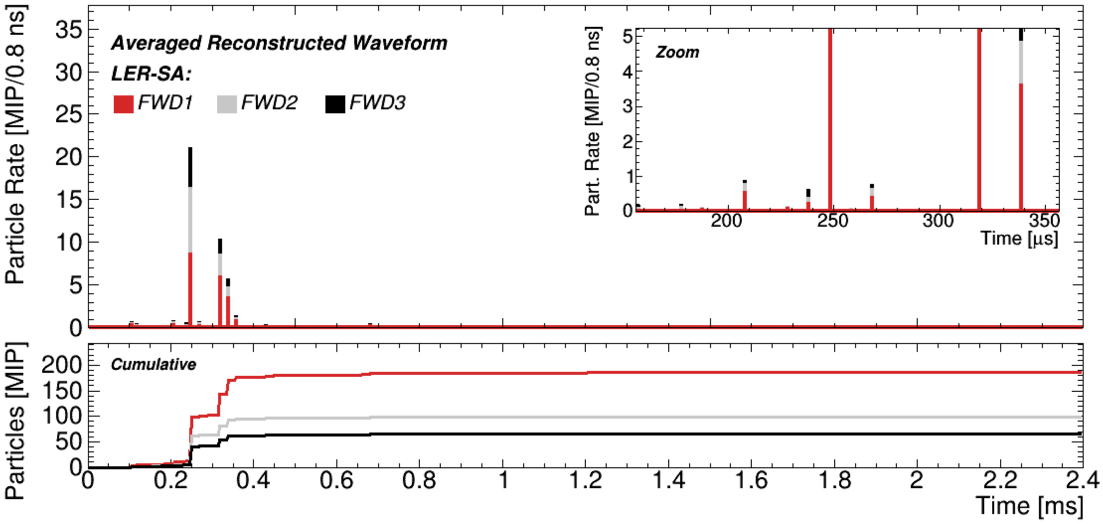

Figure B.12: Background time distribution for the LER-SA data set for all three channels stacked on top of each other (*top*) and their cumulatives separately for each channel (*bottom*).

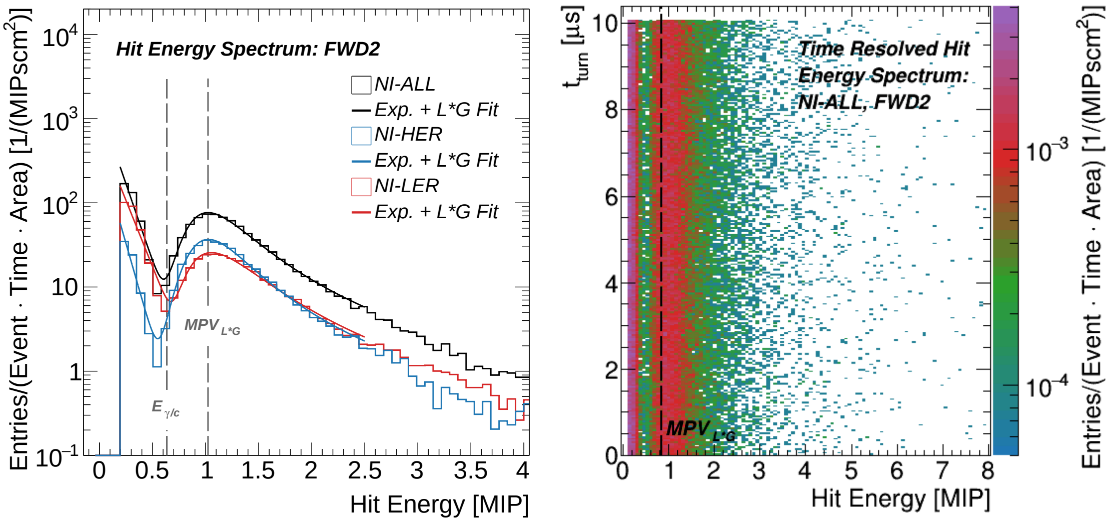

Figure B.13: Distributions of hit energies for given non-injection data sets for the channel FWD2 (*left*). The distribution of the time in turn versus the hit energy, or time resolved hit energy distribution, for NI-ALL for channel FWD2 (*right*). All distributions are normalized to the number of events, the length of the waveforms and the area of the sensors.

B.2 Hit energy spectra

Figure B.13 compares the hit energy spectra of the NI-HER, NI-LER and NI-ALL data sets (*left*) and shows the time resolved hit energy distribution for the NI-ALL set (*right*) for channel FWD2 (see Section 7.2.2). Figure B.14 compares the hit energy spectra of the NI-HER, NI-LER and NI-ALL data sets (*left*) and shows the time resolved hit energy distribution for the NI-ALL set (*right*) for channel FWD3 (see Section 7.2.2). Figure B.15 compares the hit energy spectra of different HER injection data sets to the corresponding non-injection data set NI-HER (*left*) and the hit energy spectra of different LER injection data sets to the corresponding non-injection data set NI-LER (*right*) for channel FWD2 (see Section 7.3.2). Figure B.16 compares the hit energy spectra of different HER injection data sets to the corresponding non-injection data set NI-HER (*left*) and the hit energy spectra of different LER injection data sets to the corresponding non-injection data set NI-LER (*right*) for channel FWD3 (see Section 7.3.2). Figure B.17 shows the time resolved hit energy spectrum for the HER-ALL (*left*) and the LER-ALL (*right*) data sets for channel FWD2 (see Section 7.3.2). Figure B.18 shows the time resolved hit energy spectrum for the HER-ALL (*left*) and the LER-ALL (*right*) data sets for channel FWD3 (see Section 7.3.2).

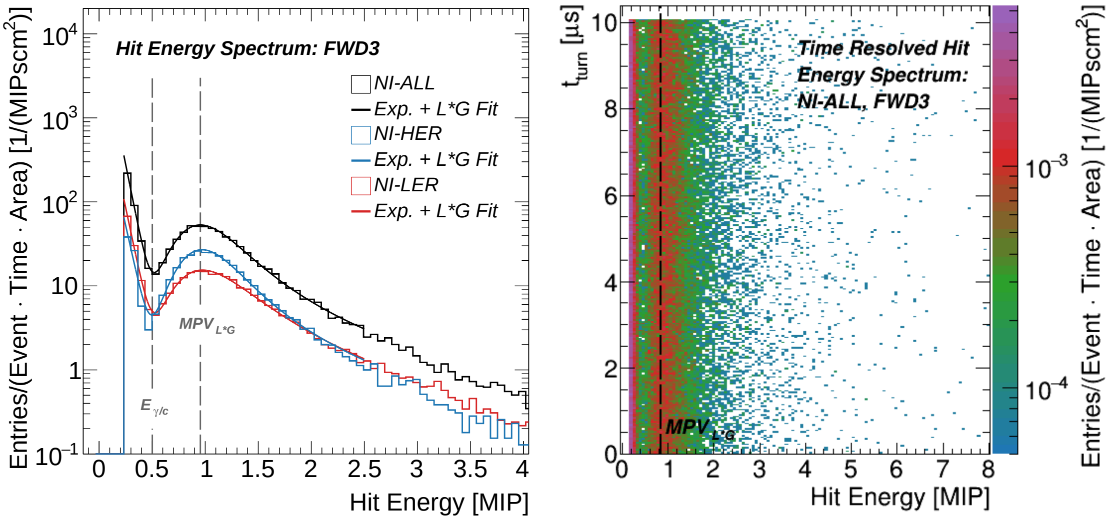

Figure B.14: Distributions of hit energies for given non-injection data sets for the channel FWD3 (*left*). The distribution of the time in turn versus the hit energy, or time resolved hit energy distribution, for NI-ALL for channel FWD2 (*right*). All distributions are normalized to the number of events, the length of the waveforms and the area of the sensors.

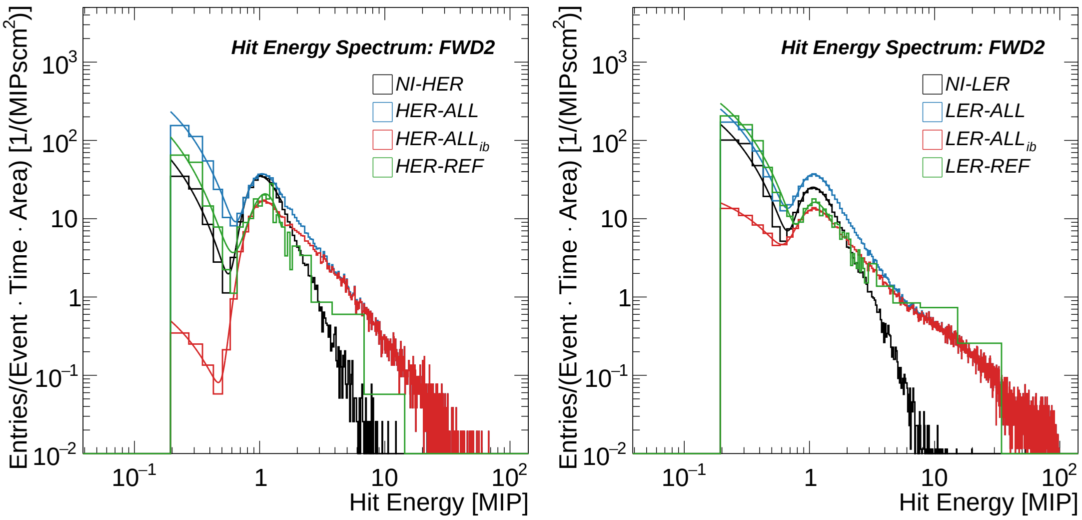

Figure B.15: Distributions of hit energies for the given HER (*left*) and LER (*right*) injection data sets for channel FWD1. The distributions are normalized to the length of the waveforms, the area of the sensors and the number of events. For the HER-REF and LER-REF data sets, the bin size for higher energies is logarithmic due to limited statistics.

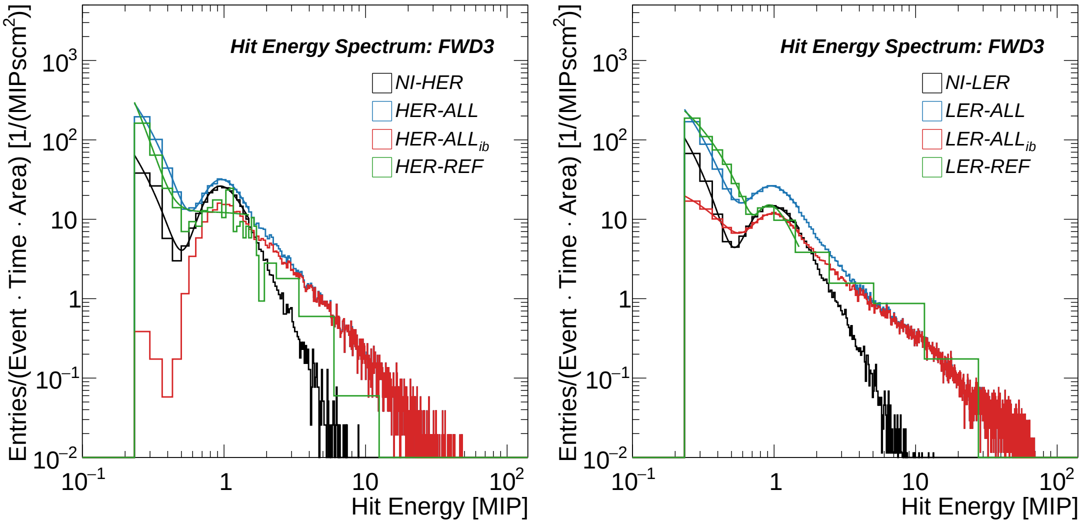

Figure B.16: Distributions of hit energies for the given HER (*left*) and LER (*right*) injection data sets for channel FWD1. The distributions are normalized to the length of the waveforms, the area of the sensors and the number of events. For the HER-REF and LER-REF data sets, the bin size for higher energies is logarithmic due to limited statistics.

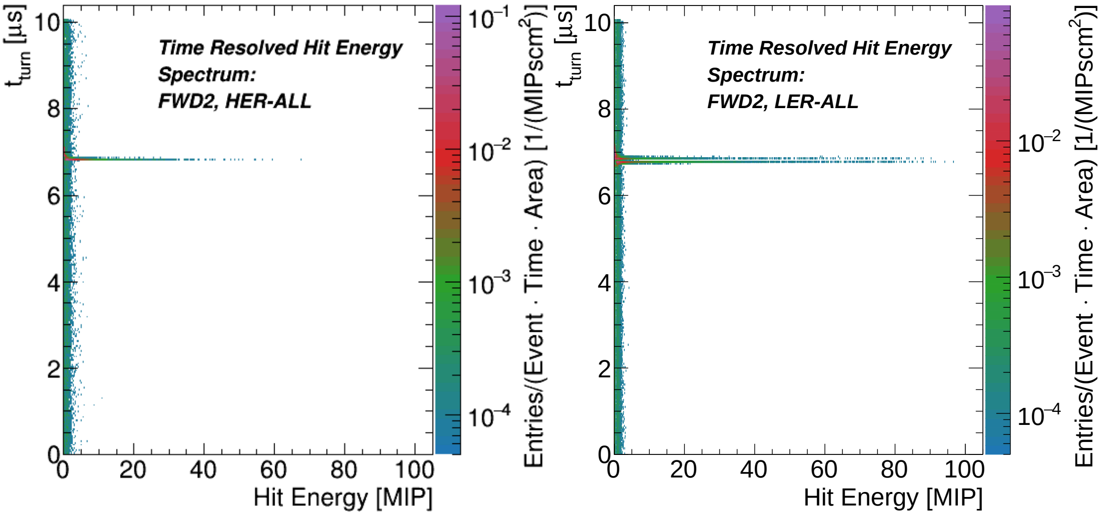

Figure B.17: The distributions of hits for the time in turn, t_{turn}, versus the hit energy for HER-ALL (*left*) and LER-ALL (*right*) for channel FWD1. Both distributions are normalized to the length of the waveforms, the area of the sensors and the number of events.

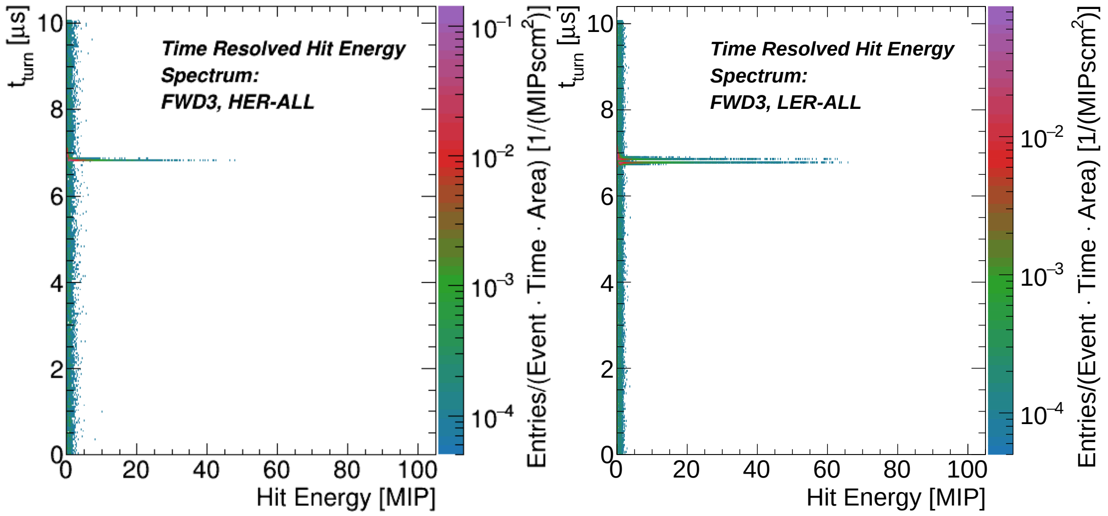

Figure B.18: The distributions of hits for the time in turn, t_{turn}, versus the hit energy for HER-ALL (*left*) and LER-ALL (*right*) for channel FWD1. Both distributions are normalized to the length of the waveforms, the area of the sensors and the number of events.

B.3 Rate in turn

Figure B.19 shows the averaged particle rate as a function of the t_{turn} (*left*) and a zoom into the region around the peak associated with the injection bunch for the same distribution (*right*) for the HER-REF data set for channel FWD2 (see Section 7.3.1). Figure B.20 shows the averaged particle rate as a function of the t_{turn} (*left*) and a zoom into the region around the peak associated with the injection bunch for the same distribution (*right*) for the HER-REF data set for channel FWD3 (see Section 7.3.1).

Figure B.21 shows the averaged particle rate as a function of the t_{turn} (*left*) and a zoom into the region around the peak associated with the injection bunch for the same distribution (*right*) for the LER-VACS data set for channel FWD2 (see Section 7.3.1). Figure B.22 shows the averaged particle rate as a function of the t_{turn} (*left*) and a zoom into the region around the peak associated with the injection bunch for the same distribution (*right*) for the LER-VACS data set for channel FWD3 (see Section 7.3.1).

B.4 Decay behavior

Figure B.23 compares the fraction of E_{ib}/E (*left*) and the fraction of $E_{ib}(t < 500\,\mu s)$ for the HER-ALL and the LER-ALL data sets for channel FWD2 (see Section 7.3.3).

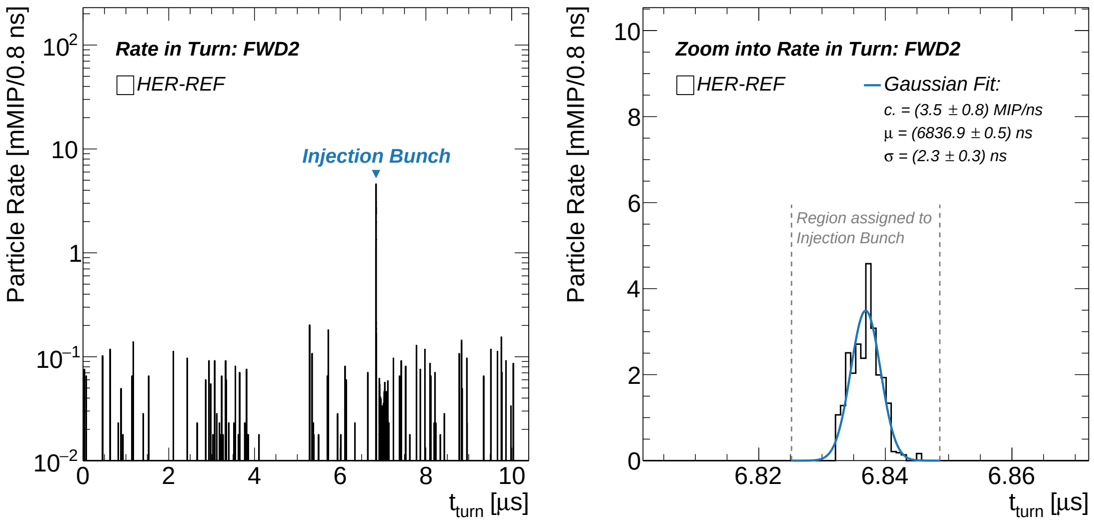

Figure B.19: Averaged particle rate as a function of the time in turn for the HER-REF data set and channel FWD2 (*left*). Cutout highlighting the part associated with signals of the injection bunch (*right*). The distribution is normalized to the ratio of the length of the waveforms to T_{rev} (i.e. the number of turns) and to the number of events. Stated parameters and corresponding uncertainties are obtain by a maximum likelihood fit with a Gaussian to the injection bunch signal region.

Figure B.24 compares the fraction of E_{ib}/E (*left*) and the fraction of $E_{ib}(t < 500\,\mu\text{s})$ for the HER-ALL and the LER-ALL data sets for channel FWD3 (see Section 7.3.3). Figure B.25 shows the distributions of the time of the last transit for the HER-ALL (*left*) and LER-ALL (*right*) data sets for channel FWD2 (see Section 7.3.3). Figure B.26 shows the distributions of the time of the last transit for the HER-ALL (*left*) and LER-ALL (*right*) data sets for channel FWD3 (see Section 7.3.3).

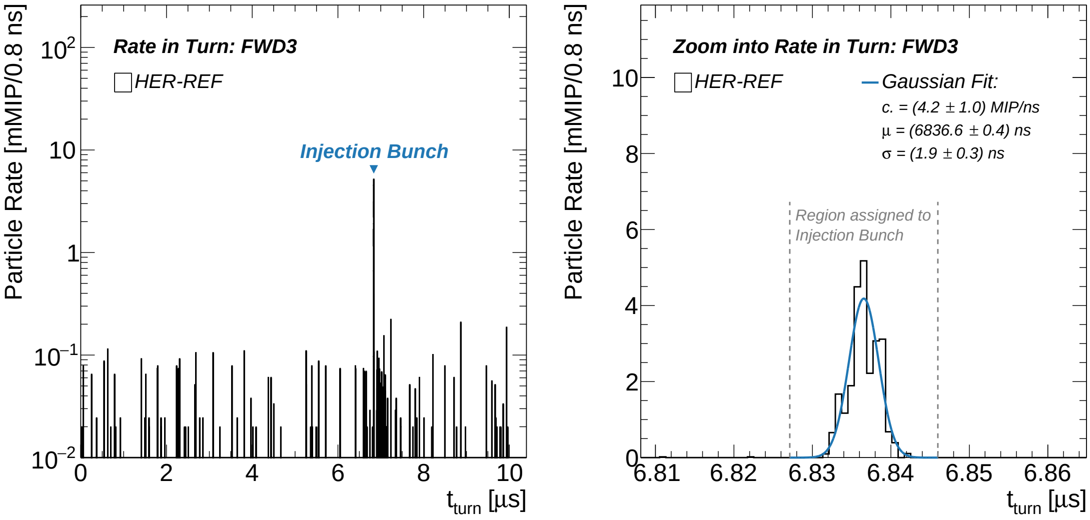

Figure B.20: Averaged particle rate as a function of the time in turn for the HER-REF data set and channel FWD3 (*left*). Cutout highlighting the part associated with signals of the injection bunch (*right*). The distribution is normalized to the ratio of the length of the waveforms to T_{rev} (i.e. the number of turns) and to the number of events. Stated parameters and corresponding uncertainties are obtain by a maximum likelihood fit with a Gaussian to the injection bunch signal region.

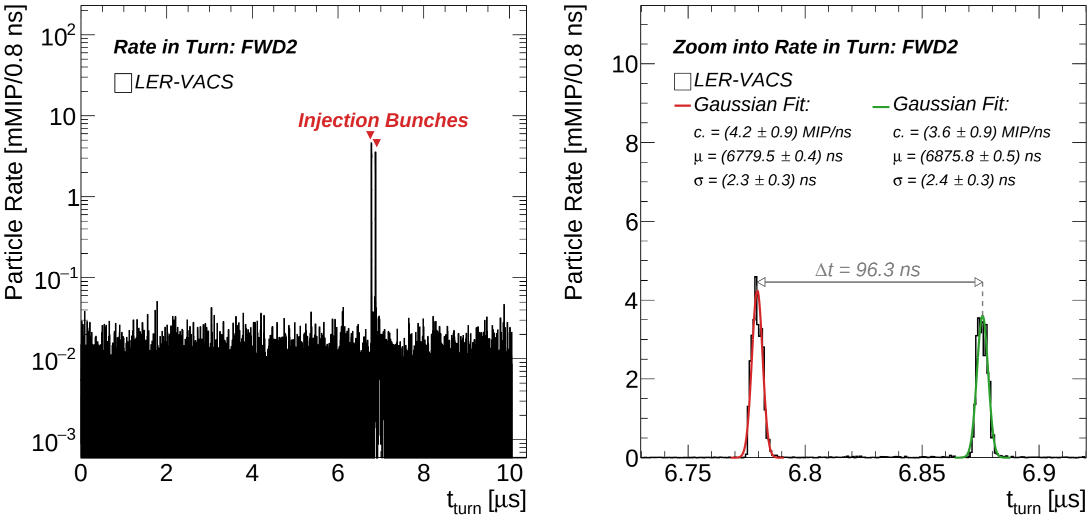

Figure B.21: Averaged particle rate as a function of the time in turn for the LER-VACS data set for channel FWD2 (*left*). Cutout highlighting the part associated with signals of the injection bunches (*right*). The distribution is normalized to the ratio of the length of the waveforms to T_{rev} (i.e. the number of turns) and to the number of events. Stated parameters and corresponding uncertainties are obtain by maximum likelihood fits with Gaussians to the injection bunch signal region.

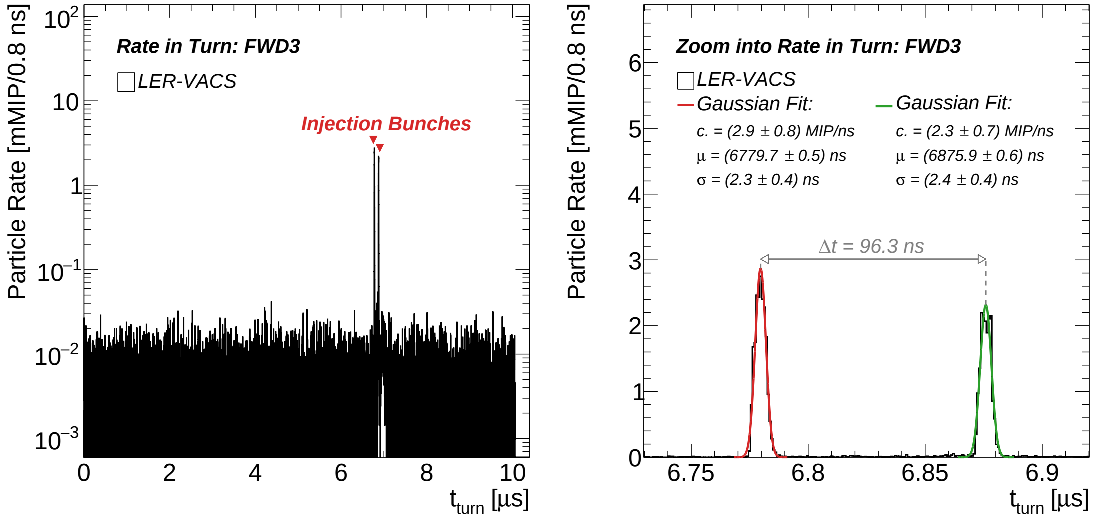

Figure B.22: Averaged particle rate as a function of the time in turn for the LER-VACS data set for channel FWD3 (*left*). Cutout highlighting the part associated with signals of the injection bunches (*right*). The distribution is normalized to the ratio of the length of the waveforms to T_{rev} (i.e. the number of turns) and to the number of events. Stated parameters and corresponding uncertainties are obtain by maximum likelihood fits with Gaussians to the injection bunch signal region.

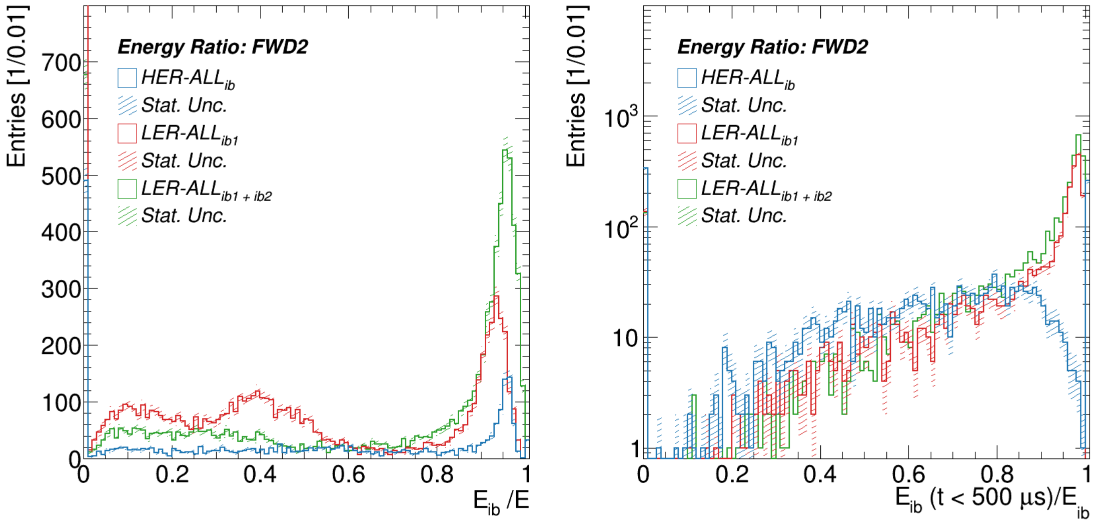

Figure B.23: Distributions of ratios of energy deposited only by the injected bunch, E_{ib}, to the total energy, E, for channel FWD1 (*left*). Distributions of ratios of energy deposited by the injected bunch within the first 500 µs after the first transit, $E_{ib}(t < 0.5\,\mu s)$, to the full bunch energy, E_{ib} for channel FWD1 (*right*).

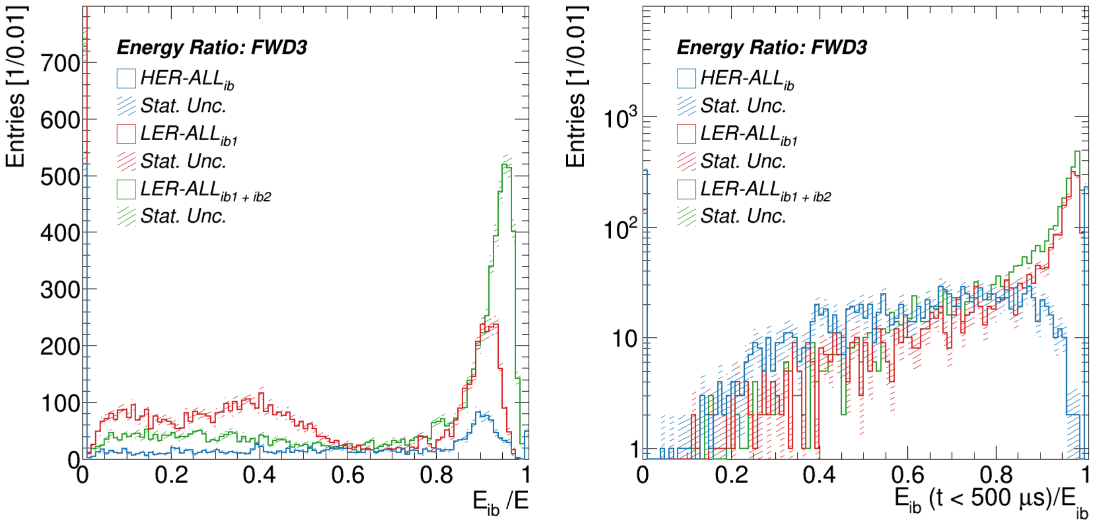

Figure B.24: Distributions of ratios of energy deposited only by the injected bunch, E_{ib}, to the total energy, E, for channel FWD1 (*left*). Distributions of ratios of energy deposited by the injected bunch within the first 500 µs after the first transit, $E_{ib}(t < 0.5\,\mu\text{s})$, to the full bunch energy, E_{ib} for channel FWD1 (*right*).

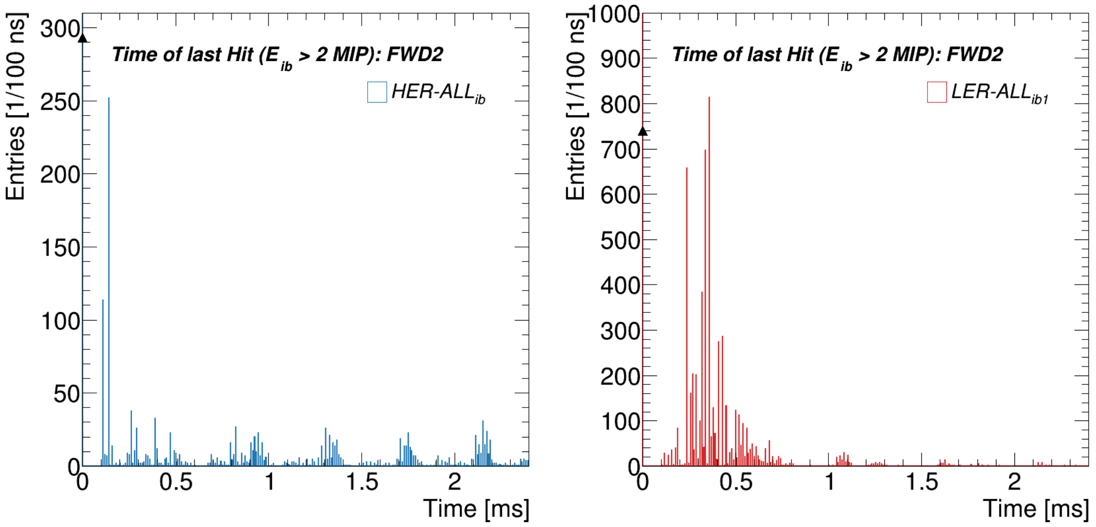

Figure B.25: Distributions of the time of the last transit in which the energy per transit was larger than 2 MIP for channel FWD1 for HER-ALL (*left*) and LER-ALL (*right*).

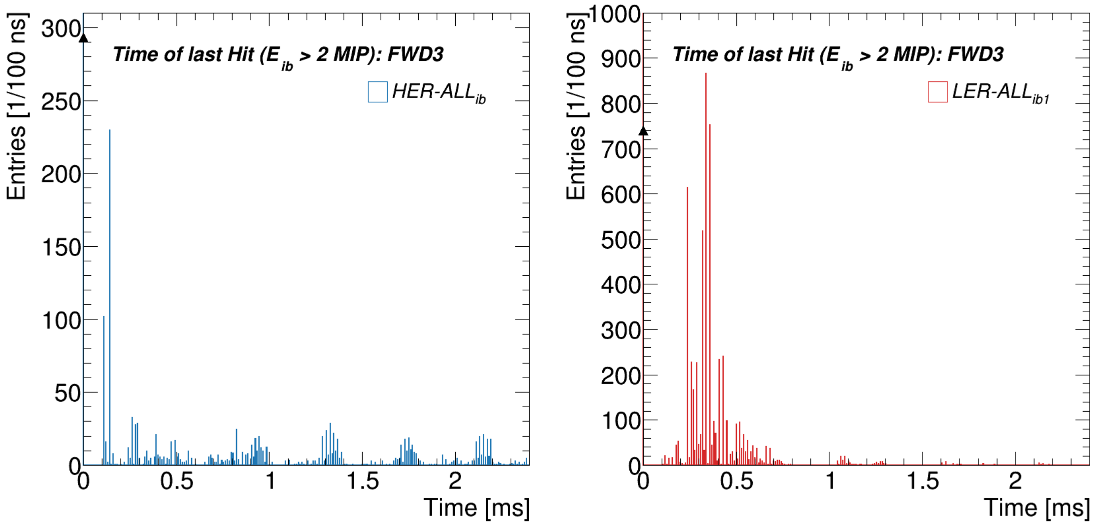

Figure B.26: Distributions of the time of the last transit in which the energy per transit was larger than 2 MIP for channel FWD1 for HER-ALL (*left*) and LER-ALL (*right*).

Appendix C

Additional figures for the study of timing patterns

In this appendix, we provide additional figures for the channels FWD2 and FWD3 for the the PEAK analysis and the FFT analysis presented in Chapter 8.

C.1 PEAK analysis

Figures C.1 (FWD2) and C.2 (FWD3) show the distribution of weighted distances for a PEAK analysis applied to the LER-ALL data set (see Section 8.1). Subsequently, Figures C.3 (FWD2) and C.4 (FWD3) compare the ranges of the weighted distance distributions which highlight the effects of the on/off-pattern and the long betatron pattern for the HER-REF (*left*) and the LER-REF (*right*) data sets (see Section 8.1). Finally, Figures C.5 (FWD2) and C.6 (FWD3) present the full PEAK spectrum for the HER-ALL (*left*) and the LER-ALL (*right*) data sets which highlight the response form synchrotron oscillations performed by the newly injected beam particles (see Section 8.1).

C.2 FFT analysis

Figures C.7 (FWD2) and C.8 (FWD3) show the frequency spectrum as a result of a discrete Fourier transform applied to the NI-VACS data set (see Section 8.2). In addition, Figures C.9 (FWD2) and C.10 (FWD3) show the frequency spectrum obtained from a discrete Fourier transform applied to the LER-ALL data set (see Section 8.2).

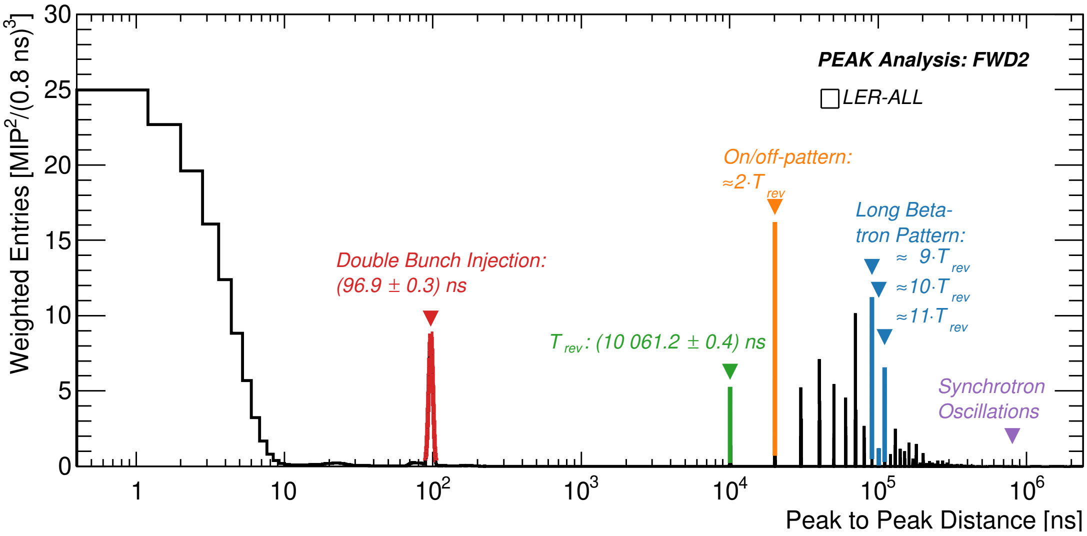

Figure C.1: Distribution of weighted distances between signals for the LER-ALL data set for channel FWD2. Colored Gaussian fits and corresponding labels indicate responses of specific timing patterns connected to properties of the accelerator.

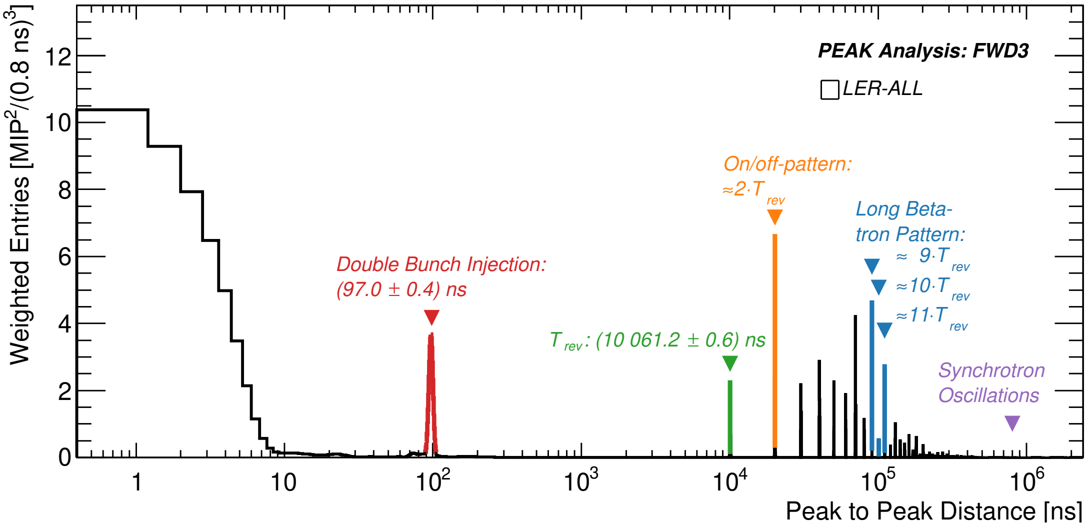

Figure C.2: Distribution of weighted distances between signals for the LER-ALL data set for channel FWD3. Colored Gaussian fits and corresponding labels indicate responses of specific timing patterns connected to properties of the accelerator.

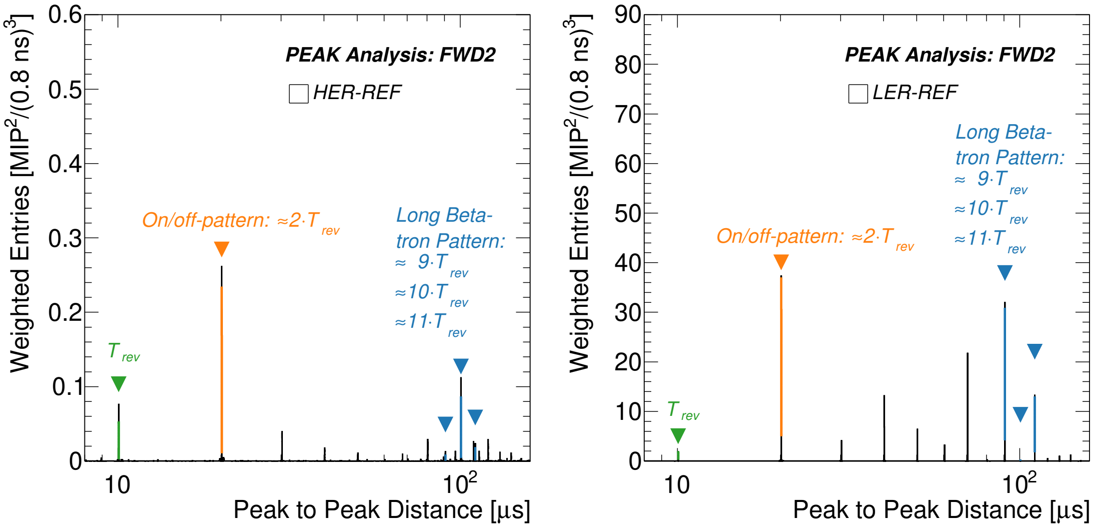

Figure C.3: Section of the distributions of weighted distances between signals for HER-REF (left) and LER-REF (right) data sets for channel FWD2. Colored Gaussian fits and corresponding labels indicate response of specific timing patterns connected to properties of the accelerator.

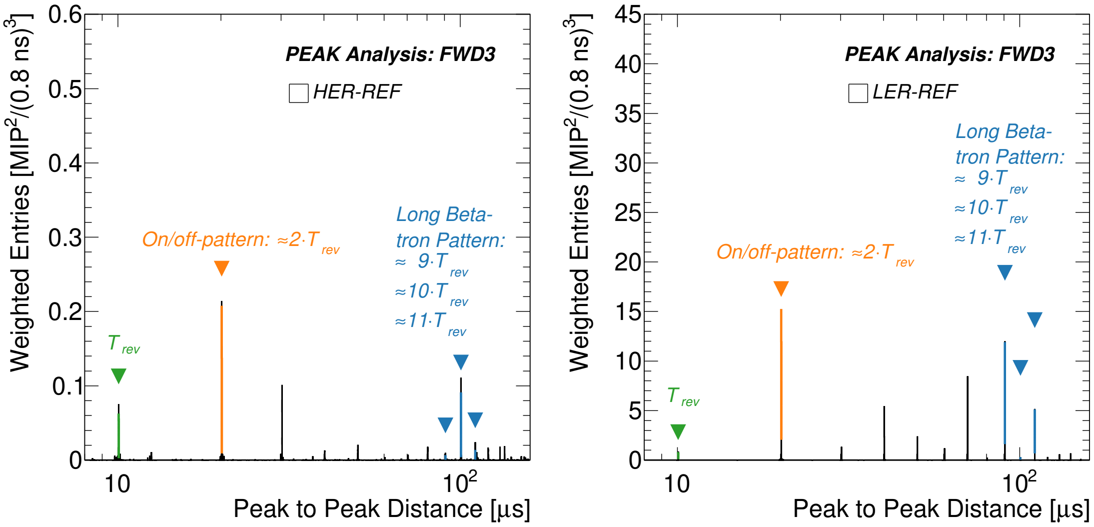

Figure C.4: Section of the distributions of weighted distances between signals for HER-REF (left) and LER-REF (right) data sets for channel FWD3. Colored Gaussian fits and corresponding labels indicate response of specific timing patterns connected to properties of the accelerator.

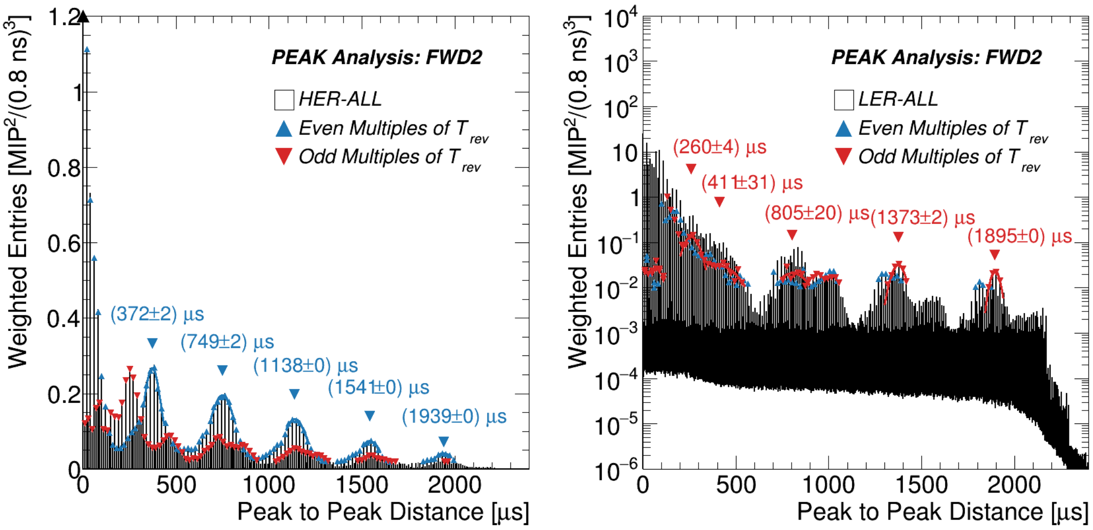

Figure C.5: Distributions of weighted peak distances for HER-ALL (left) and LER-ALL (right) data sets for channel FWD2. Colors and markers indicate responses attributed to odd and even numbered transits of the injected bunch at the IP.

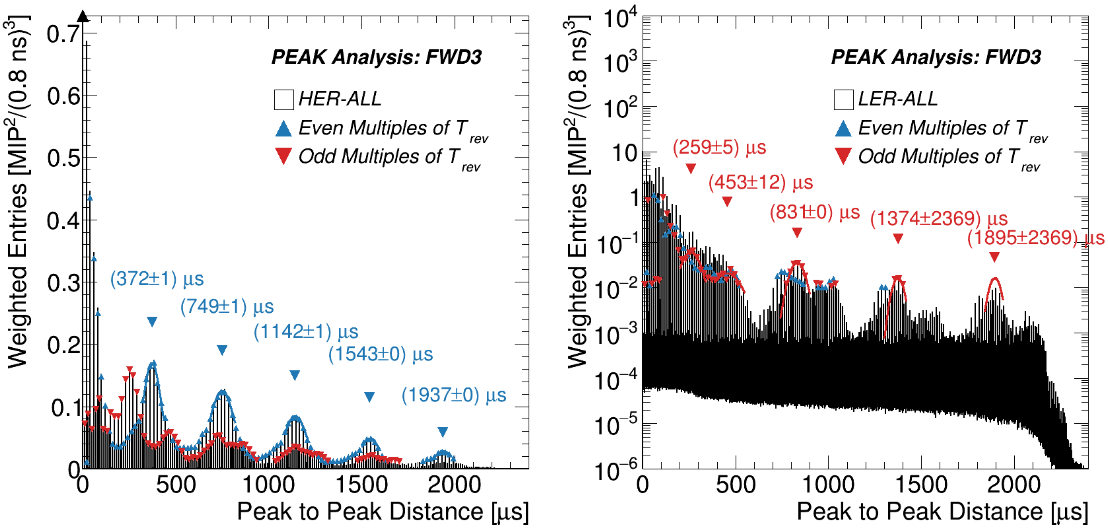

Figure C.6: Distributions of weighted peak distances for HER-ALL (left) and LER-ALL (right) data sets for channel FWD3. Colors and markers indicate responses attributed to odd and even numbered transits of the injected bunch at the IP.

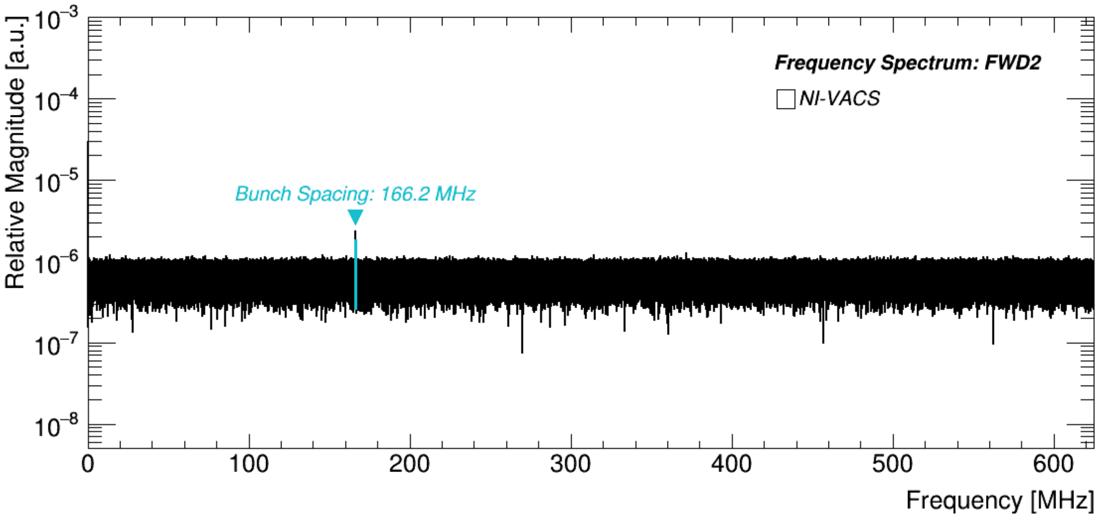

Figure C.7: Frequency spectrum as a result of a discrete Fourier transform of the NI-VACS data set for channel FWD2. Spectrum is normalized to unity in order to show relative magnitudes of the respective frequencies.

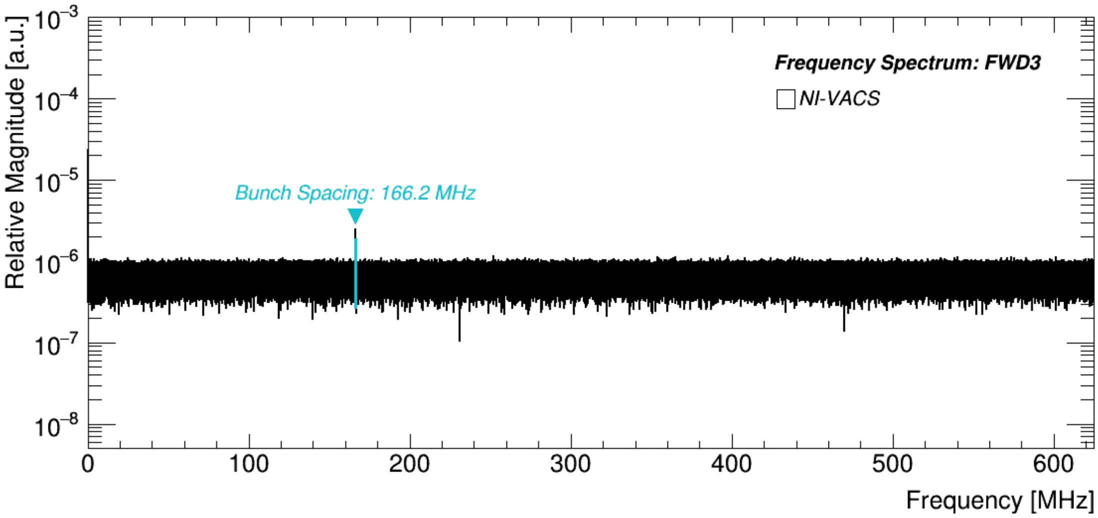

Figure C.8: Frequency spectrum as a result of a discrete Fourier transform of the NI-VACS data set for channel FWD3. Spectrum is normalized to unity in order to show relative magnitudes of the respective frequencies.

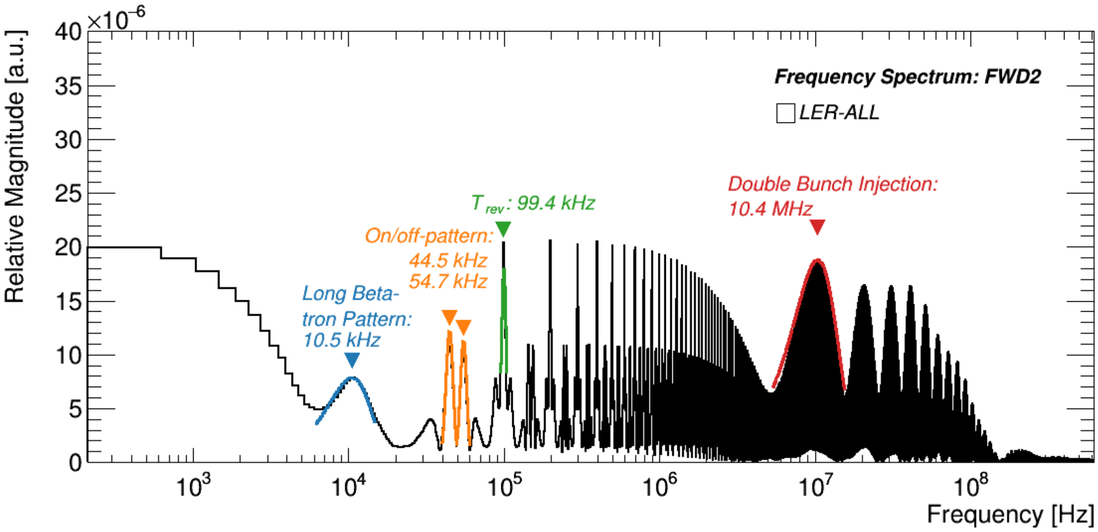

Figure C.9: Frequency spectrum as a result of a discrete Fourier transform of the LER-ALL data set for channel FWD2. Spectrum is normalized to unity in order to show relative magnitudes of the respective frequencies.

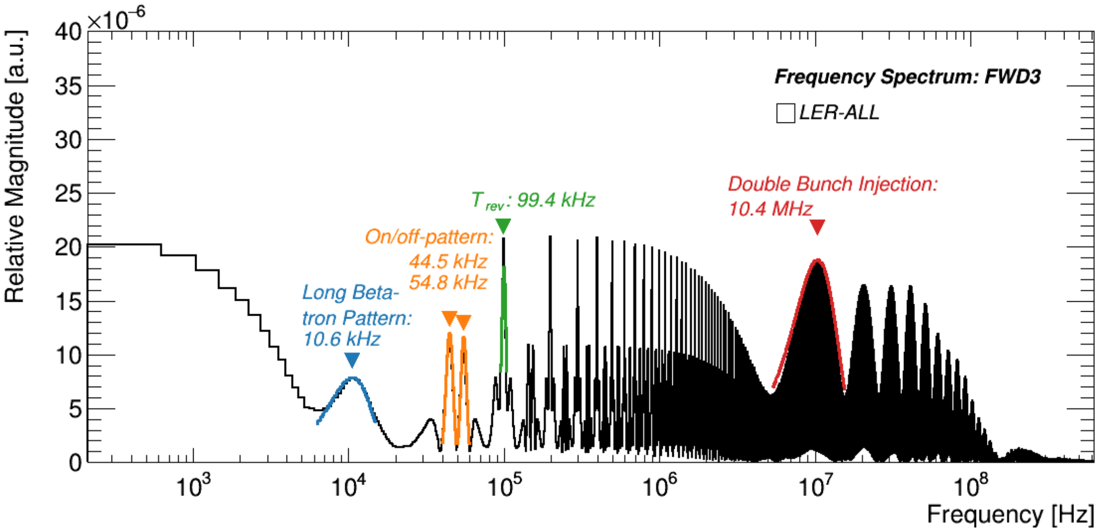

Figure C.10: Frequency spectrum as a result of a discrete Fourier transform of the LER-ALL data set for channel FWD3. Spectrum is normalized to unity in order to show relative magnitudes of the respective frequencies.

Appendix D

Additional figures for the beam-gas and Touschek study

In this appendix, we provide additional figures for the channels FWD2 and FWD3 for the combined measurement of beam-gas and Touschek backgrounds presented in Chapter 9. Figures D.1 (FWD2) and D.2 (FWD3) show the final fits using the most-predictive CCG for the size sweep scans in the HER (*left*) and the LER (*right*) (see Section 9.3).

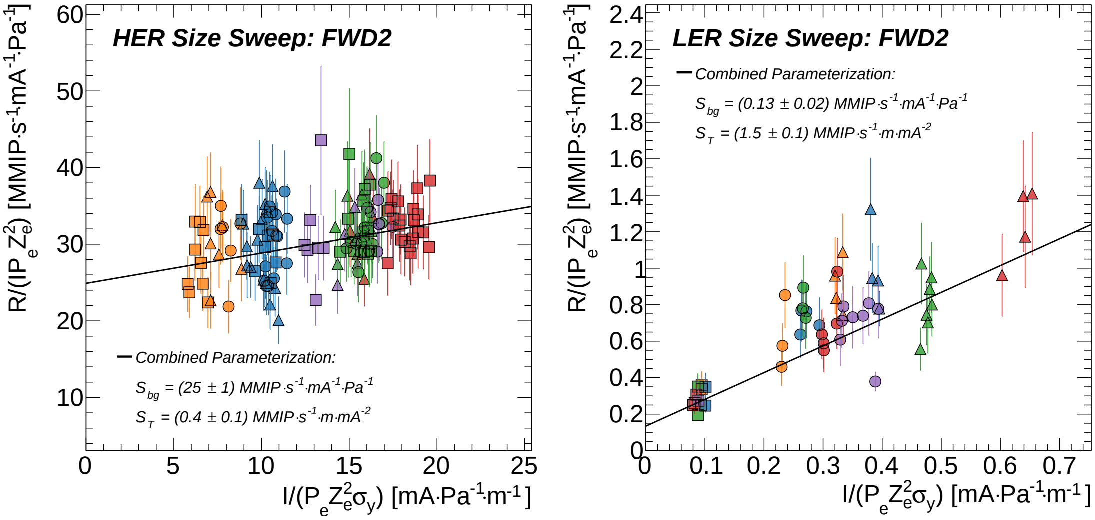

Figure D.1: Fit of the combined parameterization of beam-gas and Touschek backgrounds given by Equation 9.5 to data obtained in size-sweep scans for the HER (*left*) and the LER (*right*) for channel FWD2. Shapes reflect different beam currents, whereas colors indicate vertical beam sizes. Uncertainties on the data are solely statistical; uncertainties on the parameters are adopted from the fit.

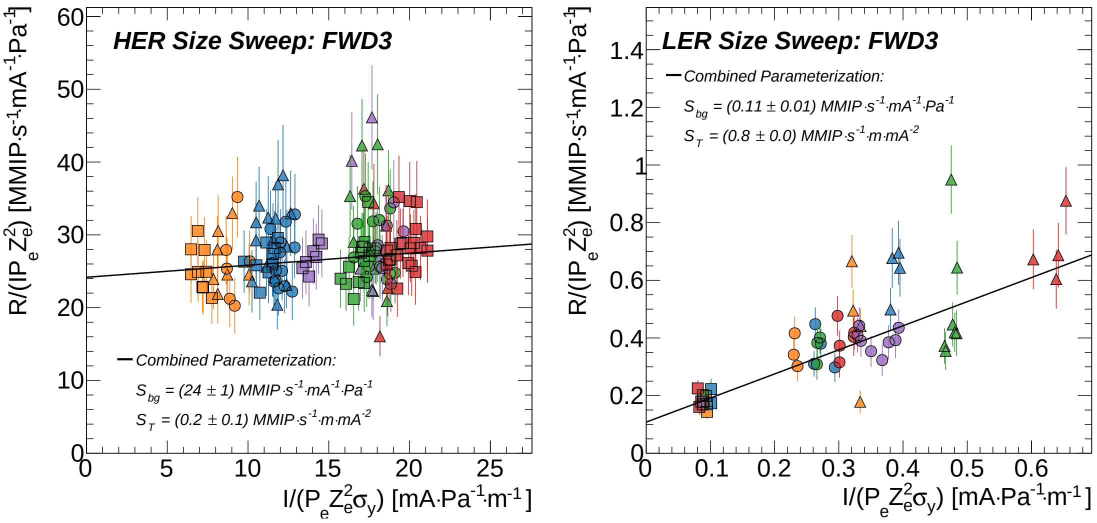

Figure D.2: Fit of the combined parameterization of beam-gas and Touschek backgrounds given by Equation 9.5 to data obtained in size-sweep scans for the HER (*left*) and the LER (*right*) for channel FWD3. Shapes reflect different beam currents, whereas colors indicate vertical beam sizes. Uncertainties on the data are solely statistical; uncertainties on the parameters are adopted from the fit.

Bibliography

[1] Planck, R. Adam et al.,
Planck 2015 results. I. Overview of products and scientific results,
Astron. Astrophys. **594** (2016) A1, arXiv: `1502.01582 [astro-ph.CO]`.

[2] ATLAS, G. Aad et al., *Observation of a new particle in the search for the Standard Model Higgs boson with the ATLAS detector at the LHC*,
Phys. Lett. **B716** (2012) p. 1, arXiv: `1207.7214 [hep-ex]`.

[3] CMS, S. Chatrchyan et al., *Observation of a New Boson at a Mass of 125 GeV with the CMS Experiment at the LHC*, Phys. Lett. **B716** (2012) p. 30,
arXiv: `1207.7235 [hep-ex]`.

[4] Super-Kamiokande, Y. Fukuda et al.,
Measurements of the solar neutrino flux from Super-Kamiokande's first 300 days,
Phys. Rev. Lett. **81** (1998) p. 1158, [Erratum: Phys. Rev. Lett.81,4279(1998)],
arXiv: `hep-ex/9805021 [hep-ex]`.

[5] B. T. Cleveland et al., *Measurement of the solar electron neutrino flux with the Homestake chlorine detector*, Astrophys. J. **496** (1998) p. 505.

[6] J. H. Christenson et al., *Evidence for the* 2π *Decay of the* K_2^0 *Meson*,
Phys. Rev. Lett. **13** (1964) p. 138.

[7] T2K, K. Abe et al., *Search for CP Violation in Neutrino and Antineutrino Oscillations by the T2K Experiment with* 2.2×10^{21} *Protons on Target*,
Phys. Rev. Lett. **121** (2018) p. 171802, arXiv: `1807.07891 [hep-ex]`.

[8] T2K, E. D. Zimmerman,
Neutrino Physics Results from T2K with 2.62×10^{21} *protons on target*,
PoS **NOW2018** (2019) p. 001.

[9] LHCb, A. A. Alves Jr. et al., *The LHCb Detector at the LHC*,
JINST **3** (2008) S08005.

[10] BaBar, D. Boutigny et al., "BaBar technical design report", *BaBar Technical Design Report EPAC Meeting Stanford, California, March 17-18, 1995*, 1995, `http://www.slac.stanford.edu/BFROOT/doc/TDR`.

[11] A. Abashian et al., *The Belle Detector*, Nucl. Instrum. Meth. **A479** (2002) p. 117.

[12] ATLAS, G. Aad et al.,
The ATLAS Experiment at the CERN Large Hadron Collider,
JINST **3** (2008) S08003.

[13] CMS, S. Chatrchyan et al., *The CMS Experiment at the CERN LHC*,
JINST **3** (2008) S08004.

[14] O. S. Bruning et al., *LHC Design Report Vol.1: The LHC Main Ring*, (2004).

[15] SuperKEKB, K. Akai, K. Furukawa, and H. Koiso, *SuperKEKB Collider*,
Nucl. Instrum. Meth. **A907** (2018) p. 188,
arXiv: `1809.01958 [physics.acc-ph]`.

[16] Belle-II, T. Abe et al., *Belle II Technical Design Report*, (2010),
arXiv: `1011.0352 [physics.ins-det]`.

[17] CERN, *'First turns' for SuperKEKB*, CERN Courier **56** (2016) p. 11,
`https://cds.cern.ch/record/2139891`.

[18] M. Thomson, *Modern particle physics*,
New York: Cambridge University Press, 2013, `http://www-spires.fnal.gov/spires/find/books/www?cl=QC793.2.T46::2013`.

[19] I. I. Bigi and A. I. Sanda, *CP Violation*, 2nd ed.,
Cambridge University Press, 2009.

[20] Y. Grossman, "Introduction to flavor physics",
Flavianet School on Flavour Physics Karlsruhe, Germany, September 7-18, 2009,
[,73(2014)], 2014 p. 111, arXiv: `1006.3534 [hep-ph]`.

[21] BaBar, D. Boutigny et al.,
"The BABAR physics book: Physics at an asymmetric *B* factory",
Workshop on Physics at an Asymmetric B Factory (BaBar Collaboration Meeting) Pasadena, California, September 22-24, 1997, 1998, `http://www-public.slac.stanford.edu/sciDoc/docMeta.aspx?slacPubNumber=SLAC-R-504`.

[22] T. Aushev et al., *Physics at Super B Factory*, (2010),
arXiv: `1002.5012 [hep-ex]`.

[23] Belle-II, W. Altmannshofer et al., *The Belle II Physics Book*, (2018), ed. by E. Kou and P. Urquijo, arXiv: `1808.10567 [hep-ex]`.

[24] E. Noether, *Invariant Variation Problems*, Gott. Nachr. **1918** (1918) p. 235, [Transp. Theory Statist. Phys.1,186(1971)], arXiv: `physics/0503066 [physics]`.

[25] C. S. Wu et al., *Experimental Test of Parity Conservation in Beta Decay*, Phys. Rev. **105** (1957) p. 1413.

[26] T. D. Lee, R. Oehme, and C.-N. Yang, *Remarks on Possible Noninvariance Under Time Reversal and Charge Conjugation*, Phys. Rev. **106** (1957) p. 340.

[27] A. D. Sakharov, *Violation of CP Invariance, C asymmetry, and baryon asymmetry of the universe*, Pisma Zh. Eksp. Teor. Fiz. **5** (1967) p. 32, [Usp. Fiz. Nauk161,no.5,61(1991)].

[28] N. Cabibbo, *Unitary Symmetry and Leptonic Decays*, Phys. Rev. Lett. **10** (1963) p. 531, [,648(1963)].

[29] S. L. Glashow, J. Iliopoulos, and L. Maiani, *Weak Interactions with Lepton-Hadron Symmetry*, Phys. Rev. **D2** (1970) p. 1285.

[30] L. Wolfenstein, *Parametrization of the Kobayashi-Maskawa Matrix*, Phys. Rev. Lett. **51** (1983) p. 1945.

[31] CKMfitter Group, J. Charles et al., *CP violation and the CKM matrix: Assessing the impact of the asymmetric B factories*, Eur. Phys. J. **C41** (2005) p. 1, updated results and plots available at: `http://ckmfitter.in2p3.fr`, arXiv: `hep-ph/0406184 [hep-ph]`.

[32] Particle Data Group, M. Tanabashi et al., *Review of Particle Physics*, Phys. Rev. **D98** (2018) p. 030001.

[33] Belle, K. Abe et al., *Improved measurement of CP-violation parameters* $\sin(2\phi_1)$ *and* $|\lambda|$*, B meson lifetimes, and* $B^0 - \overline{B}^0$ *mixing parameter* Δm_d, Phys. Rev. **D71** (2005) p. 072003, [Erratum: Phys. Rev.D71,079903(2005)], arXiv: `hep-ex/0408111 [hep-ex]`.

[34] I. Adachi et al., *Precise measurement of the CP violation parameter* $\sin(2\phi_1)$ *in* $B^0 \to (c\bar{c})K^0$ *decays*, Phys. Rev. Lett. **108** (2012) p. 171802, arXiv: `1201.4643 [hep-ex]`.

[35] LHCb, R. Aaij et al., *Observation of CP Violation in Charm Decays*, Phys. Rev. Lett. **122** (2019) p. 211803, arXiv: `1903.08726 [hep-ex]`.

[36] P. M. Lewis et al., *First Measurements of Beam Backgrounds at SuperKEKB*, Nucl. Instrum. Meth. **A914** (2019) p. 69, arXiv: `1802.01366 [physics.ins-det]`.

[37] Y. Ohnishi et al., *Accelerator design at SuperKEKB*, PTEP **2013** (2013) 03A011.

[38] SuperB, M. Bona et al., *SuperB: A High-Luminosity Asymmetric e^+e^- Super Flavor Factory. Conceptual Design Report*, (2007), arXiv: `0709.0451 [hep-ex]`.

[39] H. Wiedemann, *Particle Accelerator Physics*, Graduate Texts in Physics, Berlin, Germany: Springer, 2015, `http://www.springer.com/us/book/9783319183169?wt_mc=ThirdParty.SpringerLink.3.EPR653.About_eBook`.

[40] S. Myers and H. Schopper, eds., *Elementary Particles - Accelerators and Colliders*, vol. 21C, Landolt-Boernstein - Group I Elementary Particles, Nuclei and Atoms, Springer, 2013.

[41] A. W. Chao and M. Tigner, *Handbook of Accelerator Physics and Engineering*, Singapore: World Scientific, 1999, `https://cds.cern.ch/record/384825`.

[42] Y. Ohnishi et al., "Commissioning of the Phase-I SuperKEKB B-Factory and Update on the Overall Status", *Proceedings, 2nd North American Particle Accelerator Conference (NAPAC2016): Chicago, Illinois, USA, October 9-14, 2016*, 2017 MOB3IO01, `http://accelconf.web.cern.ch/AccelConf/napac2016/papers/mob3io01.pdf`.

[43] C. Kiesling, personal communication, 2018.

[44] H. Kaji, personal communication, 2019.

[45] M. Aiba, *Injection: Electron beams*, CERN Yellow Rep. School Proc. **5** (2018) p. 121.

[46] B. Goddard, "Injection and Extraction Techniques", *Elementary Particles - Accelerators and Colliders*, ed. by S. Myers and H. Schopper, 2013, `http://link.springer.com/chapter/10.1007%2F978-3-642-23053-0_8#page-1`.

[47] T. Mori et al., "Electron Beam Injection System for SuperKEKB Main Ring", *Proceedings, 5th International Particle Accelerator Conference (IPAC 2014): Dresden, Germany, June 15-20, 2014*, 2014 MOPRO025, `http://jacow.org/IPAC2014/papers/mopro025.pdf`.

[48] A. Piwinski, *The Touschek effect in strong focusing storage rings*, (1998), arXiv: `physics/9903034 [physics]`.

[49] SuperKEKB Commissioning Group, Belle II Commissioning Group, Y. Ohnishi, "Highlights from SuperKEKB Phase 2 Commissioning", *Proceedings, 62nd ICFA Advanced Beam Dynamics Workshop on High Luminosity Circular e^+e^- Colliders (eeFACT2018): Hong Kong, China, September 24-27, 2018*, 2019 MOXAA02, arXiv: `1904.10236 [physics.acc-ph]`.

[50] J. Kemmer and G. Lutz, *New detector concepts*, Nucl. Instrum. Meth. **A253** (1987) p. 365.

[51] F. Müller, *Characterization and optimization of the prototype DEPFET modules for the Belle II Pixel Vertex Detector*, PhD thesis, 2017, `http://nbn-resolving.de/urn:nbn:de:bvb:19-210714`.

[52] *Experimental Physics and Industrial Control System*, `https://epics.anl.gov/` (accessed on 07/16/2019).

[53] F. Simon, C. Soldner, and L. Weuste, *T3B — an experiment to measure the time structure of hadronic showers*, JINST **8** (2013) P12001, arXiv: `1309.6143 [physics.ins-det]`.

[54] CALICE, C. Adloff et al., *The Time Structure of Hadronic Showers in highly granular Calorimeters with Tungsten and Steel Absorbers*, JINST **9** (2014) P07022, arXiv: `1404.6454 [physics.ins-det]`.

[55] Y. Liu et al., "A Design of Scintillator Tiles Read Out by Surface-Mounted SiPMs for a Future Hadron Calorimeter", *Proceedings, 21st Symposium on Room-Temperature Semiconductor X-ray and Gamma-ray Detectors (RTSD 2014): Seattle, WA, USA, November 8-15, 2014*, 2016 p. 7431118, arXiv: `1512.05900 [physics.ins-det]`.

[56] F. Simon and C. Soldner, *Uniformity Studies of Scintillator Tiles directly coupled to SiPMs for Imaging Calorimetry*, Nucl.Instrum.Meth. **A620** (2010) p. 196, arXiv: `1001.4665 [physics.ins-det]`.

[57] NA62 Collaboration, F. Hahn et al., "NA62: Technical Design Document", tech. rep. NA62-10-07, CERN, 2010, `https://cds.cern.ch/record/1404985`.

[58] F. Simon, *Silicon Photomultipliers in Particle and Nuclear Physics*, Nucl. Instrum. Meth. **A926** (2019) p. 85, arXiv: `1811.03877 [physics.ins-det]`.

[59] Hamamatsu Photonics, *MPPC S13360-1325PE*, `https://www.hamamatsu.com/eu/en/product/type/S13360-1325PE/index.html` (accessed on 07/17/2019).

[60] 3M, *Daylighting Film DF20000MA*, `http://multimedia.3m.com/mws/media/746469O/3m-daylighting-film-df2000ma.pdf` (accessed on 07/18/2019).

[61] H. Windel, *Scintillator Tiles with SiPM Readout for Fast Timing in SuperKEKB Commissioning*, Master's thesis: Technische Universität München, 2017.

[62] Mini-Circuits, *ZFL-500+ Low Current, General Purpose Amplifier, 0.05 to 500 MHz*, `https://www.minicircuits.com/WebStore/dashboard.html?model=ZFL-500%2B` (accessed on 07/29/2019).

[63] Mini-Circuits, *HAT-20-75+ FXD ATTEN / BNC / RoHS*, `https://www.minicircuits.com/WebStore/dashboard.html?model=HAT-20-75%2B` (accessed on 07/29/2019).

[64] Pico Technology, *PicoScope 6000 Series*, `https://www.picotech.com/oscilloscope/6000/picoscope-6000-overview` (accessed on 06/01/2018).

[65] FUJITSU, *FUJITSU Workstation CELSIUS C740*, `https://www.fujitsu.com/fts/products/computing/pc/workstations/celsius-c740/` (accessed on 07/29/2019).

[66] Keysight Technologies, *N6700B Low-Profile Modular Power System Mainframe*, `https://www.keysight.com/de/pd-838422-pn-N6700B/low-profile-modular-power-system-mainframe-400w-4-slots?cc=DE&lc=ger&lsrch=true&searchT=N6700B` (accessed on 07/19/2019).

[67] *PCASpy*, `https://github.com/paulscherrerinstitute/pcaspy` (accessed on 07/29/2019).

[68] *Control System Studio*, `http://controlsystemstudio.org/` (accessed on 07/29/2019).

[69] R. Brun and F. Rademakers, *ROOT: An object oriented data analysis framework*, Nucl. Instrum. Meth. **A389** (1997) p. 81.

[70] *GSL-GNU Scientific Library*, `https://www.gnu.org/software/gsl/` (accessed on 07/03/2018).

[71] *OpenMP*, `https://www.openmp.org/` (accessed on 06/28/2018).

[72] M. Kattau, *Bestimmung der Zeitauflösung von Szintillatorkacheln mit Silizium-Photomultipliern anhand kosmischer Myonen*, Bachelor's Thesis: Technische Universität München, 2016.

[73] J. R. Taylor, *An Introduction to Error Analysis*, 2nd ed., University Science Books, 1997.

[74] J. W. Flanagan et al., *Observation of Vertical Betatron Sideband due to Electron Clouds in the KEKB Low Energy Ring*, Phys. Rev. Lett. **94** (2005) p. 054801, arXiv: `physics/0407149 [physics]`.

[75] O. Gröbner et al., *Studies of photon induced gas desorption using synchrotron radiation*, Vacuum **33** (1983) p. 397, `http://www.sciencedirect.com/science/article/pii/0042207X83906590`.

[76] *Strategic Accelerator Design*, `http://acc-physics.kek.jp/SAD/` (accessed on 01/08/2019).

[77] R. Landau, M. Paez, and C. Bordeianu, *Computational Physics: Problem Solving with Computers*, Wiley, 2007, `https://books.google.de/books?id=RBg-vgAACAAJ`.

[78] *Geant4*, `https://geant4.web.cern.ch/` (accessed on 08/21/2019).

Acknowledgements

Finally, I would like to express my gratitude to all the people that supported me throughout this thesis and my time at the Max Planck Institute for Physics (MPP).

First and foremost I would like to thank my supervisor Frank Simon. It is safe to say that I could not have done this thesis without him. I am deeply thankful for all the knowledge, wisdom and support he gave me throughout these many years and for all the things he taught me about physics, Lufthansa and so much more. And of course, thank you for the many hours spent for proof-reading my thesis.
I would also like to express my gratitude to Prof. Allen Caldwell for accepting me as a PhD student and for giving me the opportunity for this thesis. I am also grateful for inspiring my interest in statistics and introducing me to the next level of data analysis. And of course, thank you to Prof. Christian Kiesling for his guidance and lectures over the years and for proof-reading parts of my thesis.
Furthermore, I would like to thank my collaborators Alexandre Beaulieu, Michael Hedges, Igal Jaegle, Sam de Jong, Christian Kiesling, Peter Lewis, Hiro Nakayama, Riccardo de Sangro, Sven Vahsen, Hendrik Windel and all the other people working with me on BEAST and the commissioning of SuperKEKB. Peter, it has been a pleasure spending so many nights and days in paradise with you. Thank you Alex, Michael and Hendrik for filling up my progress bar every now and then. Thanks to all my colleagues in the Future Detectors and Belle groups for enriching my day to day life during the numerous lunch and coffee breaks, while playing a kicker match and during so many fruitful discussions. A special thanks goes to Hendrik, my office mate and BEAST partner. Thank you for all the fun and the awesome memories and for making this project such a pleasure to work on.
While being at the MPP, I had the honor to serve as one of the PhD representatives. I would like to thank the other reps and all the other people involved for making this such an outstanding experience for me.

Moreover, I would like to thank all of my friends and especially my flatmates Basti, Domi, Julia and Stine for still being friends with me despite me ditching you so many times because of this thesis.

Finally, I would like to thank Isabella and Karolina Gabriel for their unlimited support, no matter how hard the times have been, and last but not least, thank you Katha! Thank you for proof-reading my thesis, thank you for supporting me throughout this stressful time and thank you for being there for me when I needed it. I can't tell you what it means to me to have you in my life.